

**DYNAMICS OF DROP DEFORMATION AND BREAKUP
IN TIME-DEPENDENT FLOWS AT LOW REYNOLDS NUMBERS**

Thesis by
Howard Alvin Stone

*In Partial Fulfillment of the Requirements
for the Degree of
Doctor of Philosophy*

California Institute of Technology
Pasadena, California

1988

(Submitted January 12, 1988)

To my parents

ACKNOWLEDGEMENTS

There are many people who have contributed knowingly, or unknowingly, to the completion of thesis. First of all, I would like to take this opportunity to thank my advisor, Professor Gary Leal, for his support, advice, the confidence he has shown in me and, most of all, his friendship. I have benefitted personally very much from my interaction with Gary. In addition, I am indebted to Professor John Brady for his patient explanation of many basic principles and for taking the time to share his many ideas. Barry Bentley not only showed great patience with me as I was beginning my research, but also he built a unique experiment that survived my graduate years and he (and the apparatus) taught me much about experimental work.

The Caltech community has been very supportive during my graduate years. I feel very fortunate to have had the opportunity to be a part of Caltech. It is a very special learning and research environment with many avenues for scientific enlightenment. My financial support has come from a variety of sources, including Shell Oil Company, IBM and the Chemical Engineering Department. This research was supported by NSF. To all of these organizations I say thank you.

My friends have always been very supportive and understanding. To my housemates over these past few years: Tom DiChristina, Chris Chow, Keith Bentley, Mike Chobotov and Tina Morris - I feel very fortunate to have shared time with you. Each of you constantly amazed me with your unique and well-rounded personalities and talents. I am lucky indeed if some of it has rubbed off.

The members of the Leal, Herbolzheimer and Brady groups have taught me more fluid mechanics than I ever dreamed of knowing. They have shared their time and thoughts with me and have improved my ability to analyze and solve problems. Other members of the Chemical Engineering Department and from around Caltech have been good friends and never missed an opportunity to contribute to my education (scientific or otherwise). Among those that deserve

special mention: Jim Stoos and his wife Ruth, Roger Bonnezaze, Lou Durlinsky, Dave Dandy and Sonia Kreidenweis-Dandy, Ed Ascoli, Ardith El Kareh, In Seok Kang, Seung Man Yang, Ron Lagnado and Enrique Geffroy-Aguilar. Buddie Mullins was always available for discussions and continually sought to broaden my thinking and John Doyle allowed me access to his computer.

In addition, I must acknowledge the contributions from my friends outside Caltech, especially those who have stayed in touch over the years. They have helped me to grow in so many ways and constantly reminded that there is more to life than science. Special thanks to Tom and Kelly Williams for their companionship, to Deanna Mah for her many words of encouragement over the years and to Lila Basilgo for her special friendship.

Along the way to graduate school I have been very lucky to have had many outstanding teachers. UC Davis deserves special recognition for creating an environment that I found very attractive for learning. Foremost among my teachers there, I must mention Stephen Whitaker for his special concern and approach to education. He demonstrates that outstanding teachers do indeed make a difference.

Finally, I wish to thank my family, especially my parents, for their continual support. Although they couldn't always appreciate the highs and lows of graduate school, their support was constant and they never questioned my goals.

ABSTRACT

This thesis is concerned with time-dependent free-boundary problems at low Reynolds numbers. The primary objective is to use a combined experimental and numerical investigation to examine the deformation and breakup characteristics of a single phase Newtonian liquid drop suspended in a second immiscible Newtonian fluid undergoing a prescribed linear flow. Two related studies grew naturally out of this work and are also discussed here: (1) an analytic and numerical examination of the behaviour of concentric double emulsion droplets in linear flows, and (2) an introduction to the effect surfactants have on drop deformation in extensional flows.

Specifically, the breakup of a Newtonian liquid drop is studied under well-defined flow conditions. Experiments are performed in a computer-controlled four-roll mill and a detailed numerical investigation using the boundary integral method is presented. Particular attention is given to the dynamics of drop breakup and many experimental and numerical examples are shown of the actual fragmentation process. Transient effects associated both with nonspherical initial shapes and time-dependent velocity gradients are studied. Although the time-dependent velocity fields are limited to step changes in flow conditions, these investigations provide valuable insight into the breakup phenomenon and are a necessary first step toward understanding more complicated flow situations. The effects of viscosity ratio, flow-type and capillary number are discussed thoroughly. Overall, these studies of drop breakup provide a nice illustration of the influence of an interfacial-tension-driven flow that arises because of curvature variations along the fluid-fluid interface (the interfacial tension is constant). The interaction of this interfacial-tension-driven flow with the prescribed time-dependent velocity field produces very interesting breakup processes, often without large scale stretching of the drop. Also, for highly elongated drops, finite-amplitude capillary waves are observed experimentally and numerically.

The study of drop deformation and breakup leads naturally to considera-

tion of other systems involving deformable microstructures. Double emulsion droplets, which arise in applications involving liquid membranes, are frequently treated by drawing analogies with the known behaviour of single phase droplets. We present a fundamental investigation of concentric double emulsion drops in extensional flows. The analytic results allow calculation of the first effects of flow-induced deformation and the effective viscosity of a dilute emulsion of these particles. The analysis suggests interesting deformation and interaction of the two drop surfaces so a numerical investigation of the finite deformation of these particles is described. The critical capillary number for breakup is determined, the dependence on physical and flow parameters is outlined and possible mechanisms for breakup are discussed that differ from the single phase droplet results. Finally, the effect of different flow-types, i.e., uniaxial or biaxial extensional flows, is shown in some instances to suggest breakup of the inner droplet even though the outer droplet maintains a steady shape.

The thesis closes with an introduction to the effect surface-active agents have on drop deformation. Because the distribution of surfactant along the fluid-fluid interface produces interfacial tension variations, the calculation of the drop shape as a function of time is intimately coupled with the convection and diffusion of surfactant along the drop surface. We present an approximate numerical procedure to study finite deformations and surfactant transport. The results are not extensive but suggest several interesting aspects of the deformation of drops due to the presence of surfactant.

Table of Contents

Dedication	ii
Acknowledgements	iii
Thesis Abstract	v
CHAPTER 1. Thesis Introduction	1
References	8
CHAPTER 2. An Experimental Study of Transient Effects in the Breakup of Viscous Drops	9
Abstract	11
1. Introduction	12
2. Problem Statement	15
3. The Experiment	17
3.1 Data analysis using digital image processing	19
3.2 Procedure	20
4. Results	22
4.1 Qualitative behaviour	22
4.2 Effect of flow-type	24
4.3 Effect of viscosity ratio	26
4.4 Effect of L/a ; critical elongation necessary to ensure breakup once the flow is stopped	28
4.5 Capillary waves	30
5. Discussion	33
5.1 A qualitative description of end pinching	33
5.2 Numerical solution of the motion of an elongated drop via the boundary integral method	36
References	40
Figure Captions	43
Figures	45
CHAPTER 3. Relaxation and Breakup of an Initially Extended Drop in an Otherwise Quiescent Fluid	65
Abstract	67
1. Introduction	68
2. Numerical Procedure / Implementation	73
3. Results	81

3.1	Comparison with small deformation theory	81
3.2	Relaxation of highly extended droplets : the effects of viscosity ratio and initial shape	83
3.2.1.	$\lambda > O(0.05)$; shapes with bulbous ends	84
3.2.2.	$\lambda < O(0.01)$; shapes with nearly pointed ends	87
3.2.3.	The mechanism of end pinching	88
3.2.4.	Quantitative comparison of experimental and theoretical results	90
3.3	Capillary waves	91
	References	101
	Figure Captions	104
	Figures	108
CHAPTER 4: The Influence of Initial Deformation on Drop Breakup in Subcritical Time-Dependent Flows at Low Reynolds Numbers		126
	Abstract	128
1.	Introduction	129
2.	Problem Statement	134
3.	The Experiment	136
4.	Numerical Procedure	138
5.	Results/Discussion	140
5.1	Step changes in shear rate; flow-type constant	140
5.2	Step changes in flow-type; shear rate constant	149
5.3	Simultaneous changes in flow-type and shear rate	151
5.4	Numerical study of step changes	155
5.5	Breakup for large λ in weak flows with vorticity	161
6.	Conclusions	162
	References	164
	Figure Captions	167
	Figures	171
CHAPTER 5 : Breakup of Concentric Double Emulsion Droplets in Linear Flows		206
	Abstract	208
1.	Introduction	209
2.	Problem Statement	214
3.	Small Deformation Analysis	217
3.1	Analytic solution	218
3.2	Results	225
4.	Numerical Study of Highly Deformed Globules	231

4.1 Numerical scheme - application of the boundary integral method	231
4.2 Results of the numerical investigation	236
Appendix A	244
Appendix B	245
References	247
Figure Captions	252
Figures	254
CHAPTER 6 : A Numerical Study of the Effect of Surfactants on Drop Deformation and Breakup	281
Abstract	282
1. Introduction	283
2. Problem Statement	287
3. Numerical Method / Implementation	292
3.1 Calculation of the interfacial velocity using the boundary integral method	292
3.2 Calculation of the surfactant distribution using the convective-diffusion equation	295
3.3 Approximate numerical procedure to solve the coupled system of equations	298
4. Results	300
4.1 Convergence of the numerical method	300
4.2 Initial observations	301
4.3 The effect of Pe_s	302
5. Conclusions	303
References	304
Figure Captions	308
Figures	309
CHAPTER 7 : Thesis Summary	319
APPENDIX 1 : Drop Deformation in Biaxial Flows	324
1. Introduction	325
2. Numerical Procedure	328
3. Results / Discussion	330
3.1 Steady-state calculations	330
3.2 Transient effects	332
4. Conclusions	335
References	336
Figure Captions	337
Figures	339

APPENDIX 2 : Implementing the Boundary Integral Method	348
1. Governing Equations	349
2. Simplification for Axisymmetric Problems	352
3. Discretization of the Integral Equations	355
References	359

CHAPTER 1

THESIS INTRODUCTION

In this thesis we are interested in the deformation and breakup of Newtonian liquid droplets at low Reynolds numbers. Our focus will be on the dynamics of the breakup process. Both experimental and numerical investigations will be used to detail and understand qualitative and quantitative features of this problem. We also include two extensions of these ideas to related topics: (1) deformation and breakup of concentric double emulsion droplets and (2) an introduction to the effects surface-active agents have on drop deformation in extensional flows.

There exist many industrial processes that use studies of drop deformation as a prototype. For example, the classical motivation for this research includes applications to the mixing of immiscible liquids, the blending of polymers, the dispersion of agglomerates of small particles in fluids, and the desire to obtain a better understanding of the complex rheology of fluids with a deformable microstructure.

In addition to many of the practical concerns outlined above, the study of drop deformation remains a classical example of a free-boundary problem in fluid mechanics. The deformable nature of the fluid-fluid interface implies that the interface location is a priori unknown. Therefore, instead of being given the boundary location as part of the problem statement, the boundary location must be found as part of the problem solution. Perturbation methods have been in use for many years to describe shapes that depart only a little from a known equilibrium shape (e.g., a sphere, cylinder or plane), but it has only been in recent years that efficient numerical methods capable of describing finite deformation have been developed. In this thesis we will use the boundary integral method to study time-dependent, finite deformation and breakup of droplets in extensional flows.

Basic research concerning the fluid dynamics of drop deformation began with two classic papers by G.I. Taylor in the 1930s. Taylor, who was interested in the study of emulsions, distilled the complicated problem of emulsification

down to the meaningful and relatively straightforward analysis of a single droplet suspended in a second immiscible fluid undergoing a prescribed linear flow. The observations and results of Taylor's investigations serve as the starting point for more than 50 years of drop deformation research reported in the fluid mechanics literature, in addition to remaining among the most important and relevant results in the field. An early overview of drop breakup phenomena is given by Hinze (1955). Experimental, numerical and theoretical studies describing much of the recent work have been summarized in two excellent review articles by Acrivos (1983) and Rallison (1984). A related work that makes a more direct connection with actual applications, particularly polymer blending processes, has been written by Han (1981).

Physically, the problem of drop deformation would appear to be straightforward. A droplet immersed in a nonuniform velocity field will deform because of viscous stresses exerted on the fluid-fluid surface. The deformation is resisted by interfacial tension. If the velocity gradient is sufficiently large, in most instances the drop cannot maintain a steady shape, but rather begins to continually stretch in the flow. In the literature, this nonexistence of a steady drop shape is generally called "drop burst" or "drop breakup." Since the stretching process produces shapes that are roughly cylindrical near the middle of the drop, a common approach used to predict drop size distributions is to study the capillary instability of an infinite fluid cylinder. However, it should be stated clearly that there exist in the literature very few direct observations of the drop breakup process for *finitely* deformed drops. Furthermore, there are two aspects related to transient drop deformation that have received very little attention in the literature and deserve further investigation; namely, the effect of time-dependent velocity gradients and the effect of nonspherical initial shapes, which drive motion even in the absence of any external flow. Han (1981) makes this point very clear when discussing how the prototypical steady-state drop deformation studies may apply to real systems.

Therefore, the goal of the research reported in this thesis is to obtain a better understanding of drop breakup with particular attention given to the effect of simple time-dependent flows and to a description of the mechanism of drop breakup. Although only step changes in flow conditions will be examined, such experiments are a necessary first step toward understanding more complicated transient flows. Overall, these studies will include both experimental and numerical investigations of drop breakup in well-defined flow conditions.

The experiments are performed in a computer-controlled four-roll mill, designed and constructed by Barry Bentley as part of his PhD research. A detailed description of the design and operation of this device can be found in Bentley's PhD thesis (1985). The four-roll mill is ideal for studying particle deformation and breakup in linear flows where the magnitude of strain rate exceeds that of the vorticity (so-called "strong" flows). The computer-controlled apparatus allows these studies to be performed in well-controlled steady-state and transient flow fields.

One modification to the experiment that we have introduced in this thesis is the development of a technique to store and analyze digital images of the deformed drop. Previously, drop deformation as a function of time was monitored using 35 mm photographs. For the large number of experiments it is necessary to perform in this study of time-dependent effects, the use of digital image analysis is an important step in monitoring the rapid changes that occur during the deformation and breakup of the drop. The implementation of this procedure is discussed in more detail in Chapter 2.

In order to understand the details of the experimental observations, a complementary numerical investigation based on the boundary integral method is described. The boundary integral method is a powerful method for solving time-dependent free-boundary problems. This technique provides a clear picture of the evolution of the interface during the breakup process, even for the highly distorted drop shapes examined here, and the associated velocity fields internal

and external to the droplet are illustrated in order to better understand the mechanism of breakup.

The net result of the studies described in Chapters 2-4 is a much improved understanding of drop breakup, including a description of effects associated with (simple) time-dependent flows. The experimental and numerical investigations allow for a complete study of the effects of nonspherical initial shapes, the viscosity ratio of the two fluids, the flow-type of the external flow, and the capillary number. The role of capillary waves is examined also.

The final two chapters of this thesis describe how the methodologies used in the course of this research and the understanding that developed as a result of this research, can be extended to two other interesting free-boundary problems. In Chapter 5 we examine the deformation and breakup of concentric double emulsion droplets. An analytic solution is developed to study nearly spherical compound drops and a complete numerical solution, again applying the boundary integral method, is described to account for finite deformation and possible mechanisms of breakup. In Chapter 6 we provide an introduction to the effect surfactants have on drop deformation in extensional flows. This is a very difficult problem and, although the numerical procedure used is approximate, it provides valuable insight concerning the behaviour of finitely deformed drops that have interfacial tension variations produced by the distribution of surfactant along the fluid-fluid interface.

For the most part, each chapter is selfcontained with its own abstract, introduction, description of experimental and numerical methods, and results section. In Appendix 1 of this thesis the little studied problem of drop breakup in *biaxial* flows is discussed and in Appendix 2 a complete description of the boundary integral method is provided to bridge the gap between the discussion in the text and actual numerical implementation.

Rather remarkably, the fundamental studies mentioned above, are finding applications outside of the classical fluid mechanics arena. The ideas that have

developed from the basic research involving drop deformation are currently being used, and may prove to be potentially useful, in such varied disciplines as material science, biology and geology. In all of these fields, there will often be a complex deformable microstructure whose response must be understood in order to predict system behaviour, characterize bulk properties, etc.

For example, Stookey & Araujo (1968) have studied the deformation of silver particles imbedded in a glass matrix and Seward (1974) has studied phase separated glass materials (a glass matrix with very small second phase glass particles imbedded in it). When the matrix is elongated, the discrete phase is also elongated, sometimes being stretched into a long thread-like shape. Under the conditions of the experiment both phases behave like Newtonian fluids. Upon removal of the applied force, small droplets of the second phase glass are formed by the disintegration of the narrow thread. In almost all cases, this breakup process did not occur uniformly along the thread, but rather was confined to the *end* of the thread (Seward 1974). These observations are very similar to experimental and numerical observations of the breakup of elongated droplets that we discuss in Chapters 2 and 3.

From a biological view point, some aspects of the behaviour and deformation of cells, especially red blood cells, can be usefully studied with the understanding and methods developed in fundamental studies of drop deformation. A general discussion of some of these ideas is given by Goldsmith & Skalak (1975) and a recent mechanical model of a cell as a drop with an elastic membrane is discussed by Barthes-Biesel (1980). Additional discussion of the deformation of cells and the role it plays in transport processes in the microcirculation is provided by Caro, Pedley, Schroter & Seed (1978). Although no direct reference to the fluid mechanics literature is given by Caro *et al.*, it would appear that techniques developed to examine deformation of a liquid drop may prove useful in this context also.

Finally, there is even mention recently in the geology literature of ideas con-

cerning the information that can be extracted by accounting for the deformation of droplets during studies of the flow of immiscible liquids†.

It is our hope that some of the ideas introduced in this thesis may prove to be useful in related problems areas as well.

† We wish to thank Ichiro Sugioka, a graduate student in Aeronautics, for bringing this line of thought to our attention.

REFERENCES

- Acrivos, A. 1983 The breakup of small drops and bubbles in shear flows. *4th Int Conf. on Physicochemical Hydrodynamics, Ann. N.Y. Acad. Sci.* **404**, 1-11.
- Barthes-Biesel, D. 1980 Motion of a spherical microcapsule freely suspended in a linear shear flow. *J. Fluid Mech.* **100**, 831-853.
- Bentley, B.J. 1985 *Drop deformation and burst in two-dimensional flows*. PhD. Dissertation. California Institute of Technology.
- Caro, C.G., Pedley, T.J., Schroter, R.C. and Seed, W.A. 1978 *The Mechanics of the Circulation*. Oxford University Press.
- Goldsmith, H.L. & Skalak, R. 1975 Hemodynamics. *Ann. Rev. Fluid Mech.* **7**, 213-247.
- Han, C.D. 1981 *Multiphase Flow in Polymer Processing*. Academic Press.
- Hinze, J.O. 1955 Fundamentals of the hydrodynamic mechanism of splitting in dispersion processes. *AIChE J.* **1**, 289-295.
- Rallison, J.M. 1984 The deformation of small viscous drops and bubbles in shear flows. *Ann. Rev. Fluid Mech.* **16**, 45-66.
- Seward III, T.P. 1974 Elongation and spheroidization of phase-separated particles in glass. *J. Non-Crystalline Solids* **15**, 487-504.
- Stookey, S.D. & Araujo, R.J. 1968 Selective polarization of light due to adsorption by small elongated silver particles in glass. *Applied Optics* **7**, 777-779.
- Taylor, G.I. 1932 The viscosity of a fluid containing small drops of another fluid. *Proc. R. Soc. Lond.* **A138**, 41-48.
- Taylor, G.I. 1934 The formation of emulsions in definable fields of flow. *Proc. R. Soc. Lond.* **A146**, 501-523.

CHAPTER 2

AN EXPERIMENTAL STUDY OF TRANSIENT EFFECTS IN THE BREAKUP OF VISCOUS DROPS

The basic text of Chapter 2 consists of an article which appeared in the G.I. Taylor Centenary Symposium of the *Journal of Fluid Mechanics*, Volume 173, pages 131-158, December 1986.

**An experimental study of transient effects
in the breakup of viscous drops**

H. A. Stone, B. J. Bentley[†] and L. G. Leal

Department of Chemical Engineering

California Institute of Technology

Pasadena, California 91125

March 1986

[†] Current address: Bentley Systems, Inc., 180 Gordon Dr., Lionville, PA
19353

ABSTRACT

A computer-controlled four-roll mill is used to examine two transient modes of deformation of a liquid drop: elongation in a steady flow and interfacial-tension-driven motion which occurs after the flow is stopped abruptly. For modest extensions, drop breakup does not occur with the flow on, but may occur following cessation of the flow as a result of deterministic flows associated with internal pressure gradients established by capillary forces. These relaxation and breakup phenomena depend on the initial drop shape and the relative viscosities of the two fluids. Capillary wave instabilities at the fluid-fluid interface are observed only for highly elongated drops. This study is a natural extension of G. I. Taylor's original studies of the deformation and burst of droplets in well-defined flow fields.

1. INTRODUCTION

Basic research on the deformation and breakup of a liquid drop due to the motion of an immiscible, viscous suspending fluid dates back to the pioneering work of G. I. Taylor (1932, 1934, 1964). The problem is of considerable fundamental interest in fluid mechanics as an example of a time-dependent free-boundary problem and as a prototype for flow-induced deformation of a variety of flexible bodies such as red-blood cells, macromolecules, flocs, elastic particles, etc. It is also closely related to dispersion processes in commercial blenders and mechanical emulsifiers. As a consequence, many investigations have appeared since Taylor's original papers. Two excellent reviews by Acrivos (1983) and Rallison (1984) provide a comprehensive description of this more recent work.

The remarkable feature of Taylor's early investigations is that he actually discovered most of the interesting phenomena that are characteristic of drop deformation and breakup in steady flows. However, to stop at this point in a description of Taylor's contribution to the drop deformation and breakup problem does not do justice to the importance of his work. To experimentally simulate a planar extensional flow, Taylor invented the four-roll mill, which has subsequently been used in many laboratories for studies of drop breakup, extension of macromolecules, floc stability, and many related topics. To provide a theoretical description of small deformations of the drop, Taylor used the asymptotic method of domain perturbations. Later, to describe the motion of the highly elongated shapes characteristic of low viscosity drops, Taylor pioneered slender-body theory for low Reynolds number flow.

Taylor's (1934) experimental observations in steady simple shear and planar extensional flows show clearly that drops at first deform under the combined action of viscous and pressure forces through a series of steady shapes as the shear rate is increased, until finally a point of maximum steady deformation is reached beyond which further increases in the shear rate usually lead to a transient, steadily increasing extension of the drop with time. As Taylor was

first to note, however, there is a fundamental difference between simple shear flow and two-dimensional extensional flow. In particular, a drop with a viscosity that exceeds the suspending fluid viscosity by more than approximately a factor of 4 does not become stretched in simple shear flow, but rather achieves a steady, slightly deformed shape for all large shear rates. Thus, at low Reynolds number, it is impossible to break a sufficiently viscous drop in steady, simple shear flow regardless how large the shear rate becomes. In two-dimensional extensional flow, on the other hand, drops of any viscosity ratio extend continuously so long as the strain rate exceeds a certain critical value. This fundamental distinction, first discovered by Taylor, between simple shear flow and planar extensional flow is of considerable practical importance despite the restriction to low Reynolds numbers, simply because the drops that we attempt to break in blending devices are frequently very small, and are thus characterized by low Reynolds numbers.

In spite of the major accomplishments of Taylor and subsequent researchers over the intervening 50 years, however, many important qualitative questions remain to be answered:

- (a) What is the role of flow-type in the deformation and breakup processes? In particular, what is the nature of the transition between simple shear and two-dimensional extensional flows?
- (b) What are the mechanisms for breakup and how do they depend on the parameters of the system, including the degree of deformation of the drop?
- (c) What is the role of flow transients in the deformation and breakup processes?
- (d) What is the role of rheology if one or both fluids are non-Newtonian?

The research reported here and in two earlier publications from our laboratory (Bentley & Leal, 1986a,b) represent the first steps in a series of experimental (and theoretical) studies that are designed to address these and related questions. These experiments are based upon a computer-controlled version of Taylor's four-roll mill designed to maintain the drop at the stagnation point of

the flow, with minimal disturbance, for either steady or unsteady flows. The complete spectrum of linear, two-dimensional flows can be generated from pure rotation to two-dimensional straining flow (the latter being the only motion studied by Taylor with the four-roll mill). A complete description of this device was published by us in our earlier paper, Bentley & Leal (1986a).

In our initial investigation, Bentley & Leal (1986b), we studied the steady state shape and orientation for drops in five different types of steady two-dimensional flows, from pure extension ('hyperbolic flow') to a flow with only slightly more strain than vorticity and for drops with viscosity ranging from 10^{-3} to 10^2 that of the suspending fluid. Critical conditions for breakup were also determined for all these cases, the critical condition being identified as the capillary number (dimensionless shear rate) beyond which the drop undergoes continuous extension. The Bentley-Leal study of drop deformation in steady flows was a natural outgrowth of preceding research in the field and concentrated mainly on the measurement and prediction of steady shapes and of conditions where steady shapes could not be achieved in steady flows.

The present paper represents a first step toward generalization of preceding studies to investigate transient effects on the deformation and breakup of a liquid drop. In particular, we examine the continuous elongation of a liquid drop for steady two-dimensional flows at capillary numbers (shear rates) that are equal to or slightly above the critical value for 'breakup', and, the subsequent interfacial-tension-driven relaxation of the extended drop when the flow is stopped abruptly. Relatively few previous studies have examined any aspect of time-dependent behaviour in the deformation and breakup process. Capillary wave instability on infinite, stationary fluid cylinders has been considered by Tomotika (1935), Rumscheidt & Mason (1962), Lee & Flumerfelt (1981) and Lee, Yu & Flumerfelt (1981), while Tomotika (1936) and Mikami, Cox & Mason (1975) have studied capillary wave growth on extending fluid threads of infinite length. Of course, extended drops differ from an infinite cylinder in the sense that they are always

closed at their ends, and thus do not represent a possible equilibrium state. We shall see that the final drop length plays a critical role in both the extension of the drop and its relaxation when the flow is removed, with the result that capillary wave instability plays a role only if the droplets are extremely elongated. The closest experimental study to that reported here is due to Grace (1971), who reports data on the elongation necessary to achieve rupture in the relaxation process, the resulting drop-size distribution, and some interesting effects due to abrupt changes in shear-rate for simple shear and planar extensional flows. Torza, Cox & Mason (1972) also investigated experimentally some effects of the time-history of the flow field. From a theoretical point of view, three types of analyses have been used to study transient phenomena. Hinch & Acrivos (1980) and Hinch (1980) used slender-body theory to investigate the behaviour of low-viscosity drops, and found that the equilibrium shapes corresponding to subcritical shear rates were accessible only if the shear rate was increased slowly. It was also shown that the existence of a waist in the initial shape always led to breakup. Nearly spherical drops of arbitrary viscosity ratio were studied via domain perturbation techniques by Cox (1969) and Rallison (1980), and shown to attain steady shapes in an oscillatory manner in flows with vorticity. Finally, Rallison & Acrivos (1978) and Rallison (1981) have used the boundary integral method to investigate some aspects of the time evolution of the drop shape and observed that the critical shear rate and mode of drop burst depended on the history of the flow.

2. PROBLEM STATEMENT

We consider a Newtonian liquid droplet, with undeformed radius a , density $\hat{\rho}$, and viscosity $\hat{\mu}$, suspended in a second immiscible Newtonian fluid of density ρ and viscosity μ , which is undergoing a linear, two-dimensional flow at infinity. The undisturbed velocity field is $\mathbf{u} = \mathbf{\Gamma} \cdot \mathbf{x}$, where the velocity gradient tensor

Γ is

$$\Gamma = \frac{G}{2} \begin{pmatrix} 1 + \alpha & 1 - \alpha & 0 \\ -1 + \alpha & -1 - \alpha & 0 \\ 0 & 0 & 0 \end{pmatrix} \quad (1)$$

with α being a 'flow-type' parameter and G the fluid shear rate. An approximation to this flow field is generated near the center of a four-roll mill. The flow-type parameter α provides a measure of the ratio of the rate of strain relative to the vorticity in the undisturbed flow and varies between $\alpha = +1.0$, a hyperbolic (or extensional) flow, and $\alpha = -1.0$, a purely rotational flow. Simple shear flow corresponds to $\alpha = 0.0$. We will be interested in flows with $\alpha > 0$, the so-called 'strong' flows, as they are capable of producing the greatest deformation for a given value of G . The streamlines for several of these flows are illustrated in figure 1. The fluid-fluid interface is characterized by a constant interfacial tension σ .

Provided the Reynolds number $\frac{\rho G a^2}{\mu}$ is sufficiently small, the behaviour of a neutrally buoyant drop in a steady flow can be characterized by three dimensionless parameters: the viscosity ratio $\lambda = \frac{\mu}{\mu}$, the capillary number $C = \frac{\mu G a}{\sigma}$ (which provides a measure of viscous forces causing deformation relative to interfacial tension forces which resist deformation), and the flow-type parameter α . The orientation of the drop relative to the principal axis of strain (in our device, this is the x-axis for all flow types) is denoted by θ and is sketched in figure 2. Two scalar deformation measures have been used in drop deformation studies and are also shown in figure 2. These are: $D = \frac{L-B}{L+B}$, where L and B are the half-length and half-breadth of the drop, respectively, which is appropriate for mildly deformed drops; and L/a , the elongation ratio, which is appropriate for highly extended drops. As discussed by Bentley & Leal (1986b), the orientation angle is important because the effectiveness of a particular flow in deforming the drop depends on the orientation of the drop relative to the principal axis of strain of Γ . This same concept will arise later when we consider the transient elongation of drops in steady flows characterized by different flow types.

For sufficiently small values of the capillary number C a steady drop shape exists in a steady two-dimensional flow for all α and λ . Indeed, for each flow type $\alpha \neq 1$, there exists a viscosity ratio above which the drop attains a steady shape for any value of the capillary number (provided, of course, that the Reynolds number remains small). In such cases, drop burst is impossible. In the majority of cases, though, there exists a critical capillary number above which a steady drop shape no longer exists and viscous forces cause the drop to continually elongate. This transient deformation is examined in the present study. If at some time during this elongation process the flow is stopped, the problem becomes that of an extended liquid drop suspended in a fluid that is otherwise quiescent. Because the extended drop is not an equilibrium shape, an evolutionary, interfacial-tension-driven flow occurs and the drop rapidly changes shape, either returning to a sphere or breaking into smaller drops via a complicated, time-dependent motion. The entire dynamics of this interfacial-tension-driven flow are characterized by the viscosity ratio and the initial drop shape, and this includes the determination of whether the drop breaks or returns to its native spherical shape. Interfacial tension determines the velocity scale for the drop's motion, and hence the time scale of the relaxation or breakup process, but has no role in determining the qualitative characteristics of the phenomena. In the present study we examine this evolution of extended drops as a function of both viscosity ratio and initial elongation ratio L/a at the time flow is stopped. One objective is to determine the elongation ratio that is necessary if the drop is to break, including any dependence of this critical condition on the viscosity ratio or the flow-type during the elongation process (the latter presumably affecting the initial elongated shape).

3. THE EXPERIMENT

The experiments reported in this paper were performed using the computer-controlled four-roll mill described previously (Bentley & Leal, 1986a). Here, we discuss only those features of the device that are important to the present work.

The drop position in the device is sensed using a digital television camera. A minicomputer uses the digital representation of the drop to determine the location of its center of mass. A control scheme which models the response of the flow to changes in roller speed and the drop's response to changes in the flow field then regulates the speeds of the rollers in order to maintain the drop at the center of the device, under the constraint that the shear rate G and flow type α remain constant. Typically, about five control cycles occur each second.

Since the drop position is controlled via small but finite modifications of the flow several times per second, an obvious question is whether these changes introduce any discernible change in the shape of the drop. A qualitative indication of the success of the control scheme is illustrated by the sharp fluid-fluid interfaces shown in the time-exposure photographs of figure 3. Photo 3a is an eight-second exposure (approximately 40 control cycles) of a drop at $G = 0.11 \text{ sec}^{-1}$, $\alpha = 1.0$, while photo 3b is an eight-second exposure with $G = 0.165 \text{ sec}^{-1}$, $\alpha = 0.2$. The different light intensity at the center is due the lens effect of the drop. Previous four-roll mills, including Taylor's original device, could be controlled only by manual manipulation of the roller speeds. This resulted in strong, time-dependent changes in the flow, and restricted the studies to steady, hyperbolic flow, $\alpha = 1.0$, only. The present apparatus dramatically increases the reliability and utility of the four-roll mill by reducing the flow disturbances to a minimal level and by allowing the full range of both steady and time-dependent two-dimensional flows to be performed.

In our previous studies, the deformation and deformation history of the drop was followed via 35 mm photographs. However, this procedure is demanding of the operator's time and is limited in the range of time-dependent motions that can be followed (the minimum time increment between successive photographs for a Canon A-1 motor-driven camera is approximately 0.8 sec). Furthermore, it is expensive with regard to film and developing costs. Thus, one change introduced for the present study is the development of a technique for direct

analysis of the existing digital image of the drop to determine the degree of drop deformation.

3.1 Data analysis using digital image processing

Digital image processing techniques have found a wide variety of uses in experimental fluid mechanics. However, so far as we are aware, the only utilization similar to that described below is due to Girault, Schiffrin and Smith (1982, 1984) who used a video digitizing technique to determine the shapes of stationary pendant drops for the measurement of interfacial tension.

In our experiment, the sensor of the digital television camera effectively consists of a 224x112 grid of discrete picture elements (pixels), the light intensity at each pixel being represented by an eight-bit digital signal. This gray level information is thresholded by hardware to a one-bit (or two-state) signal, effectively replacing the entire gray level image by a black drop in a white background. The thresholded information is sent via direct memory access to the computer's memory and used in the control scheme to rapidly determine the position of the center of mass of the drop. In our previous studies, this was the sole use of the threshold image. In the present work, however, the thresholded digital image is saved in a data file at the command of the operator, and then analyzed, following completion of the experiment, to determine the characteristic scalar measure of the degree of drop deformation; i.e. D or L/a . During rapid deformation, many images could be saved, if desired.

The resolution of the digital television camera is 110.2 pixels/cm in the x-direction and 72.5 pixels/cm in the y-direction (directions are shown in figures 1 and 2). The undeformed radius of the drop was typically 0.1 cm, but during the elongation and breakup experiments the drops often attained half-lengths of approximately 1 cm with very narrow waists, approximately 0.02 cm in diameter. The narrow cylindrical waist was often very difficult for the digital camera to resolve.

Two digital images of deforming drops are shown in figure 4, along with

corresponding still photographs. These images are typical of the transient deformation that was the topic of interest of this paper. The basic features of the shape are captured by the digital image. Following determination of the center of mass, we calculated L/a by determining the distance separating the farthest edge bit from the center of mass. Edge bits were located by scanning the image, from the outside toward the inside, until we found the first bit on each scanning line such that two out of three successive bits were 'dark'. Such a screening process was necessary to be sure that extraneous dark bits due to 'noise' in the digital image were not inadvertently identified as edge bits. A representative comparison of data from 35 mm still photographs with the results of analyzing the digital image in this manner is shown in figure 5. Results are presented for three different viscosity ratios and two different flow types for a series of experiments on the transient elongation of a liquid droplet, described in further detail in Section 3.2. Agreement is typically to within five percent.† With this level of accuracy, the digital image analysis procedure was adopted and used extensively for determination of the degree of drop deformation in the present investigation of transient effects.

3.2 Procedure

The experiments reported here are a straightforward extension of the drop deformation studies described by Bentley & Leal (1986b). With a drop maintained at the center of the four-roll mill, the shear rate is increased by small increments of about 0.01 sec^{-1} until a steady drop shape no longer exists. The corresponding shear rate is termed the critical shear rate G_c , or, in dimensionless terms, the critical capillary number C_c . At this point the drop elongates continuously in the local flow field. When a certain elongation ratio L/a is

† It may be noted that there is a small, but definite systematic increase in the data from still photographs relative to the digital image data for low viscosity ratio drops. This difference is a consequence of a small time lag in manually triggering the still picture relative to the moment when a digital image is obtained. This time lag is accentuated for low viscosity ratio drops because they stretch more rapidly.

reached, the flow is stopped. Depending on the viscosity ratio and the degree of elongation, the drop then either breaks up into a series of 'daughter' drops or else relaxes back to a spherical shape through a rather complex motion.

The objective of the experiments in which the flow is stopped is to approximate an abrupt step change in the suspending fluid from a steady motion to a state of rest. In order to achieve this, a necessary condition is that the characteristic time scale for the viscous response of the velocity field in the four-roll mill to changes in roller speed is small compared with any time scale of drop deformation. The present study was performed using Pale-4 Oil (an oxidized castor oil available from Cas Chem, Inc., Bayonne, N.J.) as the suspending fluid, with viscosity of approximately 50 poise. The characteristic viscous response time for changes in the four-roll mill flow, $\frac{l_c^2}{\nu}$, is thus 0.3 sec (here, l_c is the characteristic apparatus length scale, and ν is the kinematic viscosity of the suspending fluid). On the other hand, the characteristic time scale for interfacial-tension-driven changes in drop shape is $\frac{\mu\alpha(1+\lambda)}{\sigma}$ and this is usually large compared with the viscous response time for the flow. In general, then, when the rollers are stopped, drop motion is driven strictly by interfacial tension and is a consequence of the nonequilibrium shape of the extended drop in an otherwise quiescent fluid.

All of the experiments were recorded on video tape for qualitative viewing and the results were quantified by analyzing digital images of the deformed drop or by occasionally taking 35 mm still photographs. Experiments were performed for ten viscosity ratios between 0.01 and 12 and for five flow types, $\alpha = 1.0, 0.8, 0.6, 0.4$ and 0.2 . The drop fluids were a series of Dow Corning Silicone oils. The properties of these fluid systems were tabulated by Bentley & Leal (1986b). The undeformed drop radius varied between 0.05 cm and 0.1 cm and, in all cases, was small enough that the elongated drop remained in the central region of the device where the flow field is given approximately by (1). The Reynolds number $\frac{\rho G a^2}{\mu}$ was about 10^{-4} for these experiments.

4. RESULTS

In this section we present the results of our experimental study of the elongation of liquid drops in two-dimensional strong flows, and the subsequent relaxation and/or breakup of the drops after the flow is stopped. First, we report qualitative observations of drop deformation and breakup, including the effects of varying both flow type and viscosity ratio. Second, we present quantitative results for the drop elongation ratio L/a as a function of time, as well as the critical elongation ratio necessary to ensure breakup for this special flow history. Our results will be compared with two existing theoretical analyses: (1) an extending, infinite fluid cylinder in an axisymmetric extensional flow and (2) capillary wave growth on an infinite, stationary liquid cylinder in a quiescent fluid. In the final section, we present a qualitative explanation for the dynamics of the observed relaxation and breakup phenomena and we describe briefly a new solution for the motion of an elongated drop in a quiescent fluid generated using the boundary integral technique which supports this qualitative explanation.

4.1 Qualitative behaviour

We begin by describing the elongation and subsequent interfacial-tension-driven breakup in qualitative terms, using the results for the case $\lambda = 2.4$, $\alpha = 1.0$, shown in figure 6*a,b* to illustrate the phenomena. The first photograph in figure 6*a* is the undeformed drop, and the remaining photos exhibit the transient deformation of the drop while the flow is maintained at the critical capillary number, $C_c = 0.117$. The times listed to the right of the photographs (and all other photographs shown in this paper) are nondimensionalized with respect to $G_c\sqrt{\alpha}$ ($\bar{t} = G_c\sqrt{\alpha}t$) and it is clear from the values listed that the initial elongation process is very slow. This is, in fact, true for all viscosity ratios, though the rate of elongation in this initial stage of transient deformation is observed to decrease as the viscosity ratio increases. During this slow initial elongation process, the sides of the drop are gradually flattened until the drop eventually develops a waist. Once the waist develops, the rate of drop elongation

increases, as seen in the last three photos in figure 6a, eventually approaching the rate of elongation of a fluid line element in the linear flow. During this period, the central section of the drop decreases rapidly in radius. Meanwhile, the ends retain their bulbous shape and appear to translate with only a small change in volume. While the flow is on, there is no evidence of capillary waves on the central cylindrical section. This was true for all the systems examined and will be discussed more fully in Section 4.5. Furthermore, we found no case where the extending drop in a steady flow fractures at the middle while the flow was on, though it should be noted that the total elongation in our experiments was limited by the finite dimensions of the four-roll mill.

The sequence of photos, figure 6b, shows the drop behaviour after the flow is stopped. The times shown are measured relative to the instant that the flow is turned off and, for consistency, have also been nondimensionalized with respect to $G_c\sqrt{\alpha}$. The most interesting and important observation is that the breakup process, illustrated by the series of photos, is entirely different from the capillary wave instability mechanism that is the basis for all existing theories of drop breakup! The motion leading to breakup is obviously driven by the finite interfacial tension of the interface. However, this motion is clearly a consequence of capillary pressure variations near the ends of the drop rather than the instability of infinitesimal disturbances in the drop shape. We first notice that the ends immediately become almost spherical after stopping the flow, forming a dumbbell-like shape, while the overall length decreases. The ends then proceed to pinch off, leaving a cylindrical thread of fluid which relaxes rapidly while the newly formed ends bulb up. However, in this particular case, the ends do not pinch off and the central thread relaxes to form a single spherical drop. Just barely visible between each pair of drops is a tiny satellite drop. During the relaxation and breakup process exhibited in figure 6b, capillary waves are never visible on the central, cylindrical section. Although this is not true in general, as we will see in Section 4.5, evidence of capillary wave instability only appears

for the most elongated drops that could be achieved in our four-roll mill while still maintaining the drop within the central region of homogeneous flow.

Qualitatively, the behaviour observed in figure 6*b* is typical of all fluid systems studied. We call the new breakup mechanism ‘end pinching’. It appears that the final drop size distribution obtained via the ‘end pinching’ mechanism is determined by the rate at which the ends bulb up and contract toward the drop center, relative to the rate at which the ends pinch off. Evidently, the interfacial-tension-induced flow responsible for ‘end pinching’ occurs on a much shorter time scale than the growth of capillary waves, at least for the particular case shown in figure 6. Theories of drop breakup and resulting predictions of drop size distributions based upon a capillary wave instability mechanism will clearly not suffice in such circumstances.

4.2 Effect of flow type

Before considering the effect of varying the viscosity ratio on the dynamics of the elongation and ‘end pinching’ processes, it is worthwhile to examine the effect of flow type. Bentley & Leal (1986*b*) have shown that a drop that passes through a series of quasi-steady states becomes oriented with its long axis along the exit streamline of the flow (figure 1) as the critical capillary number is approached. At this orientation, the effective strain rate of the fluid on the drop (i.e. the strain-rate along its axis) is $G_c\sqrt{\alpha}$.

Now, figure 7 illustrates the elongation and breakup process for $\lambda = 0.09$ and two different flows, $\alpha = 0.6$ and $\alpha = 0.2$, respectively. The main difference, other than flow type, is that the critical shear rate G_c is approximately 1.5 times larger for the $\alpha = 0.2$ flow. Otherwise, the similarities are rather remarkable. As before, the drop undergoes a very slow initial elongation followed by a period of rapid extension prior to stopping the flow. Notice that the $\alpha = 0.6$ drop was allowed to stretch further before the flow was stopped, which leads to more drop fragments being formed. The dynamics of the breakup process, though, are very similar for the two cases in spite of the fact that the final extended shapes

are somewhat different. This suggests that drop breakup in a quiescent fluid depends primarily on the *global* geometry (rather than on any local feature of the shape) and the basic shape of the elongated drops generated by these flows is very similar. The ‘end pinching’ mechanism is observed and, in these cases, the process repeats itself on the middle thread. Since the shape of this thread, immediately after its formation, is different from the shape of the originally stretched drop, we again see that it is the overall elongated shape and not local details that denominates and is responsible for the ‘end pinching’ breakup process.

Figure 8 illustrates the rate at which the elongation ratio L/a varies with dimensionless time $G_c\sqrt{\alpha}t$ for the drops shown in figure 7. Additional data are also presented for the same λ but different α . Here we focus attention on the rate of elongation as a function of flow type, for constant λ . Hence, the data for each experiment end when the flow is stopped. Because $G_c\sqrt{\alpha}$ is the effective extension rate along the exit streamline where the elongated drops align, it is a reasonable choice for scaling the time while the flow is on, and this is indicated by the agreement in the data of figure 8 for the various values of α .

It should be noted that the very slow elongation process that characterizes the initial stage of transient deformation means that a small error in experimentally determining the critical capillary number makes a large difference in the origin of the time axis for each experiment. Consequently, all the plots of L/a versus time in this paper have been adjusted so that the steeply sloping portions of the curves overlap. This adjustment affects the relative position of the curves, but has no effect on their shape. From figure 8 it is clear that the effect of flow type α is only to modify the time scale for elongation of the drop, at least for the particular flow history that we examine in this paper. Hence, the photographs in figure 7 and the rate of elongation data presented in figure 8 demonstrate that the qualitative nature of the transient deformation and relaxation processes are essentially independent of flow type for a given value of $G_c\sqrt{\alpha}$.

4.3 Effect of viscosity ratio

Figure 9 illustrates the elongation and breakup process for the entire range of viscosity ratios that we studied. Although the flow type is different for the various cases shown in figure 9, we have already demonstrated that α has no effect other than determining the critical shear rate and hence the time scale for elongation. The differences apparent among the experiments shown in figure 9 are a consequence of changes in the viscosity ratio λ .

Figure 9a shows a sequence of photographs illustrating the transient behaviour of a drop with viscosity ratio 0.01. In low viscosity ratio experiments such as this one, the drop attains highly elongated *steady* shapes prior to achieving the critical shear rate where continuous elongation occurs, and the ends of the drop are much more pointed than we saw in either figures 6 or 7. During elongation with the flow on, the shape of the drop does not change dramatically. Except for a small region near the ends which remains almost pointed, the width of the elongating drop is nearly constant over its entire length at any instant. When the flow is stopped, however, the ends rapidly become rounded, the overall length is reduced significantly, fluid drains from the center and the drop breaks. Two daughter droplets are formed in the case illustrated here with a barely visible satellite drop between them.

Two intermediate viscosity ratio cases $\lambda = 0.046$ and $\lambda = 1.37$ are shown in figure 9b,c respectively, and the qualitative behaviour is very similar to the cases $\lambda = 1.4$ and $\lambda = 0.09$ examined in figures 6 and 7, respectively. In the present figures, the initial onset of stretching of the drop occurs at moderate deformations. In other words, the maximum steady deformation is relatively small in these cases, as already shown by Bentley & Leal (1986b). For both experiments, breakup is evidently a consequence of the ‘end pinching’ mechanism.

Figure 9d illustrates the drop behaviour for the highest viscosity ratio examined in this study, $\lambda = 11.3$. The new qualitative, dynamical feature we observe is that the drop relaxes back to a spherical shape after the flow is stopped, even

though it is highly elongated and the ends bulb up to produce a dumbbell-like shape. No pinching off of the ends occurs. Instead, the ends are pulled toward the drop center and engulf the cylindrical portion of the drop as they move. It is interesting that the diameter of the central portion of the drop remains essentially constant until the separation between the drop ends is approximately equal to the end diameter. Again, capillary waves are not observed.

Examination of the photographs in figure 9*b-d* illustrates that, despite the 300-fold difference in viscosity ratio, the shapes of the intermediate and high viscosity ratio drops are remarkably similar while the drop is elongating in a steady flow at the critical capillary number. Furthermore, the rates of stretching of these different viscosity drops, following the slow initial deformation, are also remarkably similar. This is clearly evident in figure 10 which presents the elongation ratio L/a as a function of dimensionless time $G_c\sqrt{at}$ for the experiments shown in figure 9*b-d*. Data are only presented for the period while the flow is on, the results having been adjusted so that the steeply sloping portions of the curves overlap. As is evident in the photographs, however, the similarities in behaviour ended after the flow is stopped. Not only does the high viscosity ratio drop not fragment in spite of having a comparable initial L/a and shape as the intermediate viscosity ratio drops, but, as is to be expected, the time period over which relaxation occurs is much longer the larger the viscosity ratio (when examining the relaxation process it is necessary to remember that the time has been scaled with respect to $G_c\sqrt{a}$ and, for $\lambda \lesssim 10$, G_c decreases with increasing λ). Because the degree of elongation in the three cases is similar, the differences observed for the high λ case are evidently due to the effects of viscosity ratio.

With reference to the lowest viscosity ratio, $\lambda = 0.01$, if the drop is allowed to stretch further than shown in figure 9*a*, we find that it also stretches at the same rate as the higher viscosity ratio drops shown in figure 10. However, the dynamics following cessation of the flow appear qualitatively different from

the intermediate and high λ experiments due both to the lower viscosity ratio and the initial, pointed shape (which, of course, is also a consequence of the lower viscosity ratio). A qualitative explanation for the effect of viscosity ratio on the elongation/breakup process, as exhibited by these photographs, will be presented in the discussion section.

4.4 Effect of L/a ; critical elongation necessary to ensure breakup once the flow is stopped

We have yet to address specifically the question of how the initial degree of elongation affects the relaxation and breakup dynamics. First, we must reiterate that in no case did we observe breakup while the flow was on. Drop breakup, and, consequently, the final drop size distribution for a given viscosity ratio, were dependent on the elongation ratio L/a prior to stopping the flow.

It should not be surprising, in the light of the photographs presented in this paper, that drops that were extended only a little past their steady shape relaxed back to a sphere without fragmenting over the entire range of viscosity ratios studied. In addition, in all cases there existed a critical elongation ratio above which the drop fragmented when the flow ceased.

For each of the viscosity ratios studied, several experiments were performed to determine the critical elongation ratio for drop breakup. One way to illustrate the results of varying the elongation ratio is to examine data for L/a as a function of dimensionless time. Such data are shown in figure 11*a-f* for $\lambda = 0.018, 0.036, 0.20, 0.47, 2.2$ and $\lambda = 5.7$, respectively, and for a range of final elongation ratios at the point when the flow is stopped. These plots are very similar to figures 8 and 10. Here, however, we systematically vary L/a , holding λ constant, and observe the effect on the relaxation/breakup process and subsequent drop size distribution. For each experiment, we mark by a horizontal arrow, the point where the flow is stopped. Measurements of L/a then are continued until the first fragment separates from the main drop. The value of L/a at this instant is indicated by the last data point for each symbol. Although motion

is driven by interfacial tension after the flow is stopped so that a more appropriate time scale is $\frac{\mu a(1 + \lambda)}{\sigma}$, for convenience, the time-scale was not changed in this portion of the plot. In each figure, data that return to $L/a = 1$ indicate that the drop relaxes back to a sphere without fragmenting. When breakup does occur, we also include a photograph of the final dispersed state of the drop after breakup and indicate the fractional increase in interfacial area, denoted by A/A_0 , that is generated by the fragmentation process (the bottom photograph in figure 11c shows the drop shortly before it fragments into two equally sized droplets). These figures reiterate some features that were exposed earlier by the photographs, namely that provided L/a is not too large, a considerable shortening of drop length occurs prior to fragmentation, and the relaxation is slower for higher viscosity ratios. Finally, the solid, almost vertical line in each figure illustrates the expected slope if the drop were to stretch at the same rate as a fluid element in the linear flow. It is clear that as the drop becomes increasingly elongated this asymptotic behaviour is approached.

These figures illustrate that for small enough L/a the drop relaxes back to a sphere. However, above a critical elongation ratio the drop breaks and the number of drop fragments (and hence interfacial area) increases with increasing L/a beyond this critical value.

For all viscosity ratios, the critical elongation ratio necessary to guarantee drop breakup for the flow history that we examined is summarized in figure 12. The squares denote the largest elongation ratio for which the drop relaxed back to a sphere and the triangles denote the smallest elongation ratio for which breakup was observed upon cessation of the flow. The cross-hatched region therefore denotes the uncertainty in the magnitude of the critical elongation ratio. The dotted line in this figure represents L/a for the most deformed *steady* shapes that were observed experimentally by Bentley & Leal (1986b). Examination of the unsteady elongation and breakup for $\lambda \approx 10^{-3}$ has been very difficult because the steady shapes are very long and slender. The data in figure

12 illustrate, as found by Grace (1971), that the critical elongation necessary to ensure breakup is large compared with the maximum *stable* shape.

Figure 12 also clearly illustrates a difficulty in breaking drops with either a high or low viscosity ratio. As shown by the photographs in figure 9, high λ drops are able to relax back to a spherical shape before either capillary wave instabilities on the central cylindrical portion or the dynamics of 'end pinching' cause fragmentation. On the other hand, low viscosity ratio drops are difficult to break primarily because a high degree of elongation (and a high capillary number) is necessary before the drop even begins to elongate with time in a steady flow.

The graph exhibits a minimum in the critical L/a in the range $0.1 \lesssim \lambda \lesssim 2.0$ and this is qualitatively similar to results reported by Grace (1971) for hyperbolic flow. A quantitative comparison is difficult, however, because Grace reported all results in terms of D , which is very insensitive to increased extension for the highly elongated drops formed in these experiments. As discussed above, our results hold for all α .

4.5 Capillary waves

In Sections 4.1, 4.3 and 4.4, we have noted that capillary wave instability is *not* observed during the elongation of drops in the present experiments. Furthermore, there is at least a range of elongation ratios where the drop is highly elongated but the breakup mode, in the absence of any external flow, is due to 'end pinch off' and not due to the growth of capillary waves. Both of these results are surprising in view of the previous work on the drop breakup problem and deserve further discussion and investigation.

First, we consider the fact that no capillary waves are observed during the elongation of the drop, even though the midsection of the drop becomes long and cylindrical and L/a values as large $O(15)$ are attained. Mikami et al. (1975) published a theoretical stability analysis for an *infinite* fluid cylinder in a second fluid that is undergoing an axisymmetric extension. The theory shows that the

fluid cylinder behaves exactly as a fluid element in this flow and we have seen already that this asymptotic behaviour is approached as the drop elongates during the experiment. In general, though, the theoretical results are quite complicated with the net effect being that the elongation of the thread decreases the overall growth rate of capillary waves. Nevertheless, some disturbances are *still* predicted to grow exponentially and this suggests that breakup is possible via capillary wave growth even when the drop is extending. In addition, Mikami *et al.* (1975) demonstrate that the predictions of the linear stability analysis are valid for the two-dimensional extensional flow generated in the four-roll mill. Indeed, these investigators report experimental observations that qualitatively support their analysis and show breakup of a fluid thread in a steady two-dimensional hyperbolic flow. The main difference between their experiment and ours is that they achieved much greater elongation ratios than the maximum values of 0(15) that we obtained in our experiments. Presumably, a drop must become much more elongated before capillary wave instabilities become evident during its extension, but this could not be tested in our apparatus because of constraints imposed by the size of the linear flow region and by resolution limits of the video camera in the control system.

When the flow is turned off after the drop has been highly extended, the midsection would appear, even with the ends being shed via 'end pinching', to approximate a stationary liquid cylinder. The stability of an infinite, stationary fluid cylinder in a second viscous fluid was studied by Tomotika (1935), Rumscheidt and Mason (1962) and Lee *et al.* (1981a,b). As demonstrated by Tomotika, although an infinite fluid cylinder suspended in a quiescent fluid is a perfectly valid solution to the governing equations, $u = 0$ everywhere, it is unstable with respect to small disturbances with wavelength greater than the cylinder circumference. Crudely, then, capillary wave instability cannot occur on elongated drops unless the length is greater than the circumference. However, for longer drops, capillary wave growth should be expected. The fact that we see

no evidence of capillary waves in the majority of our experiments, even when the initial length of the extended drop is several times its circumference, is probably because the 'end pinching' process occurs on a short time scale relative to the time required for small capillary wave disturbances to achieve finite amplitude. Thus, the drop is reduced to a length that can no longer support capillary wave growth before significant growth of the initial disturbances can occur. However, this 'explanation' suggests that capillary waves should eventually become evident if we simply make the drop long enough - for such a long drop, breakup will occur initially via the 'end pinching' mechanism, but now capillary waves may appear on the remaining elongated thread simply because the drop was so long initially that the time scale for its complete breakup via 'end pinching' exceeds the time scale for growth of capillary waves.

Based upon these ideas, we set out to search for evidence of capillary wave growth by simply producing increasingly more-elongated drops. The results of this search confirm our qualitative explanation. Several examples of cases that show significant capillary wave growth are shown in figure 13. In these cases, the presence of capillary wave instability produces a striking and abrupt transition in the mode of breakup in the middle of the breakup process. At first, the drop begins to break up via the 'end pinching' mechanism which we identified earlier in this paper. Then, however, there is an abrupt appearance of finite amplitude waves on the remaining thread, which leads to simultaneous breakup into a line of small drops. The fact that this latter process is due to capillary wave instability is confirmed by the comparison, shown in figure 13d, between the wavelength obtained from the experiments and the wavelength of the fastest growing linear mode calculated from the linear stability theory in the limit of negligible inertial effects, $\frac{\rho\sigma R_o}{\mu^2}, \frac{\dot{\rho}\sigma R_o}{\dot{\mu}^2} \ll 1$, where R_o is the thread radius. Experimentally, $\frac{\rho\sigma R_o}{\mu^2} \approx 10^{-4}$. The agreement is excellent for $\lambda = 0.1$ and $\lambda = 1.3$. The discrepancy for $\lambda = 12.2$ may be due to the fact that there is a relatively strong flow induced in the fluid by the initial contraction in length

which occurs to a much greater extent for drops with a large viscosity ratio. Of course in the capillary wave theory, an infinite, stationary thread is assumed and it is perhaps surprising that there is good agreement between the theory and experimental data for an elongated drop in any case.

5. DISCUSSION

Of all the experimental observations described in the preceding section, the most important, and interesting, is the identification of the mode of interfacial-tension-driven breakup that we have termed 'end pinching'. Qualitatively, it is clear that the mechanism is a consequence of motion generated via capillary pressure gradients in the region near the end of the drop. An obvious question, though, is why drops of intermediate viscosity ratio break via this mechanism when they are only modestly extended, while more viscous drops do not break until L/a is considerably larger. From our observations, it can be seen that a general precursor to 'pinch off' is the development of a local 'waist' just inside the bulbous end. Once such a local minimum in the radius occurs, there will be an associated local pressure maximum inside the drop due to capillary forces and an obvious mechanism for increase in the depth of the minimum, subsequently leading to pinch-off. However, this simple observation does not explain why the local minimum in radius occurs in the first place, nor why it occurs less readily for drops of large viscosity ratio compared with $\lambda = O(1)$. This latter question is particularly perplexing in view of the fact that the drop shapes in the initial stages of the relaxation/breakup process are very similar.

5.1 A qualitative description of 'end pinching'

A starting point in attempting to understand 'pinch-off' is the recognition, from dimensional analysis, that the qualitative features of the interfacial-tension-driven flow are determined completely by the viscosity ratio and the initial shape of the drop, including the value of L/a . One might, at first, suppose that the differences between the relaxation/breakup process for drops of intermediate and large viscosity ratio are a result of some viscosity ratio dependent detail of

the drop shape at the instant when the external flow is stopped. However, this appears unlikely for several reasons. First, when 'end pinching' occurs, it does so for any elongation ratio greater than some minimum value even though the initial drop shape (as described, say, by the ratio of the radius of the bulbous end to the radius of the cylindrical midsection) varies with L/a . Second, the initial shapes for small and intermediate λ are markedly different in the region near the end of the drop and yet 'end pinching' occurs in both cases. Finally, when 'end pinching' initially takes place, it often leaves an elongated central fragment which develops bulbous ends and may pinch off in the same manner in spite of the fact that its shape is clearly different from the original extended shape. Hence, it would appear that the mechanism of 'end pinching' depends on the global geometry of the drop (and viscosity ratio), rather than on any local details of the shape. This was indicated previously in the discussion of figure 7.

A more plausible suggestion is that the difference between moderate and high viscosity ratio systems is due to differences in the *relative* rates of the flow in different regions of the drop which arise from the relative viscosities of the drop and continuous phases. In order to develop this concept, it is necessary to begin with a general description of the relaxation process. Let us begin by considering the internal pressure distribution associated with capillary forces for an interface of the shape shown in figure 14a, which is qualitatively typical of the observed drop shapes in all cases soon after the flow is stopped. For illustration purposes, we have chosen the radius of the bulbous end to be twice the radius of the cylindrical midsection. Let us denote the stress tensor as \mathbf{T} and the unit normal from the droplet phase to the continuous phase as \mathbf{n} . Then, if the drop surface is described in cylindrical coordinates as $r = f(z)$, the normal stress jump is given by

$$(\mathbf{T} \cdot \mathbf{n} - \hat{\mathbf{T}} \cdot \mathbf{n}) \cdot \mathbf{n} = \frac{1}{R_1} + \frac{1}{R_2} = \frac{1}{[1 + f'^2]} \left[\frac{1}{f} - \frac{f''}{1 + f'^2} \right] \quad (2)$$

where R_1 and R_2 are the principal radii of curvature of the surface, and f' and f'' are the derivatives of the shape function f , with respect to the axial coordinate

z . The normal stress jump corresponding to the shape plotted in figure 14a is depicted qualitatively in figure 14b. Now, let us suppose that the shape is fixed, so that the normal stress jump can be interpreted in terms of capillary pressure variations within the drop. Then, we see that the pressure is highest near the end of the drop where the radius of curvature is concave in planes both parallel and perpendicular to the drop axis, goes through a minimum with decreasing z because the drop surface in the plane parallel to the drop axis becomes convex, and finally increases to a constant value in the central portion of the drop.

This capillary pressure gradient will tend to induce flow both from the end of the drop and from the central cylindrical region. However, the flow from the end of the drop can occur without large velocity gradients in the internal fluid, since the drop end can translate without a significant change in shape. Thus, this motion is resisted mainly by viscous effects in the *outer* fluid. Motion of the bulbous end towards the pressure minimum causes the convex region (and hence the pressure minimum) to move toward the drop center as well, so that the driving force for continued end movement is maintained. On the other hand, the dynamics of the flow from the central portion of the drop towards the pressure minimum is qualitatively different, because this flow requires significant velocity gradients within the inner fluid (note that the fluid is stagnant at the drop center). As a consequence, this motion is inhibited primarily by the *droplet* viscosity. It will be noted, however, that a local 'neck' in the shape will tend to form as a consequence of a flux of fluid from the cylindrical region towards the pressure minimum.

Given this qualitative picture of interfacial-tension-driven changes in the drop shape, the observed differences between high and low viscosity ratio systems may be 'explained' in the following manner. In high viscosity ratio systems, the ends are drawn toward the middle as described above, with the rate of this process controlled mainly by the relatively low viscosity outer fluid. Drainage from the central portion, on the other hand, is comparatively slow since it is

controlled by the higher viscosity droplet fluid. As a result, movement of the pressure minimum and of the bulbous ends occurs sufficiently fast relative to the flow from the central region that a significant ‘neck’ in the shape cannot form unless the drop is highly elongated. In contrast, in lower viscosity ratio systems, fluid flows readily from the central region towards the pressure minimum (and the relative motion of the bulbous end is slower) causing a local minimum in the drop radius. The ends ‘pinch off’ due to flow away from the corresponding maximum in capillary pressure, which causes the ‘neck’ to become more pronounced and eventually ‘pinch’. Notice that the higher curvature at the ends of very low viscosity ratio drops should lead to a rapid bulbing of the ends (i.e. high velocities near the end of the drop) followed by the pinching process just discussed. This is seen clearly for $\lambda = 0.01$ in figure 9a.

5.2 Numerical solution of the motion of an elongated drop via the boundary integral method

In order to test the qualitative description presented above and to understand more about the dependence of the dynamics on the initial shape and viscosity ratio, a numerical study of the interfacial-tension-driven motion of an elongated drop in a quiescent fluid is currently in progress using a boundary integral method. Here we present calculations for the case $\lambda = 1$ only in order to show that the numerical simulation agrees with the description of the physics presented in Section 3.1.

The boundary integral method has been applied to the low Reynolds number deformation of bubbles and drops in an external flow by Youngren & Acrivos (1976), Rallison & Acrivos (1978) and Rallison (1981). The technique is well-suited to free-boundary problems since the interfacial velocities may be obtained directly, without the necessity of determining the velocity field in the entire flow domain.

Our overall objective is the examination of the dynamics of an initially extended liquid droplet that is suspended in a second immiscible fluid which is

at rest at infinity. Inertial effects are negligible with respect to viscous effects provided $\frac{\rho\sigma l_c}{\mu^2(1+\lambda)} \ll 1$, where l_c is some characteristic length scale of the deformed drop. As discussed specifically by Rallison and Acrivos (1978), for the special case $\lambda = 1$, the velocity field, nondimensionalized with respect to $\frac{\sigma}{\mu(1+\lambda)}$, at any point, \mathbf{x} in the fluid domain, is given by

$$\mathbf{u}(\mathbf{x}) = \frac{-1}{4\pi} \int_S \left[\frac{\mathbf{I}}{|\mathbf{x} - \boldsymbol{\xi}|} + \frac{(\mathbf{x} - \boldsymbol{\xi})(\mathbf{x} - \boldsymbol{\xi})}{|\mathbf{x} - \boldsymbol{\xi}|^3} \right] \cdot \mathbf{n}(\boldsymbol{\xi}) [\nabla_s \cdot \mathbf{n}(\boldsymbol{\xi})] dS(\boldsymbol{\xi}) \quad (3)$$

where S represents the drop surface. Here, \mathbf{n} is the unit outward normal from the drop surface and $\nabla_s \cdot \mathbf{n}$ is the surface curvature. Thus, for the case when the drop and suspending fluids have the same viscosity, the velocity field may be thought of as generated by a ‘membrane of Stokeslets distributed along the interface’ with a density proportional to the local curvature. If we wish to follow the interface motion, equation (2) is used in conjunction with the kinematic condition, which may be stated symbolically as $\frac{dS}{dt} = \mathbf{u} \cdot \mathbf{n}$ for $\mathbf{x} \in S$ (time has been nondimensionalized with respect to $\frac{l_c \mu (1 + \lambda)}{\sigma}$). As is evident from equation (3), the evolution of the drop shape is completely dependent on the initial drop geometry and the only role interfacial tension plays is to determine the characteristic velocity scale and, hence, the time scale of the relaxation/breakup process.

In this short discussion, we aim to demonstrate that the drop shape evolves in a manner representative of the ‘end pinching’ phenomenon and then examine the interior velocity field to see whether the behaviour is qualitatively consistent with the proposal of the preceding section. The details of the numerics and more comprehensive results will be reported in a future communication. Here we simply note that the numerical scheme incorporates methods used for similar free-boundary problems by Rallison & Acrivos (1978), Lee & Leal (1982), Geller, Lee & Leal (1986), and E.J. Hinch *et al.* (private communication). In the calculation reported below: the interface was subdivided into 24 elements; the interface shape was approximated by fitting a cubic spline to the collocation points; every few iterations the collocation points were evenly redistributed

(based on arclength) along the interface; all integrals were evaluated using a Gauss quadrature scheme; and the drop volume, monitored as time progressed, was found to change by less than one percent over several hundred iterations.

Figure 15*a* represents the time-evolution of a typical drop shape, with an initial elongation ratio $L/a = 5.3$, and an initial shape that can be approximated as a cylindrical midsection with a spherical end, the ratio of bulb to cylinder radius being 3:1. We have chosen the local radius as the characteristic length scale and t^* is the dimensionless time that identifies evolution of the drop shape. We observe that the bulbous end translates towards the drop center, a 'neck' slowly develops, and then the bulbous end rapidly begins to pinch off. This evolution is very similar qualitatively to the many photographs presented above for $\lambda = O(1)$. In order to accurately describe the details of the pinch process, more points would have to be distributed along the interface to resolve the regions of high curvature. However, our goal is primarily to show that the elongated drop does undergo an 'end pinching' process and that the interior velocity field is qualitatively consistent with the mechanism suggested in Section 5.1. For the latter purpose, it is sufficient to examine the initial velocity field at $t = 0^+$ when the surface resolution is more than adequate. These results are shown in figure 15*b*. We see that the end induces a strong, almost uniform flow toward the drop center. Furthermore, there is indeed a flow, albeit weak, from the cylindrical region towards the pressure minimum, as was suggested in the qualitative discussion in section 5.1. It is this initial flux that leads to the development of a 'neck' and, consequently, a local pressure maximum, which will eventually result in drop fragmentation via 'end pinching' as depicted in figure 15*a*. Hence, this example lends support to the qualitative explanation that we have presented to describe the relaxation/breakup process.

ACKNOWLEDGEMENTS

This work was supported by a grant from the Fluid Mechanics Program of the National Science Foundation.

REFERENCES

- Acrivos, A., 1983 The breakup of small drops and bubbles in shear flows. *4th Int Conf. on Physicochemical Hydrodynamics, Ann. N.Y. Acad. Sci.* **404**, 1-11.
- Bentley, B. J. & Leal, L. G. 1986a A computer-controlled four-roll mill for investigations of particle and drop dynamics in two-dimensional linear shear flows. *J. Fluid Mech.* **167**, 219-240.
- Bentley, B. J. & Leal, L. G. 1986b An experimental investigation of drop deformation and breakup in steady two-dimensional linear flows. *J. Fluid Mech.* **167**, 241-283.
- Cox, R. G. 1969 The deformation of a drop in a general time-dependent fluid flow. *J. Fluid Mech.* **98**, 305-328.
- Geller, A. S., Lee, S. H. & Leal, L. G. 1986 The creeping motion of a spherical particle normal to a deformable interface. *J. Fluid Mech.* **169**, 27-69.
- Girault, H. H., Schiffrin, D. J. & Smith, B. D. V. 1982 Drop image processing for surface and interfacial tension measurements. *J. Electroanal. Chem.* **137**, 207-217.
- Girault, H. H., Schiffrin, D. J. & Smith, B. D. V. 1984 The measurement of interfacial tension of pendant drops using a video image profile digitizer. *J. Colloid Interface Sci.* **101**, 257-266.
- Grace, H. P. 1971 Dispersion phenomena in high viscosity immiscible fluid systems and application of static mixers as dispersion devices in such systems. *Eng. Found. Res. Conference Mixing*, 3rd, Andover, N.H. Republished 1982 in *Chem. Engng. Commun.* **14**, 225-277.
- Hinch, E. J. & Acrivos, A. 1980 Long slender drops in a simple shear flow. *J. Fluid Mech.* **98**, 305-328.
- Hinch, E. J. 1980 The evolution of slender inviscid drops in a axisymmetric straining flow. *J. Fluid Mech.* **101**, 545-553.

- Lee, S. H. & Leal, L. G. 1982 The motion of a sphere in the presence of a deformable interface. II. A numerical study of the translation of a sphere normal to an interface. *J. Colloid Int. Sci.* **87**, 81-106.
- Lee, W.-K. & Flumerfelt, R. W. 1981 Instability of stationary and uniformly moving cylindrical fluid bodies. I. Newtonian systems. *Intl J. Multiphase Flow* **7**, 363-383.
- Lee, W.-K., Yu, K.-L. & Flumerfelt, R. W. 1981 Instability of stationary and uniformly moving cylindrical fluid bodies. II. Viscoelastic threads and experimental observations. *Intl J. Multiphase Flow* **7**, 385-400.
- Mikami, T., Cox, R. G. & Mason, S. G. 1975 Breakup of extending liquid threads. *Intl J. Multiphase Flow* **2**, 113-138.
- Rallison, J. M. 1980 Note on the time-dependent deformation of a viscous drop which is almost spherical. *J. Fluid Mech.* **109**, 465-482.
- Rallison, J. M. 1981 A numerical study of the deformation and burst of a viscous drop in general shear flows. *J. Fluid Mech.* **109**, 465-482.
- Rallison, J. M. 1984 The deformation of small viscous drops and bubbles in shear flows. *Ann. Rev. Fluid Mech.* **16**, 45-66.
- Rallison, J. M. & Acrivos, A. 1978 A numerical study of the deformation and burst of a viscous drop in an extensional flow. *J. Fluid Mech.* **89**, 191-200.
- Rumscheidt, F. D. and Mason, S. G. 1962 Breakup of stationary liquid threads. *J. Colloid Sci.* **17**, 260-269.
- Taylor, G. I. 1932 The viscosity of a fluid containing small drops of another fluid. *Proc. R. Soc. Lond.* **A138**, 41-48.
- Taylor, G. I. 1934 The formation of emulsions in definable fields of flow. *Proc. R. Soc. Lond.* **A146**, 501-523.
- Taylor, G. I. 1964 Conical free surfaces and fluid interfaces. *Proc. Int. Congr. Appl. Mech.*, 11th, Munich, 790-796.

- Tomotika, S. 1935 On the instability of a cylindrical thread of a viscous liquid surrounded by another viscous fluid. *Proc. R. Soc. Lond.* **150**, 322-337.
- Tomotika, S. 1936 Breaking up of a drop of viscous liquid immersed in another viscous fluid which is extending at a uniform rate. *Proc. R. Soc. Lond.* **A153**, 302-318.
- Torza, S., Cox, R. G. & Mason, S. G. 1972 Particle motions in sheared suspensions. XXVII. Transient and steady deformation and burst of liquid drops. *J. Colloid Interface Sci.* **38**, 395-411.
- Youngren, G. K. & Acrivos, A. 1976 On the shape of a gas bubble in a viscous extensional flow. *J. Fluid Mech.* **76**, 733-442.

FIGURE CAPTIONS

Figure 1 Streamlines for the linear flow $\mathbf{u} = \mathbf{\Gamma} \cdot \mathbf{x}$, $\mathbf{\Gamma}$ given by Eq. (1). $\alpha \geq 0$.

Figure 2 Scalar measures of deformation and orientation.

Figure 3 Eight second time-exposure photographs of drops in the four-roll mill.

The sharpness of the fluid-fluid interface demonstrates the ability of the control scheme to maintain the drop at the device center with minimal disturbances. (a) $\lambda = 1.4$, $\alpha = 1.0$, $G = 0.11 \text{ sec}^{-1}$. (b) $\lambda = 1.4$, $\alpha = 0.2$, $G = 0.165 \text{ sec}^{-1}$

Figure 4 Typical digital images of the transient deformation of highly elongated droplets in a steady flow at the critical capillary number. 35 mm photographs are shown for comparison.

Figure 5 Comparison of L/a calculated from 35 mm photographs and L/a calculated by analyzing digital images. The solid line denotes $(L/a)_{35mm} = (L/a)_{digital}$.

Figure 6 (a) Elongation of a liquid droplet in a steady flow at the critical capillary number. $\bar{t} = G_c \sqrt{\alpha} t$, $G_c = 0.132 \text{ sec}^{-1}$. (b) Relaxation and breakup after the flow is stopped abruptly - 'end pinching'. The time is measured from the instant the flow ceases and $\bar{t} = G_c \sqrt{\alpha} t$.

Figure 7 The effect of flow type on the elongation process and on the subsequent relaxation and breakup phenomena. Viscosity ratio is held constant, $\lambda = 0.09$. (a) $\alpha = 0.6$, $G_c = 0.224 \text{ sec}^{-1}$; (b) $\alpha = 0.2$, $G_c = 0.33 \text{ sec}^{-1}$.

Figure 8 The effect of flow type on the elongation process - elongation ratio L/a as a function of dimensionless time $G_c \sqrt{\alpha} t$. This figure illustrates that the effect of flow type is only to modify the time scale of the elongation process. The data for each experiment end when the flow is stopped.

Figure 9 The effect of viscosity ratio on the elongation and breakup phenomena. (a) $G_c = 0.260 \text{ sec}^{-1}$, $C_c = 0.26$. (b) $G_c = 0.235 \text{ sec}^{-1}$, $C_c = 0.21$. (c) $G_c = 0.187 \text{ sec}^{-1}$, $C_c = 0.18$. (d) $G_c = 0.135 \text{ sec}^{-1}$, $C_c = 0.14$.

Figure 10 Elongation ratio L/a as a function of dimensionless time for the ex-

periments shown in figure 9*b,c,d*. The data indicate the remarkable similarity in stretching rate for $(L/a) \gtrsim 3$ in spite of the 300-fold difference in viscosity ratio.

Figure 11 The effect of L/a on the relaxation and breakup process. (a) $\lambda = 0.018$, (b) $\lambda = 0.036$, (c) $\lambda = 0.2$, (d) $\lambda = 0.47$, (e) $\lambda = 2.2$, (f) $\lambda = 5.7$. The horizontal arrows indicate when the flow is stopped. Data points for each experiment then continue until the first fragment separates from the main drop. A/A_0 denotes the fractional increase in interfacial area due to the fragmentation. The solid, almost vertical line indicates the rate at which a fluid element stretches in the linear flow.

Figure 12 Critical elongation ratio necessary to ensure breakup, following an abrupt halt of the flow, as a function of viscosity ratio. Triangles denote the smallest L/a for which a drop was observed to break up. Squares denote the largest L/a for which a drop relaxed back to a sphere. The shaded region denotes the uncertainty in the critical elongation ratio. The dashed line indicates the L/a values of the final steady shapes.

Figure 13 Development of capillary wave instabilities. Notice that capillary waves are not visible while the drop stretches. (a) $G_c = 0.306 \text{ sec}^{-1}$, $C_c = 0.18$. (b) $G_c = 0.218 \text{ sec}^{-1}$, $C_c = 0.12$. (c) $G_c = 0.234 \text{ sec}^{-1}$, $C_c = 0.10$. (d) Comparison of experiment and theory for the instability of infinite, stationary liquid cylinders. The theoretical predictions are obtained in the limit of negligible inertial effects, $\frac{\rho\sigma a}{\mu^2} \ll 1$, $\frac{\hat{\rho}\sigma a}{\hat{\mu}^2} \ll 1$ (Lee & Flumerfelt 1981).

Figure 14 (a) Typical drop shape shortly after the flow is stopped. Radius of bulbous end is twice the radius of the cylindrical midsection. (b) Approximate normal stress jump across the interface.

Figure 15 (a) Evolution of an initially elongated drop suspended in an otherwise quiescent fluid, $\lambda = 1$. (b) The velocity field in the drop for the initial shape shown in (a).

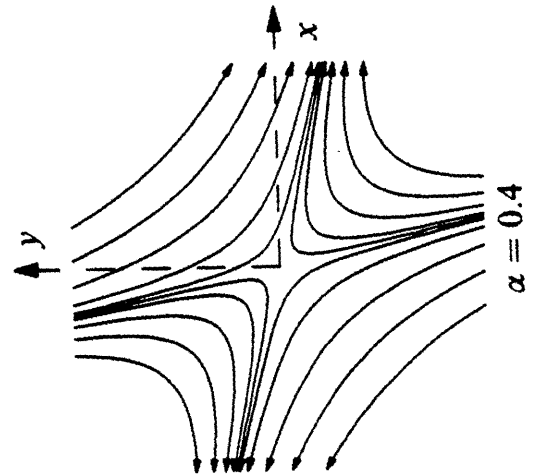
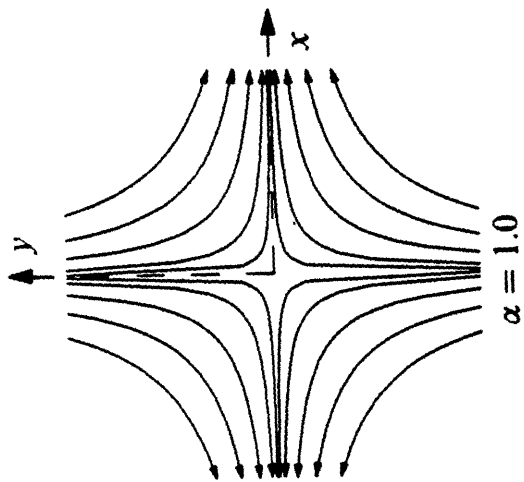
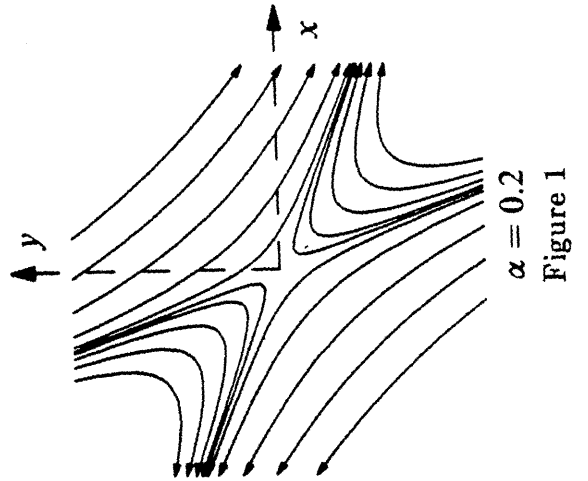
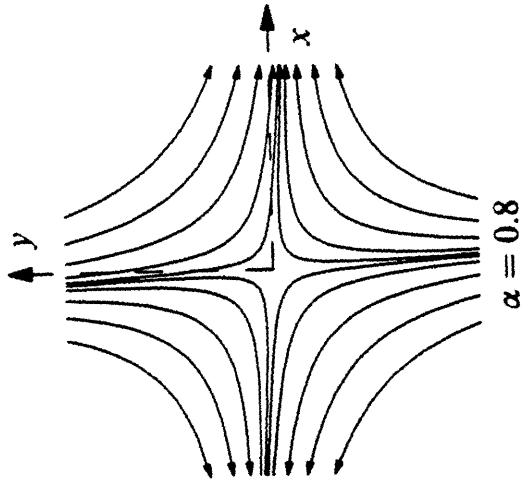
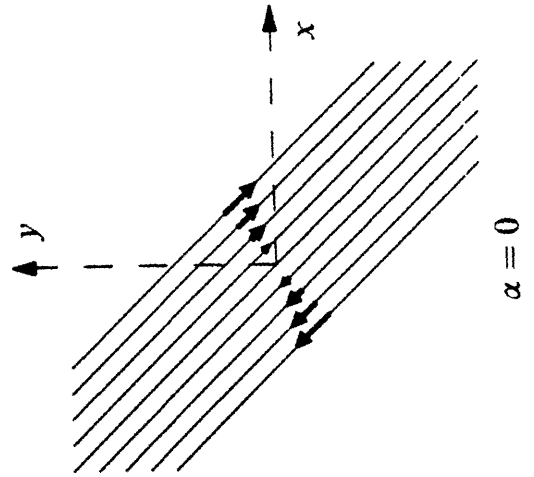
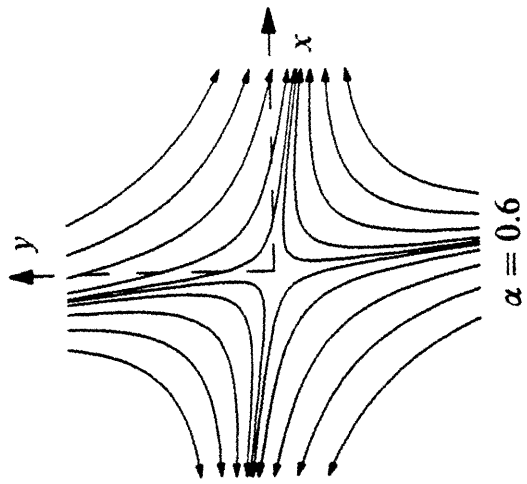


Figure 1

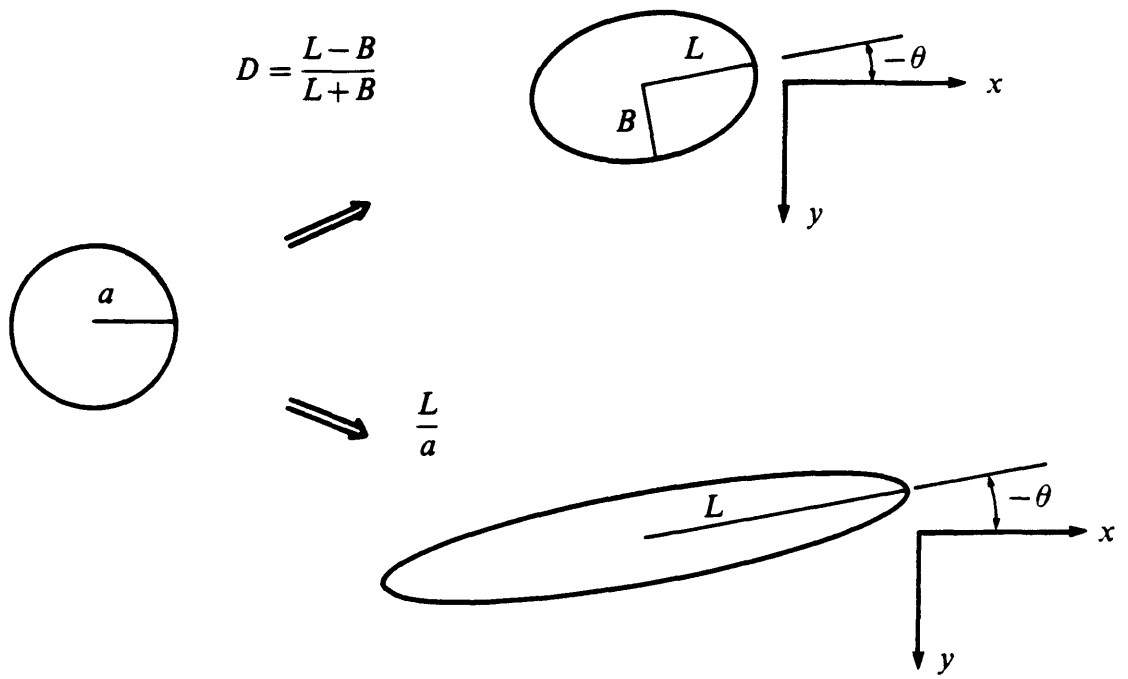
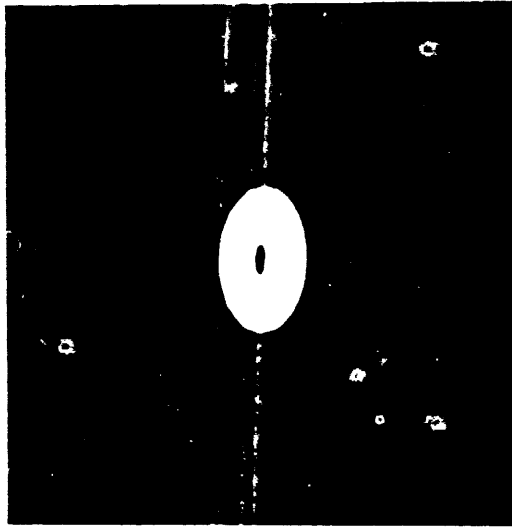


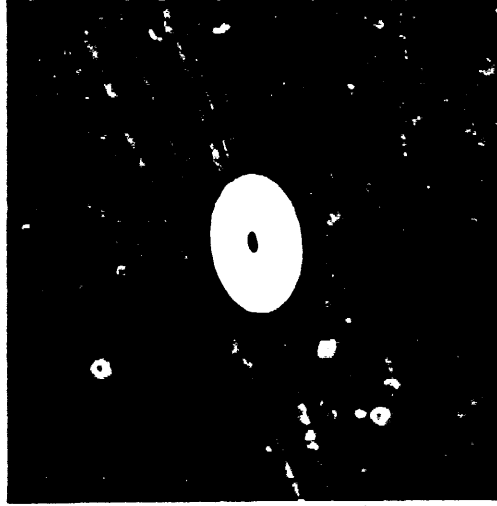
Figure 2

$\alpha = 1.0$



(a)

$\alpha = 0.2$



(b)

Figure 3

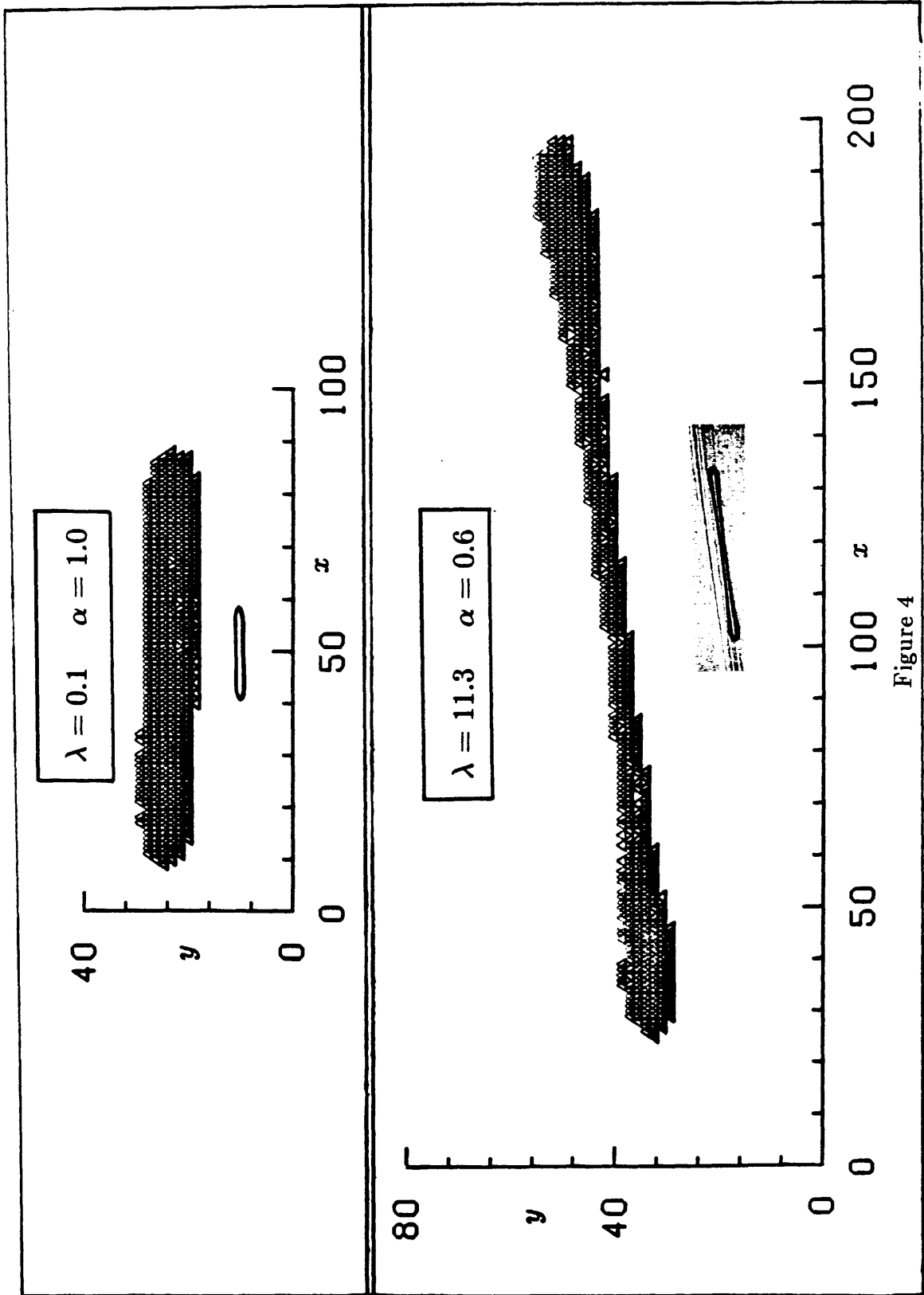


Figure 4

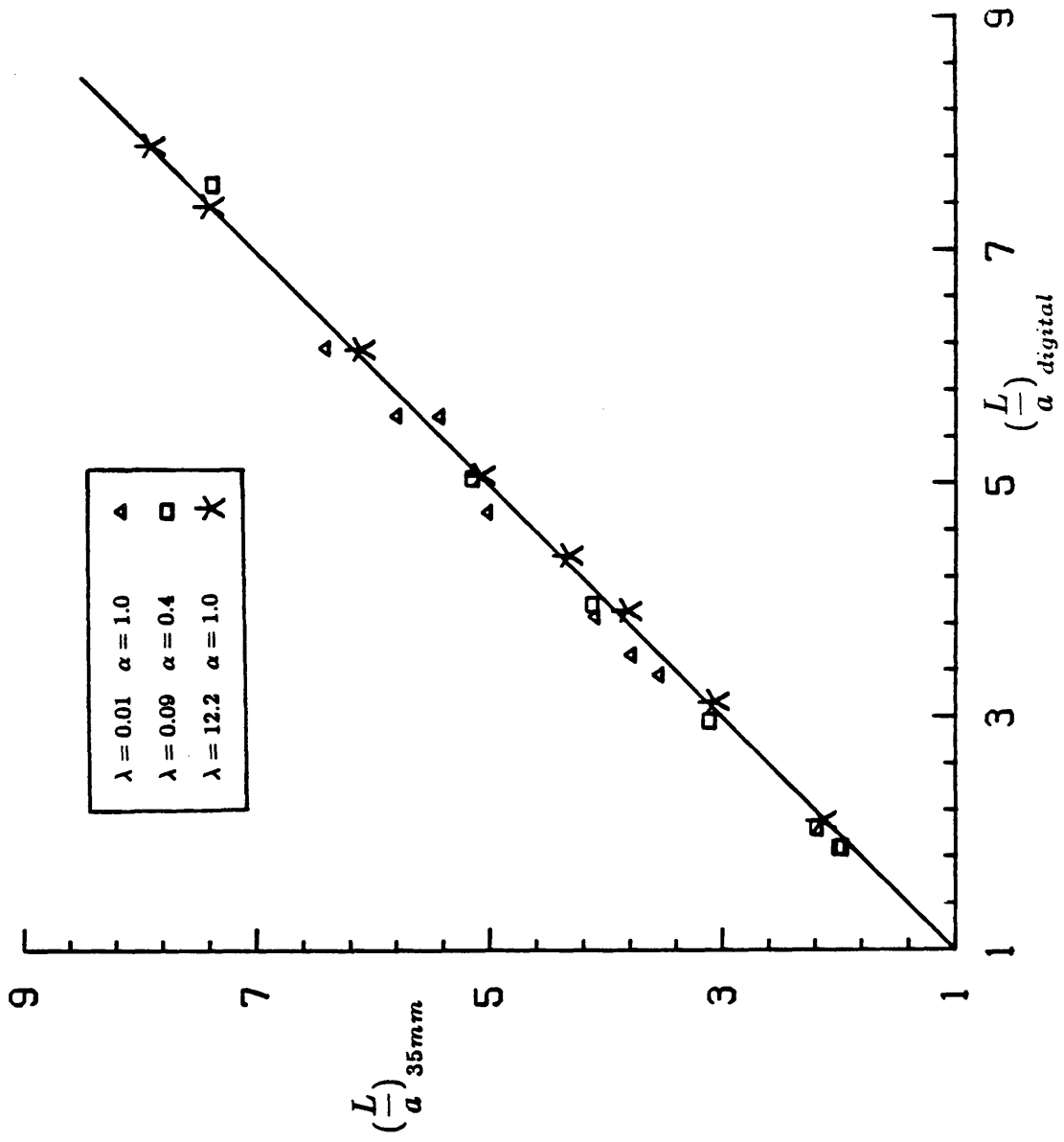


Figure 5

$\lambda = 2.4$

$\alpha = 1.0$

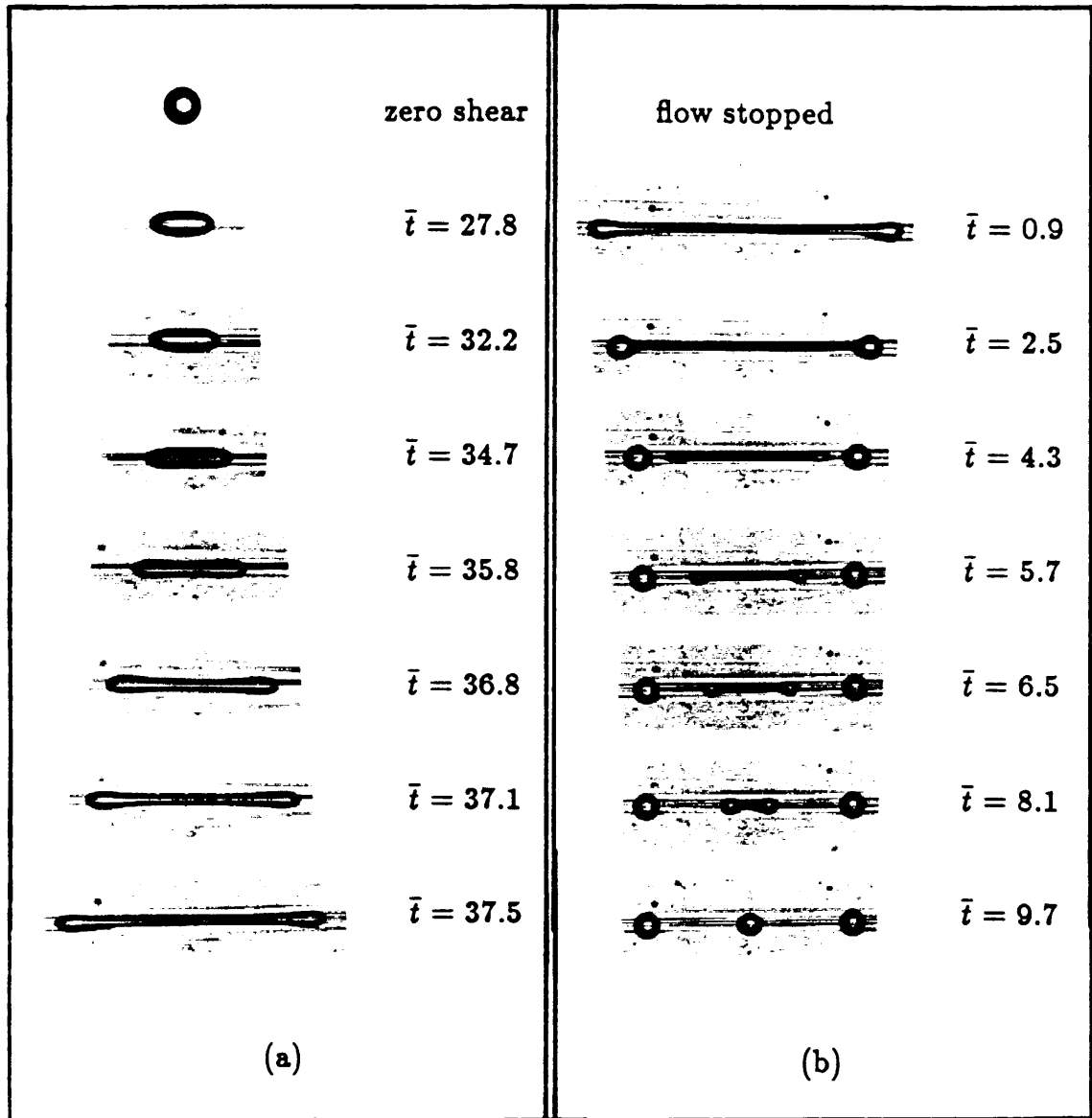


Figure 6

$$\lambda = 0.09$$

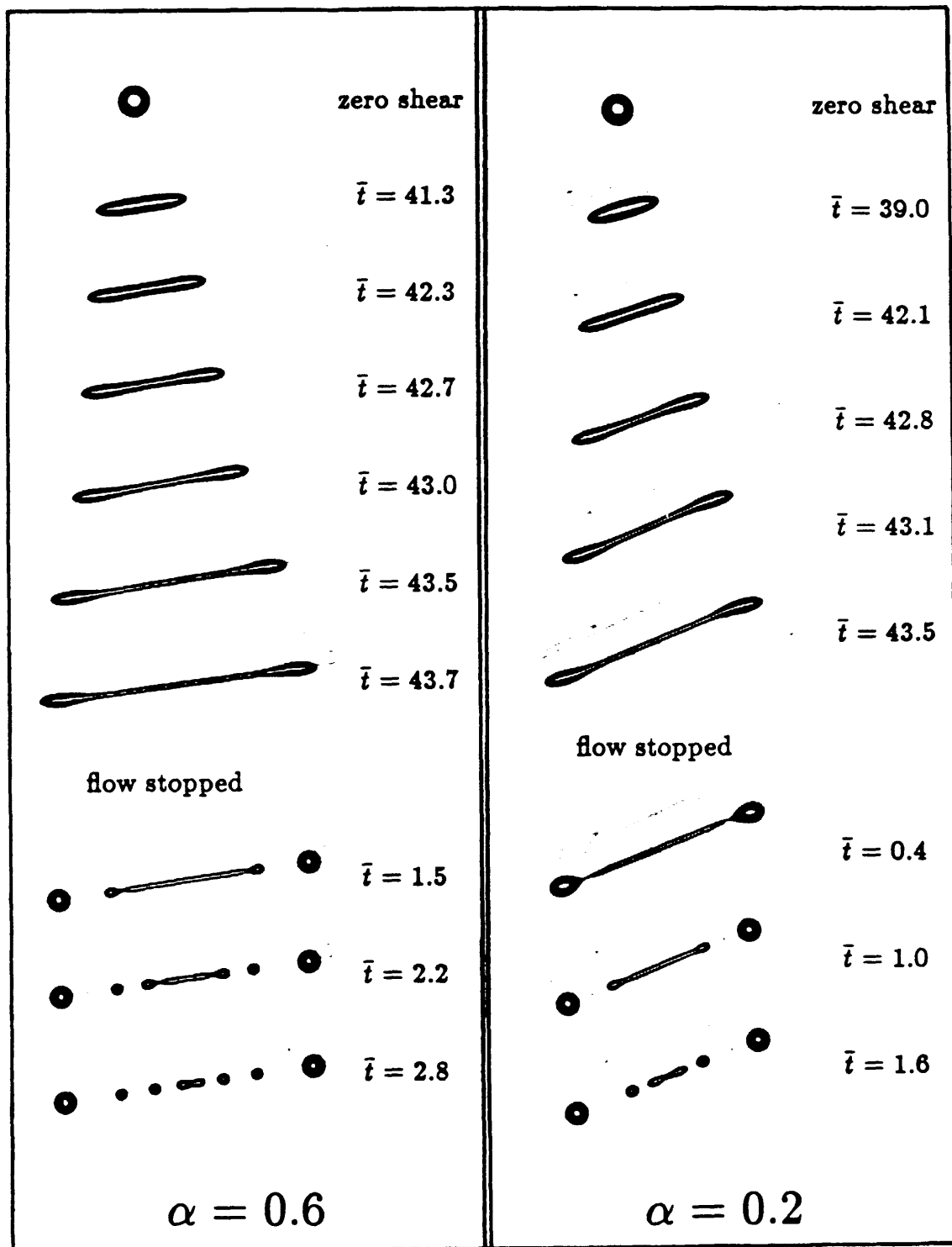


Figure 7

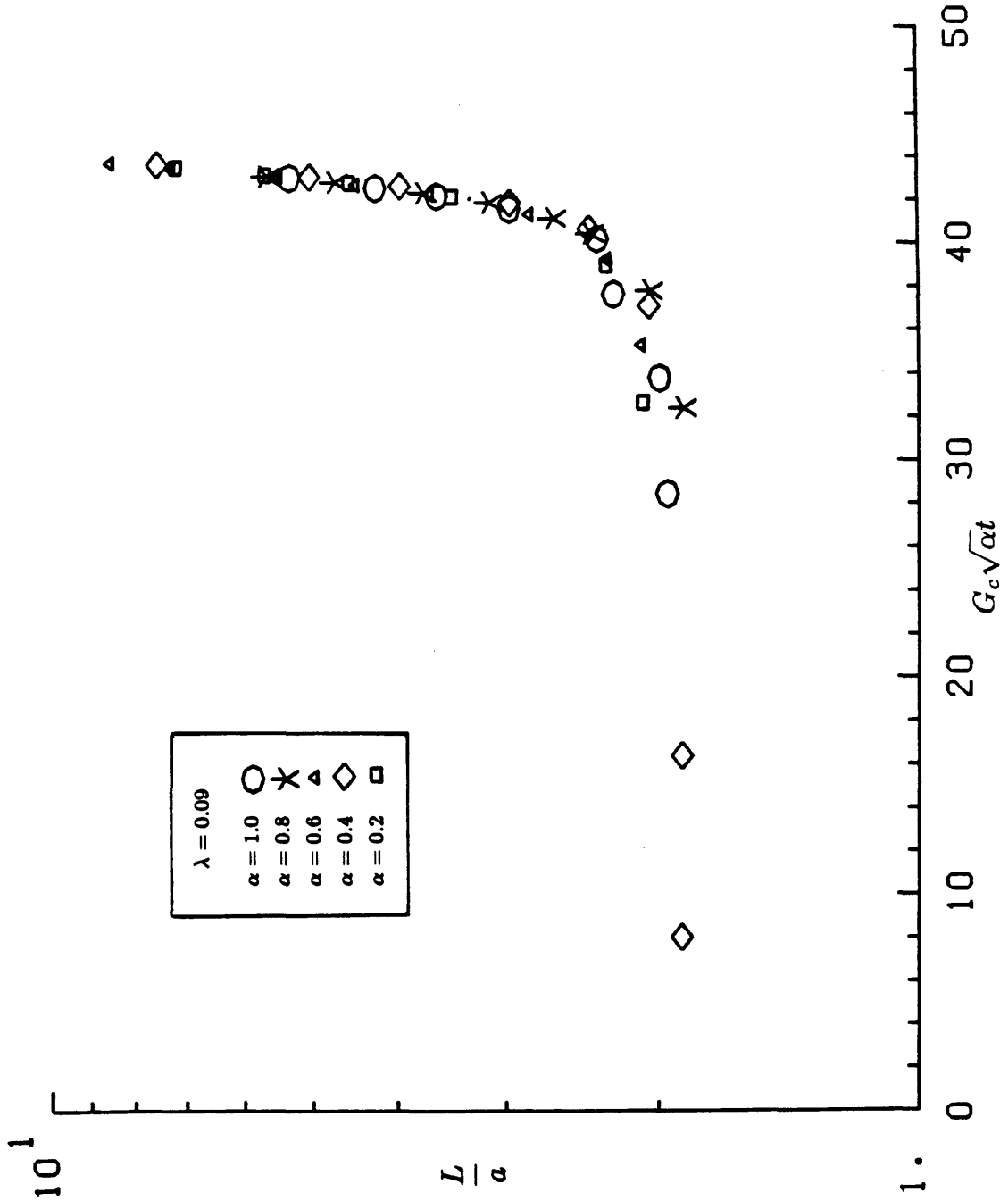


Figure 8

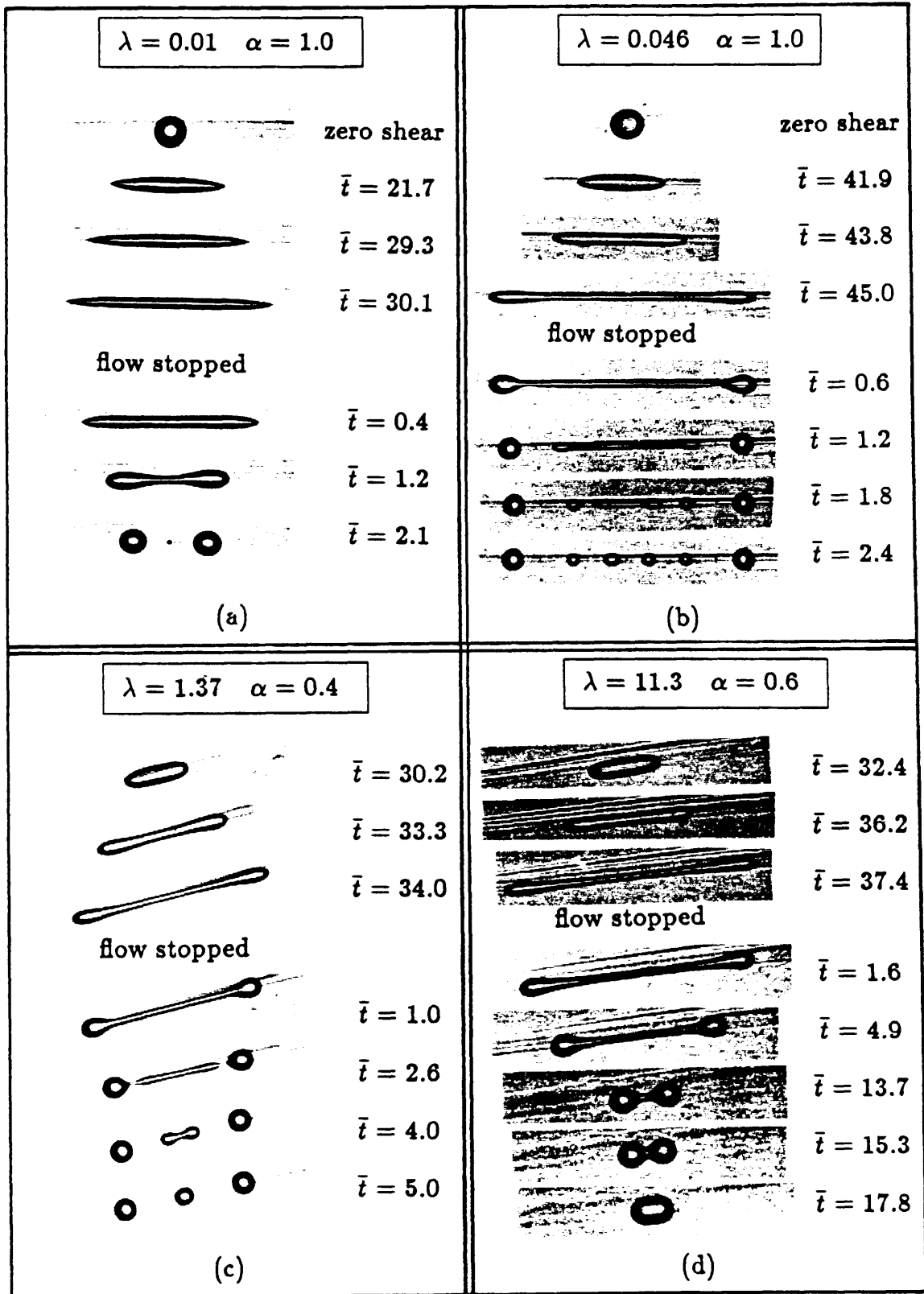


Figure 9

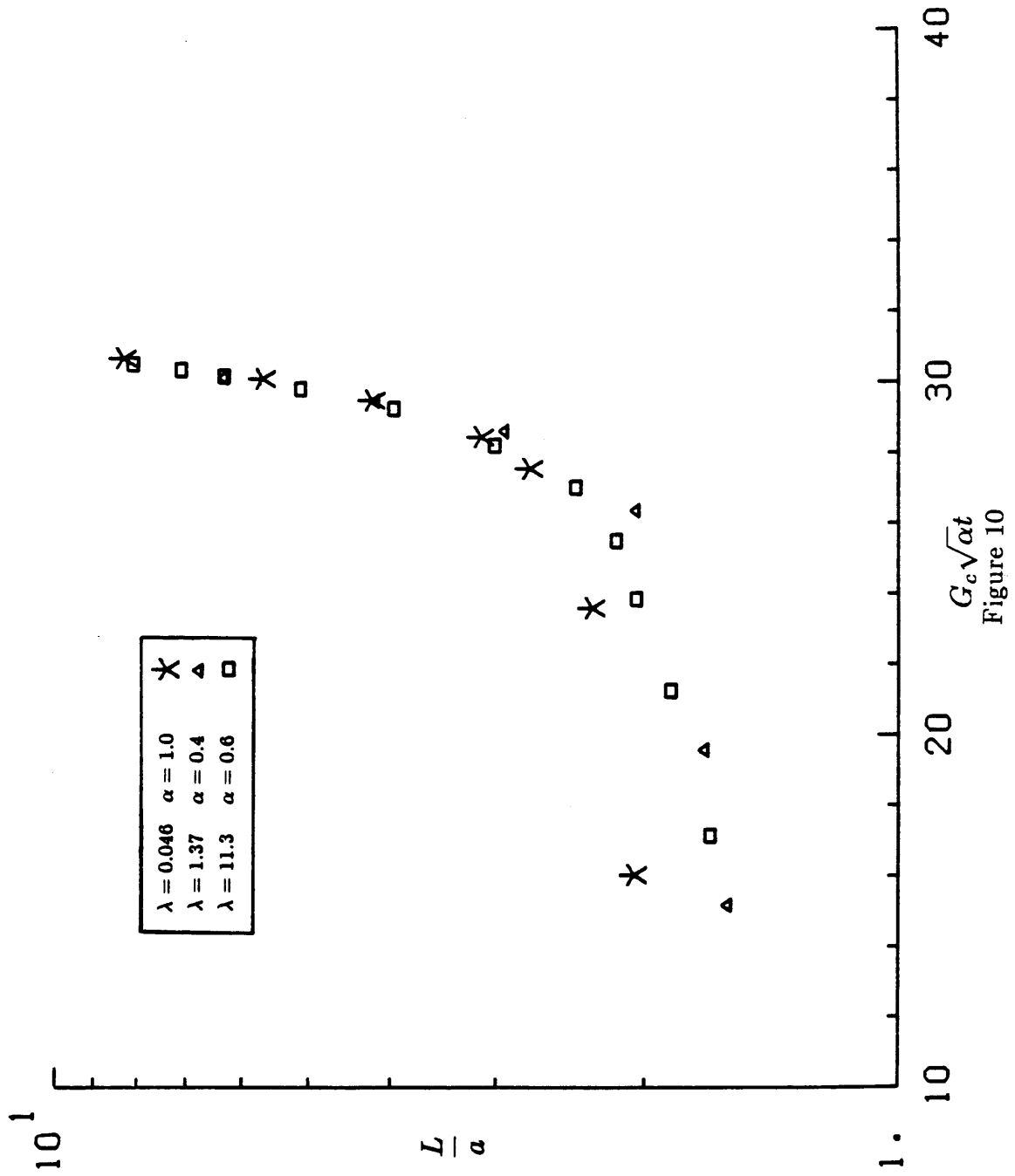


Figure 10

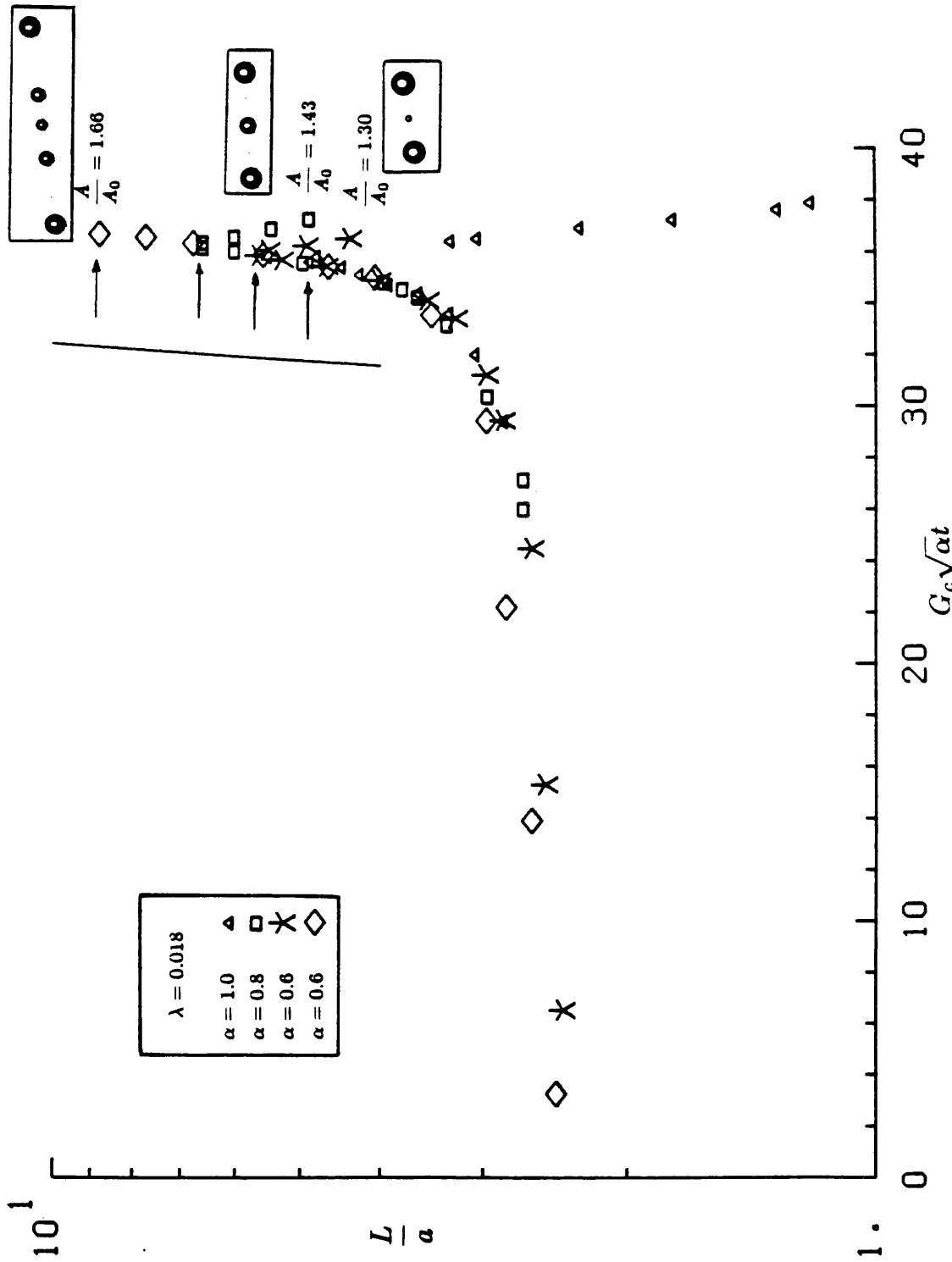


Figure 11a

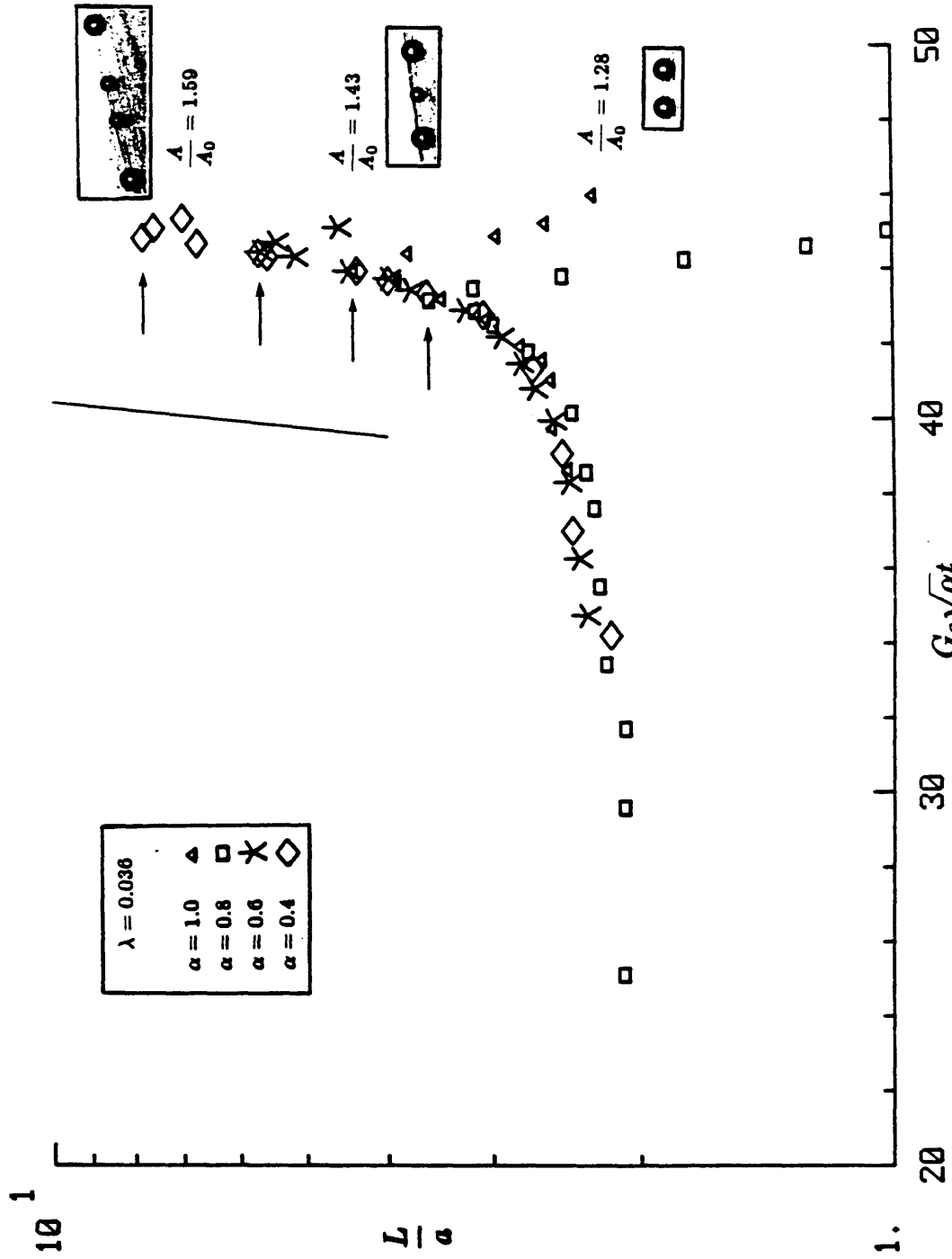


Figure 11b

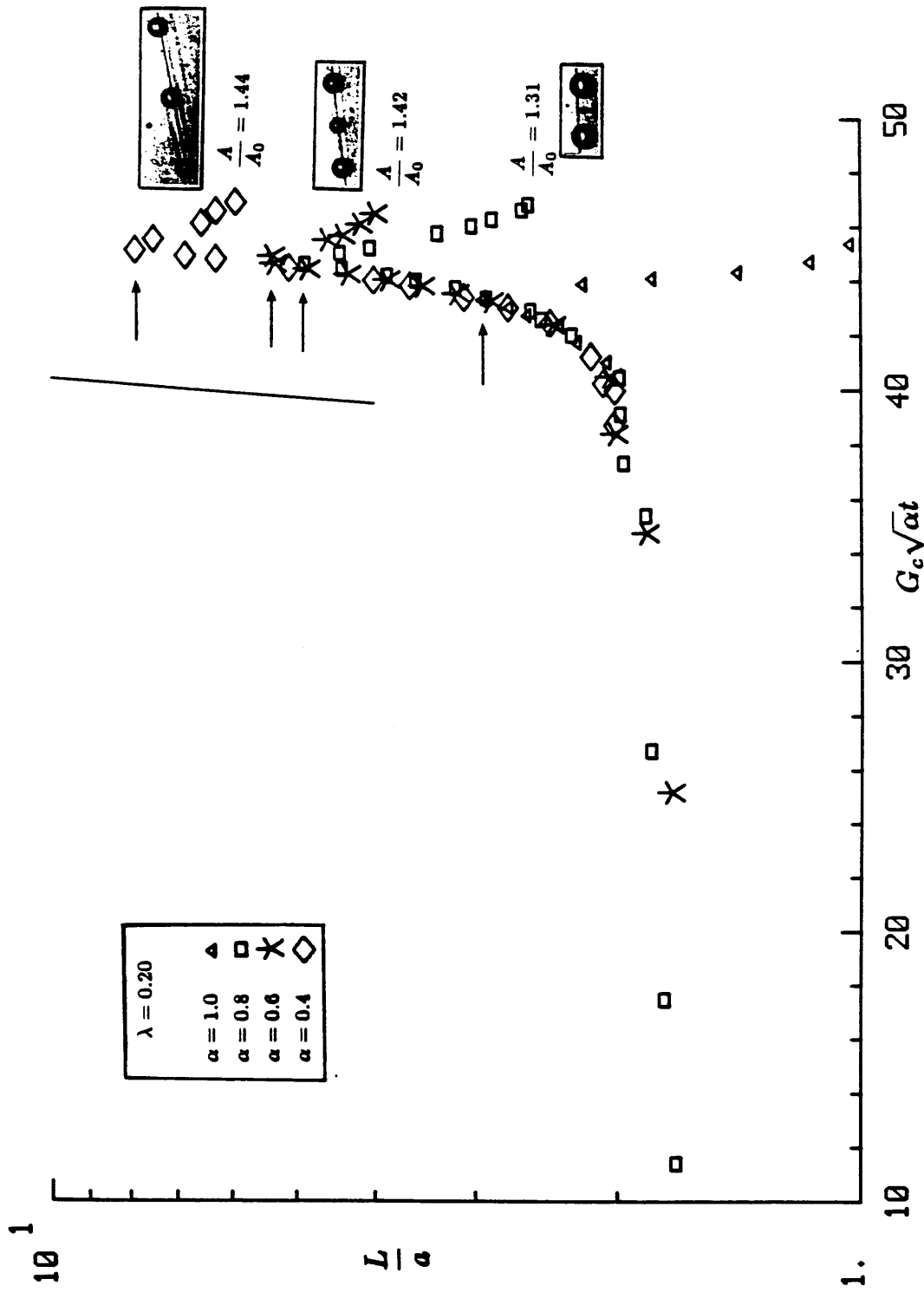


Figure 11c

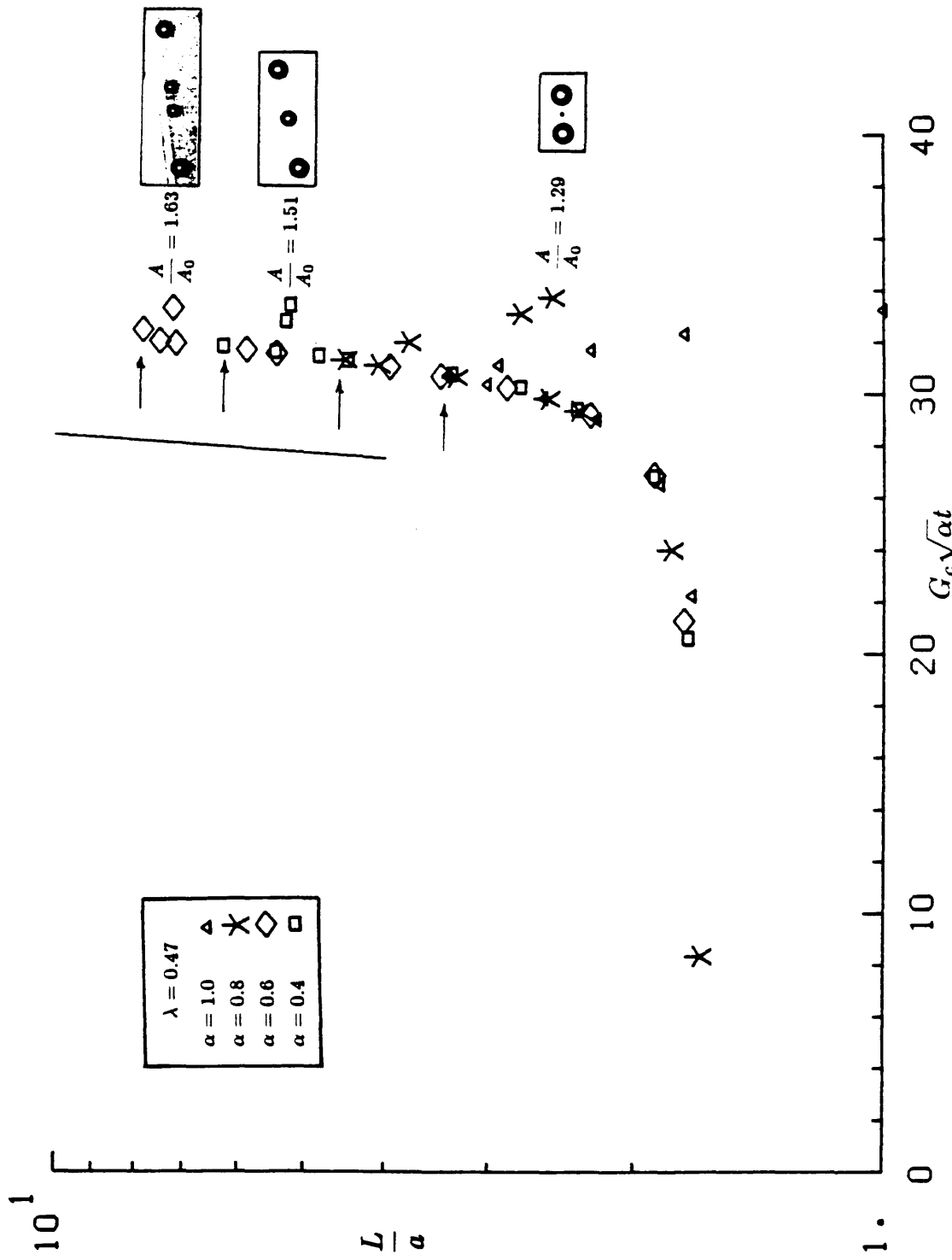


Figure 11d

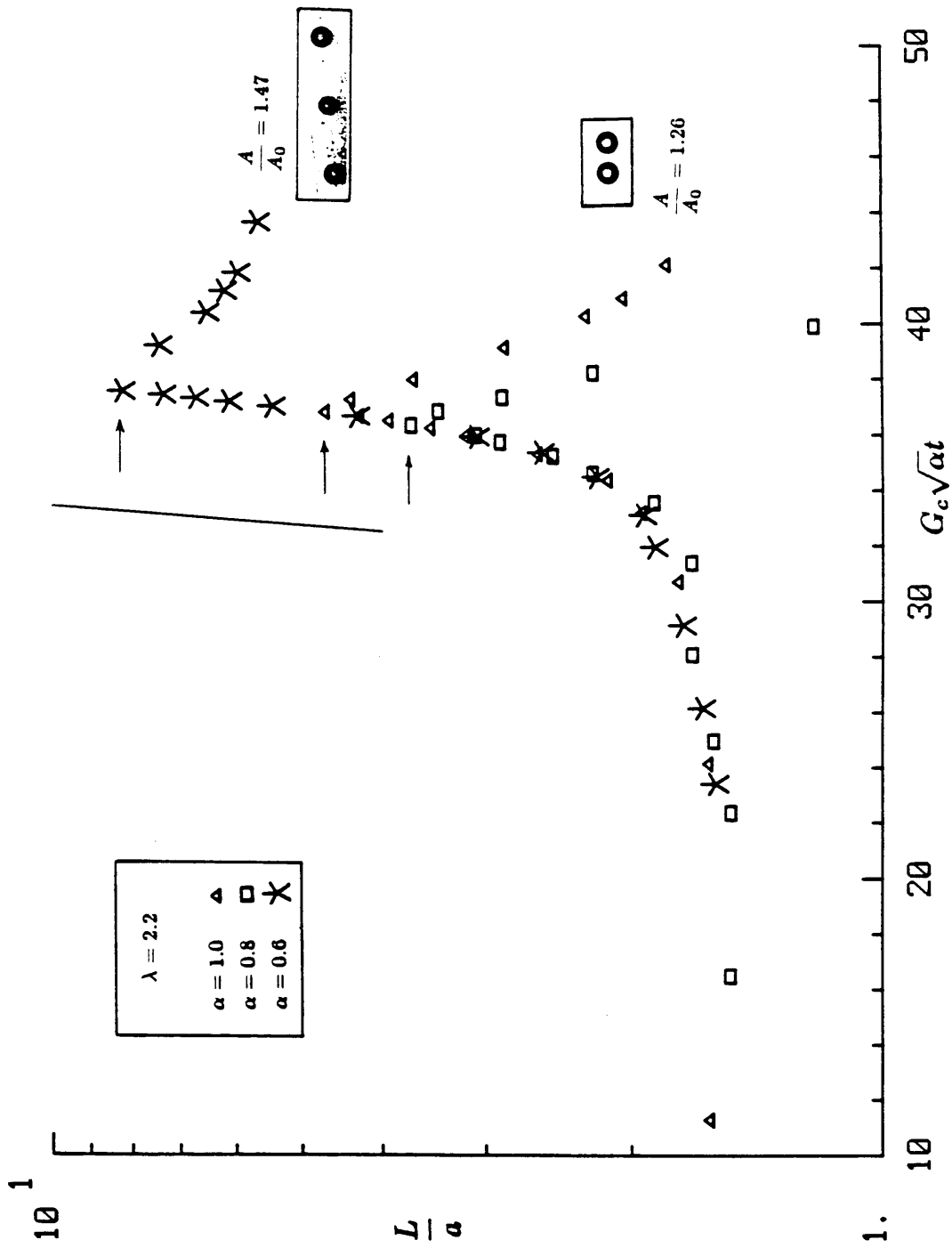


Figure 11e

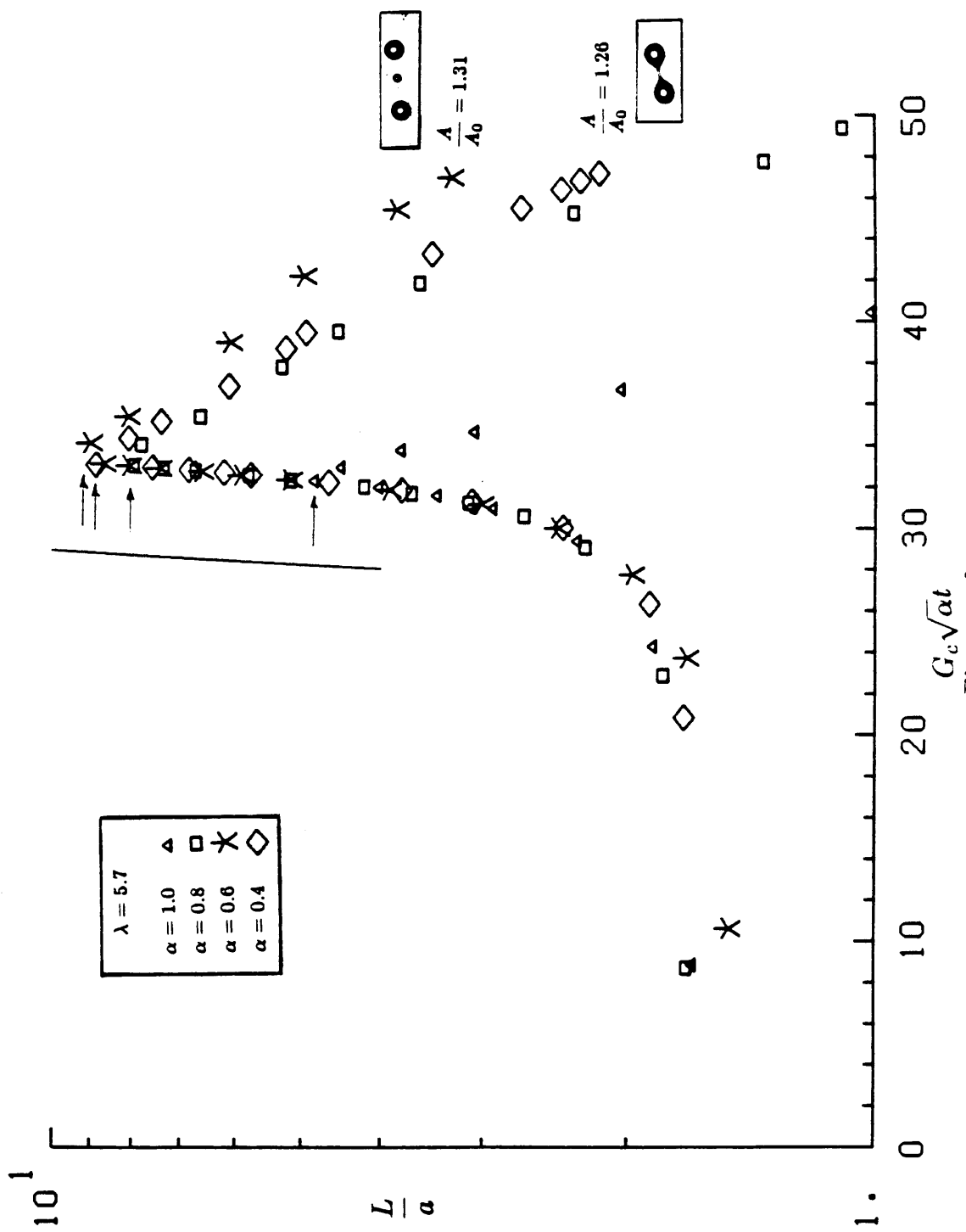


Figure 11f

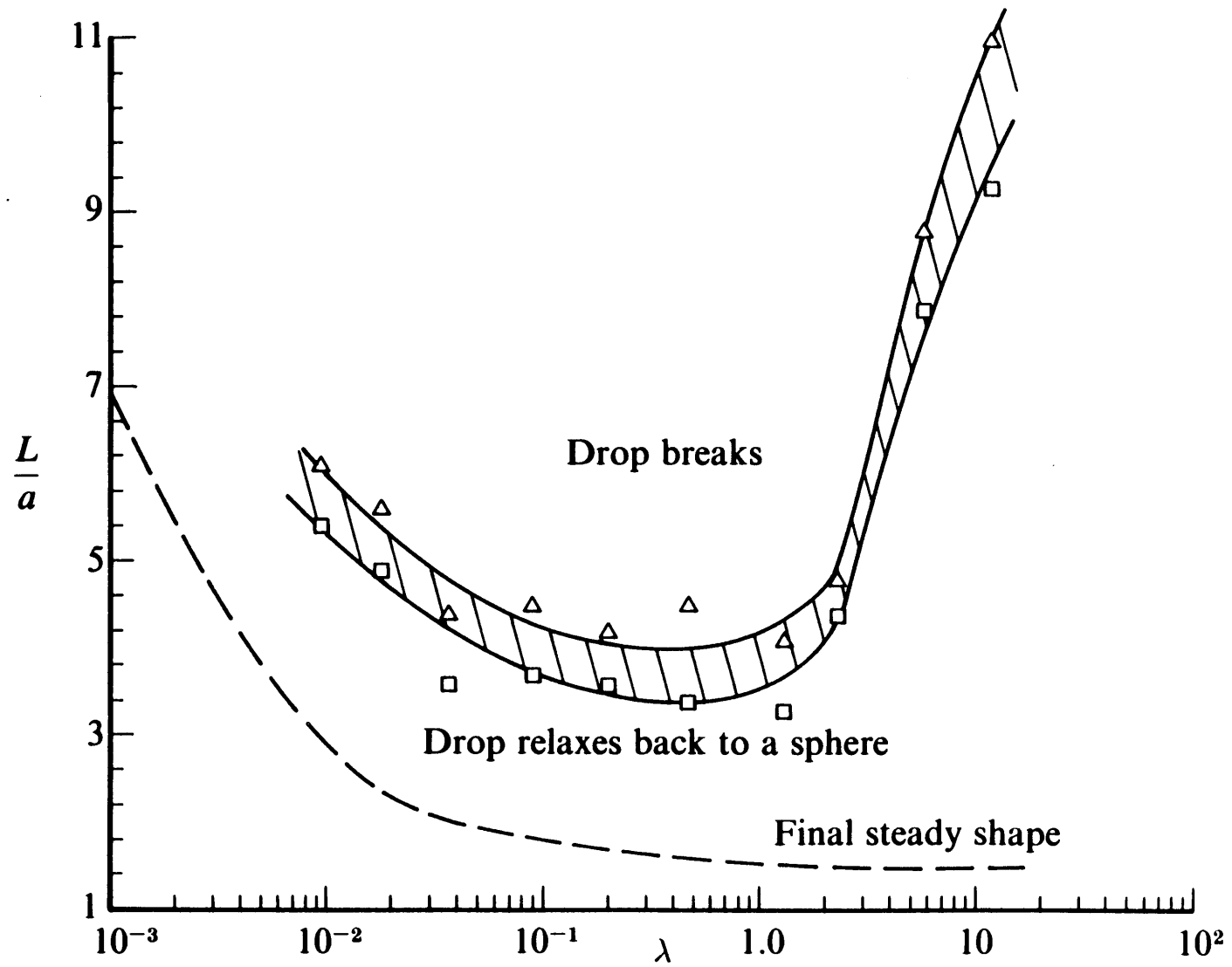


Figure 12

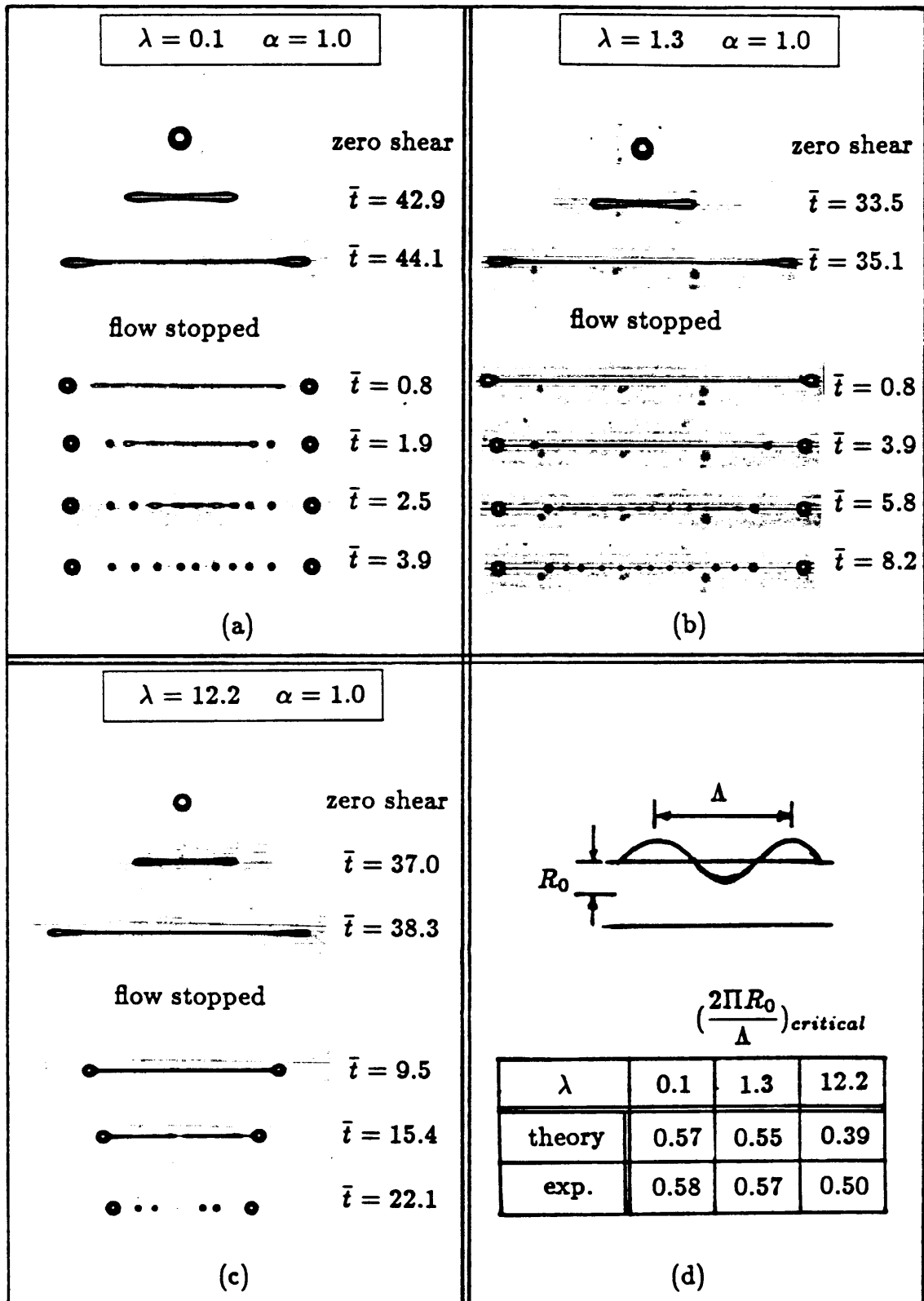


Figure 13

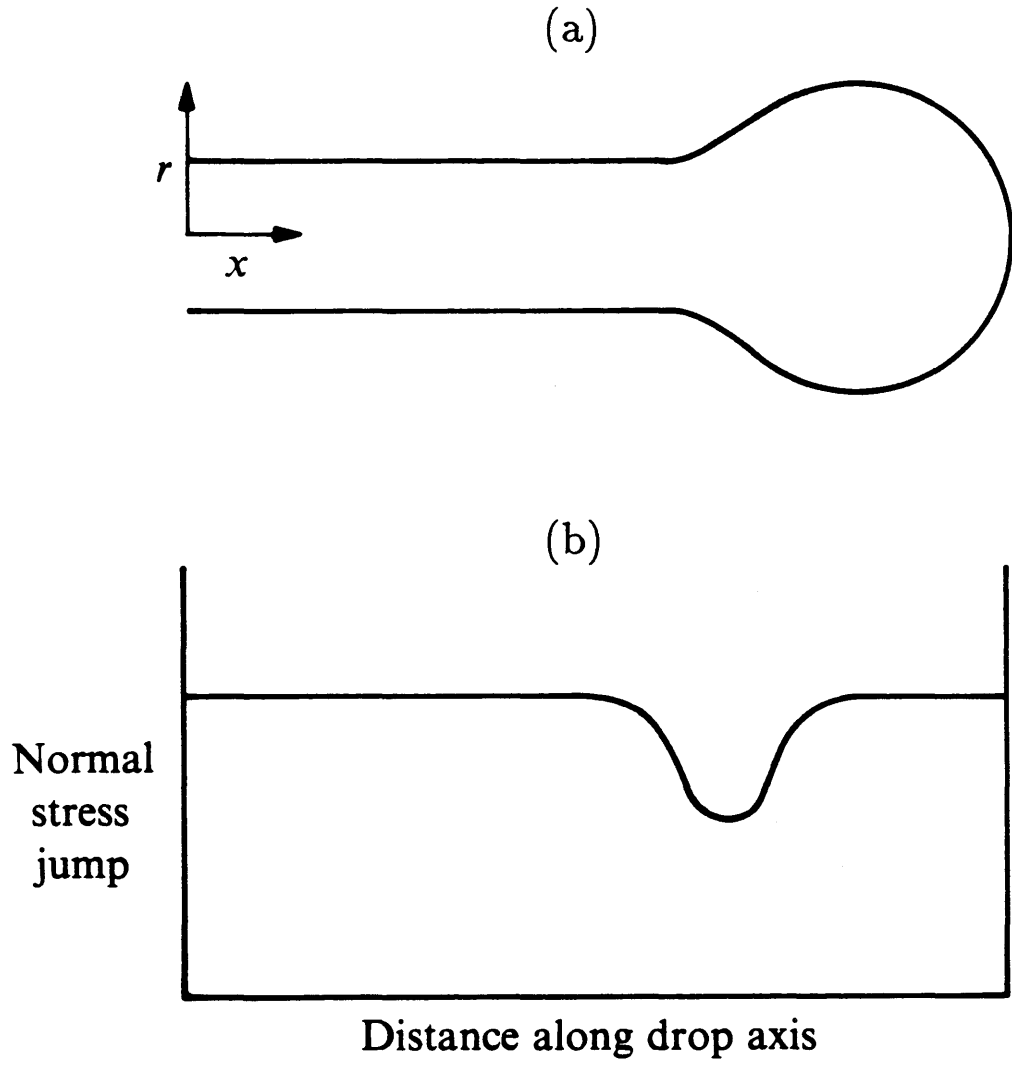


Figure 14

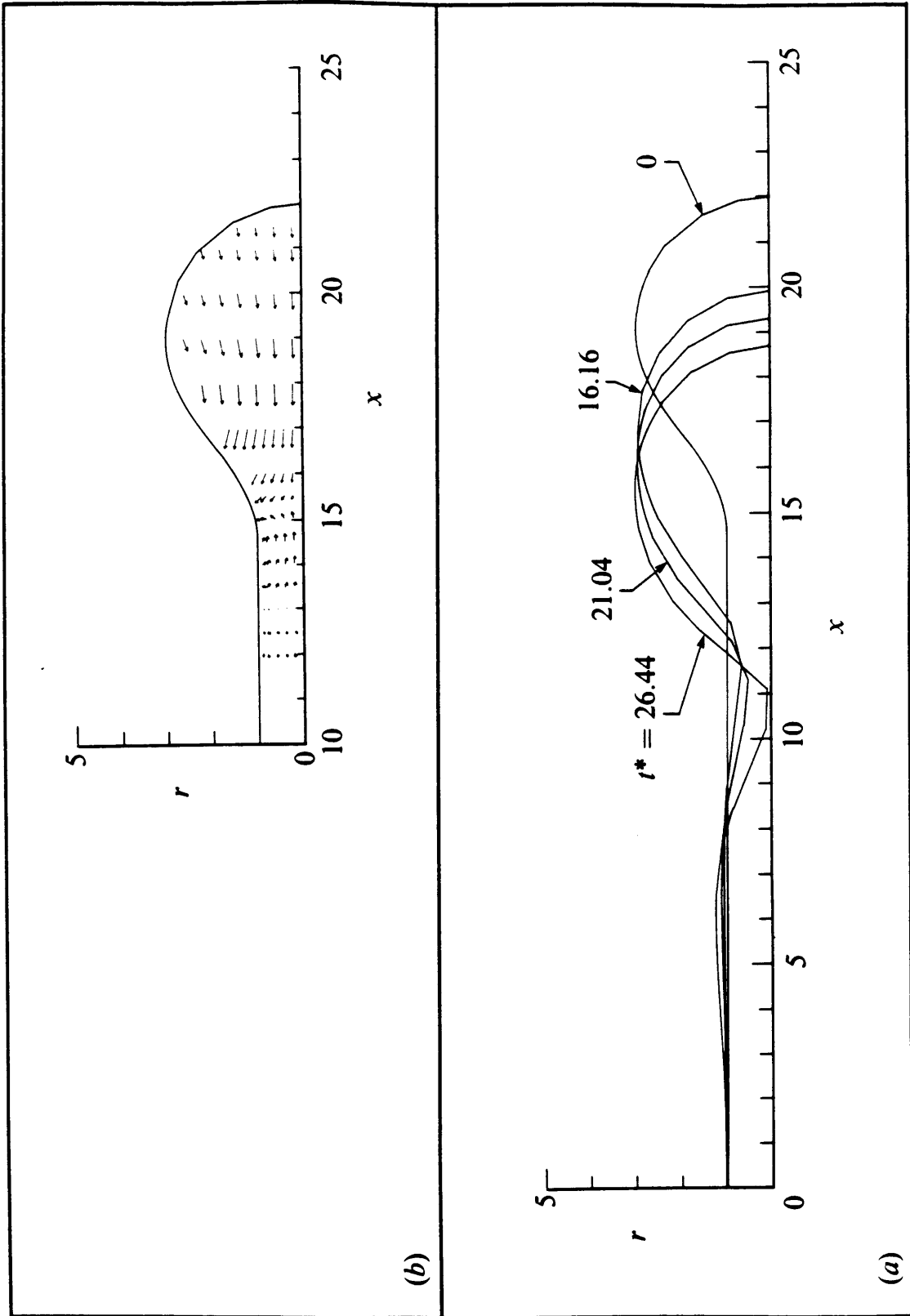


Figure 15

CHAPTER 3

RELAXATION AND BREAKUP OF AN INITIALLY EXTENDED DROP IN AN OTHERWISE QUIESCENT FLUID

The basic text of Chapter 3 consists of an article which has been submitted for publication in the *Journal of Fluid Mechanics*.

**Relaxation and breakup of an initially extended drop
in an otherwise quiescent fluid**

H.A. Stone and L.G. Leal

**Department of Chemical Engineering
California Institute of Technology
Pasadena, California 91125**

September 1987

ABSTRACT

In this paper we examine some general features of the time-dependent dynamics of drop deformation and breakup at low Reynolds number. The first aspect of our study is a detailed numerical investigation of the "end-pinching" behaviour reported in a previous experimental study. The numerics illustrate the effects of viscosity ratio and initial drop shape on the relaxation and/or breakup of highly elongated droplets in an otherwise quiescent fluid. Such flow situations provide a very nice example of fluid motion, due to interfacial tension, which arises solely because of curvature variations along the drop surface. In addition, the numerical procedure is used to study the simultaneous development of capillary wave instabilities at the fluid-fluid interface of a very long, cylindrically shaped droplet with bulbous ends. Initially small disturbances evolve to finite amplitude and produce very regular drop breakup. The formation of satellite droplets, a nonlinear phenomenon, is also observed.

1. INTRODUCTION

The study of the low Reynolds number deformation and breakup of a liquid droplet due to a nonuniform velocity field is a classical free-boundary problem which has been of longstanding interest in the fluid mechanics community, dating back to two remarkable papers by G.I. Taylor in the 1930s. In the intervening 50 years there has been considerable theoretical, numerical and experimental work aimed at achieving a more complete understanding of this problem. Part of the motivation for these studies lies in potential industrial applications which include mixing and polymer blending operations, characterization of the rheological properties of emulsions, and flow-induced deformation of flexible bodies (e.g., cells). Of course, due to the deformable nature of the fluid-fluid interface, the inherent difficulty which arises in fundamental analyses of these problems is the *a priori* unknown location of the boundary. Rather than being given in the problem statement, the interface location must be found as part of the problem solution.

Two distinct approaches have been taken in order to understand different aspects of the drop breakup problem. The first approach examines the deformation of an initially spherical droplet, with undeformed radius a , in *steady* linear flows. The major objective of these studies is the determination of the critical capillary number, $C = \frac{Ga\mu}{\sigma}$ (G is the local shear rate, μ is the suspending fluid viscosity, and σ denotes the interfacial tension), which corresponds to the limit point for *steady* drop shapes (on the branch of solutions which begin with a sphere at $C = 0$). For C larger than the critical value, the droplet stretches continuously to a highly elongated shape. This work is well-summarized in review articles by Acrivos (1983) and Rallison (1984), though an important extension is presented by Bentley & Leal (1986) who systematically investigate the inhibiting effect of vorticity on the deformation and breakup process, a feature first observed and explained by Taylor (1934). The term 'drop burst', as used in these investigations, denotes the flow conditions corresponding to continuous

elongation. In general, actual fragmentation of the droplet is not discussed in these studies.

At the critical capillary number, the drop shapes characteristic of the continuous stretching process have long cylindrical midsections with generally bulbous ends. This elongated shape is used as a starting point and motivation for the second major class of studies on drop breakup. In this case, the droplet is modeled as an infinite fluid cylinder of initially constant radius which breaks up in quiescent or sheared flows due to the growth of capillary wave instabilities. Within the confines of linear stability theory, the effects of viscosity ratio and disturbance wavelength on the disturbance growth rate and resulting drop size distribution are examined by Tomotika (1935), Rumscheidt & Mason (1962) and Lee & Flumerfelt (1981) for the case of quiescent fluids and by Tomotika (1936), Mikami, Cox & Mason (1975) and Khakhar & Ottino (1987) for droplets in a shearing flow. For the equivalent problem where inertial effects rather than viscous effects are important, perturbation methods have been used to examine some nonlinear details of the interface evolution (for example, see the review article by Bogoy 1979). However, as far as we are aware, nonlinear effects have not been studied for the Stokes flow problem.

While these studies have been very valuable in understanding the basic physics of flow induced changes in the drop shape, and have yielded some insight into the factors which control drop size distributions on breakup, it is nevertheless true that real processes almost always involve time-dependent flows (as seen by the drop) and it is important to ask how transient effects may alter the deformation and breakup process. Furthermore, there remain many outstanding problems related to capillary wave growth on extended fluid drops. For example: what role does the end of the droplet play? how do finite amplitude disturbances evolve? and how are nonlinear effects evident? These aspects of the drop deformation problem have received relatively little attention in the literature. There are probably two reasons for this. First, until recently it was

difficult experimentally to study the deformation of an object in a well-defined, time-dependent flow and, second, it has only been in recent years that numerical methods have been developed that are capable of examining transient dynamics of significantly deformed viscous drops.

In a previous publication (Stone, Bentley & Leal 1986) we took the first step in an attempt to better characterize the time-dependent dynamics of modestly deformed drops. Specifically, we experimentally examined droplet stretching near the critical capillary number in two-dimensional linear flows generated in a computer-controlled four-roll mill and investigated the relaxation dynamics which occur if the imposed flow is stopped abruptly with the droplet in a stretched, nonequilibrium state. In the relaxation experiments it was frequently observed that drop breakup occurred due to deterministic flows established by capillary forces associated with curvature variations along the interface. The observed motion consisted of a relatively rapid bulbing of the end of the droplet followed by break off of the bulbous end from the central portion of the drop. This breakup process, called "end-pinching", was shown to have a rather strong dependence on the ratio of drop viscosity to suspending fluid viscosity, λ ($\lambda = \frac{\hat{\mu}}{\mu}$ where $\hat{\mu}$ is the droplet viscosity). Specifically, for $\lambda > O(1)$, the mechanism leading to breakup was damped and much larger elongations were necessary to guarantee breakup as the viscosity ratio was increased. The effect of increasing the droplet extension prior to stopping the flow was also examined, and, for sufficiently long drops, capillary waves were shown to play an important role in the final stages of the breakup process. Finally, a qualitative explanation of the "end-pinching" process was proposed and a brief supporting numerical computation presented for the special case $\lambda = 1$.

In this paper we present more detailed numerical calculations using the boundary integral method to further elucidate the end-pinching mechanism for a highly extended droplet of constant interfacial tension in an otherwise quiescent fluid. Our basic interest is to probe the effects of viscosity ratio and initial

drop shape on the relaxation and breakup process, with a particular emphasis on understanding the end-pinching behaviour. Qualitative and quantitative comparisons with experimental observations from Stone *et al.* (1986) also confirm that the experimental system corresponds closely to the assumption of constant interfacial tension. The last part of the study uses the numerical procedure to probe some (nonlinear) features associated with the growth of capillary wave instabilities on a highly elongated droplet. Specifically, we follow the entire evolution of an initially arbitrary, small amplitude disturbance to finite amplitude and consequent drop breakup. Although not extensive, to our knowledge these calculations are among the first which exhibit the implicitly nonlinear behaviour of finite amplitude disturbances on a cylindrical fluid interface. In addition, the calculation simultaneously resolves the behaviour near the end of the droplet. Perhaps the most interesting aspect of the simulation is the *predicted* formation of small satellite drops.

In a general sense, the numerics illustrate application of the boundary integral method to a problem involving large, time-dependent deformations and interfacial-tension-driven flows that are caused by variations in curvature along the interface (the interfacial tension is constant). Of course, an obvious and, from the standpoint of applications, important question is the role of surface tension gradients in drop deformation and breakup due, for example, to the presence of surfactants at the fluid-fluid interface. This is currently under study and will be addressed in a future communication.

In our previous study we have made a distinction between the end-pinching motion and motion due to capillary wave instabilities. It is important to recognize that *both* are interfacial-tension-driven flows and the same characteristic velocity scale, $\frac{\sigma}{\mu(1+\lambda)}$, may be used to describe the dynamics in each case. However, the *source* of the two motions is different. End-pinching specifically refers to deterministic motions induced by the significant curvature variations which occur near the closed end of the droplet. The initial drop shape is *not* an equi-

librium solution of the governing equations and boundary conditions and the shape must therefore evolve toward some steady conformation. The term capillary wave instability is traditionally used to describe the evolution of arbitrary, infinitesimal disturbances on an infinite circular fluid cylinder. The difference is that the infinite cylinder is an *equilibrium* shape (albeit an *unstable* equilibrium shape) in the absence of any disturbances. However, it should be clear that once finite amplitude disturbances have developed these two types of motion are due to the same mechanism : curvature variations of the order of the drop radius give rise to velocities which are $O\left(\frac{\sigma}{\mu(1+\lambda)}\right)$.

It is worth noting that the transient dynamics described in this paper are related to other free-boundary problems which arise in quite varied processes. For example, similar relaxation and breakup processes are illustrated by Lasheras, Fernandez-Pello & Dryer (1979) in an experimental study of the combustion characteristics of fuel droplets and by Greenspan & McCay (1981) for the retraction of an initially extended droplet which wets a solid planar surface.† Another closely related problem is the capillary instability of inviscid liquid jets, which has been widely studied due to a variety of practical applications. For example, similar dynamics to aspects of this work are illustrated and nicely discussed by Goedde & Yuen (1970).

† We wish to thank these authors for bringing these studies to our attention.

2. NUMERICAL PROCEDURE / IMPLEMENTATION

One objective of this study is to examine the details of relaxation and breakup of highly elongated droplets suspended in an otherwise quiescent fluid or in a subcritical flow. A very efficient numerical scheme for this free-boundary problem is the boundary integral method. The basic boundary integral formulation is fairly widespread in the fluid mechanics literature. For example, at low Reynolds numbers it has been used to study flow past solid particles by Youngren & Acrivos (1975), the approach of a particle or drop toward a fluid-fluid interface by Leal and coworkers (Lee & Leal 1982, Geller, Lee & Leal 1986) and flow over two-dimensional slits by Higdon (1985).

The first application of the boundary integral method to the droplet deformation problem was presented by Youngren & Acrivos (1976) in a study of bubbles in an axisymmetric extensional flow, and by Rallison & Acrivos (1978) for the general case of viscous drops. Specifically, the latter authors calculate steady drop shapes for viscosity ratios λ in the range $0.3 < \lambda < 100$. For the special case $\lambda = 1.0$ the calculations were extended by Rallison (1980) to deformation in a simple shear flow and the method has also been applied to drop deformation in electric and magnetic fields by Sherwood (1987). Our long term interest is in using the boundary integral method to study the drop shape evolution in time-dependent flows. The numerical procedure incorporates ideas presented in the above mentioned studies in addition to those of Hinch (private communication).

For the sake of completeness we summarize the necessary integral equations below. For more details, the reader is referred to Rallison & Acrivos (1978). The formulation is given for the general situation with $\mathbf{u}_\infty \neq 0$, though, for the most part, it is applied in this paper only for the case of a quiescent far-field flow, $\mathbf{u}_\infty = 0$. The dimensionless governing equations are the quasi-steady Stokes equations and continuity equation for each phase:

$$\nabla^2 \mathbf{u} = \nabla p \quad \nabla^2 \hat{\mathbf{u}} = \nabla \hat{p}$$

$$\nabla \cdot \mathbf{u} = 0 \quad \nabla \cdot \hat{\mathbf{u}} = 0.$$

Variables associated with the droplet phase are denoted by the symbol $\hat{\cdot}$. All velocities have been nondimensionalized by $u_c = \frac{\sigma}{\mu}$, time by the convective time scale $t_c = \frac{l_c}{u_c}$ where l_c is a characteristic length scale and pressures by $p_c = \frac{\mu u_c}{l_c}$, $\hat{p}_c = \frac{\hat{\mu} u_c}{l_c}$. The choice of characteristic velocity is motivated by the desire to study relaxation of initially elongated droplets in an otherwise quiescent fluid. For a nearly spherical drop the undeformed radius, a , is an appropriate length scale while for a highly extended droplet the midsection radius is more appropriate.

The boundary conditions are

$$\begin{aligned} \mathbf{u}(\mathbf{x}) &\rightarrow \mathbf{u}_\infty \quad \text{as } |\mathbf{x}| \rightarrow \infty \\ \mathbf{u} &= \hat{\mathbf{u}} \quad \text{for } \mathbf{x} \in \mathbf{x}_s \\ \mathbf{n} \cdot \mathbf{T} - \lambda \mathbf{n} \cdot \hat{\mathbf{T}} &= \mathbf{n} (\nabla_s \cdot \mathbf{n}) \quad \text{for } \mathbf{x} \in \mathbf{x}_s \end{aligned}$$

and the kinematic condition

$$\frac{d\mathbf{x}_s}{dt} = \mathbf{n}(\mathbf{u} \cdot \mathbf{n})$$

describes the evolution of the drop shape. The position vector \mathbf{x} denotes a point in the fluid domain while \mathbf{x}_s specifically indicates a point at the fluid-fluid interface, \mathbf{T} and $\hat{\mathbf{T}}$ denote the stress tensors for the continuous and droplet phases respectively, \mathbf{n} is the unit normal directed from the droplet phase to the continuous phase and $\nabla_s \cdot \mathbf{n}$ represents the mean curvature of the fluid-fluid interface (see figure 1). Due to our choice for u_c , the capillary number, $C = \frac{G a \mu}{\sigma}$ (G is the shear rate of the external flow \mathbf{u}_∞) appears explicitly in the definition of \mathbf{u}_∞ (see equation (4)), but does not appear in the stress balance at the interface.

The complete neglect of inertia, upon which this study is predicated, requires that both the local and convective acceleration effects are small compared to viscous effects. For relaxation phenomena when $C = 0$ this requires

$\frac{\sigma \rho l_c}{\mu^2(1+\lambda)} \ll 1$ (ρ is the density of the suspending fluid) which will generally be satisfied for small droplets suspended in viscous fluids. In the presence of an imposed linear flow, with characteristic velocity scale Gl_c , the neglect of convective inertia also requires that $\frac{\rho Gl_c^2}{\mu} \ll 1$. For time-dependent flows it is necessary to neglect inertial effects due to the transient nature of the flow. Local acceleration effects are negligible compared to viscous effects provided $\frac{\rho l_c^2}{\mu \tau} \ll 1$ where τ is the time scale characterizing the transient flow.

In the boundary integral formulation, the velocity at any point in the two phases is represented by

$$\mathbf{u}(\mathbf{x}) = \mathbf{u}_\infty(\mathbf{x}) - \int_S \mathbf{n} \cdot \mathbf{T} \cdot \mathbf{J} dS(\mathbf{y}) - \int_S \mathbf{n} \cdot \mathbf{K} \cdot \mathbf{u} dS(\mathbf{y}) \quad (1)$$

$$\hat{\mathbf{u}}(\mathbf{x}) = \int_S \mathbf{n} \cdot \hat{\mathbf{T}} \cdot \mathbf{J} dS(\mathbf{y}) + \int_S \mathbf{n} \cdot \mathbf{K} \cdot \hat{\mathbf{u}} dS(\mathbf{y}) \quad (2)$$

where

$$\mathbf{J} = \frac{1}{8\pi} \left[\frac{\mathbf{I}}{|\mathbf{x} - \mathbf{y}|} + \frac{(\mathbf{x} - \mathbf{y})(\mathbf{x} - \mathbf{y})}{|\mathbf{x} - \mathbf{y}|^3} \right]$$

$$\mathbf{K} = -\frac{3}{4\pi} \frac{(\mathbf{x} - \mathbf{y})(\mathbf{x} - \mathbf{y})(\mathbf{x} - \mathbf{y})}{|\mathbf{x} - \mathbf{y}|^5}$$

In these equations, S represents the droplet surface and \mathbf{y} is the integration variable. The pressure field can be similarly represented by surface integrals involving the velocity and stress fields at the interface. Hence, provided that the interfacial stress and interfacial velocity fields are known, knowledge of the drop shape allows the velocity and pressure fields to be determined anywhere in the fluid domain.

Making use of the boundary conditions and the well-known jump conditions to treat the singular nature of the kernel in the limit $\mathbf{x} \rightarrow \mathbf{x}_s \in S$ the general equations (1) and (2) lead to an integral equation for the interfacial velocity (Rallison & Acrivos 1978)

$$\frac{(1+\lambda)}{2} \hat{\mathbf{u}}(\mathbf{x}_s) = \mathbf{u}_\infty(\mathbf{x}_s) - \int_S \mathbf{J} \cdot \mathbf{n} (\nabla_s \cdot \mathbf{n}) dS(\mathbf{y}) - (1-\lambda) \int_S \mathbf{n} \cdot \mathbf{K} \cdot \hat{\mathbf{u}} dS(\mathbf{y}) \quad (3)$$

For a given shape, capillary number and viscosity ratio, this expression is an integral equation of the second kind for the interfacial velocity $\hat{u}(\mathbf{x}_s)$. As there exists no known analytic solution to this equation we must resort to an approximate numerical solution. The case $\lambda = 1$ is especially straightforward, as is evident from equation (3).

If the object of greatest interest is the interface evolution then it is clear from (3) that one advantage of the boundary integral method is that it is only necessary to perform computations on a two-dimensional surface rather than over the entire three dimensional domain. Furthermore, as a result of the quasi-steady nature of Stokes equations, the interfacial velocity at any time is uniquely determined by the drop shape and the imposed flow at that time. Since the drop shape evolves according to the kinematic condition, then the shape at all future times is determined by an initial condition and the time-history of the flow (Rallison 1984).

In the interest of numerical simplicity, we consider an initially axisymmetric drop which then remains axisymmetric for all time. Referring to the cylindrical coordinate system shown in figure 1, the shape is also symmetric with respect to a plane passing through $z = 0$, orthogonal to the axial (z) direction. In equation (3) the azimuthal (θ) integration can be performed analytically and the surface integrals are reduced to line integrals. The resulting one-dimensional integral equation for the interfacial velocity field is solved by discretizing the interface into $2N-2$ boundary elements with node points placed at the end of each element, and converting the integral equation to an "equivalent" linear system of coupled algebraic equations by approximating the unknown function $\hat{u}(\mathbf{x}_s)$ over each element of the surface. Due to the axisymmetry, there are two unknown components of the interfacial velocity (\hat{u}_r, \hat{u}_z) at each node point.

There are two important aspects to the discretization: (1) approximation of the variation of interfacial velocity over an element of the surface and (2) accurate representation of the drop shape and curvature. The former is treated by

assuming that the velocity field varies linearly over each element. For the highly deformed shapes typical of this study, tests with this representation demonstrated that it helped to produce smoother and more accurate interfacial velocity distributions than the more common assumption of constant velocity over each element. Accurate representation of the drop shape is crucial simply because many of the motions we wish to study are driven solely by curvature variations over the drop surface. In order to generate a smooth and accurate representation of the interface without excessive use of collocation points two alternative methods are utilized.

Since many of the shapes to be studied have cylindrical midsections with bulbous, nearly spherical ends, the first scheme makes use of cylindrical coordinates near the middle of the drop and spherical coordinates near the end of the drop (the surface, with $2N-1$ collocation node points, is described in these two cases by $r = r(z)$ and $\rho = \rho(\phi)$ respectively - see figure 1) with cubic splines used to generate twice continuously differentiable representations of the interface in each region. The two representations are patched together by requiring first derivatives to be continuous at the point of overlap and second derivatives to be continuous within some tolerance (typically 10^{-6}) at the point of overlap. In this way the drop shape is described by a smooth function which is essentially twice continuously differentiable everywhere. The second scheme uses an arclength parametrization method (Ascoli 1987). If s represents a normalized measure of arclength ($0 \leq s \leq 1$), then the collocation points on the interface, labeled using the cylindrical coordinates (r, z) , are parametrized so that $r = r(s), z = z(s)$ describes the fluid-fluid interface and again twice continuously differentiable representations are generated using cubic splines. Both methods work very well, although for a similar number of points, as might be expected, the former scheme is more successful for elongated shapes with nearly spherical ends while the latter scheme performs better for very slender shapes with nearly pointed ends.

Due to the fore-aft symmetry, the number of unknowns is halved and the net result of the discretization is a system of $2N-2$ equations and unknowns. The resulting linear system is solved using Gaussian elimination to give the interfacial velocity distribution along the fluid-fluid interface.

Typically, for relaxation of the extended drops illustrated in Section 3.2, we choose $N=35$ for drops with initial half-lengths 30-40 times the midsection radius. In a study of capillary instabilities on a highly elongated drop, described in Section 3.3, we choose $n=49$. In both studies, the collocation points initially have an average spacing of $\Delta z \approx 1.0 - 1.5$ in the cylindrical region and are more densely spaced near the bulbous end where larger curvature variations occur. With this node point spacing the numerics are capable of resolving small initial disturbances on the cylindrical region whose frequencies ω are smaller than 2. Since the drop shortens as the relaxation process proceeds (and, consequently, the average point spacing decreases), the same number of points is capable also of resolving the larger curvature variations which occur at later times, either due to the end-pinching phenomena or the growth of capillary instabilities. Limited testing in these cases with 50% more collocation elements yields the same results.

In order to demonstrate the accuracy of the shape-fitting routine, we compare analytically determined curvatures, $(\nabla_s \cdot \mathbf{n})$, with numerically generated values for an object of known shape. The test shape is shown in the inset to table 1 and consists of a uniform cylindrical midsection connected to bulbous ends. The end-to-end length of the drop is 106 times its undeformed radius. The dark symbols on the interface indicate the location of the node points. On the cylindrical midsection a sinusoidal disturbance, frequency ω and amplitude R_a , is superimposed. At each node point in the cylindrical region we calculate the relative error between the numerical and analytical values of the curvature (error = $\frac{\text{exact}-\text{numerical}}{\text{exact}}$). In table 1 we display the maximum error and square root of the mean square error. Also shown is the dominant frequency obtained from a Fourier analysis of the central cylindrical region (calculated using equa-

tion (5)). The cases $N=49$ have an average point spacing between collocation points in the cylindrical region of $\Delta z \approx 1.0$ and the cases $N=69$ have an average spacing of $\Delta z \approx 0.6$. Clearly, the numerical procedure does a good job of approximating the curvature and in all cases the Fourier spectrum has a sharp peak at the frequency of the applied disturbance. This test of the shape-fitting routine is comparable to the most severe geometry considered in this study and demonstrates the ability of the numerical scheme to resolve those details of the shape that will be important to this study. Larger amplitude disturbances or frequencies larger than $\omega \approx 2$ on this model shape would require more points to be resolved properly.

Finally, we should add that all calculations reported in this paper are done in double precision, integrals are evaluated using a five point Gauss quadrature scheme and, in the vicinity of the singularity where rapid variation of the integrand occurs, special care is taken by subdividing the interval of interest into three smaller intervals prior to integrating. A small region, typically 10^{-3} to 10^{-4} the size of an interval is cut out around the singularity and the integration over this portion is performed analytically (the singularity is integrable in the sense of a Cauchy principal value).

The interface shape is updated by solving the kinematic condition using an explicit Euler method. Preliminary calculations using a second order Runge-Kutta method to update the shape gave nearly identical results. For the majority of shapes and capillary numbers to be studied, the largest dimensionless velocities are $O(0.1-1.0)$ so the time-step chosen is typically 0.02-0.05.† This value is reduced when regions of high curvature (and hence large local velocities) de-

† For larger viscosity ratios it is more convenient in the *numerical* calculations to scale the velocity with $u_c = \frac{\sigma}{\mu(1+\lambda)}$ and the time with $t_c = \frac{l_c}{u_c}$. In this way $u = O(1)$ for all λ . For simplicity when comparing simulations involving different λ we discuss all calculations using the time scale and velocity scale introduced in the text.

velop.

Our numerical procedure is then as follows. For a given shape solve for $\hat{u}(\mathbf{x}_s)$, update the shape using the kinematic condition and repeat the procedure. Every few time-steps the collocation points are evenly redistributed based upon arclength along the interface. When a region of high curvature (the region of a neck during the end-pinching process - see figure 5) begins to develop, additional points are added in the immediate vicinity of the maximum curvature. Typically 5-8 additional points are added, at least tripling the local density of collocation points, which, coupled with the cubic spline used to represent the interface shape, maintains accurate resolution of the shape.

As we will see, for these free-boundary problems the interface evolution can be quite complicated and knowledge of the internal and external velocity and pressure fields can be useful in understanding the observed behaviour. As mentioned following equation (2), this requires determination of both the interfacial velocity and interfacial stress. Hence, when a complete picture of the velocity and pressure fields is desired, the interfacial velocity is calculated as described above and a similar discretization process must be used to solve for the unknown (interior) interfacial stress distribution, $\mathbf{n} \cdot \hat{\mathbf{T}}$. Once again, the unknown interfacial stress components are assumed to vary linearly over each element and the integral equation is recast as a system of linear equations which is solved using Gaussian elimination. Then, the exterior normal stress distribution, $\mathbf{n} \cdot \mathbf{T}$, is calculated using the normal stress boundary condition. Finally, the interfacial stress and velocity can be used in equations (1) and (2) to compute the velocity field at any interior or exterior location. A similar procedure can be followed to determine the interior and exterior pressure distribution in the fluid.

As a check on the numerics, a detailed comparison is made with the small deformation analysis of Barthes-Biesel & Acrivos (1973) for drop deformation in axisymmetric extensional flows (briefly summarized in Section 3.1) and with the velocity and pressure fields around solid prolate ellipsoids in extensional flows.

In all cases, the comparison is excellent. Also, the drop volume is monitored as a function of time and typically changes by a couple tenths of a percent over several hundred iterations. For the drop relaxation studies to be described in Section 3.2, a typical simulation requires 600-3000 iterations resulting in overall volume changes from 1-10 percent of the original drop volume. However, for simulations involving small λ , $\lambda < O(0.01)$, characterized by long slender shapes with nearly pointed ends, the volume changes are larger (as other researchers have found). In these cases, the drop dimensions are rescaled every few time-steps in order to conserve volume. Comparing results with and without rescaling indicates that the qualitative behaviour (basically the overall shape and the critical conditions for drop burst) is unchanged when the rescaling is implemented and the only significant change is a small change in the time scale for deformation.

3. RESULTS

3.1 Comparison of numerics with small deformation theory

We begin by briefly examining the deformation of an initially spherical droplet placed in an axisymmetric extensional flow, $\mathbf{u}_\infty = \Gamma \cdot \mathbf{x}$ where

$$\Gamma = \frac{C}{2} \begin{pmatrix} -1 & 0 & 0 \\ 0 & -1 & 0 \\ 0 & 0 & 2 \end{pmatrix} \quad (4)$$

where the capillary number $C = \frac{Ga\mu}{\sigma}$. The appearance of C in (4) occurs because of our choice of the characteristic velocity as $u_c = \frac{\sigma}{\mu}$ and the characteristic length scale as the undeformed drop radius, a . This numerical problem was considered by Rallison & Acrivos (1978) and, as reported by Rallison (1984), higher accuracy results have been obtained by Duffy and Blundell for the special case $\lambda = 1$. The purpose of this section is to compare our numerical simulations with the small deformation theory of Barthes-Biesel & Acrivos (1973) and the numerical work mentioned above.

Theoretical work to predict the steady drop shape as a function of capillary number began with Taylor (1932). Taylor treated the droplet as spherical, solved

for the internal and external flow fields using continuity of velocity and tangential stress boundary conditions and determined the $O(C)$ correction to the drop shape by approximately satisfying the normal stress balance at the fluid-fluid interface. Barthes-Biesel & Acrivos (1973) extended the analysis to second order in capillary number and the applicability of this work and previous work was clarified by Rallison (1980). An additional discussion, including the extension to a large number of two-dimensional linear flows, can be found in Bentley & Leal (1986).

For droplets which are only slightly deformed, an appropriate scalar measure of deformation is $D = \frac{L-B}{L+B}$, where L and B are the half-length and half-breadth of the cross-sectional shape respectively. The deformation as measured by D monotonically increases with increasing capillary number and, near the critical capillary number, D increases rapidly with small changes in C .

A comparison between the present numerical results and existing theoretical results for D versus capillary number is shown in figures 2-4 for $\lambda = 0.1, 1.0$ and 10.0 respectively. The short dashed line denotes the $O(C)$ result and the long dashed line the $O(C^2)$ result. Each analytic line ends when a capillary number is reached above which the theory predicts no steady shape. The numerical results are given by the solid line and, for completeness, several numerically generated shapes are shown in each figure. In figure 3, the open circles represent the computations of Duffy and Blundell (as reported by Rallison 1984) which are clearly in excellent agreement with our numerics. The good agreement between analytic theory and numerics is similar to the agreement previous researchers have observed upon comparison of the asymptotic theory with experimental results. The small deformation theory does a remarkable job of capturing the major features of the drop deformation even when the deformation is no longer small.

With the level of accuracy indicated by this comparison and the numerical tests outlined in Section 2, we will use the numerical method to examine the

detailed dynamics of very highly extended droplets.

3.2 Relaxation of extended droplets : the effects of viscosity ratio and initial shape

We next demonstrate numerically some dynamical features associated with the relaxation and breakup of an initially extended drop in an otherwise quiescent fluid. Here we are not specifically concerned with how the droplet reached this highly deformed state. Rather, given a highly stretched droplet, the numerics describe the evolution of the drop shape. Although these results reiterate some aspects of the experimental study we previously reported (Stone *et al.* 1986), they illustrate the underlying mechanism of the end-pinching phenomenon, and contribute to a better understanding of drop breakup.

Our goals are twofold. First we wish to demonstrate that the numerics capture the *qualitative* features of the drop relaxation dynamics. As a part of this, we wish to demonstrate that the low viscosity ratio experimental results previously reported are in accord with the same basic mechanism that is responsible for breakup at larger viscosity ratios, even though, at first, they may appear qualitatively different due to the regions of very high curvature that are characteristic of nearly pointed, low viscosity ratio drops. Second, we seek to show that the computed results based upon the assumption of constant interfacial tension are in *quantitative* agreement with the experimental data from our earlier study, Stone *et al.* (1986). Of course, a basic desire is to gain a better understanding of motion driven (at least in part) by capillary pressure gradients due to curvature variations along the surface and this illustrative section is useful in this regard. The numerics also demonstrate the usefulness of the boundary integral method for detailing the evolution of interfacial-tension-driven flows at low Reynolds numbers.

It is convenient to characterize the degree of deformation using a single scalar parameter. For the highly elongated shapes that are typical of this part of the study, a dimensionless extension ratio, $\frac{L}{a}$, is appropriate, where $2L$ is the

end-to-end drop length.

With reference to equation (3), it is worth reiterating that in the absence of an imposed velocity gradient, i.e. $C = 0$, the *only* effect of the interfacial tension is to scale the velocity and, consequently, the time. Hence, for a given initial shape, the magnitude of the interfacial tension plays no qualitative role in the dynamical evolution of the drop shape, but only determines the time scale over which these dynamics occur. In particular, the qualitative features of the relaxation and breakup dynamics are completely determined by the viscosity ratio and the initial drop shape.

3.2.1. $\lambda \geq O(0.05)$; shapes with bulbous ends

In figure 5 we show a series of typical relaxation histories for $\lambda = 0.05, 0.1, 1.0, 7.5, 10.0$. The initial shape with $\frac{L}{a} = 8.6$ is the same in each simulation and is taken from an experiment for $\lambda = 11.3$. This highly stretched initial shape with bulbous ends is typical of experimental results for all $\lambda \geq 0.05$. The times reported have been made dimensionless with respect to the time scale $t_c = \frac{R_o \mu}{\sigma}$ where the midsection radius R_o has been chosen as the characteristic length scale. The time scale is independent of the viscosity ratio so that the different simulations may be compared directly as the viscosity ratio is changed. However, because the larger of the two fluid viscosities should be expected to provide the best measure of the temporal relaxation, we also list in parentheses the modified time, $\frac{t}{(1+\lambda)}$, corresponding to the characteristic time scale $t_c^* = \frac{R_o \mu (1+\lambda)}{\sigma}$. This allows a test of the usefulness of this alternative measure of dimensionless time. These calculations provide a qualitative illustration of the effects to be expected when the viscosity ratio is varied.

The numerical scheme breaks down when end pinching causes the local radius to become very narrow (typically < 0.003) and the large local velocities calculated (corresponding to the large curvatures in this region) move collocation points across the droplet centerline. In a later simulation focussing on capillary wave instabilities (Section 3.3) we will assume that actual fragmentation of the

bulbous end from the central thread occurs at this point. Although this criterion is *ad hoc*, if our primary purpose is to examine the evolution of the interface, then it nevertheless is a reasonable approximation, as the available experiments indicate very rapid breakup as the local radius thins. In this manner we may continue calculations beyond the initial fragmentation.

The results in figure 5 illustrate several interesting aspects of the relaxation physics. For small λ , the end of the droplet translates a relatively short distance prior to pinching. At the point where the ends appear close to breaking off, a central cylindrical thread remains which itself would undergo a similar end bulbing and relaxation process. It may also be noted that the *rate* of pinching accelerates as the pinch regions develop.

As the viscosity ratio is increased the relaxation process slows as does the flow mechanism that leads to the development of a neck. Thus, the end of the drop moves closer to the mid-point prior to the development of a significant pinch. Indeed, for sufficiently viscous drops, no breakup occurs for the initial degree of extension considered in figure 5. In this case, the end of the drop translates all of the way to the middle before a significant pinch can develop, and the drop simply returns to its equilibrium spherical shape. It may be added that the central section of the droplet remains cylindrical in all cases, and, at least for the elapsed time represented by these simulations, there is no evidence of (finite amplitude) capillary waves. The simulations in figure 5 should be compared with figure 9 of our previous publication, Stone *et al.* (1986), which illustrates similar experimental observations.

From the dimensionless times $\frac{t}{(1+\lambda)}$ shown in figure 5 we observe that all the relaxation and/or breakup processes occur for $25 < \frac{t}{(1+\lambda)} < 70$. Hence, this modified time scale yields a good measure of the dimensionless time over which significant changes in shape occur for a wide range of λ .

It is very informative to examine the interior and exterior velocity fields. These are shown in figures 6-8 for $\lambda = 0.1, 1.0, 10.0$, respectively, at different

stages of the shape evolution. In each illustration the arrows denote the direction and relative magnitude of the fluid velocity. There is no connection between arrows in one simulation and those in another. Associated with each figure we show the variation of pressure in the droplet fluid, \hat{p} , along the droplet centerline. Since viscous forces are balanced by a pressure gradient, in each case we plot the difference $\hat{p} - \hat{p}_o$ where \hat{p}_o is the pressure at the droplet center ($z = 0$). When a significant pinch develops it is often difficult to resolve the interfacial stresses sufficiently to determine accurately the pressure variation in the pinch region and for this reason no pressure field is reported in figure 6d.

From these developing velocity and pressure fields we make several observations. Qualitatively, we observe that for large viscosity ratios the interior velocity gradients are small everywhere, while for small viscosity ratios large interior velocity gradients are possible. Also, there exist two relatively distinct regions of flow: the cylindrical region around the middle of the drop and the region near the bulbous end. For each viscosity ratio and for the initial shape shown, there is initially a pressure-driven flow in the cylindrical region *toward* the ends of the drop, and a counter-flow from the bulbous end *toward* the drop center. This is true even for $\lambda = 10$, where the velocities inside the cylindrical region are very small but are still directed towards the end of the drop. In the case of $\lambda = 1$, the "collision" region where these flows meet is almost identical with the location of the pressure minimum. For larger λ , the *relative* magnitude of the flow from the end is larger than that in the cylindrical region, and the zero velocity ("collision") point lies closer to the droplet center than does the pressure minimum. The converse is true for $\lambda < 1$.

In all cases, the velocity profiles in the cylindrical region are parabolic as expected from a slender body analysis (Acrivos & Lo 1978). Also, we note that in the exterior fluid which is quiescent at infinity, the velocity field decays as $\frac{1}{\bar{r}}$ (where $\bar{r}^2 = r^2 + z^2$) sufficiently far from the droplet, characteristic of a Stokes flow (which, of course, is no surprise).

3.2.2. $\lambda < O(0.01)$; shapes with nearly pointed ends

In figure 9 we show a series of relaxation histories which are characteristic of the relaxation of relatively inviscid droplets. The viscosity ratio is 0.01 and the evolution of three successively elongated droplets ($\frac{L}{a} = 5.3, 6.4, 7.5$) is shown. The basic initial shapes are sketched from a series of experiments for $\lambda = 0.011$. Notice that we have maintained the same *ratio* of midsection radius to radius of curvature at the end of the drop. These low viscosity ratio droplets have long slender shapes with nearly pointed ends. The high initial curvature at the ends of the drop results in large velocities near the ends and a very rapid initial reduction in drop length. However, if the drop is sufficiently extended so that this shortening process does not return it too close to its equilibrium spherical shape, the ends eventually bulb up which lowers the pressure in this region and the drop breaks by an end-pinching mechanism that is essentially the same as shown earlier for larger λ values. Notice that even though the initial shape had a midsection that was very nearly cylindrical, capillary waves again play no significant role in determining the final drop size distribution as the end-pinching dynamics apparently occur on a time scale that is short compared to that required for growth of finite amplitude capillary disturbances. We will examine this in more detail in Section 3.3.

In figure 9b it is interesting to notice that the thin cylindrical thread connecting the two bulbous ends at $t = 22.68$ leads to the formation of a small satellite drop as the ends fragment a short time later. Because this is difficult to see we have indicated it by a * on the figure. This provides an example of satellite drop formation due to the nonlinear evolution of the drop shape. In figure 9c, the more highly stretched initial shape leads to three almost equally sized daughter droplets.

In figure 10 the evolution of the velocity and pressure field is shown for the most highly stretched initial shape shown in figure 9. The initial pressure gradient drives the rapid relaxation and as the end becomes more spherical this

pressure gradient diminishes. It is clear that the pressure gradient in the central cylindrical region then begins to drive a flow toward the end of the droplet. This mass flux causes a neck to form in the cylindrical region, a pressure maximum develops and the breakup process accelerates.

Experimentally, the critical elongation necessary to fragment a drop with $\lambda = 0.01$ lies in the range $5.4 < \frac{L}{a} < 6.2$. Hence, the numerics are in good agreement with this qualitative result of the end-pinching dynamics. Finally, by comparison of figures 5 and 9, we can conclude that the different initial shape coupled with the lower viscosity ratio will lead to a noticeable change in the ultimate drop size distribution after breakup.

3.2.3. The mechanism of end pinching

We are now in a position to provide a qualitative explanation of the relaxation and breakup of an extended liquid drop suspended in an otherwise quiescent fluid. As this reiterates several points made in our previous experimental study, we will be brief and stress those new aspects that have been uncovered by the numerical simulations.

In all cases we have examined, the initial shapes characteristic of the elongated droplets have basically cylindrical midsections. The pressure gradient in most of this region is virtually zero, hence very little flow occurs. However, a pressure gradient favoring flow toward the end does occur in the *transition* zone where the cylindrical midsection joins the bulbous end. One possibility is that this pressure gradient may lead to a flow which uniformly decreases the radius of the cylindrical midsection. However, the observed response is more localized. The pressure gradient generates a *local* flow from the cylindrical region *toward* the end which thus causes a neck to form in the drop shape. This is a precursor to end-pinching. Therefore, the mechanism for relaxation and breakup of an extended droplet in an otherwise quiescent fluid consists of a competition between a pressure-driven flow near the end which causes translation of the end toward the droplet center and thus tends to return the drop to its spherical equilibrium

shape and a pressure-driven flow away from the center in the transition region which leads to the development of a neck and thus to breakup via a capillary pinch-off process.

Dynamics associated with $\lambda < 1$ are characterized by relatively large internal velocity gradients and, for modest extensions, the net flux toward the center of the droplet induced by end motion cannot inhibit formation of a neck and subsequent pinch-off. The pointed shapes typical of very low viscosity droplets produce large velocities from the ends toward the droplet center which, at least initially, inhibits the pinching process and allows a significant reduction in drop length prior to breakup (see figure 10). However, larger viscosity ratios are characterized by very small internal velocity gradients and the net flux induced by end motion, while initially retarded by the adverse pressure gradient and competing flux from the central section, can nevertheless dominate the flow in the transition region and thus inhibit breakup by inhibiting the formation of a pinch-point. The consequences of this are that very large extensions of a viscous droplet (i.e. $\lambda \gg 1$) are necessary to guarantee breakup in an otherwise quiescent fluid. Since the effect of the formation of a pinch is to generate a local pressure maximum which retards motion from the end of the droplet, these large extensions are necessary to allow a significant pinch to develop prior to the end translating back to the droplet center.

Overall, it is the *global* features, rather than any *local* details, of the initial drop shape which are responsible for the end-pinching dynamics. This observation was made in our previous experimental study (Stone *et al.* 1986). Similar remarks are made by Brady & Acrivos (1982) in a study of inertial effects on the breakup of slender drops.

3.2.4. Quantitative comparison of experimental and theoretical results

Until this point, the numerical calculations have helped to explain the *qualitative* features of the end-pinching dynamics. We next address the question of whether our results based on the assumption of constant interfacial tension can *quantitatively* predict the actual time-dependent evolution of the drop shape.

Figures 11 and 12 compare experimental and numerical results for drop length as a function of relaxation time for two different viscosity ratios, $\lambda = 0.45$ and $\lambda = 11.3$, respectively. The experiments, conducted in a two-dimensional flow field generated in a four-roll mill, stretch the droplet at the critical capillary number and at some point during the elongation process the flow field is turned off (Stone *et al.* 1986). The Reynolds number $\frac{\sigma R_o}{\mu^2}$ typical of the relaxation process is approximately 10^{-4} for these experiments. When the imposed flow is stopped abruptly the drop shape becomes axisymmetric on a time scale, $\frac{R_o \mu (1 + \lambda)}{\sigma} \approx 0.1 - 1$ sec, which is fast relative to the time of the overall relaxation process (30-150 sec). Therefore, a direct comparison of the experimental results with the numerical calculations is valid. In these figures the dotted lines are the experimental results and the solid lines are the results of the numerical simulations. We also compare several photographs taken during the relaxation experiment with corresponding numerically generated shapes. The small differences may be attributed to uncertainty in the exact value of the interfacial tension. In any case, the agreement between numerics and experiment illustrated in these figures is very good, both qualitatively and quantitatively. Clearly the time scale of the relaxation dynamics that we have observed is completely captured using a constant value for the interfacial tension. A numerical study concerning the effect of variations in the interfacial tension, due to the presence of surfactants, on the dynamics of drop deformation and breakup is currently in progress.

Careful reading of the literature shows that the relaxation dynamics described above and in our previous experimental paper were first observed by

Taylor (1934) and discussed by Grace (1971), though Grace interpreted the breakup in terms of capillary wave instabilities.

3.3 Capillary waves

An important aspect of the breakup process which arises in an examination of the droplet relaxation dynamics, but has not yet been explicitly considered, is the role played by capillary waves. Existing investigations concerned with predicting drop-size distributions have generally assumed that the droplet shape could be approximated as an infinite fluid cylinder which fragmented due to capillary wave instabilities. Such theoretical studies, based upon linear stability theory, have been successfully compared with experimental studies of extremely long cylindrically-shaped droplets by Rumscheidt & Mason (1962) and Lee, Yu & Flumerfelt (1981). However, as should be clear, the capillary instability mechanism cannot explain the droplet relaxation and breakup dynamics illustrated in the previous sections. Nevertheless, it is to be expected that if the droplet is very highly stretched prior to stopping the flow abruptly, then, while fragmentation still occurs at the ends due to the end-pinching mechanism, capillary waves should have enough time to evolve so as to play a role in the breakup of the central cylindrical portion of the droplet. Indeed, this premise was demonstrated experimentally by Stone *et al.* (1986).

In spite of some success in predicting the breakup of fluid cylinders, linear stability theory is not able to explain the existence or formation of satellite drops, nor is it applicable in a selfconsistent sense when the disturbances reach a finite amplitude as must inevitably occur in breakup. The goal of this section is to use the boundary integral method in order to obtain a more complete understanding of drop breakup in the presence of (finite amplitude) capillary waves. The later stages of the breakup process involve finite amplitude capillary waves growing on a cylindrical fluid thread, so the numerics also shed light on this simpler, though classic, problem.

The evolution of capillary waves has interest in several areas concerned

with drop breakup. For example, the controlled breakup of liquid jets, which is a necessary aspect of ink-drop formation in high speed ink-jet printers, has many features in common with this study. Small disturbances, which may be externally applied, result in very regular breakup of a cylindrical liquid jet. The time necessary for breakup, drop-size distributions and shedding of satellite droplets are some of the related problems that have been experimentally and theoretically studied (Bogy 1979, Beatty 1987).

A few remarks regarding capillary waves on cylindrical fluid interfaces are in order. An infinite, stationary fluid cylinder suspended in an otherwise quiescent fluid represents a solution to the governing equations and boundary conditions. This stationary solution, however, is unstable to disturbances with wavelength greater than the cylinder circumference. Linear stability theory (e.g. Lee & Flumerfelt 1981) examines the evolution of an arbitrary disturbance by superposition of individual Fourier modes; i.e., the disturbance has the form $e^{\gamma t} \cos(\omega z)$ and an eigenvalue problem is formulated for the growth rate $\gamma(\omega)$ as a function of the disturbance frequency ω . The disturbance growth rate also depends on the viscosity ratio.

The theory implicitly assumes that all disturbances are equally likely so that the observed drop sizes will correspond to the disturbance wavelength with the largest positive growth rate. If the initial amplitude of this critical disturbance is known, then the time for breakup can be estimated. For example, table 2 shows, for different viscosity ratios, the time (made dimensionless with respect to $t_c = \frac{R_0 \mu}{\sigma}$) necessary for a capillary wave to grow to half the cylinder radius as a function of the initial disturbance amplitude. An initial disturbance with amplitude 10^{-4} takes longer to evolve to half the cylinder radius than the time necessary for the examples of end-pinching that are shown in figure 5. This helps to explain why the majority of our experimental and numerical studies have not observed capillary waves; the end-pinching dynamics (at least the first fragmentation of the end) evolve on a faster time scale than the time necessary

for the growth to finite amplitude of an initially infinitesimal disturbance.

In order to understand more completely the development of capillary waves, including any nonlinearities related to finite amplitude disturbances, we numerically examine the evolution of an initial disturbance on the surface of a highly stretched droplet with a uniform cylindrical midsection. An initial disturbance on the cylindrical region is generated by the superposition of several different frequencies (including modes that, according to linear theory, are stable and unstable) and the growth of the disturbance from small to finite amplitude is observed. As a means of characterizing the details of the interface evolution beginning with an arbitrary disturbance, a Fourier decomposition of the drop shape is performed. Since the drop shape is fore-aft symmetric, the amplitude of a given frequency is calculated from

$$\hat{F}(\omega) = \int_0^l [r(z) - r_{avg}] \cos(\omega z) dz \quad (5)$$

where $r(z)$ represents the interface position, r_{avg} represents the average interface position, and l denotes the axial position where the integration is terminated. r_{avg} changes slowly as a function of time due to the flow accompanying the droplet relaxation and the growth of capillary waves. Truncating the integration at l is necessary because the droplet is not infinite and we wish to isolate capillary wave dynamics from end-pinching dynamics. Although the choice of l and the number of collocation points used to represent the interface make a small difference in the exact values of the Fourier amplitudes calculated from equation (5), the qualitative trends we observe are not changed. The resolution of the Fourier decomposition is affected in two ways: (1) because the discretization of the initial shape has only about one point every 1.5 units in the z -direction, we are not able initially to resolve disturbances for $\omega > 2$ and (2) as the integration in equation (5) is truncated at $z = l$, the numerical Fourier transform cannot accurately resolve details for frequencies $< \frac{\pi}{l}$.

In figure 13 we illustrate the complete evolution of a highly extended droplet, $\lambda = 1$, in an otherwise quiescent fluid. Numerical calculations using $\lambda = 1$ are

convenient since they produce a very simple form of equation (3) but still highlight the important dynamics. The droplet has a dimensionless initial extension ratio $\frac{L}{a} = 14$ and the drop half-length is initially 73 times the radius of the cylindrical region. Although the shape is rather extreme, we will see that even with only 49 collocation points the numerics can resolve the basic qualitative and quantitative features of capillary wave growth. The cylindrical midsection has a small disturbance superposed on it with an initial amplitude about $3 \cdot 10^{-3}$. This amplitude is large enough that numerical errors don't play a significant role in the early development of the capillary wave, yet small enough that the results should approximate those from linear theory. The disturbance is made up of a number of discrete modes and the Fourier decomposition of this disturbance is shown in figure 14a.

The droplet in figure 13 fragments initially at the ends due to the end-pinching process and fractures near the center at later times due to the growth of finite amplitude capillary waves. For numerical ease we have made the approximation that when the numerics indicate fracturing is complete (numerical difficulty occurs when large local velocities in the region of a pinch move collocation points across the droplet centerline as discussed in Section 3.2.1; e.g., figure 13d,k,m show the droplet shortly before fragmentation occurs) the end droplets are assumed to be broken off (the radius at the point of fracture is set equal to zero), the calculation is started again with the central thread only and the daughter droplets are neglected completely in ensuing calculations. Because the fracturing process creates very high curvatures at the ends of the central thread which lead to a very rapid relaxation and bulbing of the ends, the approximation made by neglecting the fragmented daughter droplets should have little effect as the calculations are continued. In other words, even though the pinch-off criterion is *ad hoc*, it plays no role in our results as the time scale associated with the bulbing process at the nearly pointed ends of the remaining central thread is very fast compared to the time scale of the capillary wave growth process. In

figure 14 we plot the square of the amplitude of the Fourier decomposition as a function of frequency, calculated using equation (5) with $l = 20$, at intermediate times during the relaxation process. Practically identical results were found with $l = 25$. Notice that the vertical scale in the plots changes as time increases.

We make the following observations concerning the relaxation and breakup process. Initially, all the interesting behaviour occurs in the vicinity of the end of the droplet where the curvature variations are the largest, figure 13*a-d*. End-pinching causes a droplet to be shed at about $t = 64$. Then, the very high curvature at the end of the remaining central thread causes rapid bulbing of the end and a significant relaxation. Capillary waves are visible (finite amplitude) at $t = 100$ and are very evident at $t = 200$. At $t = 234.6$ the end of the droplet appears ready to fragment due to a combination of the end-pinching mechanism and the capillary instability mechanism, leaving a central thread consisting of three droplets connected by thin cylindrical threads. The final fragmentation, figures 13*l-n*, produces three equally sized main drops and two smaller satellite droplets. First, the two outside drops in figure 13*l* fragment and the middle drop begins to pinch off from the thread-like regions. Continuation of the simulation shows formation of two satellite drops in figure 13*n*. Clearly, the satellite drops form from the cylindrical threads that originally connect the larger drops. The formation of satellite drops from the cylindrical thread between two bulbous reservoirs occurs following the formation of pinch points at the ends of cylindrical region. This process, involving a cylindrical region connecting bulbous “ends”, appears very similar to the basic end-pinching dynamics originally outlined in our previous study (Stone *et al.* 1986). The formation of satellite drops from the cylindrical connecting thread has been observed by, among others, Goren (1964) and Goedde & Yuen (1970). It is clear that satellite drop formation is a direct consequence of the nonlinear dynamics of interface evolution. In a related study of the breakup of liquid filaments, Bousfield, Keunings, Marrucci & Denn (1986) do *not* observe satellite drop formation in the limit of negligible inertial

effects. We have no explanation for this discrepancy other than the observation that their simulation only considers a viscous thread neglecting the environment (limit $\lambda \rightarrow \infty$).

In addition, we should mention that this numerical simulation has several features in common with the experimental observations of Rutland & Jameson (1971) concerning the formation of secondary undulations which form on the cylindrical thread connecting the primary disturbances growing on a liquid jet. These secondary undulations were explained by the nonlinear theory of Yuen (1968) in which inertial effects were assumed to dominate. It is very difficult to distinguish between our observations of the latter stages of drop breakup (figures 13*l-n*), which appears to be a deterministic consequence of nonlinear interface dynamics associated with a cylindrical thread connecting two bulbous reservoirs, and the instability mechanism observed in the above studies on jet breakup which is a result of growth of harmonics associated with the primary mode of instability.

It is interesting that the capillary wave development near the central region of the droplet is so uniform in spite of the fact that the droplet is finite and continually shortening. This suggests that there is very little flow in this central region, and hence very little effect on the capillary wave dynamics due to the continuous shortening of the drop due to the flow near the ends. The velocity profiles illustrated previously in Section 3.2 support this idea. It is for this reason that the quantitative comparison with linear theory examined below is carried out for a thread in a quiescent fluid rather than a thread in an extensional flow (e.g. Mikami, Cox & Mason 1975).

The Fourier decompositions shown in figure 14 are also very informative. Initially the dominant frequency is $\omega = 1.4$, a linearly stable mode. This was purposefully chosen in order to shed light on the evolution of stable modes in a case when their initial amplitudes were larger than that of any other (unstable) modes. Very rapidly this mode decays (as expected from linear theory) and the

new dominant modes lie within the linearly unstable range $0 < \omega < 1$. These results demonstrate that the numerics can resolve the stabilizing influence of interfacial tension for the small amplitude, short wavelength disturbances. The very rapid decay of this linearly stable mode occurs at a rate comparable to that predicted by linear theory although the growth rate is difficult to calculate accurately as the amplitude quickly decays to a point where numerical error is significant. As the disturbance continues to grow on the cylindrical interface, three modes that are present initially dominate the Fourier spectrum, $\omega = 0.44, 0.66, 0.88$. For $\lambda = 1$, the most unstable mode predicted by linear theory is $\omega = 0.56$. However, the rate of growth of the modes that we do see is in qualitative accord with expectations from linear theory. While each of these three dominant modes have positive growth rates, the frequencies $\omega = 0.44, 0.66$ have growth rates, according to linear theory, approximately twice that of $\omega = 0.88$ and, indeed, examination of the Fourier spectra in figure 14 demonstrates that these former two modes overtake the latter mode as time progresses.

A *quantitative* comparison of the rate of growth of the amplitude of the different frequencies with predictions of linear stability theory is illustrated in figure 15. This figure shows a plot of the $\ln \hat{F}^2$ versus time for the three frequencies, $\omega = 0.44, 0.66, 0.88$, in addition to the most unstable frequency (from linear theory), $\omega = 0.56$. It is only the slope of the curves that matter as the slope is directly proportional to the disturbance growth rate. The plot is stopped at $t \approx 200$ when the disturbance has grown to a finite amplitude of about 0.2 and the droplet has shortened to a point where the choice of l in the Fourier decomposition is no longer a simple matter. The solid lines are the numerical calculations and the dashed lines are the predicted slopes from linear stability theory. The results are quite good considering the numerical approximations and the very extreme initial shape, and indicate that the linear theory is quite good even as the disturbance evolves to finite amplitude. We

have no explanation for the fact that the $\omega = 0.88$ (curve d) data show more deviation from the linear theory at later times than the other frequencies nor for the observation that it is not straight initially, unlike the other curves.

Perhaps most interesting is the observation that the dominant mode corresponds to $\omega = 0.66$ and is responsible for the final drop size distribution on the central region of the droplet. The most unstable linear mode has a much smaller initial amplitude and is never able to catch up even though it has a larger growth rate. The fact that the most unstable linear mode, $\omega = 0.56$ does not dominate appears due to the very small differences in growth rate between this 'critical' frequency and nearby frequencies. This is indicated in the inset to figure 15 which shows a stability diagram with the growth rate γ plotted as a function of the disturbance frequency ω for $\lambda = 1$. In the neighborhood of $\omega = 0.56$ there is a wide-range of frequencies with growth rates close to the maximum or 'critical' value. For these frequencies the evolution depends primarily on the magnitude of the initial disturbance.

At the later times when the choice of l is difficult, we plot the $\ln u_r(z = 0)$ versus time. For a disturbance of a given frequency, linear stability theory predicts this graph to be linear with slope γ . This is illustrated in figure 16. The solid line represents the numerical simulation and the dashed line is simply a straight line with the same initial slope. The growth rate calculated from this line is $\gamma = 0.030$ which is in reasonable agreement with the growth rate, predicted from linear theory, at the dominant frequency, $\gamma(0.66) = 0.033$. Remarkably, the linear theory holds even though the disturbance is clearly finite amplitude. Very close to the point of actual fragmentation the interface evolves more rapidly than theory predicts which points out that nonlinear effects do eventually become noticeable, but only in the latter stages of the breakup process on the cylindrical thread-like region.

The simulation represented in figures 13-16 highlights several dynamical features associated with capillary wave growth on cylindrical fluid interfaces.

Perhaps the most intriguing of the observations is the fact that the linear theory is remarkably good even when the disturbance is no longer small and even though the cylinder is finite and continually shortening. The nonlinearities associated with the evolution of capillary waves are only evident close to the point of actual fragmentation and their only significant consequence appears to be the formation of the small satellite drops in the final disintegrated drop. We also note that the numerics did not select the linearly most unstable disturbance. Instead, the linearly unstable mode with the largest amplitude at $t = 0$ simply dominated for all times. This appears to be a consequence of the fact that the linear growth rates in the neighborhood of the critical mode differ by only a few percent so that for significant differences in initial amplitude, the most unstable linear mode is never able to catch up. Of course, if the initial disturbances were truly infinitesimal, the results from linear theory would apply.

A simulation was also performed with the largest initial disturbance chosen to be coincident with the linearly most unstable mode, i.e. $\omega = 0.56$. In this case the interface evolved as in figure 13 but the predominant disturbance remained $\omega = 0.56$ for all times and the growth rate calculated numerically for $\omega = 0.56$ differed from the prediction of linear stability theory by less than six percent. As mentioned previously, the qualitative observations made during these numerical simulations of finite amplitude capillary wave on stationary cylindrical interfaces are very similar to the observations made in related studies on the breakup of inviscid liquid jets (Goedde & Yuen 1970).

Finally, we recall that in our complimentary experimental study of capillary waves (Stone *et al.* 1986 - figure 13), there was excellent agreement between the linear theory and experiment for $\lambda = 0.1$ and 1.3 , but poor agreement for $\lambda = 12.2$. The difference for the higher viscosity ratio suggests that the flow from the end due to the relaxation process that is characteristic of very viscous drops may modify the selection of the most unstable wavelength. It may be noted, in this regard, that the growth rate versus frequency diagram is very flat

for $\lambda > 10$ so that there is a large range of frequencies with growth rates about equal to that of the most unstable linear mode. Hence, a small modification due to end effects may play an important role.

ACKNOWLEDGEMENTS

This work was supported by a grant from the fluid mechanics program of the National Science Foundation. One of the authors (HAS) was partially supported through an IBM Graduate Research Fellowship.

REFERENCES

- Acrivos, A. 1983 The breakup of small drops and bubbles in shear flows. *4th Int Conf. on Physicochemical Hydrodynamics, Ann. N.Y. Acad. Sci.* **404**, 1-11.
- Acrivos, A. & Lo, T.S. 1978 Deformation and breakup of a slender drop in an extensional flow. *J. Fluid Mech.* **86**, 641-672.
- Ascoli, E.P. 1987 Low-Reynolds number hydrodynamic interaction of a solid particle with a planar wall. *MS Thesis, California Institute of Technology.*
- Barthes-Biesel, D. & Acrivos, A. 1973 Deformation and burst of a liquid droplet freely suspended in a linear shear field. *J. Fluid Mech.* **61**, 1-21.
- Beatty, M.F. 1987 Some dynamical problems in continuum physics. *Dynamical problems in continuum physics* edited by J.L. Bona, C. Dafermos, J.L. Ericksen & D. Kinderlehrer, Springer-Verlag, 43-78.
- Bentley, B.J. & Leal, L.G. 1986 An experimental investigation of drop deformation and breakup in steady two-dimensional linear flows. *J. Fluid Mech.* **167**, 241-283.
- Bogy, D.B. 1979 Drop formation in a circular liquid jet. *Ann. Rev. Fluid Mech.* **11**, 207-228.
- Bousfield, D.W., Keunings, R., Marrucci, G. & Denn, M.M. 1986 Nonlinear analysis of the surface tension driven breakup of viscoelastic filaments. *J. Non-Newtonian Fluid Mech.* **21**, 79-97.
- Brady, J.F. & Acrivos, A. 1982 The deformation and breakup of a slender drop in an extensional flow: inertial effects. *J. Fluid Mech.* **115**, 443-451.
- Geller, A.S., Lee, S.H. & Leal, L.G. 1986 The creeping motion of a spherical particle normal to a deformable interface. *J. Fluid Mech.* **169**, 27-69.
- Goedde, E.F. & Yuen, M.C. 1970 Experiments on liquid jet instability. *J. Fluid Mech.* **40**, 495-511.

- Goren, S.L. 1964 The shape of a thread of liquid undergoing break-up. *J. Colloid Sci.* **19**, 81-86.
- Grace, H.P. 1971 Dispersion phenomena in high viscosity immiscible fluid systems and application of static mixers as dispersion devices in such systems. *Eng. Found. Res. Conf. Mixing, 3rd Andover, N.H.* Republished 1982 in *Chem. Engng Commun.* **14**, 225-277.
- Greenspan, H.P. & McCay, B.M. 1981 On wetting of a surface by a very viscous fluid. *Studies in Applied Math.* **64**, 95-112.
- Higdon, J.J.L. 1985 Stokes flow in arbitrary two-dimensional domains: shear flow over ridges and cavities. *J. Fluid Mech.* **159**, 195-226.
- Khakhar, D.V. & Ottino, J.M. 1987 Breakup of liquid threads in linear flows. *Intl J. Multiphase Flow* **13**, 147-180.
- Lasheras, J.C., Fernandez-Pello, A.C. & Dryer, F.L. 1979 Initial observations on the free droplet combustion characteristics of water-in-fuel emulsions. *Combustion Sci. and Tech.* **21**, 1-14.
- Lee, S.H. & Leal, L.G. 1982 The motion of a sphere in the presence of a deformable interface. II. A numerical study of the translation of a sphere normal to an interface. *J. Colloid Interface Sci.* **87**, 81-106.
- Lee, W.-K. & Flumerfelt, R. W. 1981 Instability of stationary and uniformly moving cylindrical fluid bodies - I. Newtonian systems. *Intl J. Multiphase Flow* **7**, 363-384.
- Lee, W.-K., Yu, K.-L. & Flumerfelt, R. W. 1981 Instability of stationary and uniformly moving cylindrical fluid bodies - II. Viscoelastic threads and experimental observations. *Intl J. Multiphase Flow* **7**, 385-400.
- Mikami, T., Cox, R.G. & Mason, S.G. 1975 Breakup of extending liquid threads. *Intl J. Multiphase Flow* **2**, 113-138.
- Rallison, J.M. 1981 A numerical study of the deformation and burst of a viscous drop in general shear flows. *J. Fluid Mech.* **109**, 465-482.

- Rallison, J.M. 1984 The deformation of small viscous drops and bubbles in shear flows. *Ann. Rev. Fluid Mech.* **16**, 45-66.
- Rallison, J.M. & Acrivos, A. 1978 A numerical study of the deformation and burst of a viscous drop in an extensional flow. *J. Fluid Mech.* **89**, 191-200.
- Rumscheidt, F.D. & Mason, S.G. 1962 Break-up of stationary liquid threads. *J. Colloid Sci.* **17**, 260-269.
- Rutland, D.F. & Jameson, G.J. 1971 A non-linear effect in the capillary instability of liquid jets. *J. Fluid Mech.* **46**, 262-271.
- Sherwood, J.D., 1987 Drop breakup in electric and magnetic fields. (to appear).
- Stone, H.A., Bentley, B.J. & Leal, L.G. 1986 An experimental study of transient effects in the breakup of viscous drops. *J. Fluid Mech.* **173**, 131-158.
- Taylor, G.I. 1932 The viscosity of a fluid containing small drops of another fluid. *Proc. R. Soc. Lond.* **A138**, 41-48.
- Taylor, G.I. 1934 The formation of emulsions in definable fields of flow. *Proc. R. Soc. Lond.* **A146**, 501-523.
- Tomotika, S. 1935 On the instability of a cylindrical thread of a viscous liquid surrounded by another viscous fluid. *Proc. R. Soc. Lond.* **A150**, 322-337.
- Tomotika, S. 1936 Breaking up of a drop of viscous liquid immersed in another viscous fluid which is extending at a uniform rate. *Proc. R. Soc. Lond.* **A153**, 302-318.
- Youngren, G.K. & Acrivos, A. 1975 Stokes flow past a particle of arbitrary shape; a numerical method of solution. *J. Fluid Mech.* **69**, 377-403 (corrigendum **69**, 813).
- Youngren, G.K. & Acrivos, A. 1976 On the shape of a gas bubble in a viscous extensional flow. *J. Fluid Mech.* **76**, 433-442.

FIGURE CAPTIONS

- Figure 1 Definition of variables for a deformed droplet in an extensional flow
- Figure 2 Drop deformation in a steady axisymmetric extensional flow: D vs. C ; $\lambda = 0.1$. The solid line represents the numerical simulation and the dashed lines are the predictions of the small deformation theory of Barthes-Biesel & Acrivos (1973). The short dashed line denotes the $O(C)$ result and the long dashed line the $O(C^2)$ result. Several numerically generated steady shapes are included.
- Figure 3 Drop deformation in a steady axisymmetric extensional flow: D vs. C ; $\lambda = 1.0$. The solid line represents the numerical simulation and the dashed lines are the predictions of the small deformation theory of Barthes-Biesel & Acrivos (1973). The short dashed line denotes the $O(C)$ result and the long dashed line the $O(C^2)$ result. Open circles represent the calculations of Duffy and Blundell (as reported by Rallison 1984). Several numerically generated steady shapes are included.
- Figure 4 Drop deformation in a steady axisymmetric extensional flow: D vs. C ; $\lambda = 10.0$. The solid line represents the numerical simulation and the dashed lines are the predictions of the small deformation theory of Barthes-Biesel & Acrivos (1973). The short dashed line denotes the $O(C)$ result and the long dashed line the $O(C^2)$ result. Several numerically generated steady shapes are included.
- Figure 5 Relaxation and breakup of an initially extended droplet in an otherwise quiescent fluid: dependence on viscosity ratio. The initial shape, $\frac{L}{a} = 8.6$, is taken from an experiment for $\lambda = 11.3$. This highly stretched initial shape with bulbous ends is typical of experimental results for all $\lambda > 0.05$. a) $\lambda = 0.05$; $t = 0.0, 15.75, 22.05, 24.57$ b) $\lambda = 0.1$; $t = 0.0, 16.50, 22.40, 28.97, 32.64$ c) $\lambda = 1.0$; $t = 0.0, 48.0, 76.0, 100.0$ d) $\lambda = 7.5$; $t = 0.0, 231.9, 333.9, 397.1, 418.2$ e) $\lambda = 10.0$; $t = 0.0, 173.9, 396.0, 660.0$. The modified dimensionless times $\frac{t}{(1+\lambda)}$ are shown in

parentheses for reference.

Figure 6 Velocity and pressure fields for a relaxing drop in an otherwise quiescent fluid; $\lambda = 0.1$. The pressure field $\hat{p} - \hat{p}_o$ shown is the droplet pressure along the centerline ($r = 0$) and is measured with respect to zero at the droplet center $(r, z) = (0, 0)$. a) $t = 0.0$ b) $t = 22.40$ c) $t = 28.97$ d) $t = 32.64$

Figure 7 Velocity and pressure fields for a relaxing drop in an otherwise quiescent fluid; $\lambda = 1.0$. The pressure field $\hat{p} - \hat{p}_o$ shown is the droplet pressure along the centerline ($r = 0$) and is measured with respect to zero at the droplet center $(r, z) = (0, 0)$. a) $t = 0.0$ b) $t = 48.0$ c) $t = 76.0$ d) $t = 100.0$

Figure 8 Velocity and pressure fields for a relaxing drop in an otherwise quiescent fluid; $\lambda = 10.0$. The pressure field $\hat{p} - \hat{p}_o$ shown is the droplet pressure along the centerline ($r = 0$) and is measured with respect to zero at the droplet center $(r, z) = (0, 0)$. a) $t = 0.0$ b) $t = 173.9$ c) $t = 396.0$ d) $t = 660.0$

Figure 9 Relaxation and breakup of low viscosity ratio droplets in an otherwise quiescent fluid; $\lambda = 0.01$. The initial shape is taken from an experiment for $\lambda = 0.011$. Low viscosity ratio droplets have long, slender shapes with nearly pointed ends. a) $\frac{L}{a} = 5.3$; $t = 0.0, 10.22, 20.20$ b) $\frac{L}{a} = 6.4$; $t = 0.0, 10.77, 22.68, 23.59$ c) $\frac{L}{a} = 7.5$; $t = 0.0, 7.54, 18.54, 27.74, 29.74$

Figure 10 Velocity and pressure fields for a relaxing drop in an otherwise quiescent fluid; $\lambda = 0.01$. The pressure field $\hat{p} - \hat{p}_o$ shown is the droplet pressure along the centerline ($r = 0$) and is measured with respect to zero at the droplet center $(r, z) = (0, 0)$. a) $t = 7.54$ b) $t = 18.54$ c) $t = 27.74$ d) $t = 29.74$

Figure 11 Quantitative comparison of numerical (solid curve) and experimental results (dotted curve) for relaxation of an initially extended droplet in a quiescent fluid; $\lambda = 0.45$ - a test of the constant interfacial tension

boundary condition. Still photographs and corresponding numerically generated shapes are shown.

Figure 12 Quantitative comparison of numerical (solid curve) and experimental results (dotted curve) for relaxation of an initially extended droplet in a quiescent fluid; $\lambda = 11.3$ - a test of the constant interfacial tension boundary condition. Still photographs and corresponding numerically generated shapes are shown.

Figure 13 Evolution of capillary waves during the relaxation/breakup of an initially highly extended droplet suspended in an otherwise quiescent fluid. Initial shape: $\frac{L}{a} = 14, \lambda = 1.0$. a) $t = 0.0$ b) $t = 30.0$ c) $t = 50.0$ d) $t = 63.4$ e) $t = 64.6$ f) $t = 73.0$ g) $t = 104.6$ h) $t = 170.6$ i) $t = 194.6$ j) $t = 218.6$ k) $t = 234.6$ l) $t = 235.2$ m) $t = 240.8$ n) $t = 242.0$ When fragmentation occurs, the daughter droplets shed from the end are completely neglected as the calculation is continued. Notice the formation of small satellite droplets in the latter stages of the capillary breakup of the cylindrical midsection.

Figure 14 Evolution of the Fourier spectrum of the disturbance on the central cylindrical region of the drop. Fourier decomposition calculated using equation (5) with $l = 20$. a) $t = 0.0$ b) $t = 10.0$ c) $t = 20.0$ d) $t = 30.0$ e) $t = 50.0$ f) $t = 73.0$ g) $t = 104.6$ h) $t = 170.6$ i) $t = 194.6$ Modes that are stable in the linear stability theory are $\omega > 1$. All $0 < \omega < 1$ are unstable according to the linear theory. Notice that the dominant mode initially is a linearly stable mode and it rapidly decays.

Figure 15 Comparison of numerical results with predictions of linear stability theory - $\ln \hat{F}(\omega)^2$ vs. dimensionless time, t for different frequencies. The solid lines are the numerical results and the dashed lines are the predicted slopes from linear stability theory. a) $\omega = 0.44$ b) $\omega = 0.56$ c) $\omega = 0.66$ d) $\omega = 0.88$ The inset shows the stability diagram γ versus ω for $\lambda = 1.0$. Notice that there exist a relatively wide range of

frequencies with growth rate near the maximum value.

Figure 16 $\ln u_r(z = 0)$ versus t . The solid line represents the numerical calculations. The dashed line is a straight line with the same initial slope. The slope of this line yields a growth rate of $\gamma = 0.030$ which is in good agreement with the prediction of the linear theory based on the dominant mode, $\gamma(0.66) = 0.033$. At later times the interface evolves more rapidly than the linear theory predicts.

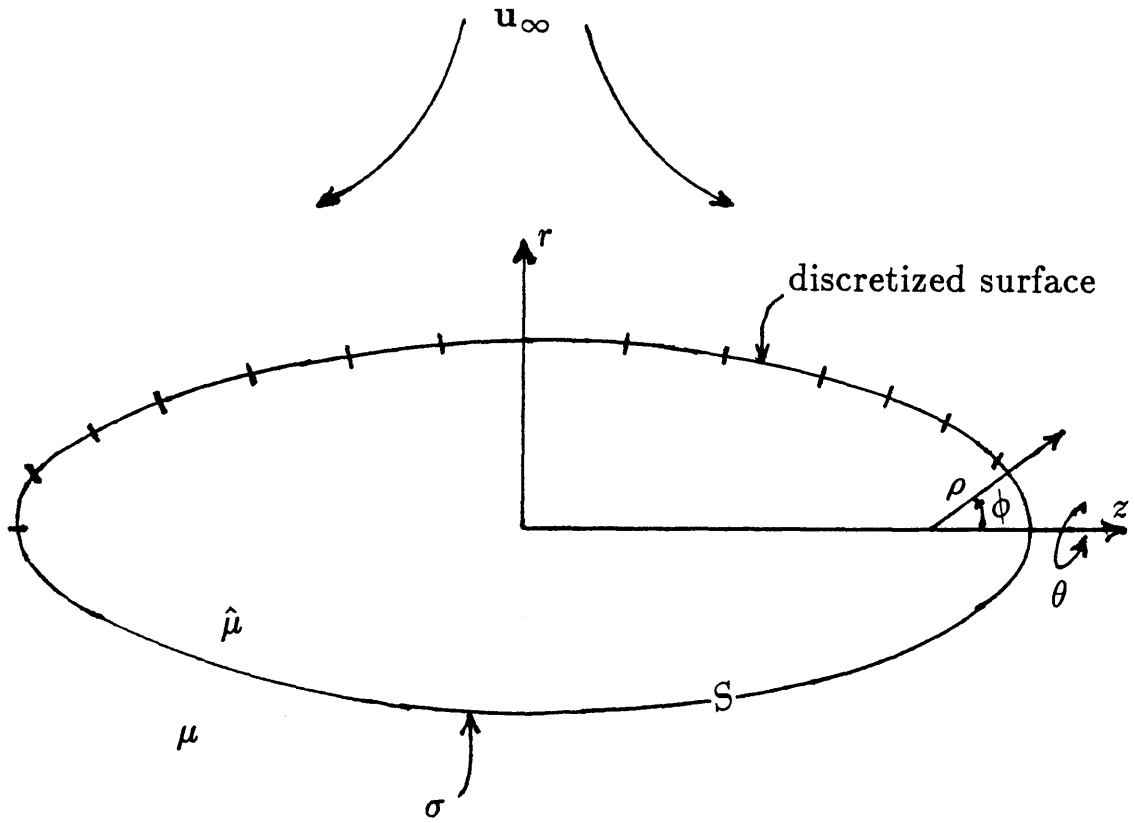


Figure 1

$$\lambda = 0.1$$

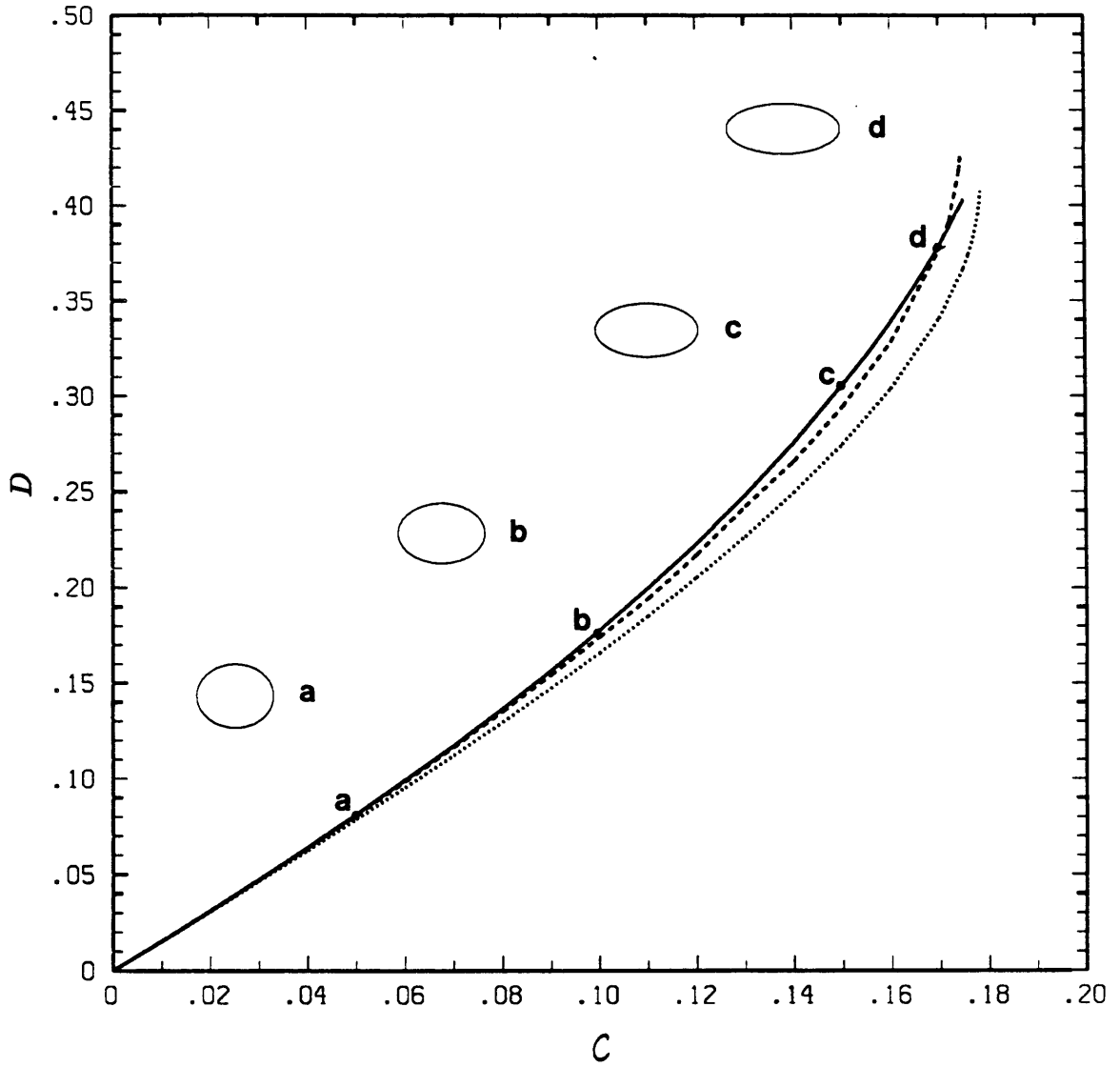


Figure 2

$$\lambda = 1.0$$

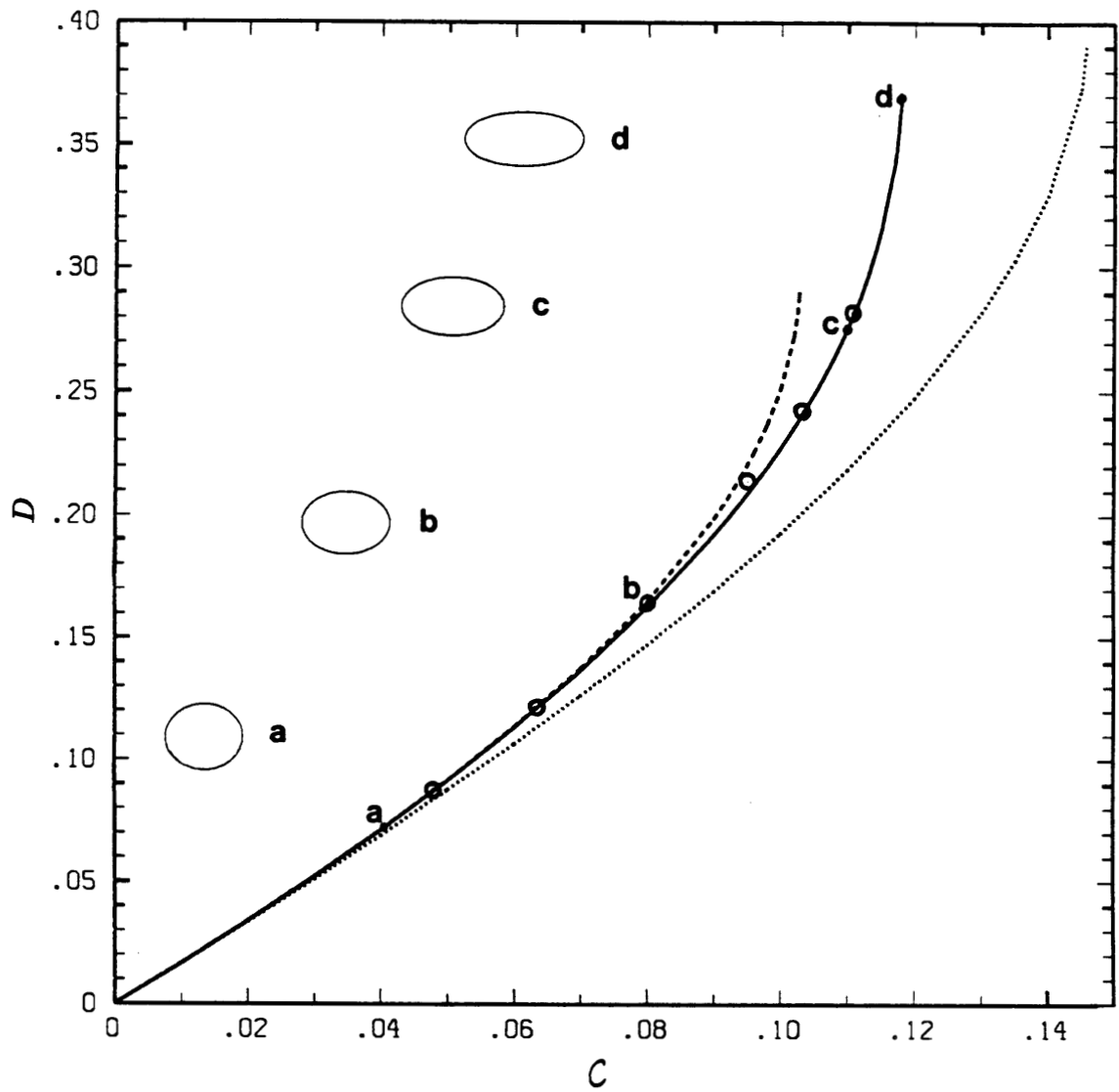


Figure 3

$$\lambda = 10.0$$

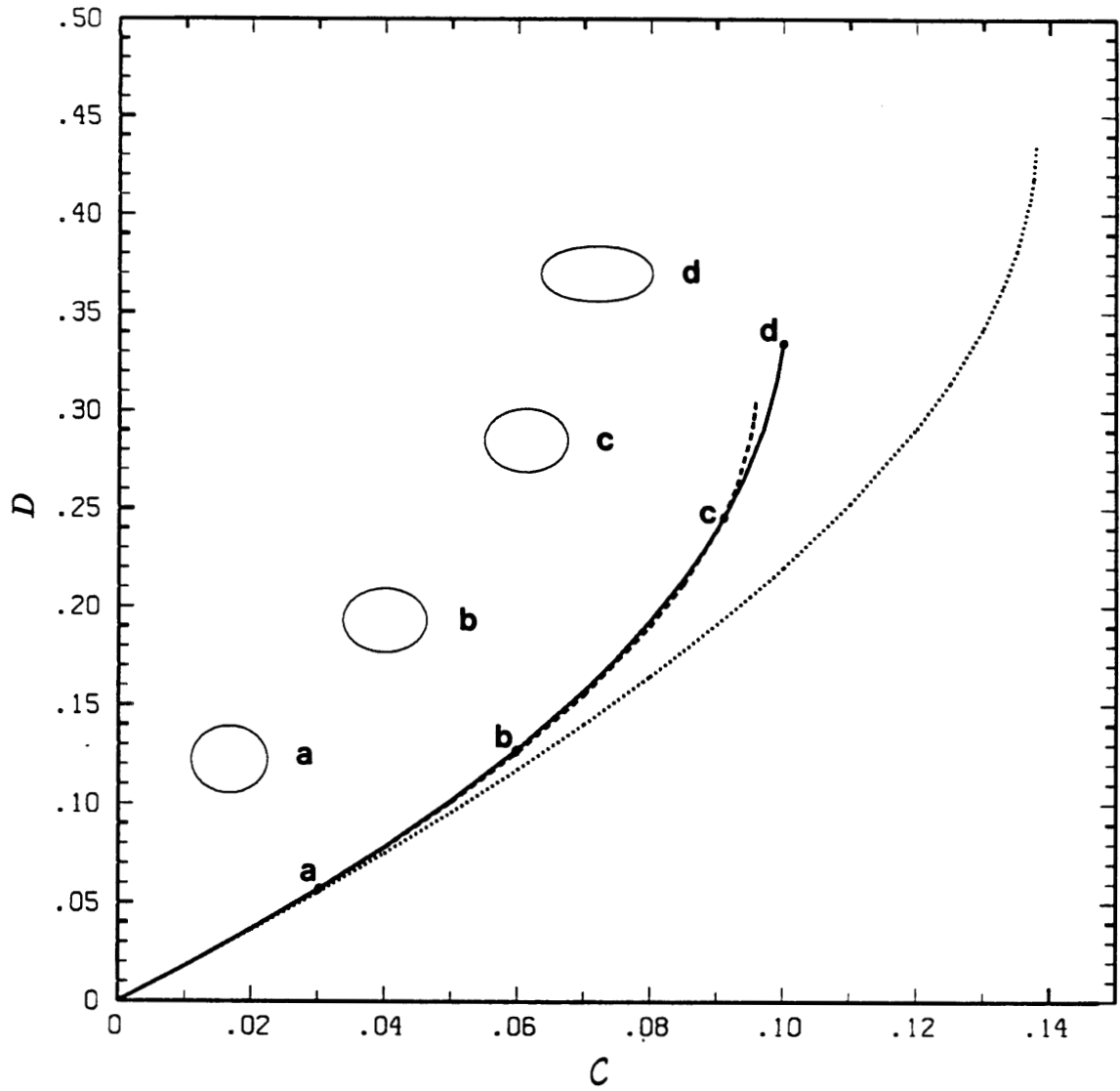
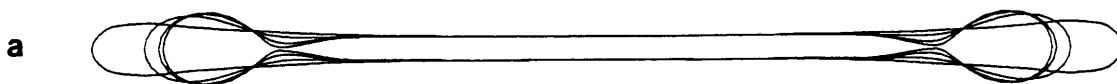


Figure 4

$$\left(\frac{t}{1+\lambda}\right) = 0.0, 15.0, 21.0, 23.4$$

$$t = 0.0, 15.75, 22.05, 24.57$$

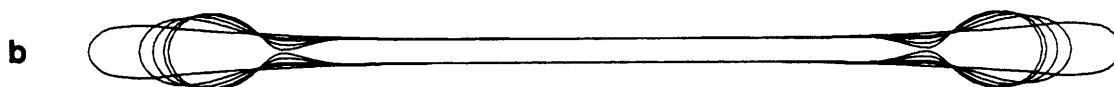
$$\lambda = 0.05$$



$$\left(\frac{t}{1+\lambda}\right) = 0.0, 15.0, 20.36, 26.34, 29.67$$

$$t = 0.0, 16.50, 22.40, 28.97, 32.64$$

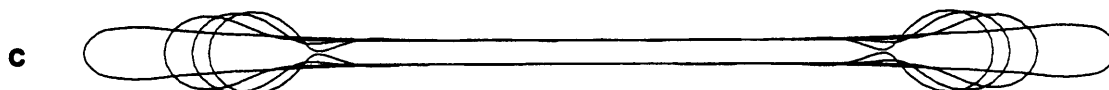
$$\lambda = 0.1$$



$$\left(\frac{t}{1+\lambda}\right) = 0.0, 24.0, 38.0, 50.0$$

$$t = 0.0, 48.0, 76.0, 100.0$$

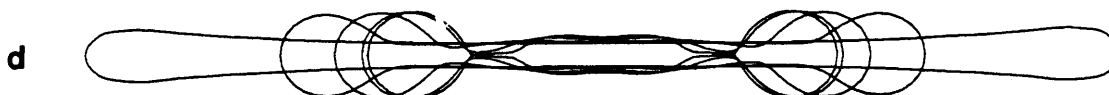
$$\lambda = 1.0$$



$$\left(\frac{t}{1+\lambda}\right) = 0.0, 27.28, 39.28, 46.72, 49.2$$

$$t = 0.0, 231.9, 333.9, 397.1, 418.2$$

$$\lambda = 7.5$$



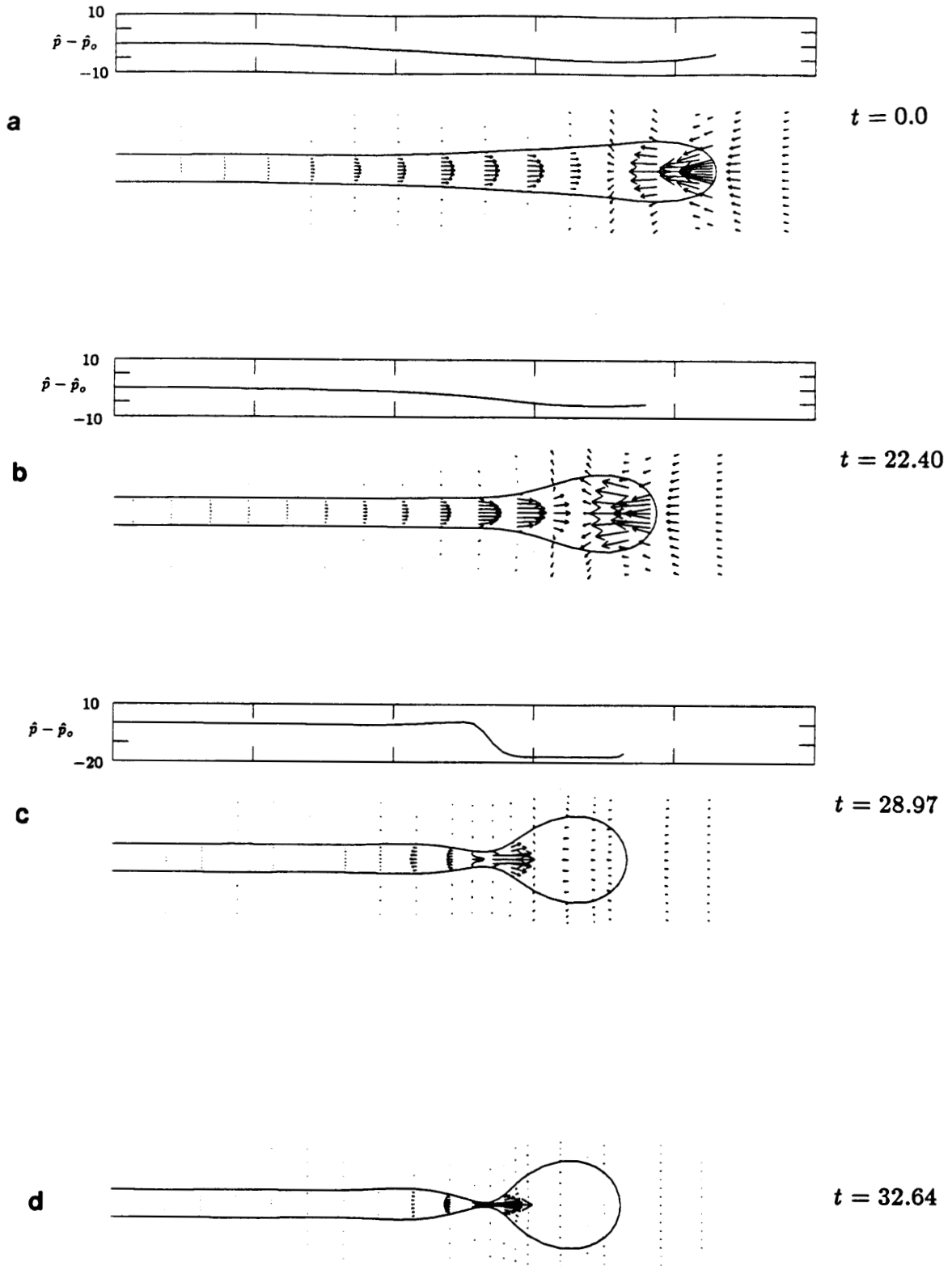
$$\left(\frac{t}{1+\lambda}\right) = 0.0, 15.8, 36.0, 60.0$$

$$t = 0.0, 173.9, 396.0, 660.0$$

$$\lambda = 10.0$$

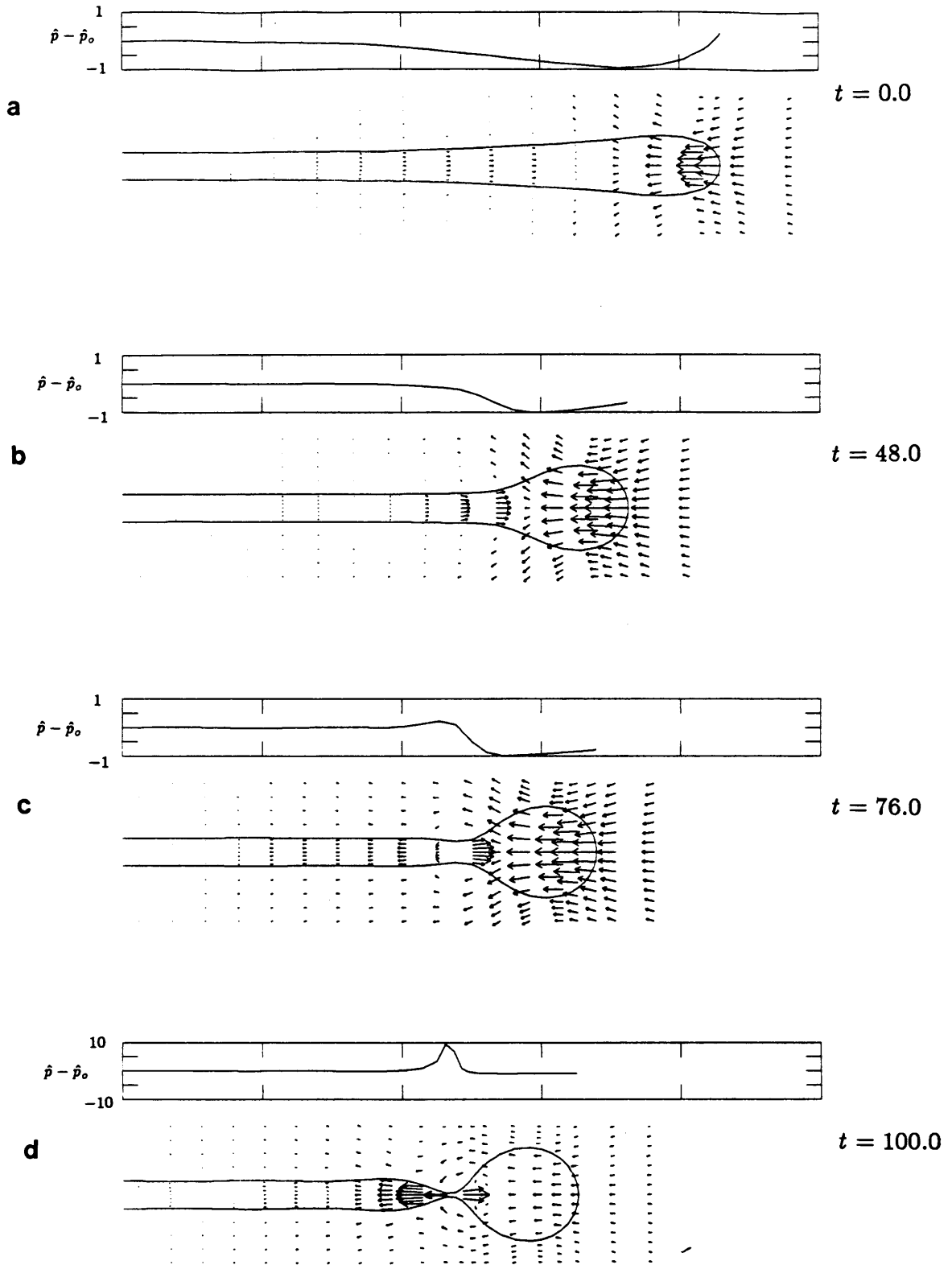


Figure 5



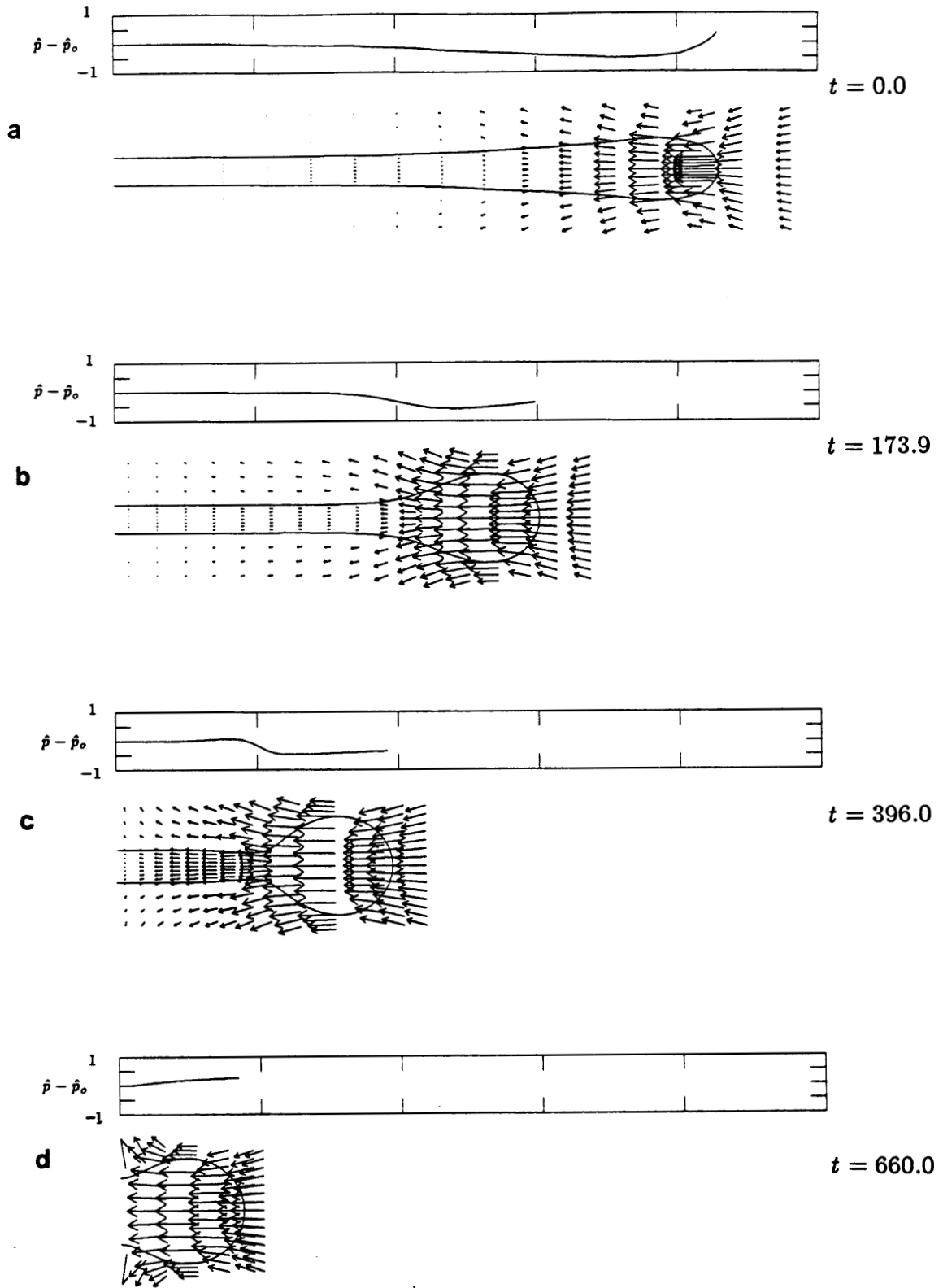
$\lambda = 0.1$

Figure 6



$$\lambda = 1.0$$

Figure 7

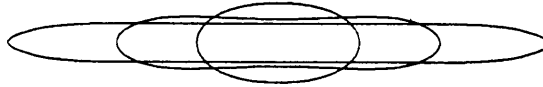


$$\lambda = 10.0$$

Figure 8 .

$t = 0.0, 10.22, 20.20$

a



$t = 0.0, 10.77, 20.20, 22.68, 23.59$

b



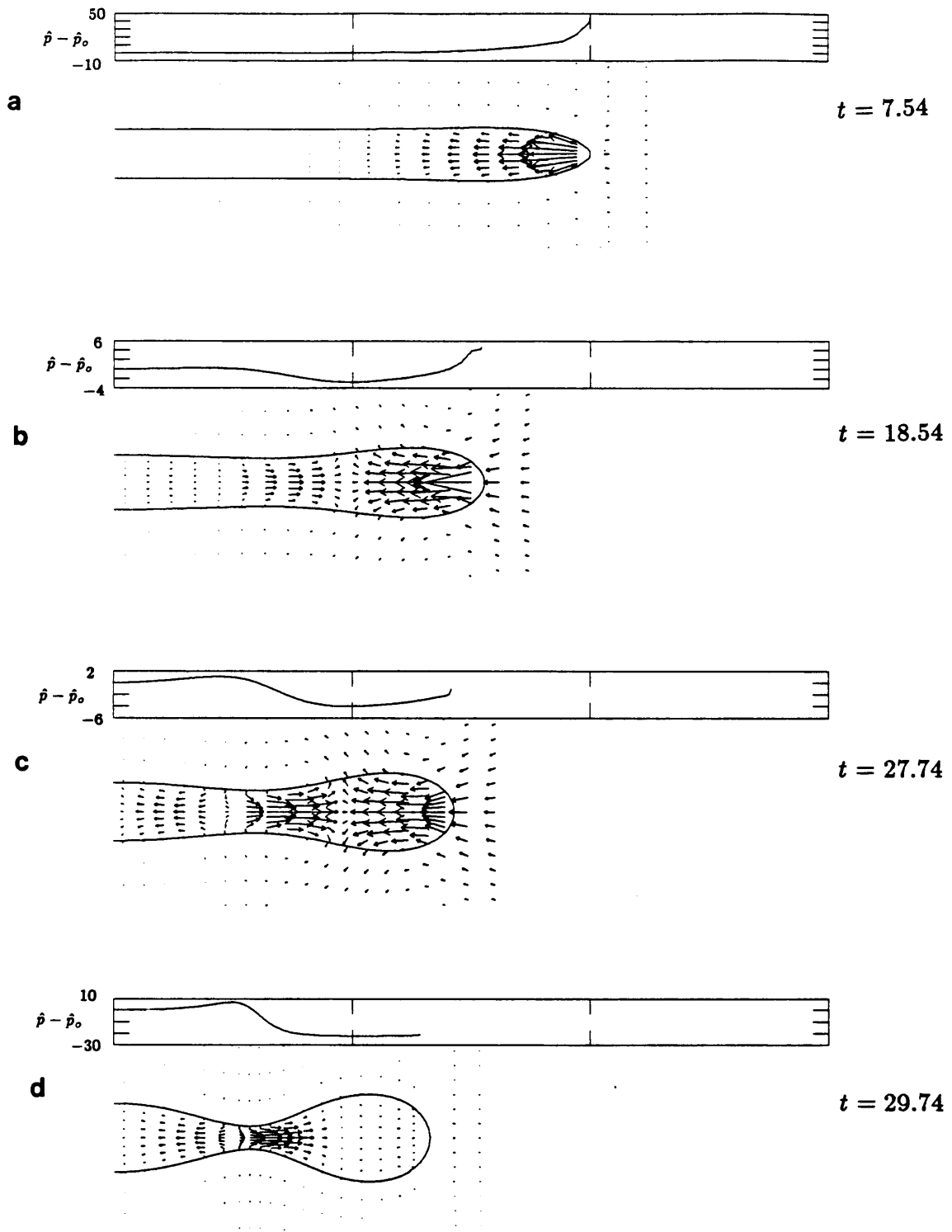
$t = 0.0, 7.54, 18.54, 27.74, 29.74$

c



$\lambda = 0.01$

Figure 9



$\lambda = 0.01$

Figure 10

$$\lambda = 0.45$$

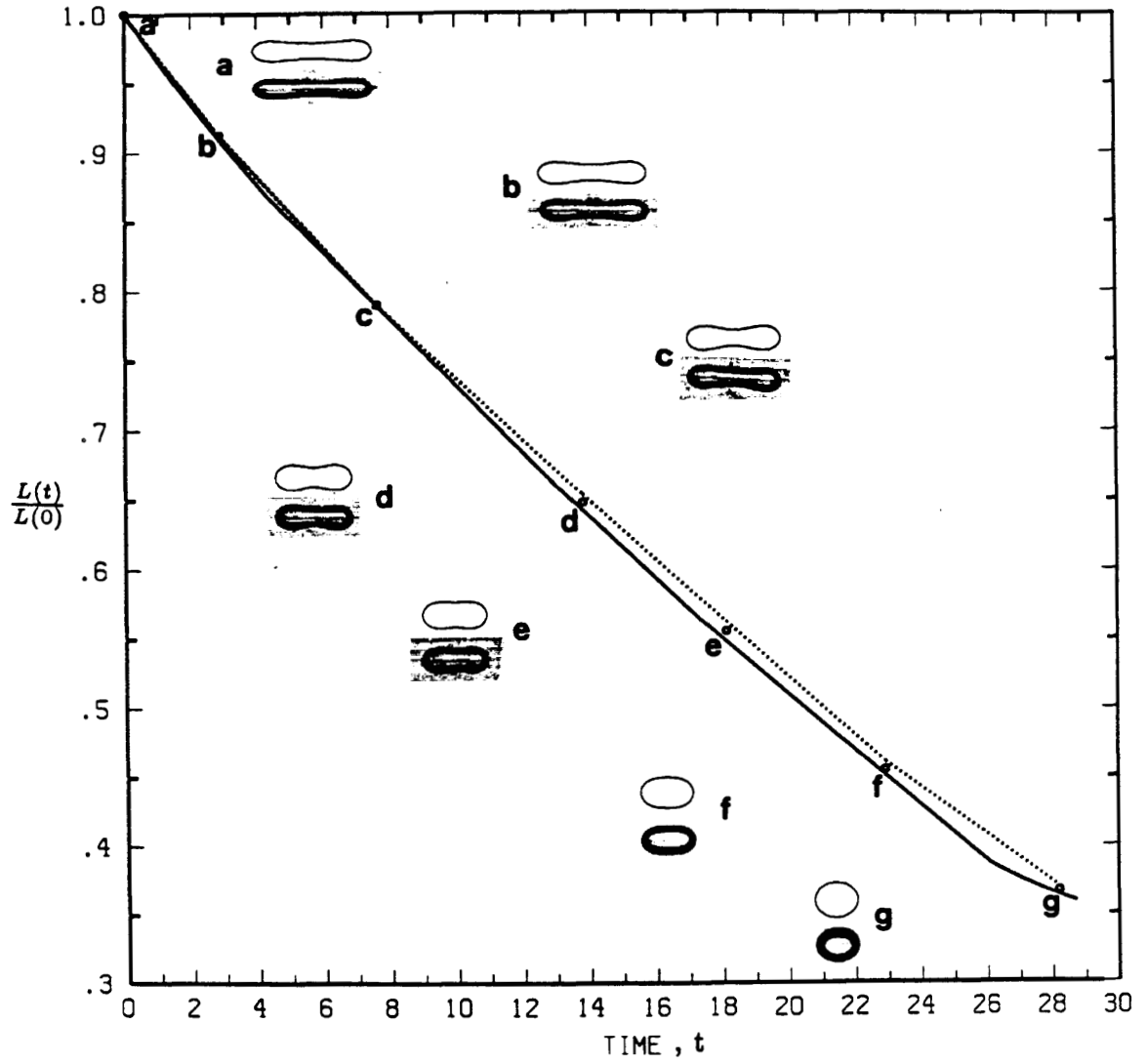


Figure 11

$$\lambda = 11.3$$

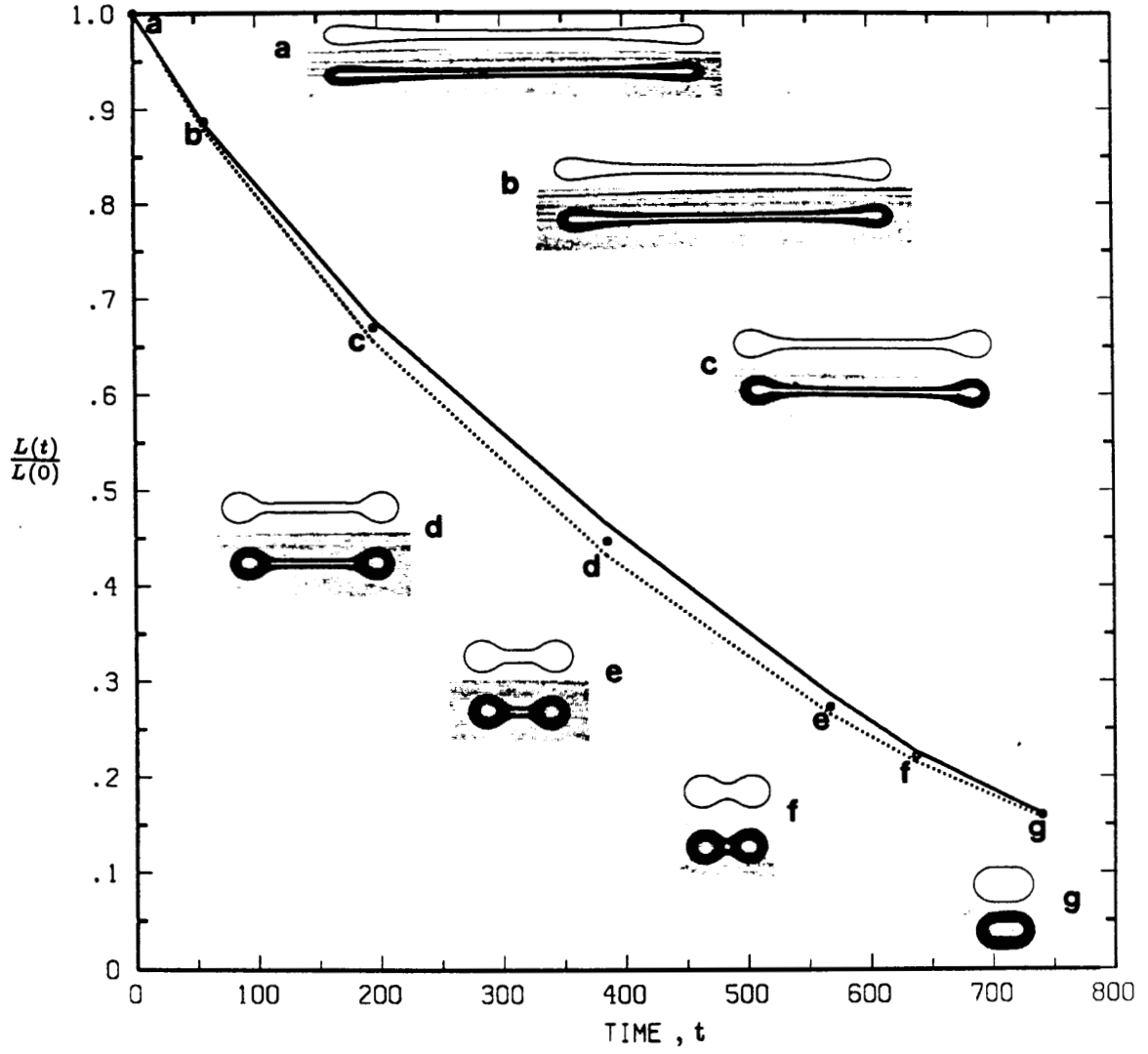


Figure 12

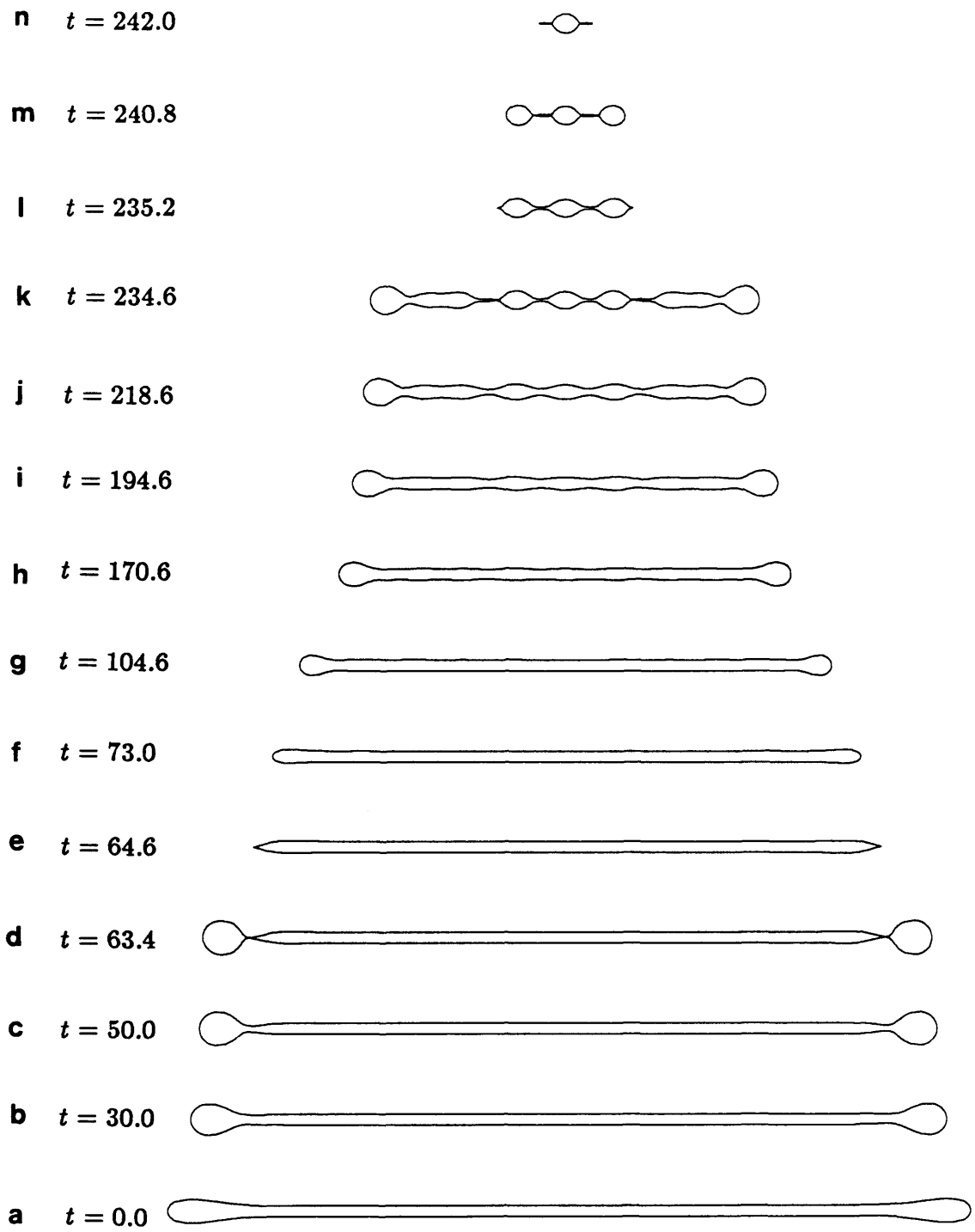


Figure 13

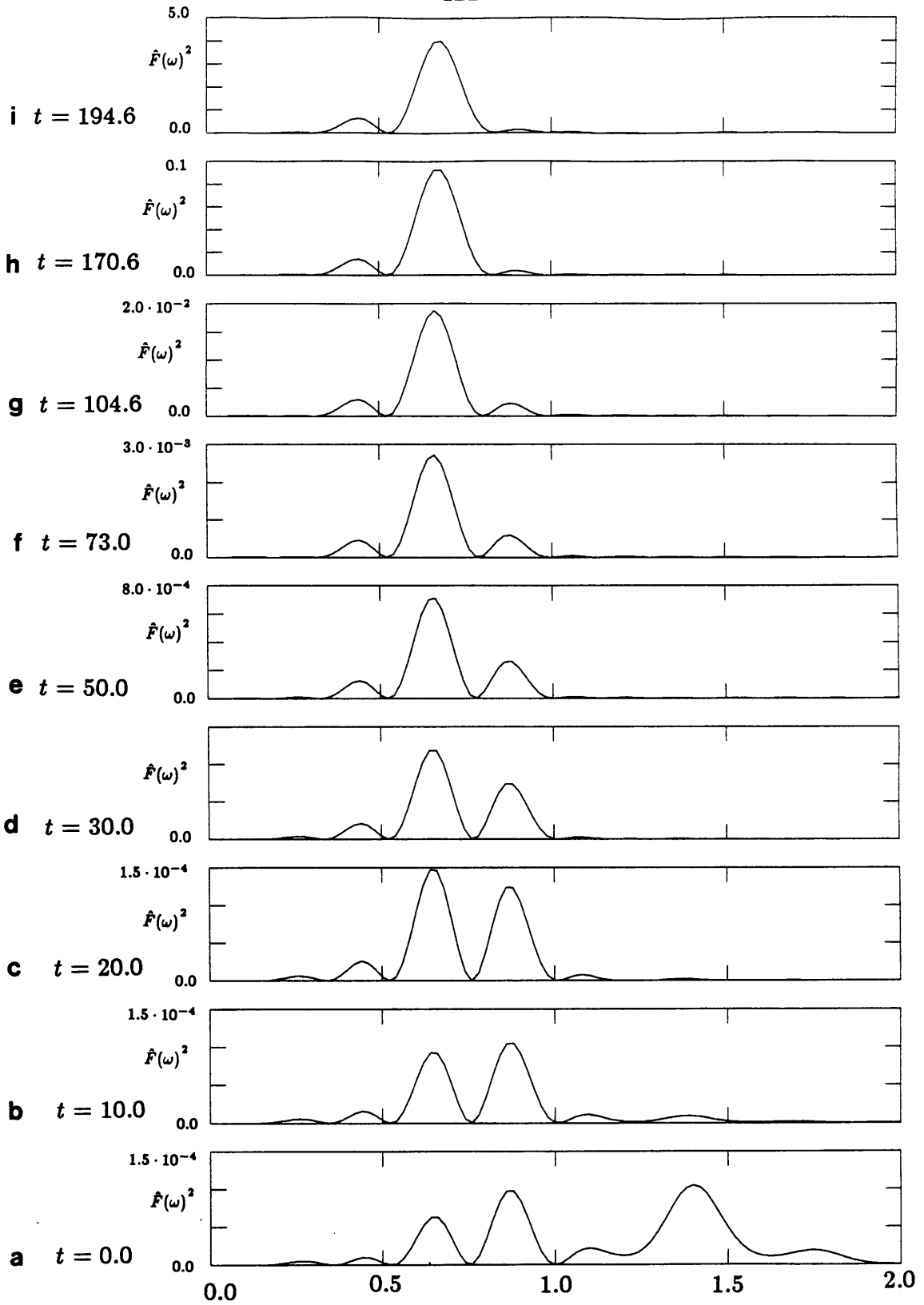


Figure 14

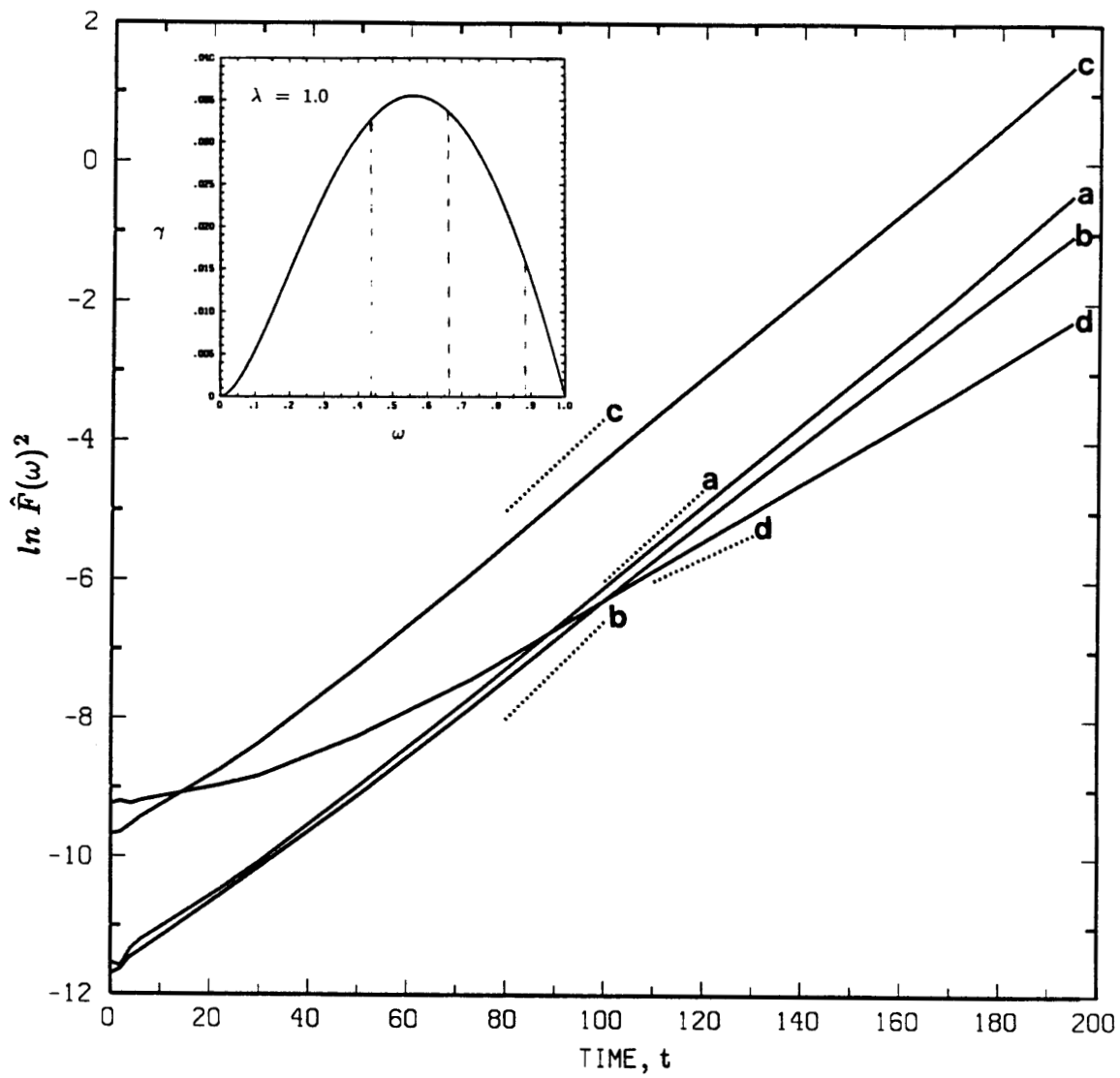


Figure 15

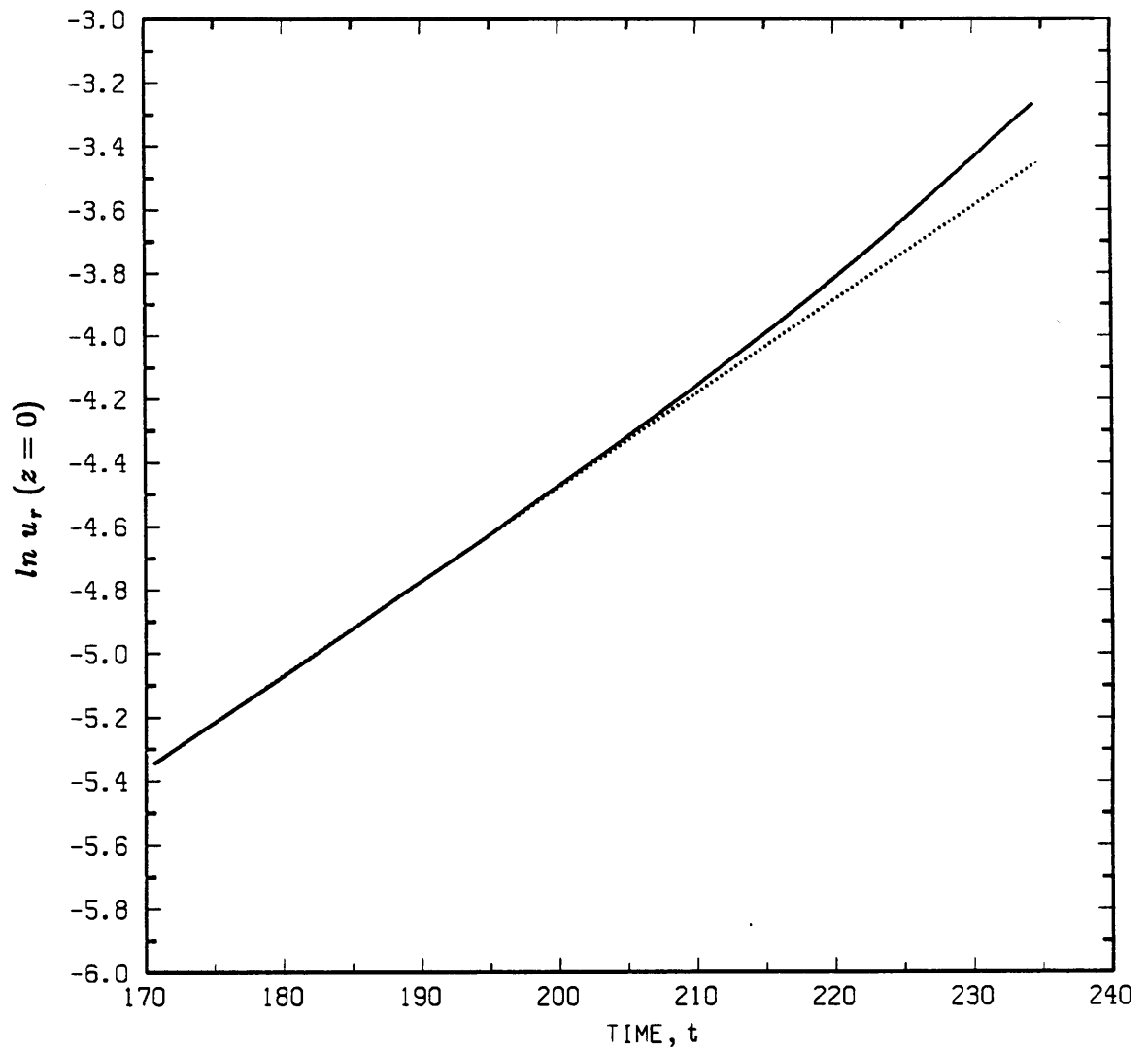


Figure 16

	N	# of Points on Midsection (0 < Z < 30)	R _a	ω	Maximum Error	Sqrt of Mean Square Error	Fourier Decomposition Frequency
1a	49	30	0.2	0.5	2.0 x 10 ⁻³	5.0 x 10 ⁻⁴	0.5
b	69	50			8.6 x 10 ⁻⁴	2.0 x 10 ⁻⁴	
2a	49	30		1.5	1.7 x 10 ⁻¹	4.3 x 10 ⁻²	1.5
b	69	50			6.6 x 10 ⁻²	1.8 x 10 ⁻²	
3a	49	30	0.02	0.5	1.8 x 10 ⁻⁵	4.8 x 10 ⁻⁵	0.5
b	69	50			8.0 x 10 ⁻⁵	2.0 x 10 ⁻⁵	
4a	49	30		1.5	1.4 x 10 ⁻²	4.4 x 10 ⁻³	1.5
b	69	50			6.4 x 10 ⁻³	1.8 x 10 ⁻³	
5a	49	30	0.002	0.5	1.9 x 10 ⁻⁵	4.6 x 10 ⁻⁶	0.5
b	69	50			8.0 x 10 ⁻⁶	2.0 x 10 ⁻⁶	
6a	49	30		1.5	1.3 x 10 ⁻³	5.0 x 10 ⁻⁴	1.5
b	69	50			6.4 x 10 ⁻⁴	1.8 x 10 ⁻⁴	
Test shape							

R_a = disturbance amplitude, ω = disturbance frequency

N = # of collocation node points, error = $\frac{\text{exact} - \text{numerical}}{\text{exact}}$

Table 1. Test of numerical procedure for determining curvature.

λ viscosity ratio	γ growth rate	time for growth			
		$R_a =$ initial disturbance amplitude			
		10^{-8}	10^{-6}	10^{-4}	10^{-2}
10^{-3}	0.399	44.4	32.9	21.3	9.8
10^{-2}	0.266	66.6	49.2	31.9	14.6
10^{-1}	0.109	163.2	120.8	78.4	36.0
1	0.0355	499.4	369.6	240.0	110.2
10	$9.82 \cdot 10^{-3}$	$1.8 \cdot 10^3$	$1.3 \cdot 10^3$	871.2	400.4
100	$1.45 \cdot 10^{-3}$	$1.2 \cdot 10^4$	$9.1 \cdot 10^3$	$5.9 \cdot 10^3$	$2.7 \cdot 10^3$

Table 2. Time for capillary wave to grow to half the cylinder radius as a function of the disturbance frequency and amplitude for different viscosity ratios. The maximum growth rate is also listed.

CHAPTER 4

**THE INFLUENCE OF INITIAL DEFORMATION
ON DROP BREAKUP
IN SUBCRITICAL TIME-DEPENDENT FLOWS
AT LOW REYNOLDS NUMBERS**

The basic text of Chapter 4 consists of an article which has been submitted for publication in the *Journal of Fluid Mechanics*.

- 127 -

**The influence of initial deformation
on drop breakup
in subcritical time-dependent flows
at low Reynolds numbers**

H.A. Stone and L.G. Leal

Department of Chemical Engineering
California Institute of Technology
Pasadena, California 91125

January 1988

ABSTRACT

Transient effects associated with drop deformation and breakup in simple time-dependent flows are experimentally and numerically examined. Both step changes in shear rate and flow-type are studied in two-dimensional linear flows generated in a computer-controlled four-roll mill and step changes in shear rate are examined numerically for axisymmetric extensional flows. For *subcritical* flow conditions abruptly applied to nonequilibrium shaped, rather modestly deformed drops, the interaction of a relaxational flow driven by interfacial tension and a stretching motion due to a velocity gradient near the droplet can give rise to complete breakup *without* large scale stretching of the droplet. This behaviour appears more pronounced for high viscosity ratios where large extensions are necessary to guarantee breakup if the flow is stopped abruptly. The sudden addition of vorticity in the external flow is characterized by rapid rotation to a new, steady orientation followed by deformation and/or breakup according to the effective flow conditions at the new orientation. For very viscous drops in flows with vorticity which typically cannot be made to break when beginning with a near spherical shape, independent of the magnitude of the capillary number, it is demonstrated experimentally that the same flow conditions can produce breakup if the initial shape is sufficiently nonspherical. Finally, the actual fragmentation of the droplet is characterized by a conically tipped central thread connected to an almost spherical end. This is geometrically very similar to other free-surface configurations observed, for example, during the breakup of pendant drops.

1. INTRODUCTION

G. I. Taylor's early investigations of the low Reynolds number deformation and breakup of liquid droplets (1932, 1934) were motivated by an interest in emulsion formation and mixing processes. In recent years, the areas of application have widened and drop deformation studies have also found use in characterizing the flow-induced deformation of flexible bodies, e.g., cells, as well as being applied in certain material science problems (Seward 1974). However, in spite of over 50 years of research, one significant aspect of the problem has received relatively little attention: namely, time-dependent deformation associated with the actual fragmentation of the droplet and how this is related to deformation and breakup in the presence of time-dependent flows. An introduction to some qualitative features associated with drop deformation and breakup in transient flows is presented in this paper.

The majority of analytic, experimental and numerical studies have considered the case of a single droplet suspended in a steady linear flow field at low Reynolds number. These studies have focussed primarily on understanding the coupled effects of the capillary number, the viscosity ratio and the vorticity of the external flow on the deformation and breakup process. The effect of vorticity is to inhibit deformation (and thus breakup) in a manner which becomes more pronounced as the ratio of the internal to external viscosity increases. Indeed, for all steady linear flows with vorticity, there exists a critical viscosity ratio above which the deformation remains finite, independent of the magnitude of the capillary number (provided that the Reynolds number remains small). In these instances, it is *not* possible to fragment the droplet in a steady flow. However, for smaller viscosity ratios, there exists a critical capillary number above which interfacial tension forces are not able to balance viscous forces and a continuous stretching motion of the droplet results (i.e., no steady shape exists). In spite of the fact that this is called 'breakup' in the literature and is characterized by a critical value of the capillary number, it should be noted that the

complete fracturing of a droplet in a *steady* linear flow has been experimentally reported by Mikami, Cox & Mason (1975) *only* for the case of extremely elongated, basically cylindrical droplets breaking due to capillary wave instabilities. Two excellent review articles concerning much of this work have been written by Rallison (1984) and Acrivos (1983). The effects of vorticity, first discovered and explained by Taylor (1934) by examining drop deformation in two-dimensional extensional flow and simple shear flow, have been extended recently by Bentley & Leal (1986b) in a comprehensive experimental study of drop breakup over the complete spectrum of two-dimensional linear flows with strain rate exceeding the magnitude of vorticity.

Although the work to date is very useful in understanding flow-induced deformation of liquid droplets and other nonrigid microstructures (flocs, cells, etc.), it focusses for the most part on the *steady state* and, consequently, does not provide much insight into the actual dynamics of drop fracture, nor does it address questions related to time-dependent flows applied to significantly deformed drops. While a comprehensive study of transient effects has not been undertaken, there have been a number of studies that provide considerable insight in several specific problem areas.

One aspect of research on time-dependent drop dynamics deals mainly with the transients associated with the breakup of droplets. The most extensive experimental study has been reported by Grace (1971) who considered both simple shear and planar extensional flows, and discovered a number of fascinating phenomena, including the effect of abruptly stopping the flow, the use of a programmed gradual reduction of the shear rate to produce breakup without gross stretching of the droplet, and a systematic study of the number of drop fragments produced when breakup occurs at a shear rate that exceeds the critical value. Some additional transient experiments are described by Torza, Cox & Mason (1972) who report that the mechanism for drop burst may depend on the rate at which the shear rate is increased. In a numerical study, Rallison &

Acrivos (1978) briefly discuss observations concerned with drop breakup due to the application of a subcritical flow to a drop originally stretched by a stronger flow.

A second class of transient studies makes use of analytic methods, but is restricted to motions that result in only small perturbations from an initial shape that is assumed known a priori. Time-dependent deformations of nearly spherical droplets have been treated analytically by Cox (1969) and Barthes-Biesel & Acrivos (1973) and reviewed by Rallison (1980). Although these small deformation theories have proven surprisingly accurate at predicting the critical capillary number necessary for drop burst, they unfortunately produce unrealistic shapes at breakup. Since these shapes and flow conditions are precisely the ones upon which we wish to concentrate our attention, these theories will be of limited use in the present investigation. There have been a number of analytic studies concerned with the stability of slender, nearly pointed shapes characteristic of low viscosity ratio droplets (Hinch 1979, Hinch & Acrivos 1980, Khakhar & Ottino 1986). Other analytic studies concerned with time-dependent aspects of drop breakup have been limited to the growth of infinitesimal capillary instabilities at the fluid-fluid interface of a stationary or extending fluid drop that is modeled as an infinite cylinder (Tomotika 1935,1936, Rumscheidt & Mason 1962, Mikami, Cox & Mason 1975, Lee & Flumerfelt 1980, Khakhar & Ottino 1987). Traditionally, this simplified model of a drop is used to make predictions of drop size distributions.

As outlined in a review article by Rallison (1984) it is clear that the effects of transients are significant, but, nonetheless, their qualitative and quantitative aspects have not been carefully studied. Indeed, recent observations indicate that complete fracturing of the droplet and hence predictions of drop size distributions will depend on the actual time-history of the flow.

As a first step toward a better understanding of transient behaviour, a combined experimental and numerical study of the time-dependent dynamics

of drop deformation and breakup is in progress in our laboratory. In the first part of our investigation (Stone, Bentley & Leal 1986), we examined experimentally the stretching of a droplet at the critical capillary number and then focussed our attention on the interfacial-tension-driven relaxation and breakup which results when the flow is stopped abruptly with the droplet in an elongated, nonequilibrium state. Curvature variations produce a rapid bulbing at the end of the droplet which frequently leads to the breaking off of the bulbous end from the central portion of the droplet, hence the description "end pinching". This fragmentation mechanism is damped for larger internal viscosities so that much larger initial elongations are necessary to guarantee breakup of high viscosity ratio systems. The second part of our study (Stone & Leal 1987) made use of the boundary integral method to probe numerically several details of this breakup phenomenon. The drop dynamics are both qualitatively and quantitatively consistent with the assumption of a constant interfacial tension boundary condition. An interesting feature of these investigations, observed both experimentally and numerically, was the role of finite amplitude capillary waves in the breakup process. These studies have provided us with a good understanding of droplet relaxation and breakup due to an interfacial-tension-driven flow in an otherwise quiescent fluid. However, this is clearly but a first step in understanding more complicated time-dependent flows.

Many (all?) real processes will be time-dependent and it is important to ask how the time-dependent features of the flow affect the qualitative and quantitative observations mentioned both in our initial studies and by other researchers. Of course, there are an infinite number of possible transient flows one could study and it is clearly not feasible, nor desirable, to have to investigate individually a great many of them. Rather, our goal is to choose several very simple flow situations and identify those aspects of the physics which will apply over a large range of flow conditions.

The novel flow situation examined in this paper is the behaviour of a mod-

estly deformed drop in a subcritical time-dependent flow. The term ‘modestly deformed’ refers to a shape more deformed than the maximum steady shape but one that has not had sufficient time to become highly elongated. In most cases these drop shapes are basically ellipsoidal. We focus experimentally on a study of step changes from the critical capillary number to *subcritical* or *weaker* flow conditions, either by decreasing the shear rate directly or by suddenly adding vorticity to the flow. The addition of vorticity indirectly *decreases* the effective shear rate experienced by the drop by rotating the drop *away* from the principal axis of strain of the undisturbed flow field. Thus, the effective shear rate (i.e., the local rate of stretching of a fluid element oriented in the direction of maximum droplet elongation) is reduced (Bentley & Leal 1986b) and, as a consequence, the effective capillary number is subcritical. Included among the interesting observations presented in this paper are several examples of *complete* breakup of a modestly extended droplet in a subcritical flow. This is a consequence of the interaction of an interfacial-tension-driven flow causing relaxation of the droplet with an external flow which tries to continue to elongate the droplet. Again, the boundary integral method can be used to probe the details of the flow field both internal and external to the droplet.

It should be mentioned that very interesting dynamics associated with transient deformation of a bubble in an axisymmetric extensional flow at *finite* Reynolds number have been described by Kang & Leal (1987) and, indeed, aspects of the behaviour detailed in their study are very similar to observations to be described here. There also appear to be other quite varied processes where interfacial-tension-driven flows play an important role. For example, Lasheras, Fernandez-Pello & Dryer (1979) observe breakup of stretched liquid droplets in an experimental study of the combustion of fuel droplets and Greenspan & McCay (1981) examine retraction of an initially extended droplet which wets a solid surface. Of course, similar transient effects should be expected in electrohydrodynamic or magnetohydrodynamic deformation and breakup of droplets

(see, for example, Torza, Cox & Mason 1971 and Sherwood 1987) if the field producing the deformation is time-dependent.

2. PROBLEM STATEMENT

Consider a neutrally bouyant Newtonian liquid droplet with undeformed radius a , viscosity $\hat{\mu}$ suspended in a second immiscible Newtonian fluid with viscosity μ . The viscosity ratio λ is defined as $\lambda = \frac{\hat{\mu}}{\mu}$. The fluid-fluid interface is characterized by a constant interfacial tension σ . The Reynolds numbers characterizing motion in both fluids are assumed vanishingly small so that all inertial effects are negligible. Far from the droplet, the undisturbed flow field is assumed to vary linearly with position, $\mathbf{u}_\infty = \mathbf{\Gamma} \cdot \mathbf{x}$ where $\mathbf{\Gamma}$, the velocity gradient tensor, may depend on time provided the time-dependent nature of the motion does not violate the low Reynolds number assumption. The assumption of a locally linear flow is often justified as an approximate description for the small drops typical of many applications since the length scale characteristic of droplet deformation is much smaller than the distance over which significant velocity gradient variations occur in the bulk flow.

In this paper we will numerically examine droplet deformation in axisymmetric extensional flows where $\mathbf{\Gamma}$ is diagonal,

$$\mathbf{\Gamma}(t) = \frac{G(t)}{2} \begin{pmatrix} -1 & 0 & 0 \\ 0 & -1 & 0 \\ 0 & 0 & 2 \end{pmatrix} \quad (1)$$

and experimentally study two-dimensional linear flows where $\mathbf{\Gamma}$ has the form

$$\mathbf{\Gamma}(t) = \frac{G(t)}{2} \begin{pmatrix} 1 + \alpha(t) & 1 - \alpha(t) & 0 \\ -1 + \alpha(t) & -1 - \alpha(t) & 0 \\ 0 & 0 & 0 \end{pmatrix}. \quad (2)$$

The shear rate G represents the magnitude of $\mathbf{\Gamma}$ and α is a flow-type parameter which provides a measure of the ratio of vorticity to the rate-of-strain. Typical streamlines for different choices of α are not reproduced here but are given in previous publications from our laboratory (e.g., Bentley & Leal 1986b). Simply note that $\alpha = 1.0$ corresponds to two-dimensional extensional flow, $\alpha = 0.0$

corresponds to simple shear flow and the vorticity of the undisturbed flow monotonically increases as α decreases from $1 \rightarrow 0$. As a result of the velocity gradient, viscous stresses generated at the droplet surface cause deformation which is resisted by interfacial tension. The relative importance of viscous forces to interfacial tension forces is measured by a capillary number, $C = \frac{\bar{G}\mu a}{\sigma}$ where \bar{G} indicates a representative value of the time-dependent shear rate.

It is convenient to characterize the degree of deformation using a single scalar parameter. For this study, most cases will consider drops which are significantly deformed and in these instances a dimensionless extension ratio, $\frac{L}{a}$, where $2L$ is the end-to-end drop length, is appropriate.

As discussed in the introduction, the great majority of studies in the low Reynolds number drop deformation literature have focussed on the steady-state effects of C , λ , and the tensorial character of Γ . Our concern is time-dependent behaviour. In this case, as outlined by Rallison (1984), two additional parameters are introduced: the initial shape of the drop (nonspherical initial shapes generate motion even in the presence of no imposed flow) and the history of the flow as specified by $\Gamma(t)$. These aspects will be studied in this paper, both experimentally using a computer-controlled four-roll mill and numerically using the boundary integral method, which is a powerful scheme for solving free-boundary problems.

The objective of this study is to approximate flows where a sudden change in either the flow-strength or the flow-type occurs. With this in mind, some simple, but illustrative flow field modifications are step changes. The experimental investigation will focus on step changes in shear rate and/or flow-type for two-dimensional flows generated in the four-roll mill. In order to learn more about the details of these motions, the boundary integral method is used to study step changes in shear rate for axisymmetrical extensional flows. Specifically, we will examine the effect of initial deformation of the droplet on the capillary number needed to produce breakup, the effect of vorticity of the imposed flow and the

role played by the viscosity ratio.

Our goal is to bring together observations made in several prior experimental, numerical and theoretical investigations, combine these with new experimental and numerical studies and consistently interpret behaviour within the framework of deformation and breakup due to competition of an imposed flow and an interfacial-tension-driven flow. The experiments take advantage of the ability of the computer-controlled four-roll mill to generate well-defined, time-dependent flows to probe different aspects of transient behaviour. Furthermore, by carefully representing the interface shape and resolving the interfacial velocity, the numerics illustrate application of the boundary integral method as a useful tool for understanding complicated time-dependent dynamics of free-boundary problems.

3. THE EXPERIMENT

Experimentally we will study drop dynamics in two-dimensional flows generated in a computer-controlled four-roll mill. The application and use of this device have been documented in two previous publications from our laboratory (Bentley & Leal 1986a,b). To summarize briefly, the four-roll mill consists of four cylindrical rollers, placed at the corners of a square, counterrotated to create an approximation to a two-dimensional linear flow field in the region between the rollers. Flows with arbitrary ratios of vorticity to strain rate can be studied, though all of our investigations have focussed on so-called strong flows ($\alpha > 0$) where the magnitude of the rate-of-strain tensor is larger than the magnitude of the vorticity tensor. For a given value of the shear rate, these flows are capable of producing larger microstructural deformation than flow fields in which vorticity dominates.

A drop is placed at the central stagnation point of the flow. Because the drop position at the stagnation point is unstable, a control scheme is used to regulate the roller speeds in a manner which keeps the droplet at the stagnation point while maintaining the shear rate and flow-type at specified values. This

control algorithm has proven very effective and we have demonstrated that the small roller speed changes that occur produce no observable additional drop deformation (Stone, *et al.* 1986). Hence, all effects seen in this study are strictly due to programmed changes in flow conditions.

The experimental parameters are such that changes in flow conditions, manifested by changes in roller speeds and vorticity diffusion into the fluid, are relatively fast compared to the time for significant drop deformation to occur. Therefore, a good approximation to step changes in flow conditions is produced (Stone, *et al.* 1986).

The experimental procedure is to slowly increase the shear rate in small increments so that the drop progresses through a series of steady states. When the critical shear rate, characterized by nonexistence of a steady shape, is reached, the droplet slowly extends. At some point, conveniently represented by the dimensionless elongation ratio, $\frac{L}{a}$, the flow conditions are altered abruptly. We will examine step changes to 'weaker' or subcritical flow conditions. In other words, the shear rate will either be decreased or the new flow conditions will have a higher vorticity to strain rate ratio (smaller α). In addition, a small number of experiments will be described where *simultaneous* step changes in shear rate and flow-type are made. Overall, the studies described in this paper are interesting dynamically and very challenging since the change to the new subcritical conditions occurs during the transient stretching of the droplet. Hence, relative to the new flow conditions the droplet is in a nonequilibrium configuration.

Step change experiments similar to the ones discussed here were first described by Grace (1971), although the results were not very extensive. This aspect of our work is meant to amplify Grace's results and examine the coupled effects of initial deformation, flow-type, viscosity ratio and subcritical flow conditions.

For the reader's reference, the undeformed drop radii are $a \approx 0.1$ cm, the suspending fluid has a viscosity $\mu \approx 50 \frac{\text{gm}}{\text{cm sec}}$ and a density $\rho \approx 1 \frac{\text{gm}}{\text{cm}^3}$ and the

interfacial tensions for the fluid-fluid systems used are $\sigma \approx 5 \frac{\text{dynes}}{\text{cm}}$. The shear rates necessary to produce breakup vary with viscosity ratio but are generally in the range $0.1 - 0.3 \text{ sec}^{-1}$ so that $0.1 < C < 0.3$. The Reynolds numbers, $\frac{\rho \sigma a}{\mu^2}$ and $\frac{\rho \bar{G} a^2}{\mu}$, are typically 10^{-4} for the experiments reported here.

As described in a previous publication (Stone *et al.* 1986), the droplet deformation as a function of time is conveniently followed by analysis of digital images obtained from a digital video camera (a central feature of the control hardware). The experiments are video taped for qualitative viewing and 35 mm still photographs are taken occasionally to document the observed dynamics.

Clearly, there are an infinite number of possible time-dependent flows that can be studied and our investigations have only concentrated on a small subclass of these possible flows. Furthermore, a comprehensive experimental program was *not* undertaken to identify all possible quantitative features associated with each special flow history. Rather, the experiments which covered $0.2 \leq \alpha \leq 1.0$ and $0.01 \leq \lambda \leq 20$ with a large number of step changes to new flow conditions, do serve to indicate qualitative, and even some quantitative, trends. The net result is that our observations appear to be rather general in nature.

4. NUMERICAL PROCEDURE

In order to illustrate some of the detailed features of the flow field during the evolution of the drop shape, a numerical study of transient dynamics is undertaken. Here we only examine step changes in shear rate to subcritical flow conditions. Of course, in addition to providing a very systematic method for examining the effect of viscosity ratio and initial drop shape, the numerical simulations offer the possibility of studying time-dependent flows that may otherwise be difficult to produce experimentally.

A powerful numerical scheme for this free-boundary problem is the boundary integral method, first applied to the drop deformation problem by Rallison & Acrivos (1978). This method is particularly well-suited for these problems as only the boundary of the region need be discretized rather than the entire

domain and, consequently, interfacial velocities are calculated directly. Here we only present calculations for a droplet in an axisymmetric extensional flow. Details of the application of the method to this problem can be found in Stone & Leal (1987). The interfacial velocity is calculated from the integral equation

$$\begin{aligned} \frac{(1 + \lambda)}{2} \hat{\mathbf{u}}(\mathbf{x}_s) + \frac{3}{4\pi} (1 - \lambda) \int_{S(t)} \mathbf{n} \cdot \left[\frac{(\mathbf{x}_s - \mathbf{y})(\mathbf{x}_s - \mathbf{y})(\mathbf{x}_s - \mathbf{y})}{|\mathbf{x}_s - \mathbf{y}|^5} \right] \cdot \hat{\mathbf{u}}(\mathbf{y}) dS \\ = C\mathbf{\Gamma} \cdot \mathbf{x}_s + \frac{1}{8\pi} \int_{S(t)} (\nabla_s \cdot \mathbf{n}) \mathbf{n} \cdot \left[\frac{\mathbf{I}}{|\mathbf{x}_s - \mathbf{y}|} + \frac{(\mathbf{x}_s - \mathbf{y})(\mathbf{x}_s - \mathbf{y})}{|\mathbf{x}_s - \mathbf{y}|^3} \right] dS \end{aligned} \quad (3)$$

where $\nabla_s \cdot \mathbf{n}$ represents the mean curvature of the surface S , \mathbf{n} is the unit normal directed from the droplet phase to the suspending phase and \mathbf{x}_s denotes a point on the fluid-fluid interface, $\mathbf{x}_s \in S$. In this equation we have assumed that all velocities have been nondimensionalized with respect to $u_c = \frac{\sigma}{\mu}$, lengths with respect to the undeformed radius $l_c = a$ and time by the convective time scale $t_c = \frac{l_c}{u_c}$. Also, $\mathbf{\Gamma}$ represents the dimensionless version of equation (2) and the characteristic shear rate \bar{G} is chosen as the shear rate prior to the step change.

For the axisymmetric drop shapes we will examine here, the azimuthal integration is performed analytically so that the surface integral is reduced to a line integral. Given the drop shape, (3) is an integral equation of the second kind for the unknown $\hat{\mathbf{u}}$. This equation is solved by discretizing the surface and converting (3) to an equivalent linear system of equations that is solved by standard Gaussian elimination techniques.

As is characteristic of Stokes equation, this integral equation highlights the fact that the instantaneous drop shape uniquely specifies the instantaneous interfacial velocity. The interface position can then be updated by using the kinematic condition $\frac{d\mathbf{x}_s}{dt} = \mathbf{n}(\mathbf{u} \cdot \mathbf{n})$. Hence, the drop shape is uniquely determined for all time by an initial shape and the history of the flow $\mathbf{\Gamma}(t)$ (Rallison 1984). The interfacial velocity field can then be used to evaluate the interior and exterior velocity fields which are helpful in understanding detailed features of the drop shape evolution (for example, Stone & Leal 1987).

Since the boundary integral method is derived from the quasi-steady form of Stokes equation, the application of this numerical technique to time-dependent problems implicitly assumes that inertial effects due to the unsteady nature of the motion are negligible. This is indeed true provided that the time scale for vorticity diffusion, $\frac{\rho a^2}{\mu}$, is much shorter than both the time characteristic of drop deformation, $\frac{\mu(1+\lambda)a}{\sigma}$ and the time representative of convective effects in the external flow, \bar{G}^{-1} . Therefore, we require $\frac{\rho\sigma a}{\mu^2(1+\lambda)} \ll 1$ and $\frac{\rho\bar{G}a^2}{\mu} \ll 1$.

5. RESULTS / DISCUSSION

We now focus on studying general features of the dynamics of drop deformation associated with step changes in flow conditions that occur with the droplet in a nonequilibrium state. The connection with our previous studies is the observation that the droplet behaviour, even in the presence of a time-dependent imposed velocity gradient, is significantly influenced by an interfacial-tension-driven flow that occurs due to the existence of curvature variations along the fluid-fluid interface.

We first outline an experimental study which highlights most of our qualitative observations, including effects related to the magnitude of the step change, the flow-type, the initial degree of elongation of the droplet and the viscosity ratio. Then, we discuss detailed numerics of similar time histories for droplets suspended in axisymmetric extensional flows. By combining careful experiments with detailed numerics it is possible to develop good physical insight into the complicated dynamics of the breakup of modestly deformed drops.

5.1 Step changes in shear rate; flow-type constant

Let us begin by examining the effect of a step change in shear rate on the dynamics of a modestly extended drop, the flow-type being maintained constant. Figure 1 illustrates the result of an abrupt reduction from the critical capillary number C_c to $C = 0.5C_c$ with three different initial extensions for $\lambda = 0.1$ and $\alpha = 1.0$, a two-dimensional extensional flow ($C_c = 0.174$). A photograph of the

undeformed droplet is shown for reference. Dimensionless time is shown to the right of each photograph where the time reported is made dimensionless with respect to the characteristic deformation time scale $t_c = \frac{a\mu}{\sigma}$. † For parameters typical of the experiments reported in this paper $t_c \approx 1$ sec. Although a more appropriate measure of time during the stretching process is $(G\sqrt{\alpha})^{-1}$ (and indeed this is used in our previous experimental study, Stone *et al.* 1986), to be consistent with the numerical work presented in this paper and with our previous numerical study (Stone & Leal 1987) we measure time using the deformation time scale. This time scale is convenient for direct comparisons of experiments with different viscosity ratios since it remains unchanged as λ varies. Whenever a step change in the velocity field occurs, the time is measured with respect to the instant the change is made. In each of the figures the first few photographs show the droplet slowly extending in a steady flow at the critical capillary number. The droplet shape during this elongation process basically consists of a cylindrical midsection with rounded ends. At the time the step reduction in shear rate occurs the droplet is in a transient, nonequilibrium state.

In figure 1a the application of the subcritical shear rate is not sufficient to cause breakup. In this case, interfacial tension drives a relaxational motion which dominates the applied flow and the drop relaxes back to a steady shape. As far as we can discern from still photographs of the cross-sectional shape of the drop, the new steady shape attained is the *same* as would be achieved by applying this capillary number, $C = 0.5C_c$, to an initially spherical drop. This is true in general. In all experiments conducted, $0.2 < \alpha < 1.0$ and $0.05 < \lambda < 20$, for a wide range of shear rate and flow-type changes, whenever a steady drop shape is achieved, it is the same as found in the steady-state experiments beginning with a spherical shape and the same final flow conditions.

† As discussed by Stone *et al.* (1986), the zero of time is subject to some error due to the small experimental uncertainty in determining the critical capillary number coupled with the very slow elongation process that accompanies stretching at C_c .

In figure 1*b* the effect of a step change in shear rate is most dramatic and interesting. Following the abrupt change to $C = 0.5C_c$ complete drop breakup occurs even though the flow would have been too weak to cause breakup in the absence of the initial deformation. Two large daughter droplets are formed with a small satellite drop visible in between. The small satellite drop forms from the fluid cylinder connecting the two large bulbous ends. This demonstrates *complete* drop breakup in a flow *without* large scale stretching of the droplet.

Figure 1*c* shows how the two competing flow mechanisms, associated with interfacial tension and the external flow, interact for a more highly stretched droplet. Shortly after the abrupt change in flow, the droplet begins to stretch at a rate similar to a line element of the fluid, but the ends are continually bulbing and the development of a pinching region near the bulbous ends is evident. This pinching eventually leads to droplet breakup if the flow field is maintained, but, in this case, the experiment is stopped when the droplet approaches the limits of the linear flow region of the four-roll mill. For clarity we will distinguish this breakup process from the complete breakup illustrated in figure 1*b*. Throughout the remainder of this paper, whenever a subcritical flow causes the droplet to continue stretching but does not produce complete fragmentation during the time the drop remains within the linear flow region of the four-roll mill, we will use the term 'breakup via continuous stretching.'

After the flow is stopped in figure 1*c* the droplet fragments according to the basic end pinching mechanism. Recall that when the flow field is stopped abruptly, the fluid comes to rest on a time scale that is short compared to the time scale for drop deformation (Stone *et al.* 1986). Therefore, in the absence of any external motion, the final stages of the dynamics are dictated by the initial drop shape. Curvature variations in the vicinity of the bulbous ends produce a deterministic flow field that leads to the breakup of the droplet. This aspect of the breakup dynamics has been extensively discussed experimentally and numerically in two previous papers from our laboratory (Stone *et al.* 1986

and Stone & Leal 1987).

A second example of the relaxation and breakup process following a step change in shear rate is shown in figure 2 for $\lambda = 5.1$. Two aspects of the shape evolution are worth emphasizing. Figure 2*a* illustrates the relaxation back to a steady shape even though intermediate drop shapes exhibit the pronounced formation of a neck in the middle of the drop. However, simultaneously with the development of the neck the ends bulb up and the drop shortens because of an interfacial-tension-driven flow in the vicinity of the end. This relaxation flow dominates the applied subcritical extensional flow that seeks to stretch the drop, and the drop returns to a steady shape. Figure 2*b* shows the complete fracturing of this viscous droplet in a subcritical flow. Roughly speaking, there are two stages to the breakup process for this high viscosity ratio system. After the reduction in shear rate, the drop shortens slightly, the ends become bulbous and the middle, cylindrical portion thins noticeably. Then, the drop begins to stretch because of the weak extensional flow and, as the middle becomes very thin, a pinch is seen to develop near the bulbous end. This pinching is a precursor to the complete fracturing in the steady subcritical flow shown in the last few photographs.

These experiments highlight several features that are common to the step change experiments discussed throughout this paper. In many cases, following the abrupt change in flow conditions, there is an observable reduction in end-to-end length followed by breakup in the subcritical flow. The "dog-bone" shaped drops (similar to the shapes formed immediately after the shear rate is reduced) typical of this initial relaxation are occasionally maintained in the flow for a significant length of time. These intermediate shapes may either relax back to a steady shape or undergo a stretching and breakup process (for example, see figure 2). Initially one might think that such conformations may be steady shapes which break because they are unstable with respect to small disturbances always present in the flow due to the action of the control algorithm. However,

the reproducible nature of this phenomenon in many experiments and numerical simulations (to be illustrated in many figures throughout this paper) suggests that this is not the case. Rather, the complicated dynamics simply evolve on a long time scale. It appears clear that these dynamics are a consequence of the interaction of the extensional character of the flow, which drains fluid from the central cylindrical region while also trying to further stretch the droplet, and an interfacial-tension-driven motion, which causes bulbing of the ends and a relaxational motion reminiscent of the end-pinching phenomenon. The detailed velocity fields which are helpful in illustrating the shape evolution will be presented in the numerical study described in Section 5.4.

One question which comes to mind at this point concerns the effect of flow-type. How are the previously illustrated dynamics affected if $\alpha \neq 1$? First of all, in the steady-state experiments of Bentley & Leal (1986b), as the critical capillary number for burst is approached, the ellipsoidally shaped droplet elongates and aligns along the outflow axis[†] of the linear flow field where it experiences an effective shear rate $G_c\sqrt{\alpha}$ (G_c is the shear rate at the critical capillary number). It follows (Stone *et al.* 1986) that for the case of transient stretching of a droplet aligned along the outflow axis the appropriate measure of time is $G_c\sqrt{\alpha}$. In such cases, the only effect of the flow-type during the transient elongation is to determine the representative time scale and critical capillary number for burst. Therefore, given a different flow-type, it should not be surprising that for a step change in shear rate only, the dynamics are quite similar to those just described in figures 1 and 2.

In order to isolate the effect of flow-type, figure 3 presents a step change in shear rate for $\lambda = 0.1$ and a flow-type $\alpha = 0.6$. Again, a step change from the critical capillary number to $C = 0.5C_c$ is studied. Recall that C_c depends on α so the critical capillary number in this case is $C_c = 0.23$. Clearly, the dynamics

[†] The outflow axis is the direction defined by the eigenvector of equation (2) with eigenvalue $+\sqrt{\alpha}$.

are very similar to those shown in figures 1 and 2. In figure 3a, following the reduction in the shear rate, we again observe complete drop breakup in a subcritical flow field with only a very small change in the end-to-end length of the drop. Also, notice that even though the capillary number is reduced, the droplet remains oriented in the direction of the outflow axis. For ellipsoidal steady shapes in these same flow conditions ($C = 0.5C_c$) the droplet, in general, would have an orientation between the principal axis of strain (the horizontal direction) and the outflow axis. In figure 3b, the more elongated initial shape is responsible for the fact that the droplet remains oriented along the outflow axis even in these subcritical flow conditions.

Figures 1 and 3 provide a direct visual comparison of the effect of flow-type for $\lambda = 0.1$ and a step reduction in shear rate. In addition to the qualitative similarities of the relaxation and breakup process, a series of experiments in addition to those displayed in figures 1 and 3 demonstrate that the critical initial elongation needed for breakup at $\lambda = 0.1$ given a reduction to $C = 0.5C_c$ is bounded by $3.0 < \frac{L}{a} < 3.2$ for the $\alpha = 1.0$ flow, while for the $\alpha = 0.6$ flow the critical elongation is bounded by $3.0 < \frac{L}{a} < 3.3$. Clearly, small details in the shape can be expected as the flow-type varies. Therefore, as in the end-pinching studies reported by Stone *et al.* (1986), the qualitative and quantitative results described above suggest that the drop dynamics, in response to a step change in shear rate, depend on the *global* features of the drop shape rather than on any *local* details.

Two additional examples of the effect of a step change in shear rate which further corroborate this point are shown in figures 4 and 5 for $\lambda = 1.3$ and $\lambda = 5.3$ respectively. Figure 4a shows a step reduction to $C = 0.75C_c$ for a flow-type $\alpha = 0.2$ and figure 4b shows the same step reduction for an $\alpha = 0.6$ flow. Again we observe relaxation back to a steady shape if the droplet is not too elongated and breakup via continuous stretching if the step change occurs with the droplet more highly elongated. In figure 5, step reduction experiments

are shown for $C = 0.5C_c$ and a flow-type $\alpha = 0.4$. The large λ experiment illustrated in figure 5*b* is particularly interesting and well documented. In the steady subcritical flow, we see complete fracturing into two large droplets with a very thin thread in between. The initial response to the abrupt step change is a reduction in end-to-end length, bulbing of the ends, and then a gradual thinning of the droplet midsection with almost no change in overall length. Finally, the droplet stretches, the middle region is drawn into a very thin cylinder and a pinch process occurs near the ends. The final photograph shows the final stage of fragmentation. After the flow is stopped, the central very thin thread, which has very pointed ends, returns to a single droplet.

The qualitative features illustrated by figures 3-5 are the same as those outlined in figures 1 and 2. Furthermore, even after the step change in shear rate, the elongated droplet maintains an orientation along the exit streamline (the effective shear rate for a fluid element at this orientation is $G\sqrt{\alpha}$) during the relaxation and breakup process. As a result of these observations, we may conclude that for changes in shear rate only, the only independent effect of flow-type is to determine the critical capillary number and the proper time scale of the stretching process.

It is informative to study the relaxation and stretching processes by displaying the dimensionless drop length as a function of time. In figure 6*a-c*, typical data for $\frac{L}{a}$ versus time are shown for the cases $\lambda = 0.1, 0.46$ and 5.3 , respectively. In the figures, each type of symbol denotes the transient behaviour of a single droplet and the horizontal arrows indicate the elongation at which a step change is made from the critical to subcritical flow conditions. The initial transient stretching is very slow and is followed by a rapid elongation when $\frac{L}{a} > 3$. In each of the figures, a change to subcritical flow conditions is shown that results in the droplets recovering a steady shape. However, for each viscosity ratio, a larger initial extension prior to the step change leads to breakup. The breakup process exhibits the interesting feature, shown pictorially in previous figures,

that the end-to-end drop length remains the same or noticeably shortens for a significant period of time. This is followed by a period of continued stretching during which time complete fracturing may occur in the flow. In figure 6*a,b* the resulting stretching process produces complete breakup in the flow when the symbols terminate. The high viscosity ratio experiments shown in figure 6*c* are characterized by stretching with the formation of a thinning cylindrical midsection, but breakup did not occur during the time the drop remained within the linear flow region of the device. The continuous stretching mode is generally observed for these very viscous drops. The stretching process in subcritical flows is a precursor to complete fragmentation since very viscous drops damp the internal flow that leads to the pinch phenomena. We will discuss this aspect of the breakup of viscous drops more fully using the numerical simulations, Section 5.4. The solid vertical line adjacent to the stretching data in figure 6 denotes the asymptotic limit of stretching at a rate equal to a line element of the fluid in the new flow conditions. Notice that after the period during which the drop shape adjusts to the weaker flow, the droplet begins to rapidly stretch again and the rate of stretching asymptotes to that of a fluid element in the new flow conditions. Finally, notice in the cases where relaxation back to a steady shape occurs, the drop length decreases monotonically and we have made no observations (experimentally or numerically) of any behaviour similar to the “inertial overshoot” discussed by Kang & Leal (1987) (the numerical calculations of inertial overshoot during transient bubble deformation were limited to moderate to high Reynolds number and were not observed for Reynolds number as low as 10).

The experiments just outlined imply that the capillary number necessary to produce breakup is dependent on the initial drop shape, as indicated, say, by the elongation ratio $\frac{L}{a}$ at the time the flow field is changed abruptly. This behaviour is entirely consistent with the properties of Stokes equations for which the instantaneous velocity field, and consequently the drop shape evolution,

depend only on the instantaneous imposed flow and the instantaneous shape. The history of the flow is only important in that it produces a definite initial shape. Some typical experimental results for the dependence of the critical extension ratio necessary for breakup (either complete fragmentation or breakup via the continuous stretching mode) as a function of the magnitude of the step change in shear rate are summarized in Table 1 for the case $\lambda = 0.46$ and in Table 2 for the case $\lambda = 5.3$. Qualitatively, the more extended the droplet, the weaker the external flow necessary to cause breakup. As should be clear these results hold for all flow-types provided the flow history consists of a step reduction in shear rate only. Perhaps the most interesting aspect of the data in these two tables is that for the large viscosity ratio data summarized in Table 2, even a weak flow can produce breakup, generally observed via the continuous stretching mode, without requiring a large initial elongation. If the flow is stopped abruptly, an initial elongation $\frac{L}{a} \approx 8$ is necessary to guarantee breakup. However, these results demonstrate that even weak extensional flows can lead to the continuous stretching and breakup of a viscous drop which has a modest initial deformation.

Finally, we directly address the effect of viscosity ratio. In our previous study (Stone *et al.* 1986), which only investigated transient behaviour following an abrupt halt of the flow, the effect of a high viscosity ratio is to severely damp the internal motion which leads to the development of a neck, a precursor to the end pinching process. Consequently, very large extensions are necessary to guarantee breakup of viscous drops in an otherwise quiescent fluid. However, as illustrated above in Table 2, figure 5 and figure 6c, if the flow is not altogether stopped, but rather reduced to a subcritical value, it is not necessarily true that large extensions are needed for breakup. As a matter of fact, the critical extension necessary to guarantee breakup or, at least, to continue the stretching process, appears to become almost independent of λ for $\lambda > O(1)$. This behaviour is shown in figure 7 where the experimental results for a step change

to $C = 0.75C_c$ are summarized. The open squares denote the largest elongation ratio for which the drop relaxes back to a steady shape (a sphere) and the open triangles denote the smallest elongation for which breakup was observed upon cessation of the flow. Similarly, the filled squares represent relaxation back to a steady shape and the filled triangles represent breakup, either complete fragmentation in the flow or breakup via the continuous stretching mode. As Tables 1 and 2 document, the qualitative behaviour of a step change in shear rate illustrated in figure 7 is representative of a wide range of step changes. For large λ it is nonetheless true that complete fracturing in the flow takes longer time and, above the critical extension ratio, the evolution and complete fracturing of the droplet is accompanied by large scale stretching (see figure 5). We emphasize that this behaviour is true for all flow-types provided the flow history consists of a step change in shear rate.

5.2 Step changes in flow-type; shear rate constant

We have examined time-dependent dynamics associated with step changes in shear rate. An equally interesting question is to ask how the drop shape evolution is influenced by changes in flow-type. Here we specifically address questions concerned with abrupt changes in flow-type, the shear rate being maintained constant, so that the new flow conditions are subcritical. Recall that as the flow-type changes from a hyperbolic flow ($\alpha = 1.0$) towards a simple shear flow ($\alpha = 0.0$), the addition of vorticity causes the drop to rotate *away* from the principal axis of strain. Thus, the effective shear rate experienced by the drop is reduced and the effective capillary number becomes subcritical. Again, in these experiments changes in flow conditions are applied with the drop undergoing a transient stretching at the critical capillary number. These experiments are very interesting and are somewhat unique in that the computer-controlled four-roll mill in our laboratory is one of the few (only?) devices currently capable of performing such a study in a well-controlled manner.

Figures 8,9 and 10 show the effects of a step change in flow-type for three

different viscosity ratios, $\lambda = 0.1, 1.3$ and 5.3 . These photographs are typical of the experimental results. The breakup processes are very similar to those previously described in figures 1-7. In figures 8-10 the step change in flow-type is followed by rapid rotation to a new *steady* orientation after which the observed behaviour is either (1) relaxation back to a steady shape, (2) breakup in the flow without large scale stretching or (3) continued stretching and breakup. No new steady shapes are observed and the new steady orientation achieved by the droplets is along the outflow axis of the new flow field. The rotation process is documented very clearly in figure 10. Clearly, the most interesting new dynamical feature associated with the sudden addition of vorticity is that for these rather modest deformations and the small capillary numbers at which the step change occurs, drop rotation appears very *rapid* relative to any significant deformation.

It is clear that the subcritical flow conditions that exist after a change in the flow-type can still produce breakup of a drop, even if the drop is initially deformed beyond the maximum steady deformation by only a modest amount. Of course, in these experiments the magnitude of the capillary number needed for breakup not only depends on the initial conditions (the drop elongation $\frac{L}{a}$ when the flow is changed) but also on the magnitude of vorticity in the new flow field. As a consequence of the rapid rotation, relative to any significant interfacial-tension-induced change of shape, the drop aligns along the outflow axis where the effective shear rate is $G\sqrt{\alpha}$.

We have qualitatively observed that the critical length for breakup given only a step change in shear rate G is nearly the same as for a given change in $\sqrt{\alpha}$. For example, in experiments with $\lambda = 0.46$, a step change from $\alpha = 1.0$ to $\alpha = 0.4$ ($\sqrt{\alpha} = 0.63$) showed rapid rotation to the new steady orientation along the outflow axis and a critical extension ratio for breakup $2.35 < \frac{L}{a} < 2.57$, which compares very well with the data illustrated in Table 1. This suggests that for these modestly extended drops the idea of an effective shear rate, $G\sqrt{\alpha}$,

corresponding to the droplet oriented along the outflow axis (the eigenvector) of the new flow, may prove to be very useful. Furthermore, it implies that when both shear rate changes and flow-type changes occur simultaneously, the critical extension ratio for breakup depends, at least qualitatively, on an effective capillary number in the modified flow $C_{eff} = \frac{G\sqrt{\alpha\mu a}}{\sigma}$. This idea does indeed prove to be valuable and we examine this in the next section.

As an aside, for those readers interested in geometric aspects of free surfaces, the photograph of the droplet just as it is fracturing in figure 8*b* shows a narrow *conically* shaped central thread attached to an almost spherical droplet. This is very similar to a remark of Peregrine (1986) on the shape of the liquid bridge joining a nascent drop to the remainder of the fluid, although viscous effects in Peregrine's experiments are generally insignificant (see also the experiments of Marschall 1985, which were brought to our attention by Professor Peregrine). The conical interface is also very similar to intermediate shapes observed in the formation of satellite drops due to capillary wave growth on cylindrical fluid interfaces (Goedde & Yuen 1970 and Van Dyke 1982). This suggests that conically shaped surfaces created during the evolution of fracturing interfaces may be a general geometrical phenomenon. Additional examples can be seen in figures 2-5 and figure 11*b,c*. However, we have not investigated this matter further.

5.3 Simultaneous step changes in shear rate and flow-type

The observations that the sudden addition of vorticity leads to rapid rotation relative to any significant drop deformation, at least for $\lambda = O(1)$, may appear, at first, somewhat surprising. This suggests that the angular velocity of a deformable drop in a linear shear field should be examined. Although a general analytic solution is not available for the orientation of a finitely deformed drop in a linear flow, nevertheless, as discussed by Bentley & Leal (1986*b*), useful ideas can be obtained by considering a solid ellipsoid of revolution. A particle in a linear shear flow will have an angular velocity proportional to G . So the

time for the ellipsoid to reorient from an initial orientation to a final steady orientation should scale with the inverse of the shear rate G^{-1} . This is the same order of magnitude as the rate of drop deformation only if the droplet is highly extended, in which case deformation similar to a fluid element in the flow is observed. The key difference with regard to our observations is that the stretching process is very slow initially (see the discussion in Stone *et al.* 1986) and the droplet does not begin to stretch like a fluid element until $\frac{L}{a} > 3$. Typically, for the rapid addition of vorticity when the droplet is only modestly deformed (say, $\frac{L}{a} \approx 2 - 3$, as in these experiments), the time scale for drop deformation is much longer than G^{-1} (see figure 6) and the rotation to a new orientation can be decoupled from the deformation process. Then, following reorientation, the effective shear rate for the extended droplet aligned along the outflow axis of the new flow is $G\sqrt{\alpha}$ (Bentley & Leal 1986b).

In order to test the idea of an effective capillary number $C_{eff} = \frac{G\sqrt{\alpha}\mu a}{\sigma} = C\sqrt{\alpha}$ for describing drop dynamics we present some experimental observations on *simultaneous* step changes in shear rate and flow-type. In figure 11*a,b* we show the results of step changes from the initial flow conditions $C = C_c$ and $\alpha = 1.0$ to the final flow conditions $C = 0.8C_c$ and $\alpha = 0.6$. Figure 11*c* illustrates the effect of a step *increase* in capillary number to $C = 1.3C_c$ when the flow-type is changed from $\alpha = 1.0$ to $\alpha = 0.25$. The drops in figure 11 have a viscosity ratio $\lambda = 0.46$. In the first case (figure 11*a,b*) the effective capillary number characterizing the new flow conditions is $C_{eff} = 0.62C_c$ and in the latter case (figure 11*c*) $C_{eff} = 0.65C_c$.

We make the following observations concerning the effects of simultaneous changes in shear rate and flow-type. In figure 11*a*, after the step change in flow conditions, the droplet relaxes back to a steady shape. However, notice that during the relaxation process the droplet clearly develops a 'waist'. Eventually, though, the relaxational motion dominates and a steady shape is established. Figure 11*b* illustrates the effect of a more elongated initial shape. The droplet

first reorients prior to any significant deformation, then breaks in the subcritical steady flow as seen in many of the earlier figures.

Figure 11*c* also shows an interesting evolution. In this case, as the droplet rotates away from the extensional axis, it initially feels a *stronger* effective shear rate since the shear rate was increased to $1.3G_c$. The droplet reorients and deforms a little, then rapidly begins to stretch and eventually fractures in the flow. Again, we observe a conically tipped thread at the end of the central portion of the droplet connected to the deformed spherical end shortly before the final fragmentation is complete. After the flow is stopped, the central thread relaxes and fragments, leaving the small satellite drops shown in the last photograph. The experiments shown in figure 11*b,c* appear to be very close to the critical length necessary for breakup, which we estimate in both cases to be $\frac{L}{a} \approx 2.4 - 2.6$. This estimate of the critical length for breakup at $C_{eff} = 0.65C_c$ is in good agreement with the data reported Table 1 that only accounts for a step change in shear rate.

In figure 12 we show another sequence of simultaneous changes in flow-type and shear rate. For this droplet, $\lambda = 0.46$, the shear rate is reduced from G_c to $0.4G_c$ and the flow-type simultaneously changed from $\alpha = 1.0$ to $\alpha = 0.25$. The effective capillary number at the new flow conditions is $C_{eff} = 0.2C_c$. First of all, figure 12*a* provides a dramatic example of a waist forming initially due to the external extensional flow only to eventually be overwhelmed by the inward capillary-driven flow generated by the bulbing end. Figure 12*b* appears to be very close to the critical length necessary for breakup as the droplet fractures in two with a very small satellite droplet in between. It is quite remarkable that at the time breakup is complete the droplet has a shorter end-to-end length than the initial shape at the time the step change in flow conditions occurs. The critical length for breakup for a step change to $C_{eff} = 0.2C_c$, as bounded by the two sets of photographs in figure 12, is $3.2 < \frac{L}{a} < 3.3$, which is again in good agreement with the data in Table 1. Therefore, it appears clear from the experiments

performed using simultaneous step changes in flow conditions, in conjunction with the effect of viscosity ratio, shear rate and flow-type described in Sections 5.1 and 5.2 that both qualitatively and even quantitatively the effective capillary number at the new flow conditions is useful for predicting behaviour for a given initial condition, provided only that droplet rotation to a steady orientation is sufficiently fast.

Several remarks regarding these dynamics are in order. First of all, it should be clear that the idea of an effective capillary number for breakup of modestly deformed drops given an abrupt change in flow conditions makes qualitative sense and is even quantitatively correct, at least for the limited number of cases we've examined. The validity of this correlation depends on the *disparate time scales* governing different aspects of the dynamics. Because the drop shape evolution depends on the global shape rather than on any local details, then, provided rotation to a new steady orientation is sufficiently fast relative to the time scale for any significant drop deformation (due either to interfacial tension or the external flow), the breakup criteria is well-approximated by the initial elongation $\frac{L}{a}$ and an effective capillary number C_{eff} . On the other hand, we might expect that for a large increase in G and a corresponding decrease in $\sqrt{\alpha}$ the drop would spend a significant length of time in a very strong flow as it rotates to the final steady orientation and the above time scale assumptions would begin to break down. Nevertheless, at least in the case illustrated in figure 11c, the breakup behaviour was still well correlated with C_{eff} . The viscosity ratio will also play a role in such time scale arguments as viscous drops deform more slowly than lower viscosity ratio drops. For viscous drops the difference between reorientation and deformation time scales will be even larger than illustrated in figures 11 and 12. Therefore, the disparate time scales arguments that suggested the idea of an effective capillary number will be even better for very viscous droplets. From these arguments we conclude that the critical extension data tabulated in Tables 1 and 2 and figure 7, which are all determined from experiments involving

step changes in shear rate only, are useful for the broader class of flows involving simultaneous changes in shear rate and flow-type provided interpretation is based upon the critical capillary number C_{eff} as described above.

5.4 numerical study of step changes

The brief numerical study we present here is designed to complement the basically qualitative description of the dynamics demonstrated by the series of experiments just described. One advantage of the numerical simulation is that it allows a systematic change in the parameters to be coupled with a detailed picture of the velocity field. For example, in step reduction experiments, it is straightforward to vary the magnitude of the subcritical flow for the same initial elongation or vary the initial elongation for a given subcritical flow. In addition, the evolution of the shape, detailed velocity fields and the effect of viscosity ratio are relatively easy to examine and will be illustrated in this section.

We begin by examining droplet extension in a uniaxial extensional flow. Starting with a spherical droplet, the capillary number is increased in small increments until a steady shape no longer exists and a continuous stretching occurs. This stretching at slightly supercritical capillary numbers is illustrated below. At different stages of the elongation process the capillary number is decreased abruptly to a subcritical value analogous to the experimental study described in Section 5.1. Two different viscosity ratios are examined, $\lambda = 1.0$ and $\lambda = 10$. The calculations with $\lambda = 1.0$ are especially straightforward and capture all the important features of the shape evolution and the velocity field. The numerical study of $\lambda = 10$ is useful for understanding the effect of subcritical flows on the relaxation and breakup processes for very viscous drops. Calculations of drop deformation in biaxial extensional flows are described by Stone (1988).

In figures 13 and 14 the solid curves show the time-dependent elongation that occurs at slightly supercritical capillary numbers for $\lambda = 1.0$ and 10.0, respectively. The evolution of the drop shape is also shown at intermediate times

during the transient stretching process. The shapes are identified by the letters a,b,c, etc. Characteristic of the deformation process, the elongation is very slow. But, as a waist develops, the drop begins to stretch rapidly, approaching the asymptotic limit of stretching at the rate of a line element of the fluid in the undisturbed flow (the solid nearly vertical line in these figures).

We next illustrate the effect of abruptly decreasing the capillary number at different times during the continuous extension. We consider a step change to $C = 0.5C_c$ for three different initial conditions. The resulting evolution is shown by the dashed lines in figures 13 and 14 and numerically generated shapes are presented. As indicated in the experimental study, there appears to be three basic modes of behaviour. In each figure, curve A shows the relaxation back to a steady shape. This is the *same* steady shape calculated by beginning with a spherical drop in this subcritical flow. Curve B illustrates a very interesting time-dependent breakup. Initially a visible relaxational motion and reduction in drop length occurs as the ends become rather bulbous. In figure 13, $\lambda = 1.0$, the formation of a significant neck leads to complete drop breakup in the flow although the drop has extended very little. In addition, the thin cylindrical thread connecting the two almost spherical ends, forms a small satellite droplet. This illustrates complete breakup in a steady flow without large scale stretching of the droplet, similar to several of the experiments discussed in Section 5.1. Finally, for the initial condition used in curve C, the droplet has a very small initial relaxation as the shape at the end responds to the weaker velocity gradient by becoming more bulbous, but then the drop rapidly extends. In the case of $\lambda = 1.0$ it is evident that the ends are pinching off, but the drop is simultaneously beginning to stretch. However, the $\lambda = 10$ droplet basically stretches during the time shown and there is no immediate evidence of the ends breaking off. This is related to the fact that the flow process internal to the droplet that leads to the end pinching phenomenon is damped by the more viscous droplet fluid. Consequently, the end pinching mechanism requires longer times for breakup of

high viscosity ratio systems so that, instead of complete fragmentation, drop deformation is characterized by a significant increase in the end-to-end drop length. Finally, the dashed almost vertical line adjacent to curve C in figures 13 and 14 illustrates the rate at which a fluid element stretches in these new flow conditions and the droplet elongation rapidly approaches this asymptotic behaviour.

In all cases, the numerics indicate that the curvature near the end decreases (i.e. the end becomes more rounded) in response to the abruptly weaker flow. This is true even in instances where the droplet continues to stretch so that the end slowly becomes more spherical as the droplet elongates. These simulations also indicate, in agreement with the experimental results discussed in Sections 5.1-5.3, that there is a narrow range of initial elongations for which complete breakup will occur without much stretching of the drop. Furthermore, because of the interaction of the extensional flow and the interfacial-tension-driven flow, the range of initial conditions that lead to complete breakup without much stretching is even narrower for viscous drops, which inhibit the flow process leading to end pinching. Nevertheless, in the experimental study, several cases of complete breakup of high viscosity ratio drops are documented (figures 2,5 and 10).

In order to better understand the evolution of the drop shape, in figures 15 and 16 we present the internal and external velocity fields for the intermediate shapes shown along curve B in figures 13 and 14. The arrows denote the direction and relative magnitude of the fluid velocity, but there is no connection between arrows in one illustration and those in another. The “competition” between the externally imposed flow, and the relaxational, interfacial-tension-driven flow is very evident. Notice how the competition between these two mechanisms for flow produces a closed *vortical* motion interior to the droplet (figures 15*a-c*). Figure 15*a* shows the velocity field just after the abrupt change in shear rate. Initially, the most noticeable motion takes place near the end of the droplet. The

ends become more spherical and, as a consequence, drive a large inward velocity. Near the droplet center, the external velocity gradient produces an extensional motion which causes the droplet to form a waist and continually thin. The precise role of the flow field produced by curvature variations along the surface will be examined in detail below. As the end becomes more rounded the driving force for inward motion becomes less pronounced while the drop continues to thin. In figure 15c the drop is beginning to lengthen slowly and a visible neck is formed near the bulbous end. This neck will eventually lead to the ends pinching off and the remaining liquid thread in the middle will form at least one satellite drop. At $\hat{t} = 113.8$ the fluid velocity in the neighborhood of the pinch is much larger than the speed at which the end translates. This is responsible for pinch off *without* large-scale stretching of the droplet. At least in the central section of the droplet the velocity profile is parabolic as expected from a slender-body analysis (Acrivos & Lo 1978). Qualitatively, very viscous drops have much flatter velocity profiles than do smaller viscosity droplets. In the $\lambda = 10$ simulation shown in figure 16 there is no pinch evident. Presumably, for the initial condition chosen, longer times, and more elongated droplets are necessary before a significant pinch can develop for higher viscosity ratio droplets.

In these simulations of a step reduction in shear rate, the mechanism of the breakup process can be seen to involve a very interesting interaction between an interfacial-tension-driven flow and a flow produced by the external velocity field. The net effect is both *competitive* and *cooperative* depending on the region of the drop and the stage of the interface evolution. In order to illustrate this last point we examine the different contributions to the two components of the interfacial velocity field (u_r, u_z) at different times during the breakup process for the cases $\lambda = 1.0$ and $\lambda = 10$, whose detailed velocity fields were shown in figures 15 and 16. In figures 17a-c, we show the r-component of the interfacial velocity field as a function of axial position and in figures 17d-f we show the z-component. In these figures the solid line is the numerically calculated interfacial velocity

field, the short dashed line is the undisturbed velocity and the long dashed line is the difference between the actual velocity and the undisturbed velocity. This difference is directly attributable to a flow produced by curvature variations along the surface and is a direct consequence of interfacial tension (see equation 3).

In figure 17a the decomposition is shown just after the step reduction in shear rate occurs and in figure 17b,c the results are shown at later times. Relaxational flows are characterized by $u_z < 0$ and the pinching process is produced by $u_r < 0$ and $u_z > 0$. The first aspect to notice is that, at first, the flow produced by interfacial tension (the long dashed line) *opposes* the thinning of the cylindrical midsection. This is evident because, near the center of the drop, the contribution to the radial velocity field is positive and the contribution to the axial velocity field is negative, corresponding to flow towards the center. Although the curvature is highest here, it must be remembered that the interfacial-tension-driven flow is not a local effect, but rather depends on the global drop shape as discussed in our study of end-pinching (Stone *et al.* 1986). Nevertheless, although the end-to-end drop length decreases, the net effect of the subcritical external flow is to cause the central region to slowly thin and form a waist (the solid curve). Clearly this is a necessary condition for eventual drop breakup. This is not a sufficient condition because the relaxational motion due to flow near the end may eventually dominate and completely reverse the flow field at the center, allowing the drop to recover a steady shape. This is clearly seen in the experimental photographs, especially figure 12a.

The later stages of the breakup process are examined in figure 17b,c. It is clear that as the middle region thins the resistance to fracturing, due to the interfacial-tension-driven flow, diminishes. In figure 17c, where the midsection is quite thin, a *cooperative* flow is produced where both the external flow and the interfacial-tension-driven flow (which only depends on the instantaneous drop shape and λ) result in fluid draining from the center. This is illustrated by the

negative values of u_r and positive values of u_z near the middle of the drop. In figure 17*b* the contribution of interfacial-tension-driven flow to the thinning of the drop midsection ($u_r < 0$) is small while at a later time shown in figure 17*c* the rapid pinching is predominately due to the interfacial-tension-driven flow. The evolution of the velocity field shown in figure 18 for $\lambda = 10$ is very similar. The main difference for this high viscosity ratio is that the internal velocity gradients are damped significantly. As a result, the radial velocity field that produces thinning of the midsection is much smaller than in the $\lambda = 1.0$ case, and it takes much longer for the interfacial-tension-driven flow to dominate and produce the end pinching effect.

It is important to point out that the undisturbed flow field alone does not produce complete fracturing. Rather, the extensional undisturbed velocity field results in a simple stretching of the droplet and, as discussed by Mikami, Cox & Mason (1975) for the special case of an infinite cylindrical thread, such a flow uniformly thins the cylindrical body of fluid. The fracturing process is a direct consequence of the *nonuniform* flow produced by curvature variations along the drop surface. It is also clear, though, that the weak external flow is necessary to cause thinning of the drop midsection until the interfacial-tension-driven flow dominates and produces breakup.

The second aspect of the transient dynamics we wish to study is the effect of the magnitude of the shear rate reduction for a given initial condition. Basically, a series of such studies amounts to determining the capillary number necessary to produce breakup as a function of the initial droplet elongation and the viscosity ratio. In figures 19 and 20 we illustrate these dynamics for $\lambda = 1.0$ and 10 for an initial elongation $\frac{L}{a} \approx 3$. These figures illustrate, for the same initial condition, a step change from stretching at the critical capillary number C_c to a subcritical flow $C = YC_c$. In every case where the drop relaxes back to a steady, ellipsoidal shape it does so monotonically and we find numerically that it is the *same* steady shape as would be generated if an initially spherical drop were placed in these

subcritical flow conditions. This is reported in the inset to these figures where the deformation parameter D^\dagger is compared for the case of an initially spherical drop placed in the flow $C = YC_c$ (the steady state established is denoted by D_{ss}) and for the transient approach to the steady state shown in figure 19 and 20 (the steady state is denoted by D_{trans}).

Clearly, figures 13-20 show that there is a quite complicated interaction between a relaxational motion, dependent on the drop shape and the viscosity ratio, and the extensional motion, which is dependent basically on the capillary number and the initial shape. The numerics indicate that there is a quite narrow range of capillary numbers where breakup is preceded by a visible reduction in end-to-end length.

5.5 breakup for large λ in weak flows with vorticity

As first pointed out by Taylor (1934) for the case of steady simple shear flow and extended to other steady two-dimensional linear flows by Bentley & Leal (1986b), the effect of vorticity in the flow is to inhibit drop breakup. For sufficiently high viscosity ratios, droplets attain a maximum steady deformation in such flows and any additional increases in capillary number are only accompanied by increased rotation of droplet fluid rather than by any noticeable deformation. For example, in simple shear flow, breakup is not possible if the viscosity ratio exceeds approximately 4, and for $\alpha = 0.2$ and 0.4 the viscosity ratios above which breakup is not possible are approximately 20 and 60 respectively.

The above remarks concerning the inhibiting effects of vorticity on the breakup process are based on the premise that the drop shape is initially spherical. Here we ask the question whether breakup of high viscosity ratio drops in flows with vorticity is possible if the initial deformation exceeds the maximum stable deformation observed in the steady-state experiments. Clearly, if the viscous drops are very highly extended prior to application of a flow with vorticity,

† $D = \frac{L-B}{L+B}$ where L and B are the half-length and half-breadth of the drop.

previous photographs and discussion in this paper would suggest that breakup would be possible if the product $G\sqrt{\alpha}$ is sufficiently large (also, the larger the extension the weaker the flow necessary to ensure breakup). Instead, using an initial condition that is more deformed than the maximum steady deformation, but still not highly stretched, we illustrate the breakup of a very viscous drop by a flow that would otherwise not burst the drop at any value of the capillary number if the initial shape were a sphere.

In figure 21 the results of one such experiment is reported for $\lambda = 19$. A photograph of the maximum steady deformation attainable by beginning with a spherical drop and increasing the capillary number in small increments is provided for reference. The breakup of this drop is now examined by initially generating a more deformed shape in a stronger flow. The initial ellipsoidal shape shown is generated by first stretching the drop in an $\alpha = 1.0$ flow at the critical shear rate so that unsteady stretching occurs. When the viscous droplet is not too highly deformed the flow is abruptly stopped, the droplet begins to relax and then a flow field with $\alpha = 0.2$ is applied. The shear rate is then increased. The photographs shown illustrate that the droplet reorients along the outflow axis of the $\alpha = 0.2$ flow and continues to stretch. It must be remarked that the weak flow coupled with the high viscosity ratio produce a very slow elongation. The experiment does not represent the lowest possible capillary number for breakup given the nonspherical initial condition, but does show that different initial conditions, even modestly deformed ellipsoidally shaped drops, can lead to breakup of very viscous systems where simple steady approaches to breakup would never succeed. Again, this experiment illustrates a point made in figure 12, that even relatively weak flows can result in breakup for high viscosity ratio droplets.

6. CONCLUSIONS

We conclude with a few observations summarizing the results of this study. In this paper general features of the time-dependent dynamics of drop breakup

have been presented for transient flows produced by making step changes in flow conditions. The effects of initial drop shape, viscosity ratio and flow-type on the critical capillary number necessary for breakup are investigated. Detailed flow features are examined using the boundary integral method. The principal conclusions are:

1. Complete drop breakup in subcritical flows may occur without large scale stretching.
2. An effective capillary number $C_{eff} = \frac{G\sqrt{\alpha a\mu}}{\sigma} = C\sqrt{\alpha}$ is useful for understanding the effect of step changes in shear rate and/or flow-type on modestly deformed droplets. In these cases, rotation to a new steady orientation is fast relative to any significant deformation.
3. The critical drop extension necessary to guarantee breakup in subcritical flows appears to become independent of λ for $\lambda > O(1)$.
4. The development of conically tipped threads connected to nearly spherical ends is very noticeable in several of the experiments.
5. This study extends observations made initially by Grace (1971). Grace suggested the use of a stage-wise process for efficient breakup. The step change studies reported here provide additional data supporting this idea and indicate that the procedure should prove useful even for very high viscosity ratio systems.
6. Finally, it should be added that there are several interesting qualitative analogies (and differences) with the numerical calculations of bubble deformation in a uniaxial extensional flow at *finite* Reynolds numbers obtained by Kang & Leal (1987).

ACKNOWLEDGEMENTS

This work was supported by a grant from the fluid mechanics program of the National Science Foundation. One of the authors (HAS) was partially supported through an IBM Graduate Research Fellowship.

REFERENCES

- Acrivos, A. 1983 The breakup of small drops and bubbles in shear flows. *4th Int Conf. on Physicochemical Hydrodynamics, Ann. N.Y. Acad. Sci.* **404**, 1-11.
- Acrivos, A. & Lo, T.S. 1978 Deformation and breakup of a slender drop in an extensional flow. *J. Fluid Mech.* **86**, 641-672.
- Barthes-Biesel, D. & Acrivos, A. 1973 Deformation and burst of a liquid droplet freely suspended in a linear shear field. *J. Fluid Mech.* **61**, 1-21.
- Bentley, B.J. & Leal, L.G. 1986a A computer-controlled four-roll mill for investigations of particle and drop dynamics in two-dimensional linear shear flows. *J. Fluid Mech.* **167**, 219-240.
- Bentley, B.J. & Leal, L.G. 1986b An experimental investigation of drop deformation and breakup in steady two-dimensional linear flows. *J. Fluid Mech.* **167**, 241-283.
- Cox, R.G. 1969 The deformation of a drop in a general time-dependent fluid flow. *J. Fluid Mech.* **37**, 601-623.
- Goedde, E.F. & Yuen, M.C. 1970 Experiments on liquid jet instability. *J. Fluid Mech.* **40**, 495-511.
- Grace, H.P. 1971 Dispersion phenomena in high viscosity immiscible fluid systems and application of static mixers as dispersion devices in such systems. *Eng. Found. Res. Conf. Mixing, 3rd Andover, N.H.* Republished 1982 in *Chem. Engrg Commun.* **14**, 225-277.
- Greenspan, H.P. & McCay, B.M. 1981 On wetting of a surface by a very viscous fluid. *Studies in Applied Math.* **64**, 95-112.
- Hinch, E.J. 1980 The evolution of slender inviscid drops in an axisymmetric straining flow. *J. Fluid Mech.* **101**, 545-553.
- Hinch, E.J. & Acrivos, A. 1980 Long slender drops in a simple shear flow. *J. Fluid Mech.* **98**, 305-328.

- Kang, I.S. & Leal, L.G. 1987 Numerical solution of axisymmetric, unsteady free-boundary problems at finite Reynolds number I. Finite-difference scheme and its application to the deformation of a bubble in a uniaxial straining flow. *Phys Fluids* **7**, 1929-1940.
- Khakhar, D.V. & Ottino, J.M. 1986 Deformation and breakup of slender drops in linear flows. *J. Fluid Mech.* **166**, 265-285.
- Khakhar, D.V. & Ottino, J.M. 1987 Breakup of liquid threads in linear flows. *Intl J. Multiphase Flow* **13**, 147-180.
- Lasheras, J.C., Fernandez-Pello, A.C. & Dryer, F.L. 1979 Initial observations on the free droplet combustion characteristics of water-in-fuel emulsions. *Combustion Sci. and Tech.* **21**, 1-14.
- Lee, W.-K. & Flumerfelt, R. W. 1981 Instability of stationary and uniformly moving cylindrical fluid bodies - I. Newtonian systems. *Intl J. Multiphase Flow* **7**, 363-384.
- Marschall, E. 1985 Zur stromungsmechanik wahrend der Tropfenbildung in flussigen zweiphasensystemen. *VDI-Forschungsheft* **632**, 13-17.
- Mikami, T., Cox, R.G. & Mason, S.G. 1975 Breakup of extending liquid threads. *Intl J. Multiphase Flow* **2**, 113-138.
- Peregrine, D. H. 1986 The dripping of drops, or the bifurcation of liquid bridges. *IUTAM Symposium: Fluid Mechanics in the Spirit of G.I. Taylor, Symposium Abstracts.*
- Rallison, J.M. 1980 A note on the time-dependent deformation of a viscous drop which is almost spherical. *J. Fluid Mech.* **98**, 625-633.
- Rallison, J.M. 1984 The deformation of small viscous drops and bubbles in shear flows. *Ann. Rev. Fluid Mech.* **16**, 45-66.
- Rallison, J.M. & Acrivos, A. 1978 A numerical study of the deformation and burst of a viscous drop in general shear flows. *J. Fluid Mech.* **89**, 191-200.

- Rumscheidt, F.D. & Mason, S.G. 1962 Break-up of stationary liquid threads *J. Colloid Sci.* **17**, 260-269.
- Seward III, T.P. 1974 Elongation and spheroidization of phase-separated particles in glass. *J. Non-Crystalline Solids* **15**, 487-504.
- Sherwood, J.D., 1987 Drop breakup in electric and magnetic fields. (to appear).
- Stone, H.A., Bentley, B.J. & Leal, L.G. 1986 An experimental study of transient effects in the breakup of viscous drops. *J. Fluid Mech.* **173**, 131-158.
- Stone, H.A. & Leal, L.G. 1987 Relaxation and breakup of an initially extended drop in an otherwise quiescent fluid. *J. Fluid Mech.* (submitted).
- Stone, H.A. 1988 Dynamics of drop deformation and breakup in time-dependent flows at low Reynolds numbers. *PhD thesis, California Institute of Technology.*
- Taylor, G.I. 1932 The viscosity of a fluid containing small drops of another fluid. *Proc. R. Soc. Lond.* **A138**, 41-48.
- Taylor, G.I. 1934 The formation of emulsions in definable fields of flow. *Proc. R. Soc. Lond.* **A146**, 501-523.
- Tomotika, S. 1935 On the instability of a cylindrical thread of a viscous liquid surrounded by another viscous fluid. *Proc. R. Soc. Lond.* **A150**, 322-337.
- Tomotika, S. 1936 Breaking up of a drop of viscous liquid immersed in another viscous fluid which is extending at a uniform rate. *Proc. R. Soc. Lond.* **A153**, 302-318.
- Torza, S., Cox, R.G. & Mason, S.G. 1971 Electrohydrodynamic deformation and burst of liquid drops. *Phil. Trans. R. Soc. Lond.* **A269**, 295-319.
- Torza, S., Cox, R.G. & Mason, S.G. 1972 Particle motions in sheared suspensions. 27. Transient and steady deformation and burst of liquid drops. *J. Colloid Interface Sci.* **38**, 395-411.
- Van Dyke, M. 1982 *An Album of Fluid Motion.* Parabolic Press, 73.

FIGURE CAPTIONS

- Figure 1 The effect of a step reduction in shear-rate; the flow-type is maintained constant. $\lambda = 0.1$; $\alpha = 1.0$. Step change from C_c to $0.5C_c$; $C_c = 0.174$.
- Figure 2 The effect of a step reduction in shear rate; the flow-type is maintained constant. $\lambda = 5.1$; $\alpha = 1.0$. Step change from C_c to $0.35C_c$, $C_c = 0.12$
- Figure 3 The effect of a step reduction in shear-rate; the flow-type is maintained constant. $\lambda = 0.1$; $\alpha = 0.6$. Step change from C_c to $0.5C_c$; $C_c = 0.23$.
- Figure 4 The effect of a step reduction in shear-rate; the flow-type is maintained constant. $\lambda = 1.3$. a) $\alpha = 0.2$; b) $\alpha = 0.6$. Step change from C_c to $0.75C_c$.
- Figure 5 The effect of a step reduction in shear-rate; the flow-type is maintained constant. $\lambda = 5.3$; $\alpha = 0.4$. Step change from C_c to $0.5C_c$.
- Figure 6 Elongation ratio $\frac{L}{a}$ as a function of time. The horizontal arrows indicate when a step change in shear rate occurs to the new flow conditions. (a) $\lambda = 0.1$, $\alpha = 1.0$, step change to $C = 0.5C_c$; (b) $\lambda = 0.46$, $\alpha = 1.0$, step change to $C = 0.65C_c$; (c) $\lambda = 5.3$, $\alpha = 1.0$, step change to $C = 0.75C_c$. The solid line denotes asymptotic stretching similar to a fluid element in the new flow conditions.
- Figure 7 Critical elongation ratio necessary to ensure breakup as a function of viscosity ratio. Both an abrupt halt of the flow ($C = 0.0C_c$) and a step change in shear rate to the new flow conditions $C = 0.75C_c$ are examined. The open triangles denote the smallest $\frac{L}{a}$ for which a drop is observed to breakup and the open squares denote the largest $\frac{L}{a}$ for which a drop relaxes back to a steady (spherical) shape when the flow is abruptly stopped. The filled triangles and squares represent similar behaviour for the case that the change is made to the subcritical conditions $C = 0.75C_c$.
- Figure 8 The effect of a step change in flow-type; the shear rate is maintained constant. $\lambda = 0.1$. Step change from $\alpha = 1.0 \rightarrow \alpha = 0.2$.

- Figure 9 The effect of a step change in flow-type; the shear rate is maintained constant. $\lambda = 1.3$. Step change from $\alpha = 1.0 \rightarrow \alpha = 0.2$.
- Figure 10 The effect of a step change in flow-type; the shear rate is maintained constant. $\lambda = 5.3$. Step change from $\alpha = 1.0 \rightarrow \alpha = 0.25$.
- Figure 11 The effect of a simultaneous change in shear rate and flow-type. $\lambda = 0.46$. a,b) Step changes from $C_c \rightarrow 0.8C_c$ and $\alpha = 1.0 \rightarrow \alpha = 0.6$. c) Step changes from $C_c \rightarrow 1.3C_c$ and $\alpha \rightarrow 0.25$.
- Figure 12 The effect of a simultaneous change in shear rate and flow-type. $\lambda = 0.46$. Step changes from $C_c \rightarrow 0.4C_c$ and $\alpha = 1.0 \rightarrow \alpha = 0.25$.
- Figure 13 Numerical simulation of step changes in capillary number for three different initial conditions. $\lambda = 1.0$; $C_c \rightarrow 0.5C_c$. The solid, almost vertical line is the asymptotic limit of stretching like a line element in the undisturbed flow. The solid curve is the time-dependent elongation of the droplet at the critical capillary number. The dashed curves are the response to a step change in shear rate to $C = 0.5C_c$. The dashed line is the asymptotic limit of stretching like a line element in the new flow conditions.
- Figure 14 Numerical simulation of step changes in capillary number for three different initial conditions. $\lambda = 10.0$; $C_c \rightarrow 0.5C_c$. The solid, almost vertical line is the asymptotic limit of stretching like a line element in the undisturbed flow. The solid curve is the time-dependent elongation of the droplet at the critical capillary number. The dashed curves are the response to a step change in shear rate to $C = 0.5C_c$. The dashed, almost vertical lines are the asymptotic limit of stretching like a line element in the new flow conditions.
- Figure 15 Numerical simulation of the internal and external velocity fields during the relaxation and breakup of a droplet after a step reduction in capillary number; $\lambda = 1.0$; $C = 0.5C_c$. The simulations correspond to the intermediate shapes shown along curve B in figure 13.

Figure 16 Numerical simulation of the internal and external velocity fields during the relaxation and breakup of a droplet after a step reduction in capillary number; $\lambda = 10.0$; $C = 0.5C_c$. The simulations correspond to the intermediate shapes shown along curve B in figure 14.

Figure 17 The contribution of an interfacial-tension-driven flow to the drop breakup process. solid line - numerically calculated interfacial velocity as a function of axial position; short dashed line - contribution of the external flow; long dashed line - difference between the actual velocity and the external velocity. $\lambda = 1.0$ a-c) u_r vs. z ; d-f) u_z vs. z . The plots (a-c) and (d-f) correspond to the first three velocity profiles shown in figure 15, respectively.

Figure 18 The contribution of an interfacial-tension-driven flow to the drop breakup process. solid line - numerically calculated interfacial velocity as a function of axial position; short dashed line - contribution of the external flow; long dashed line - difference between the actual velocity and the external velocity. $\lambda = 10.0$ a-c) u_r vs. z ; d-f) u_z vs. z . The plots (a-c) and (d-f) correspond to the first three velocity profiles shown in figure 16, respectively.

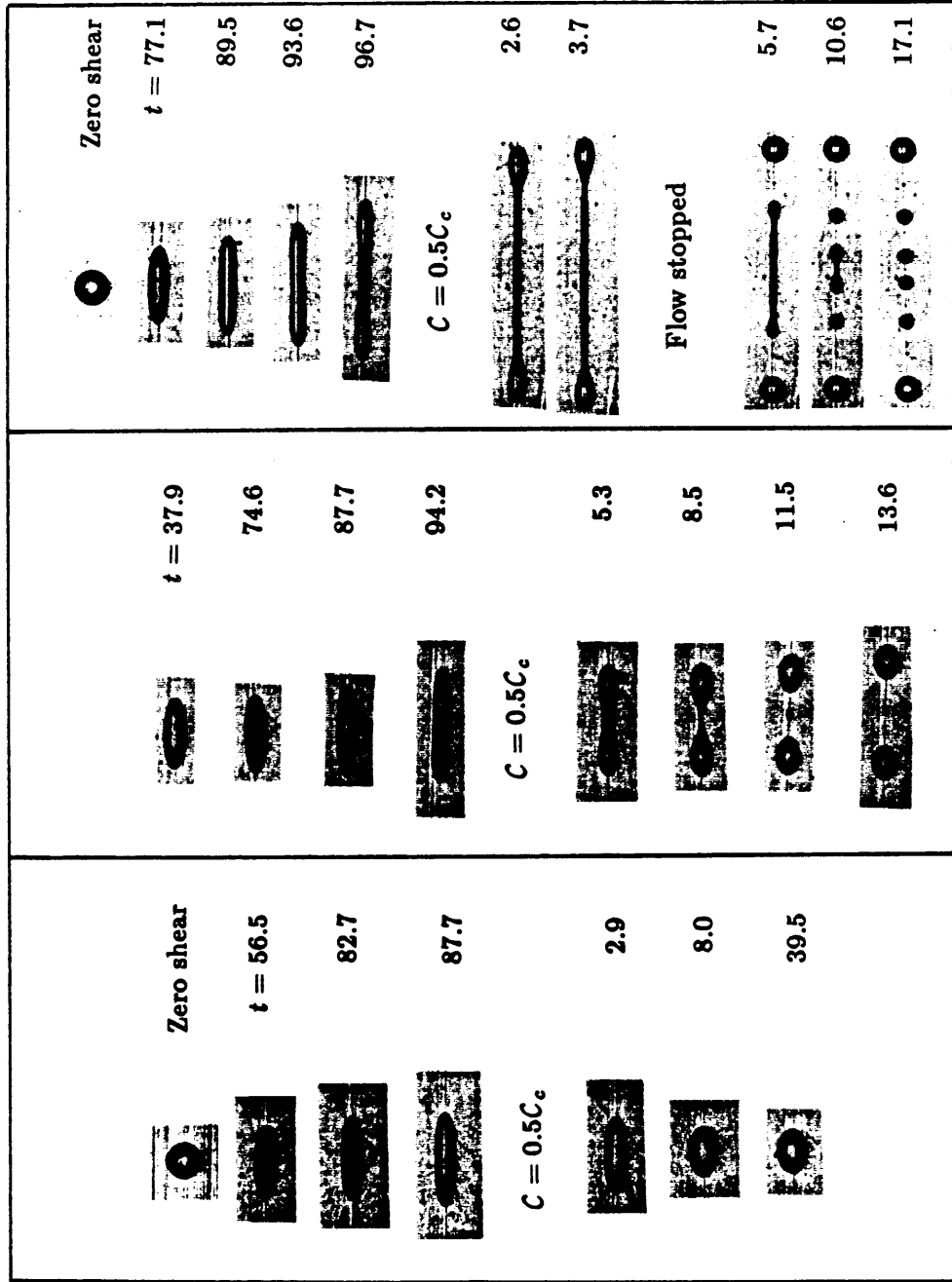
Figure 19 Numerical simulation of the effect of changes to subcritical capillary number for a given modestly deformed initial shape. $\lambda = 1.0$. D_{ss} refers to the steady shape established by beginning with a spherical initial shape and D_{trans} refers to the steady shape established in the subcritical flow by beginning with a highly stretched initial shape.

Figure 20 Numerical simulation of the effect of changes to subcritical capillary number for a given modestly deformed initial shape. $\lambda = 10.0$. D_{ss} refers to the steady shape established by beginning with a spherical initial shape and D_{trans} refers to the steady shape established in the subcritical flow by beginning with a highly stretched initial shape.

Figure 21 Breakup of a very viscous droplet beginning with a shape that exceeds

the maximum steady deformation. $\lambda = 19.0$, $\alpha = 0.2$. If the initial shape were spherical, no breakup would occur and the droplet would reach a limiting deformation shown by the first photograph.

$\lambda = 0.1$



(a)

(b)

(c)

Figure 1

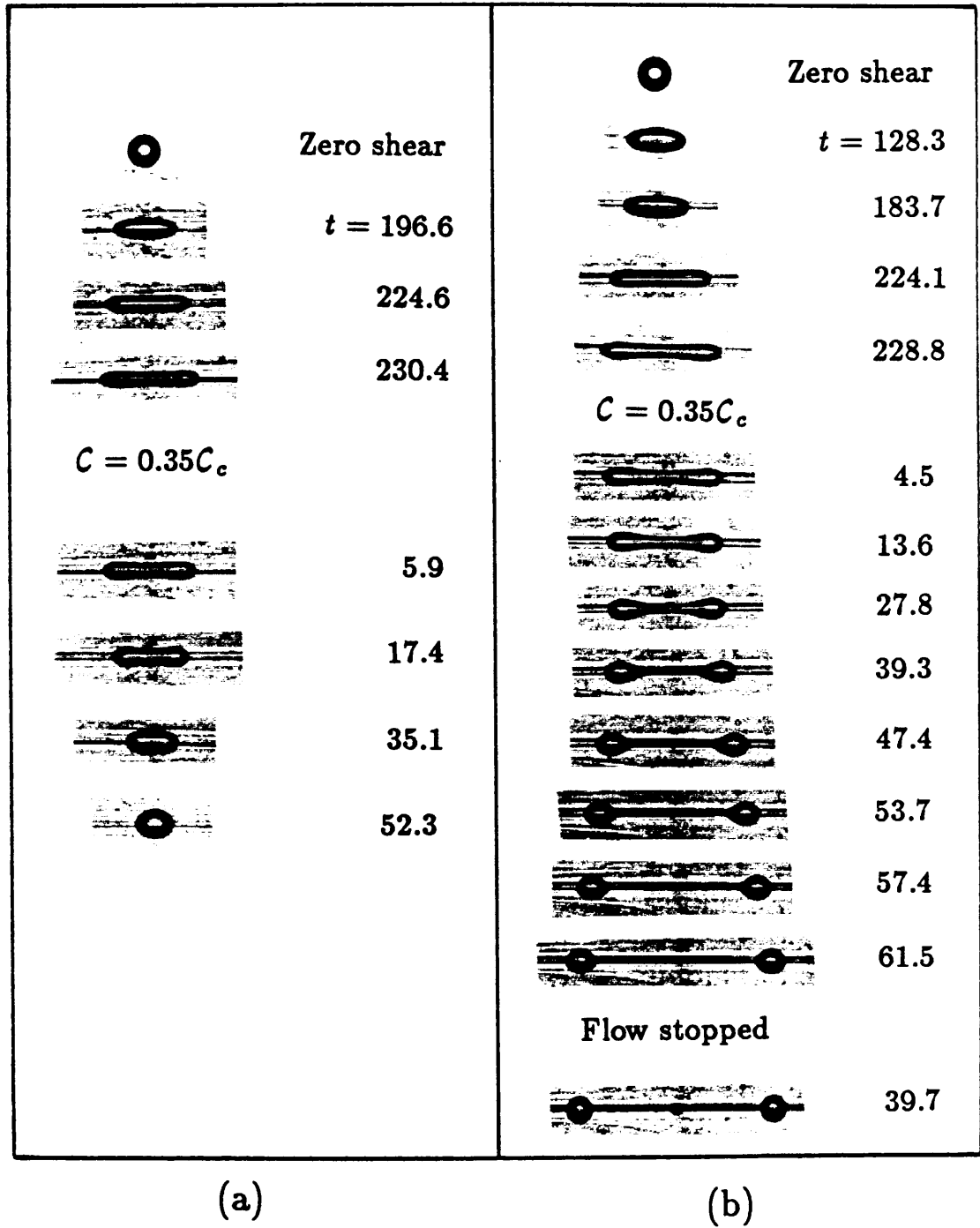
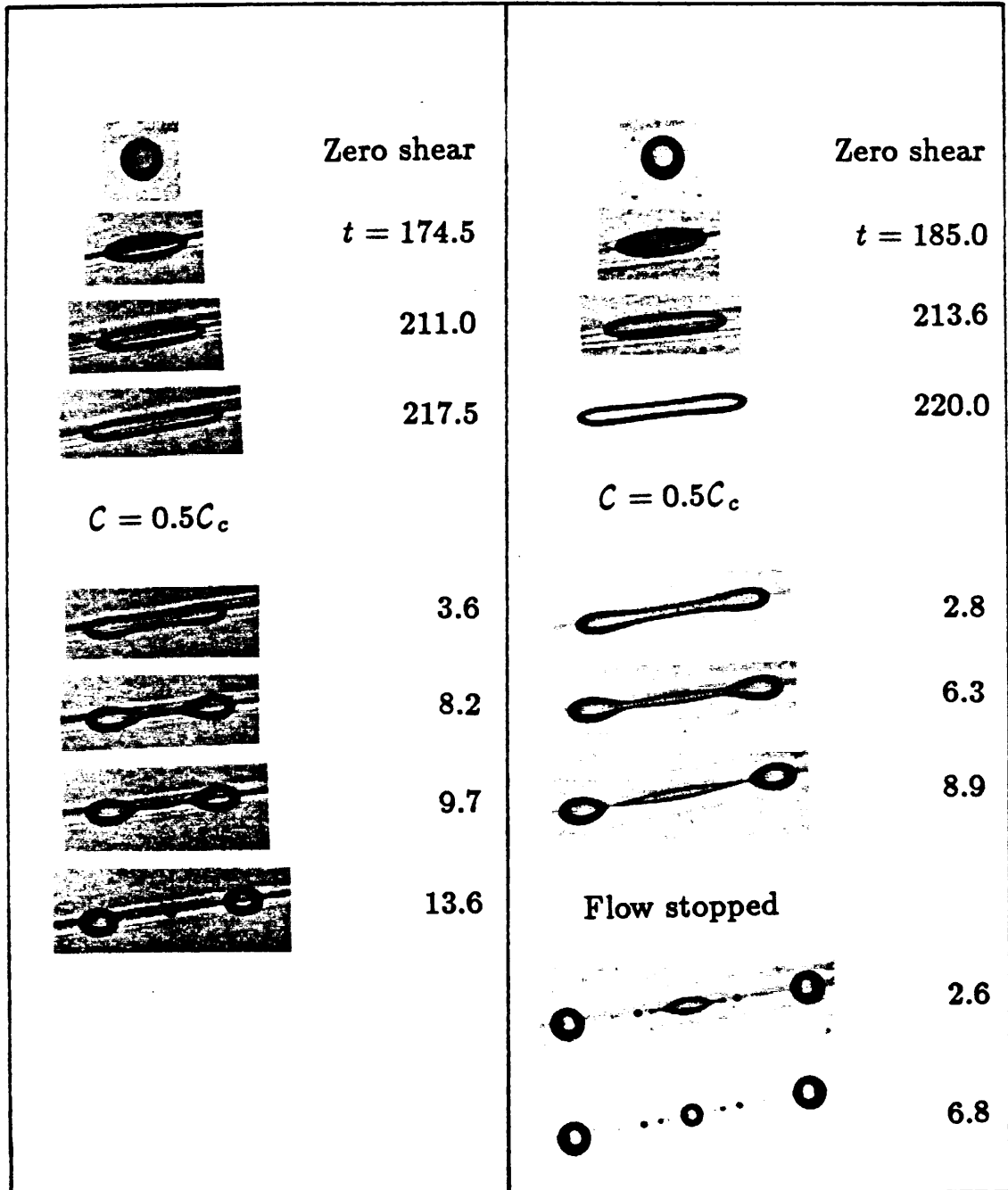


Figure 2

- 173 -
 $\lambda = 0.1$

$\alpha = 0.6$



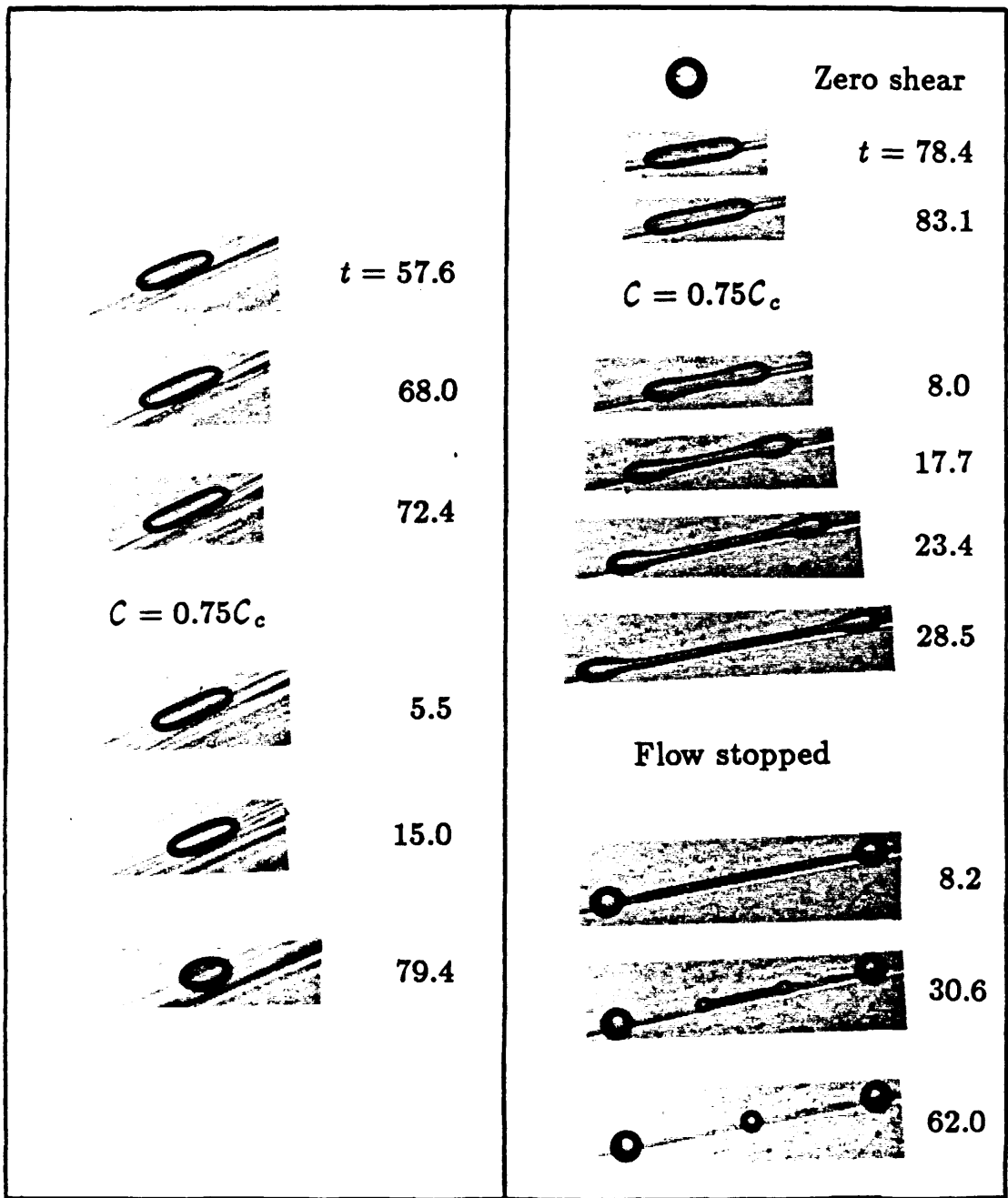
(a)

(b)

Figure 3

$\alpha = 0.2$

$\alpha = 0.6$



(a)

(b)

Figure 4

- 175 -
 $\lambda = 5.3$

$\alpha = 0.4$

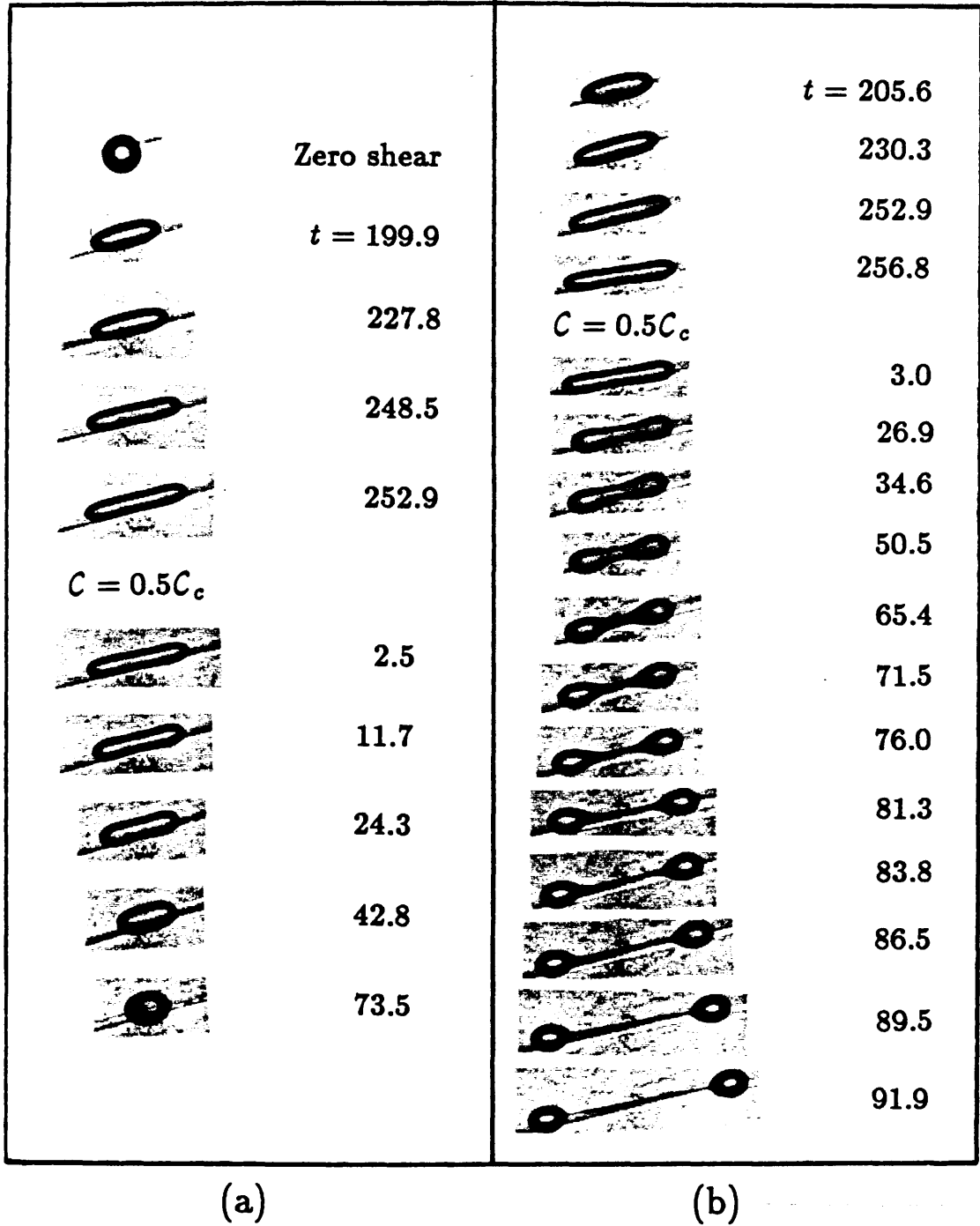


Figure 5

- 176 -

$\lambda = 0.1$

$\alpha = 1.0$

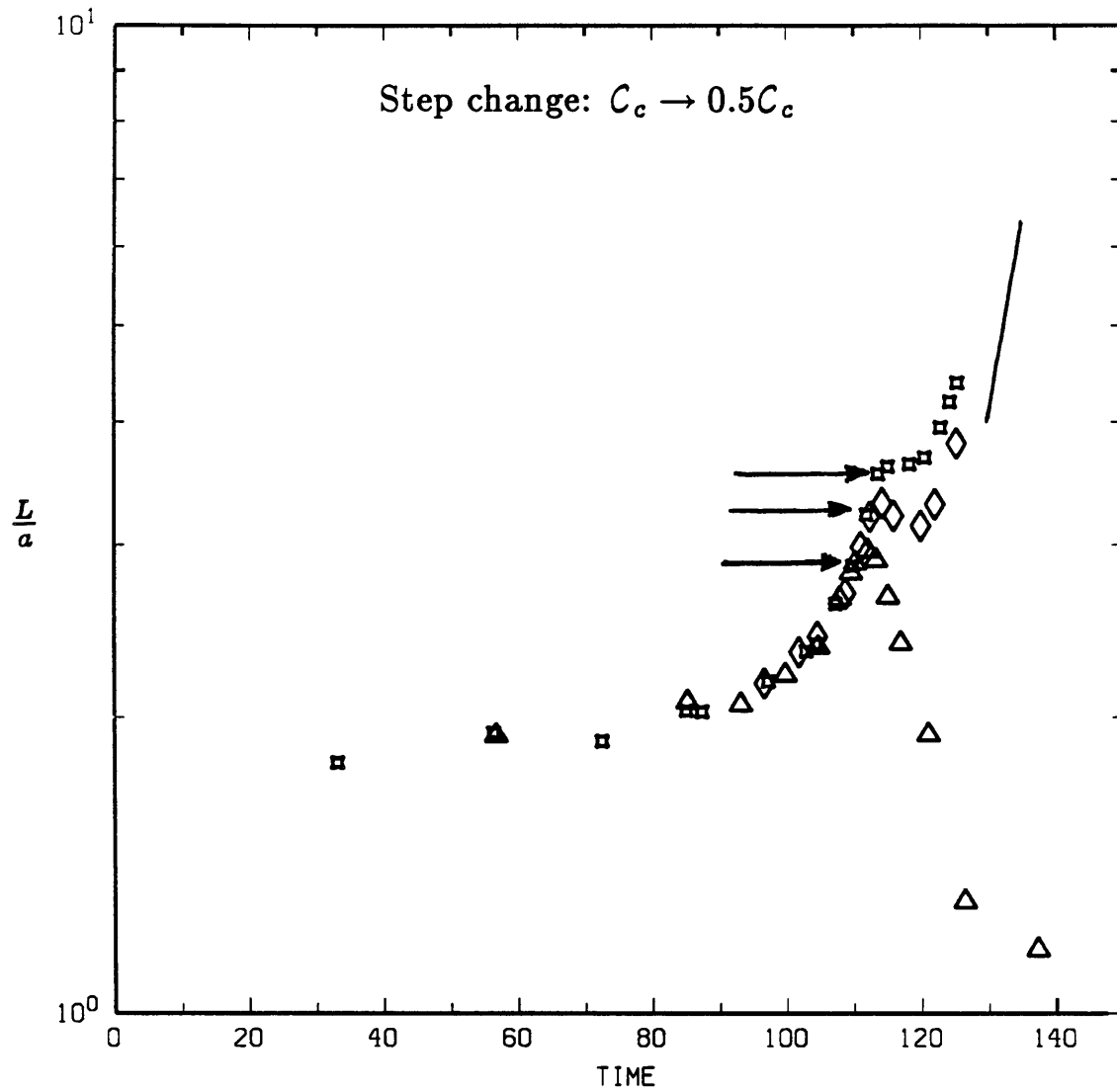


Figure 6a

- 177 -

$\lambda = 0.46$

$\alpha = 1.0$

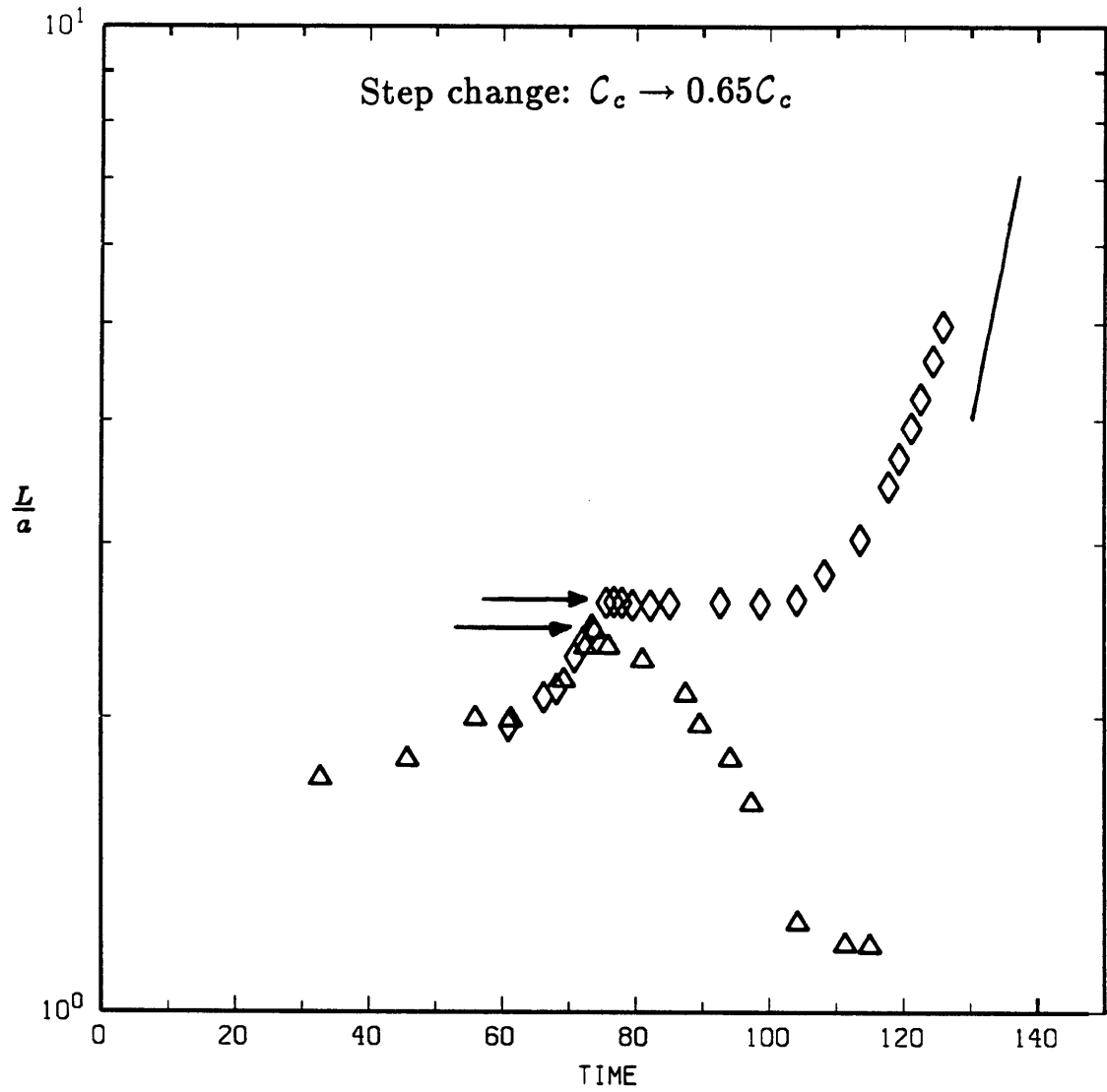


Figure 6b

$$\lambda = 5.3$$

$$\alpha = 1.0$$

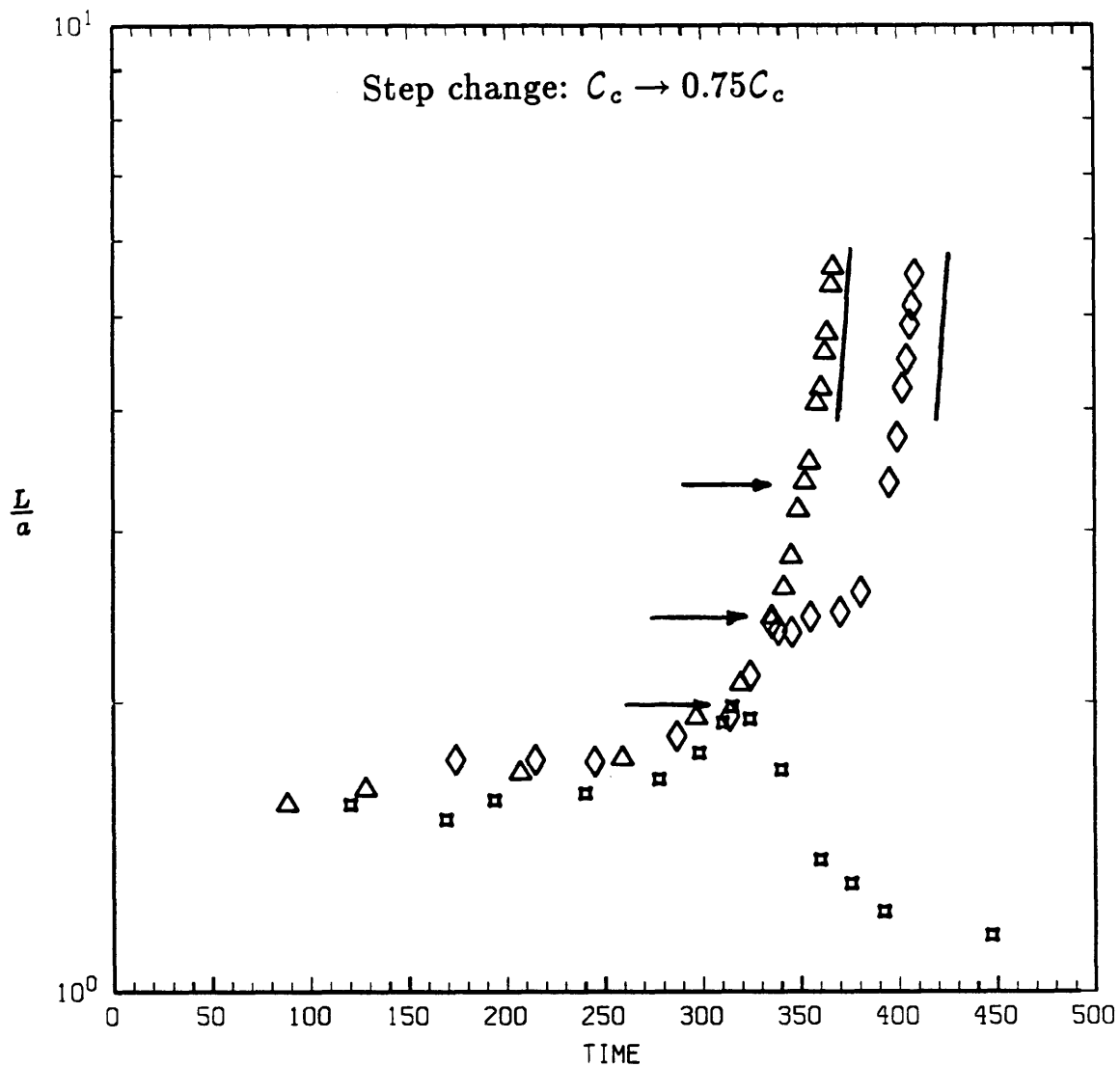


Figure 6c

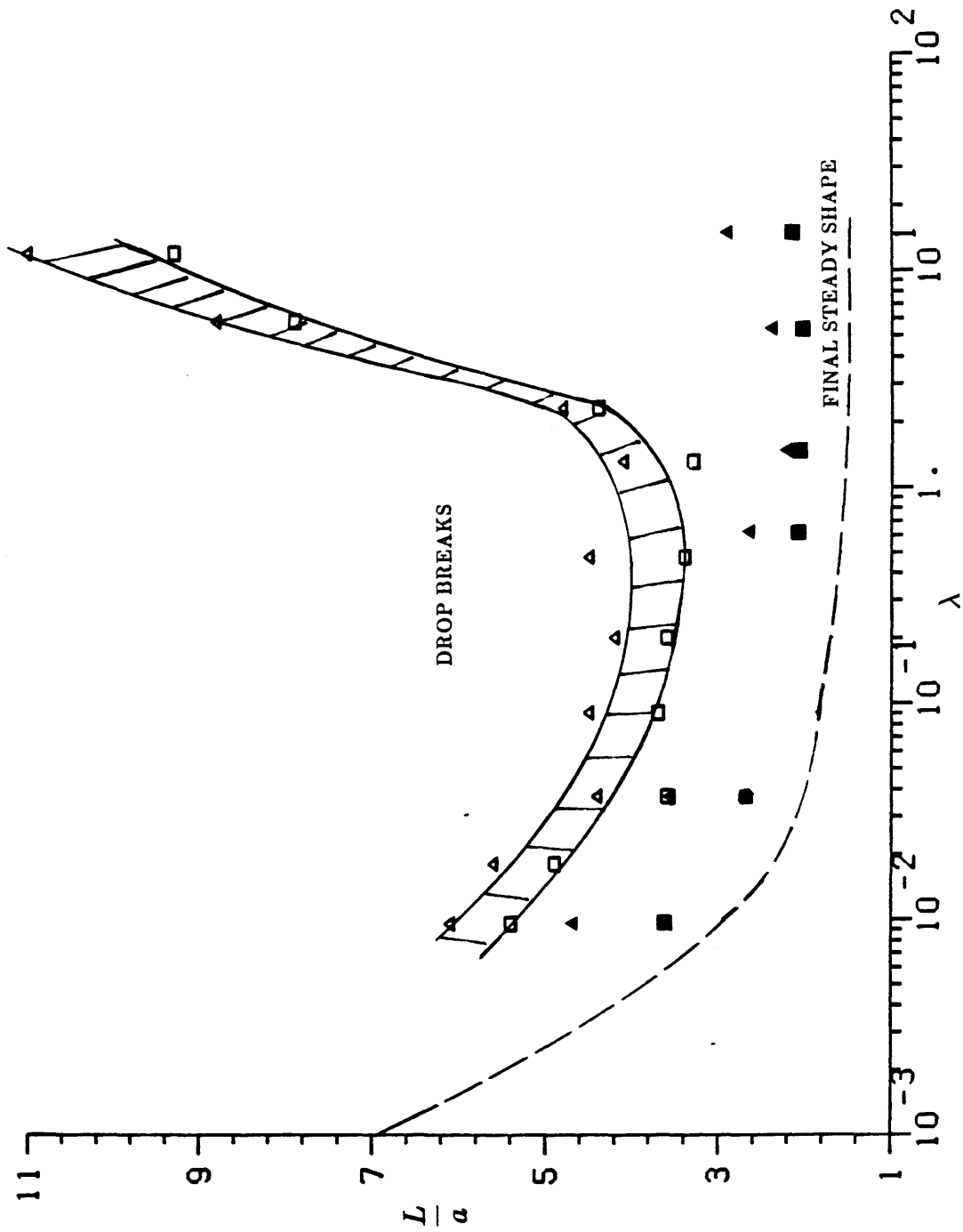
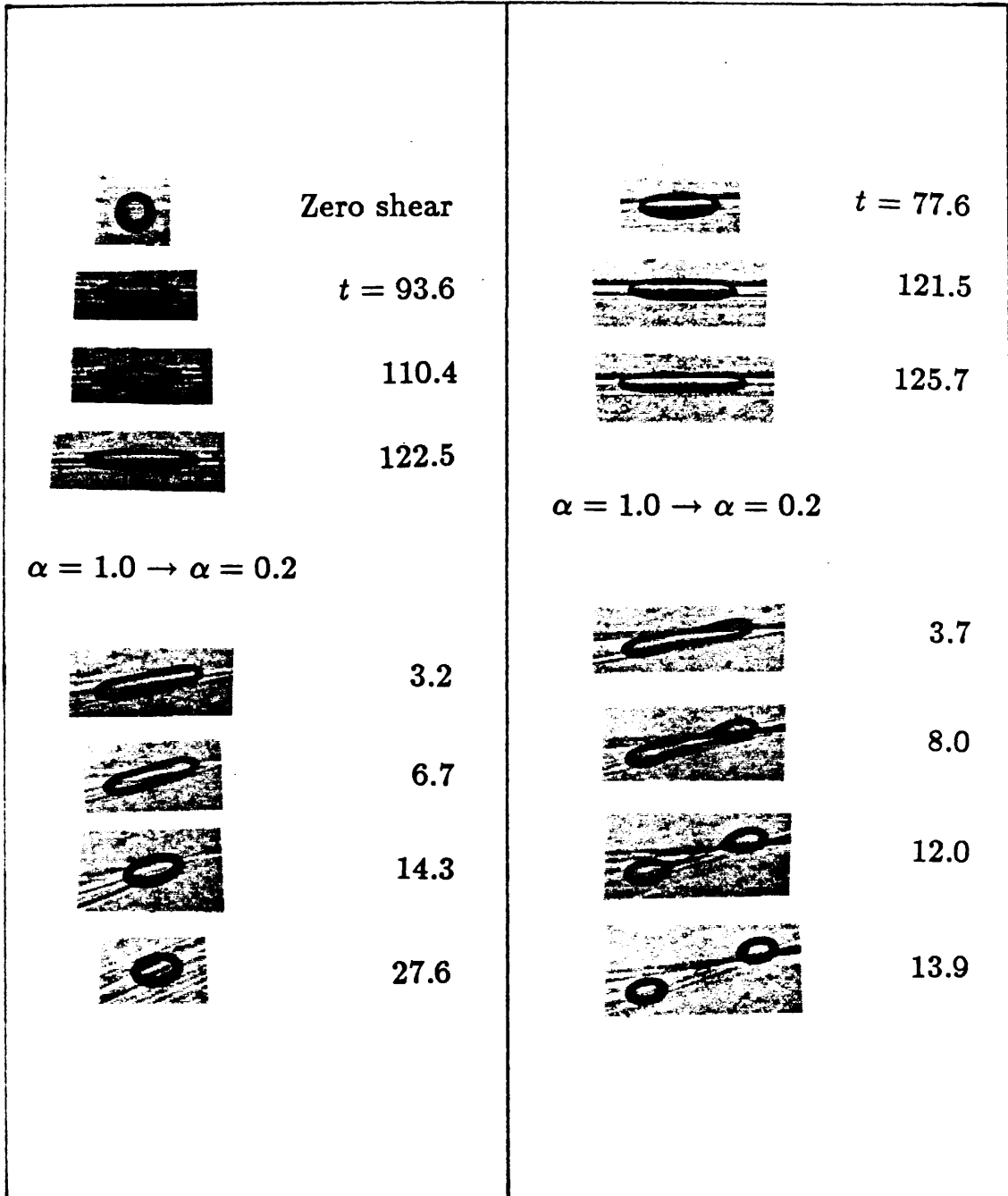


Figure 7

$$\lambda = 0.1$$

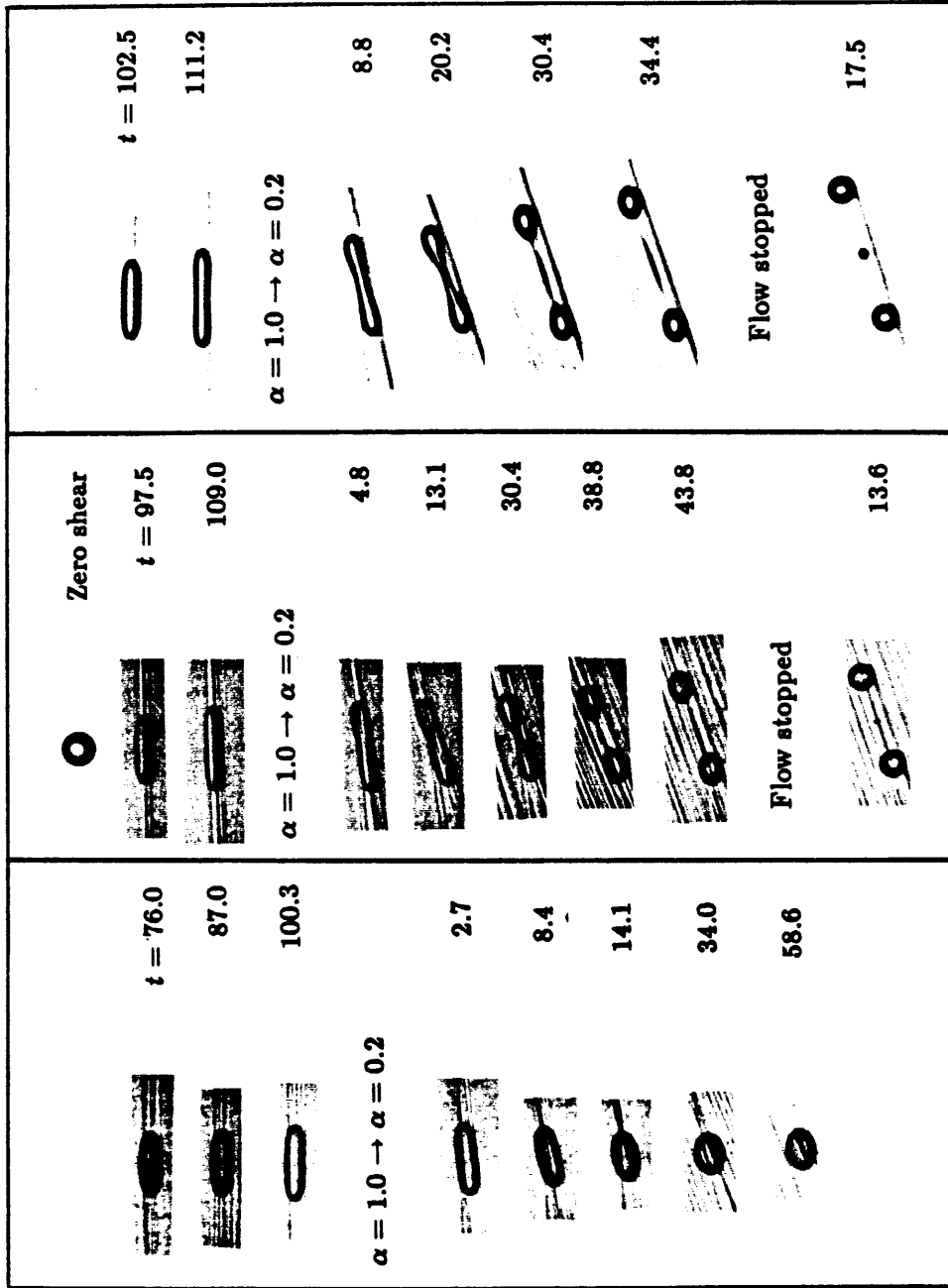


(a)

(b)

Figure 8

$\lambda = 1.3$



(a)

(b)

(c)

Figure 9

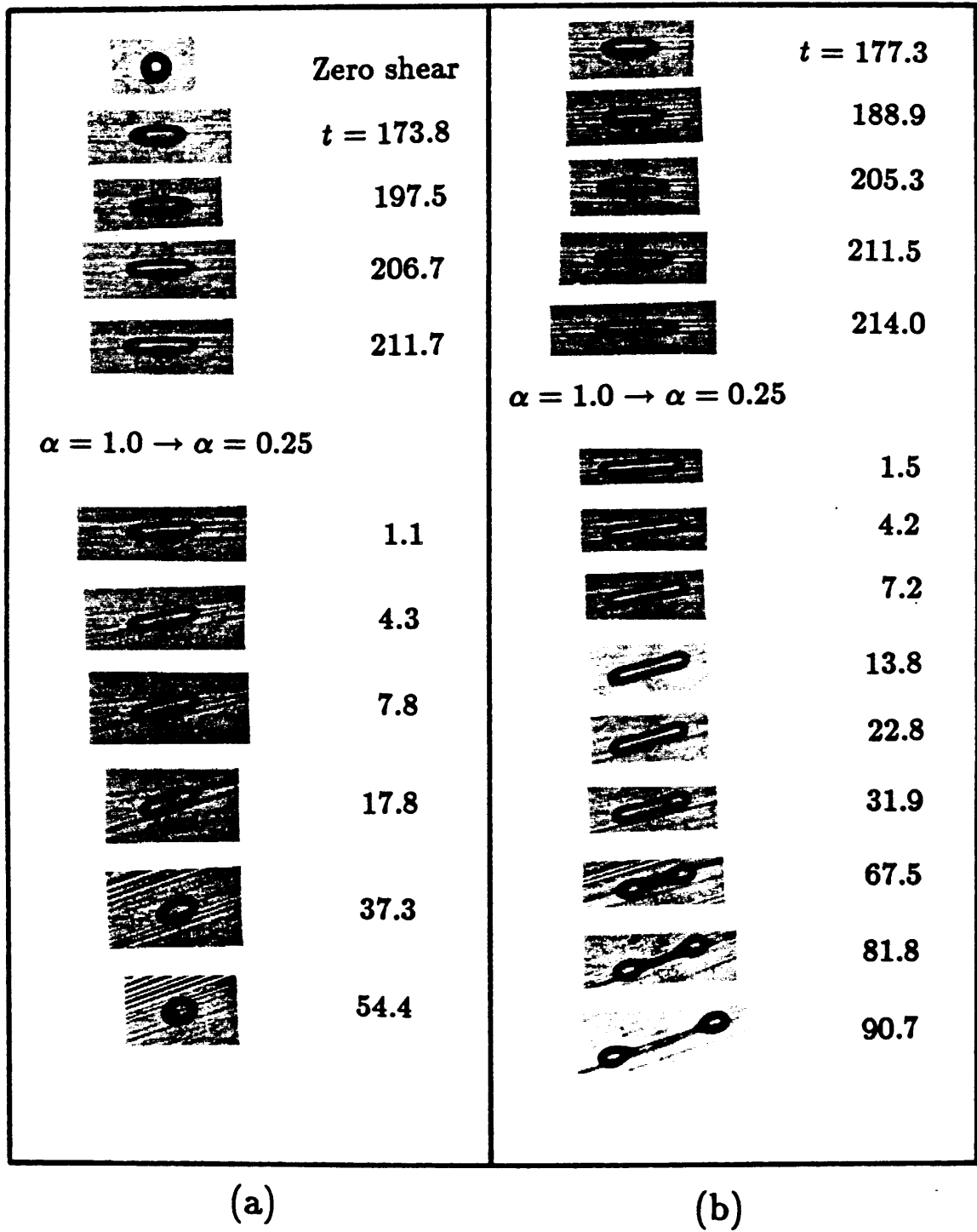
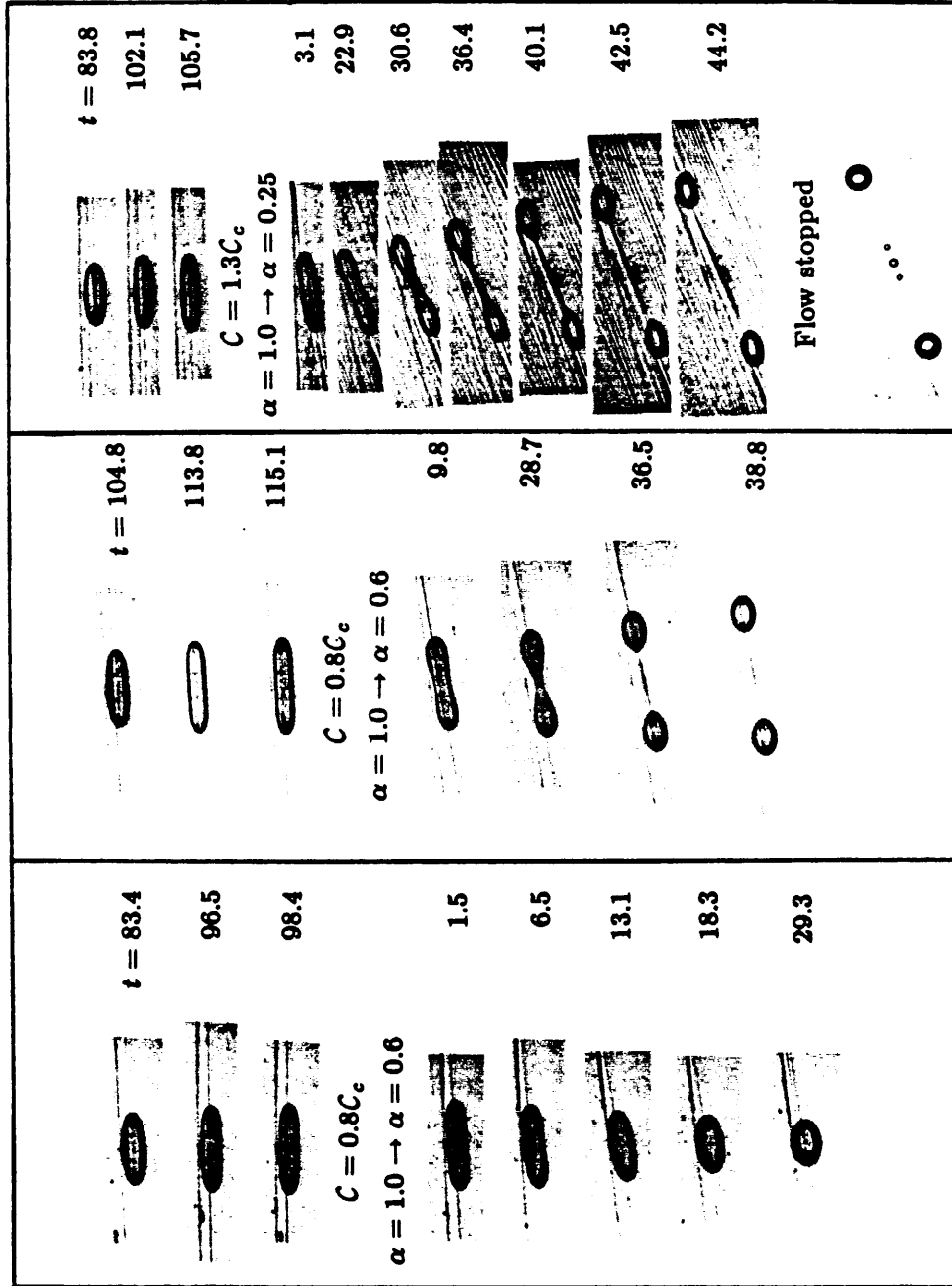


Figure 10

$\lambda = 0.46$



(a) (b) (c)

Figure 11

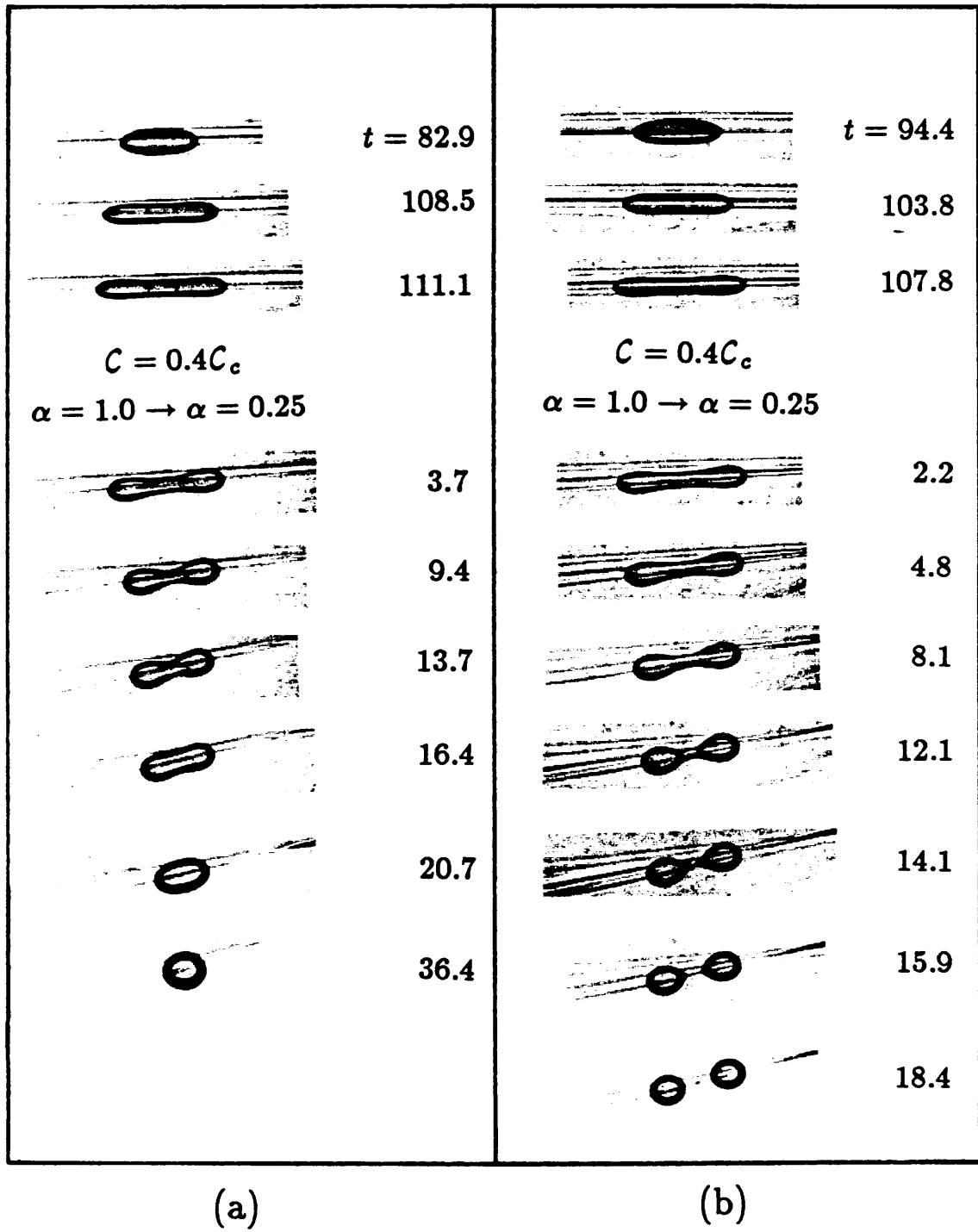


Figure 12

$\lambda = 1.0$

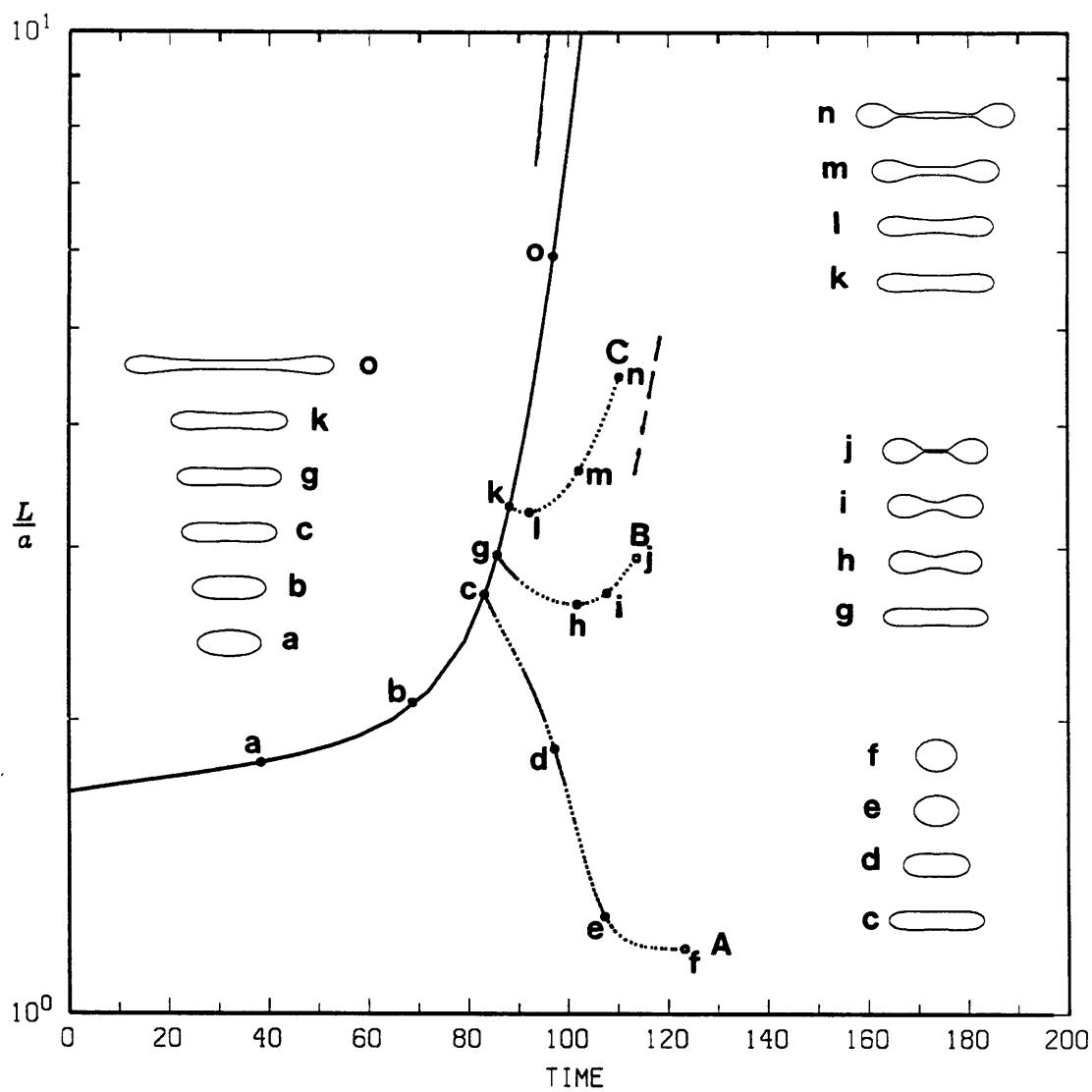


Figure 13

$\lambda = 10.0$

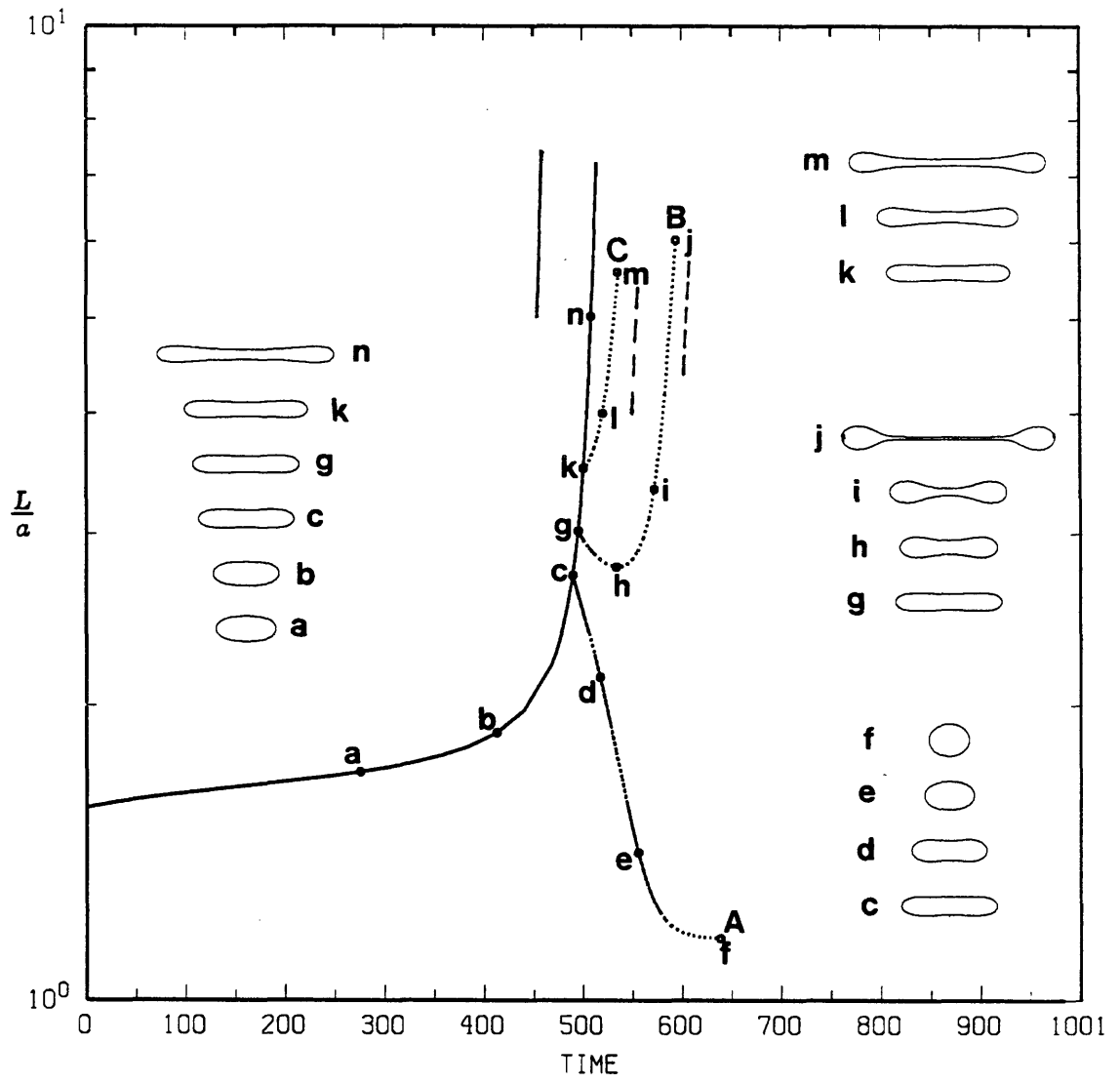
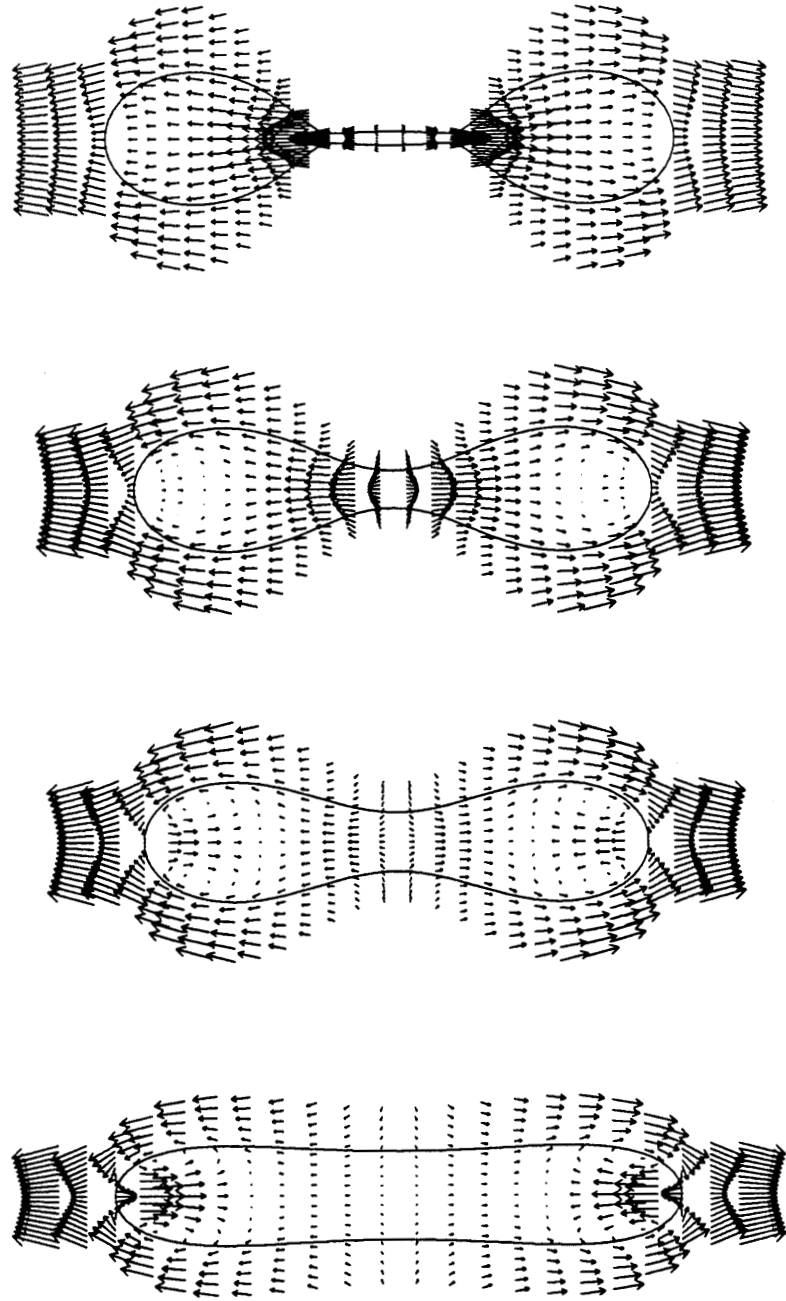
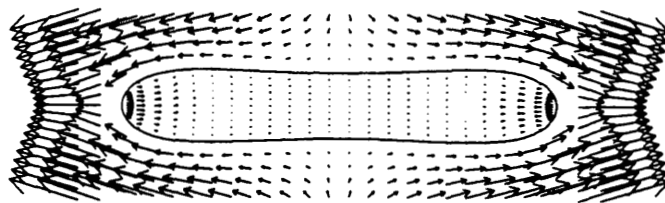
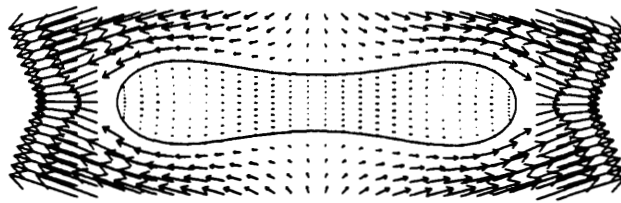
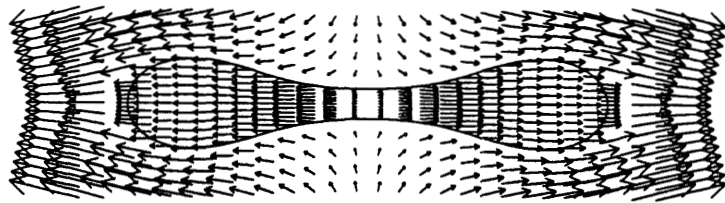
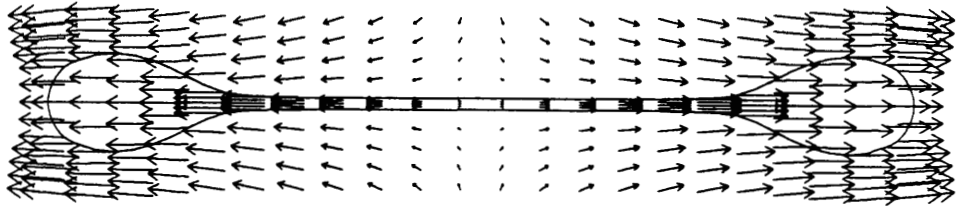


Figure 14



$\lambda = 1.0$

Figure 15



$\lambda = 10.0$

Figure 16

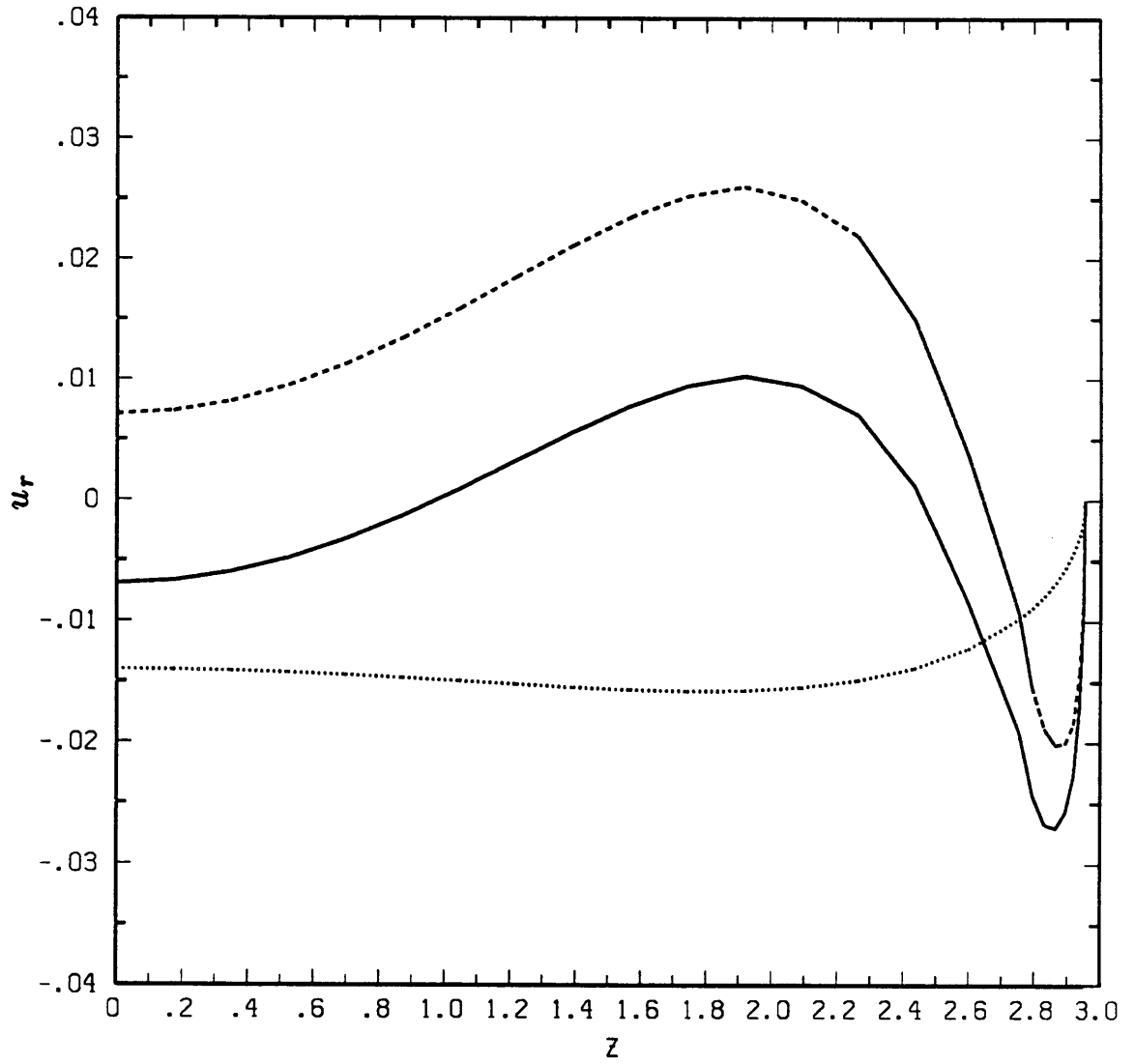


Figure 17a

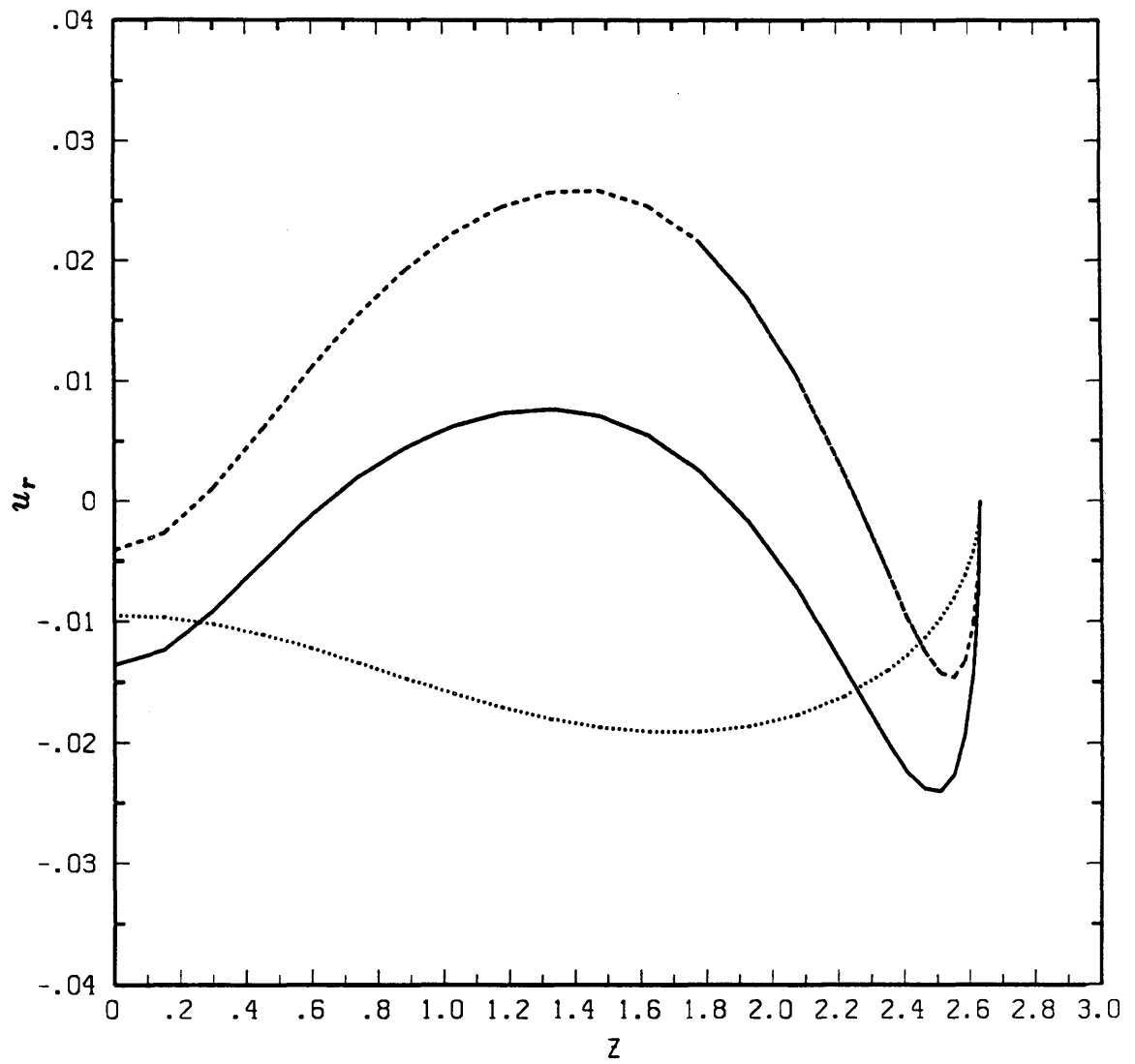


Figure 17b

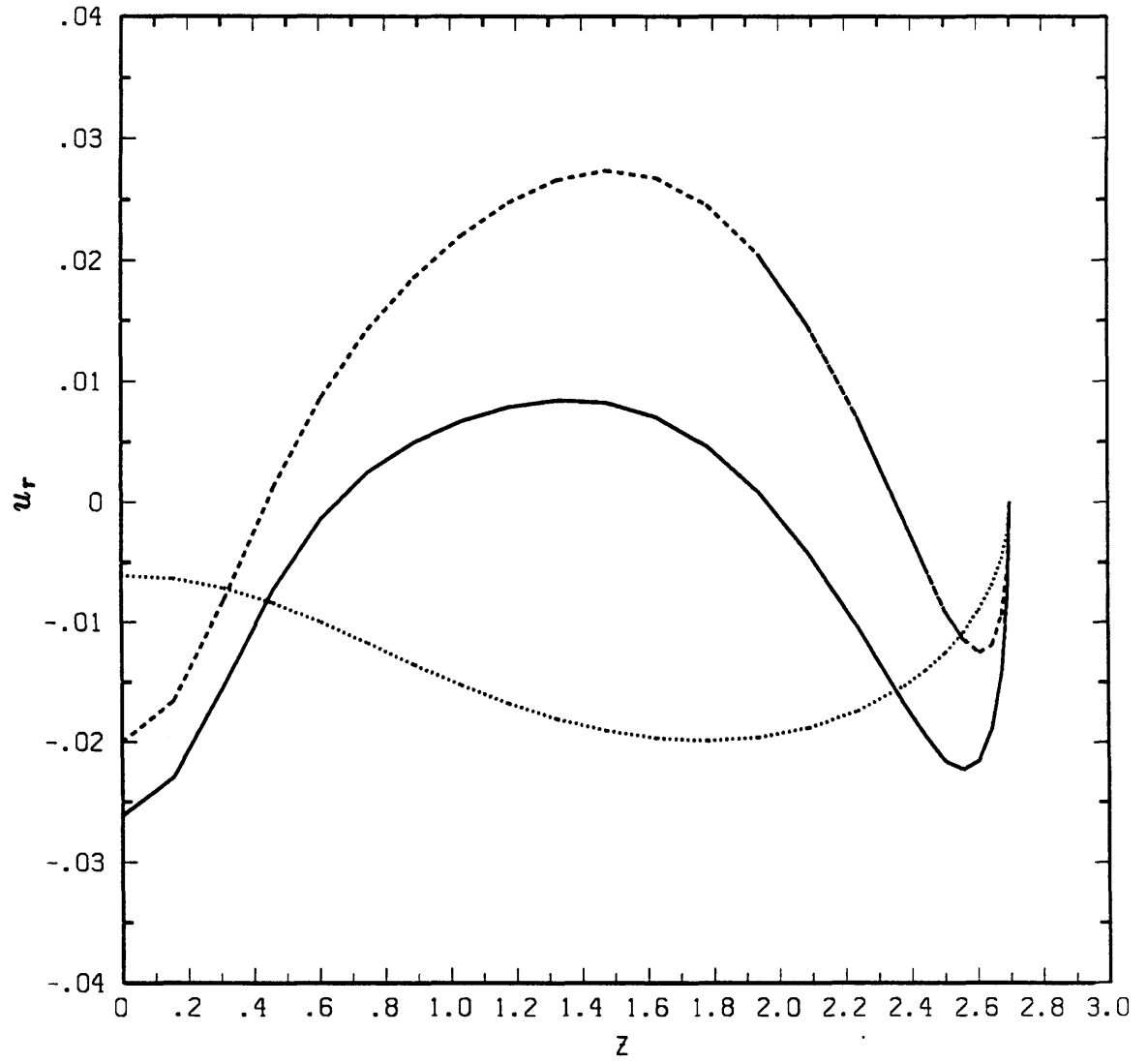


Figure 17c

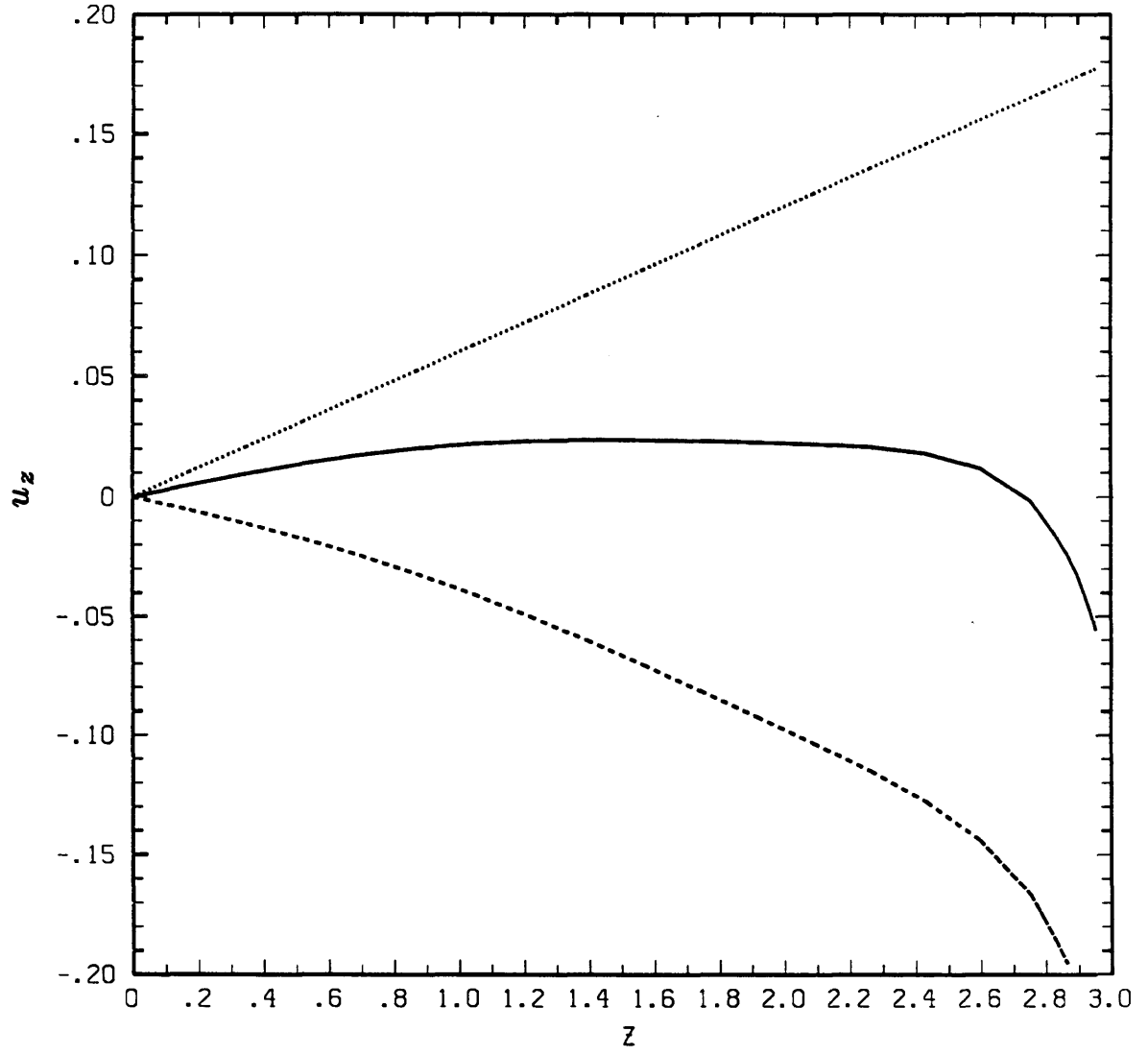


Figure 17d

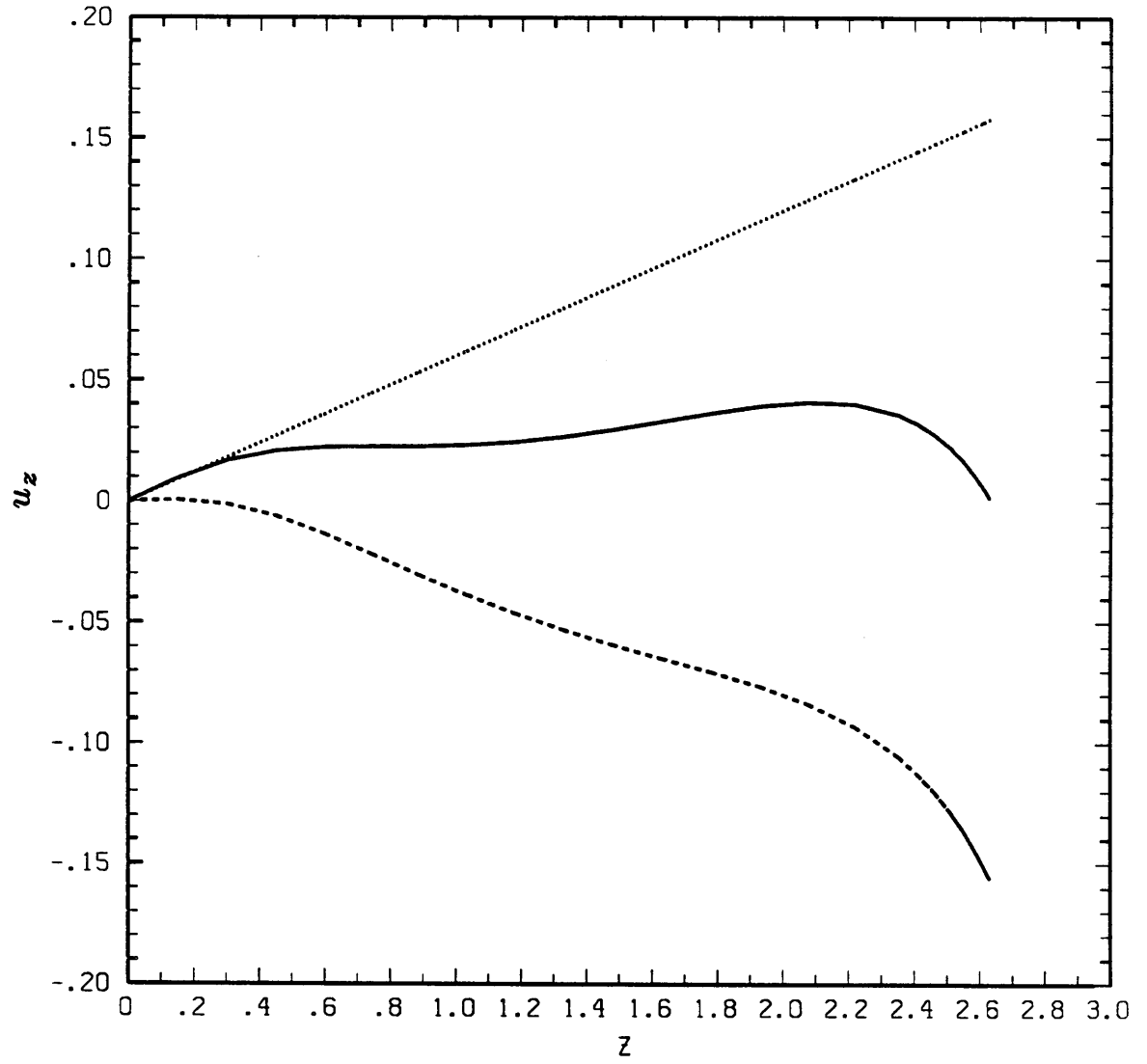


Figure 17e

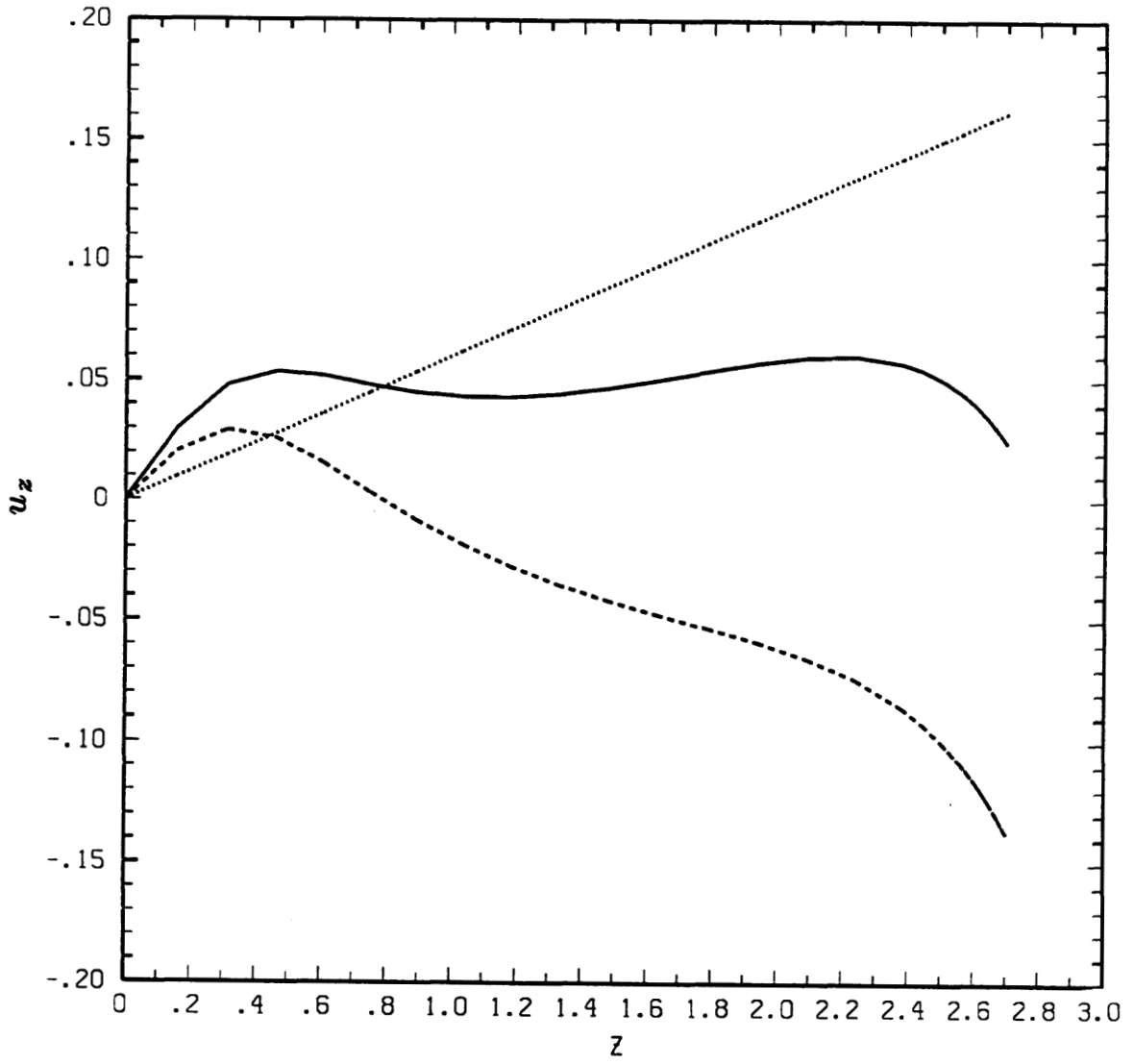


Figure 17f

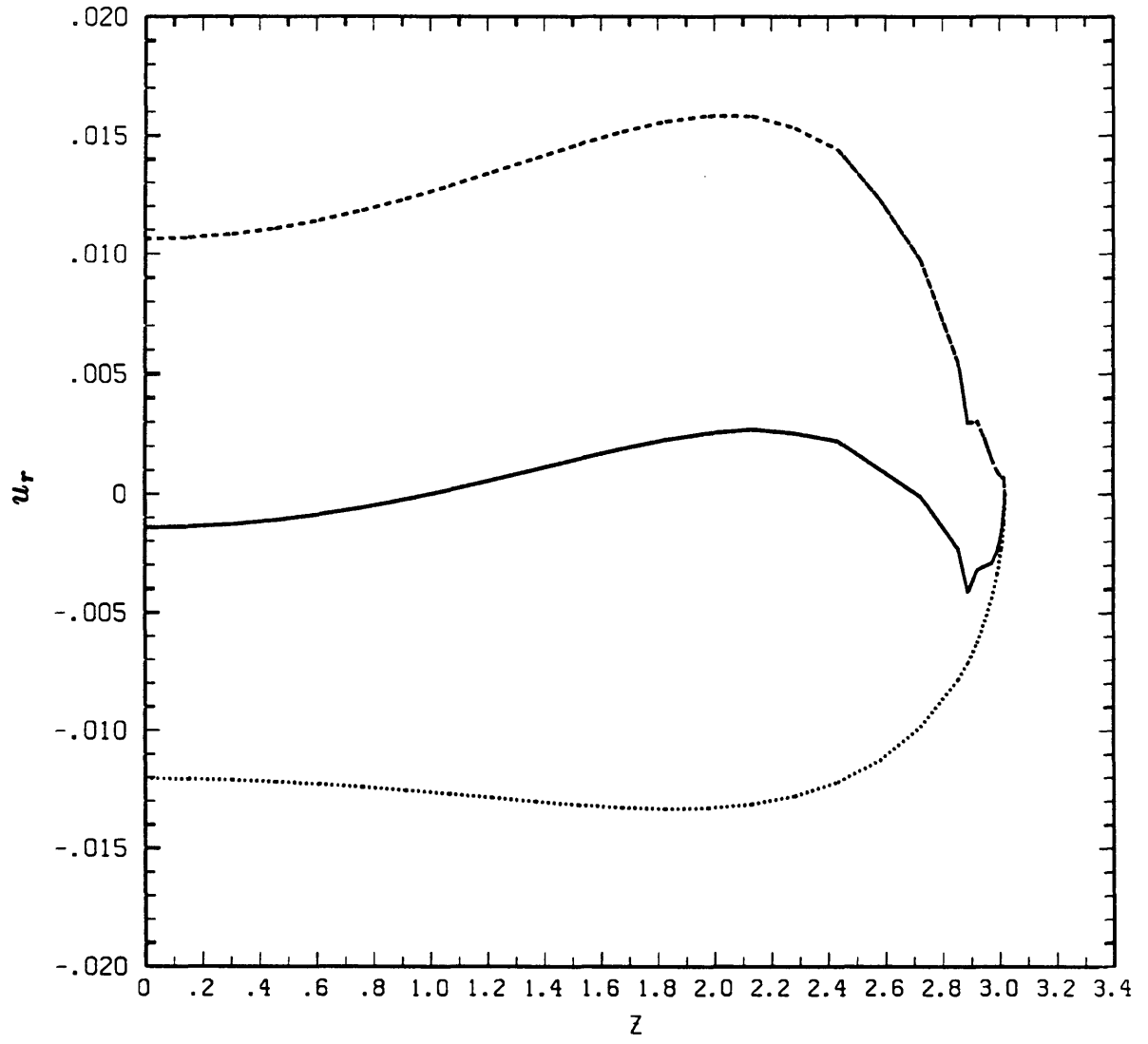


Figure 18a

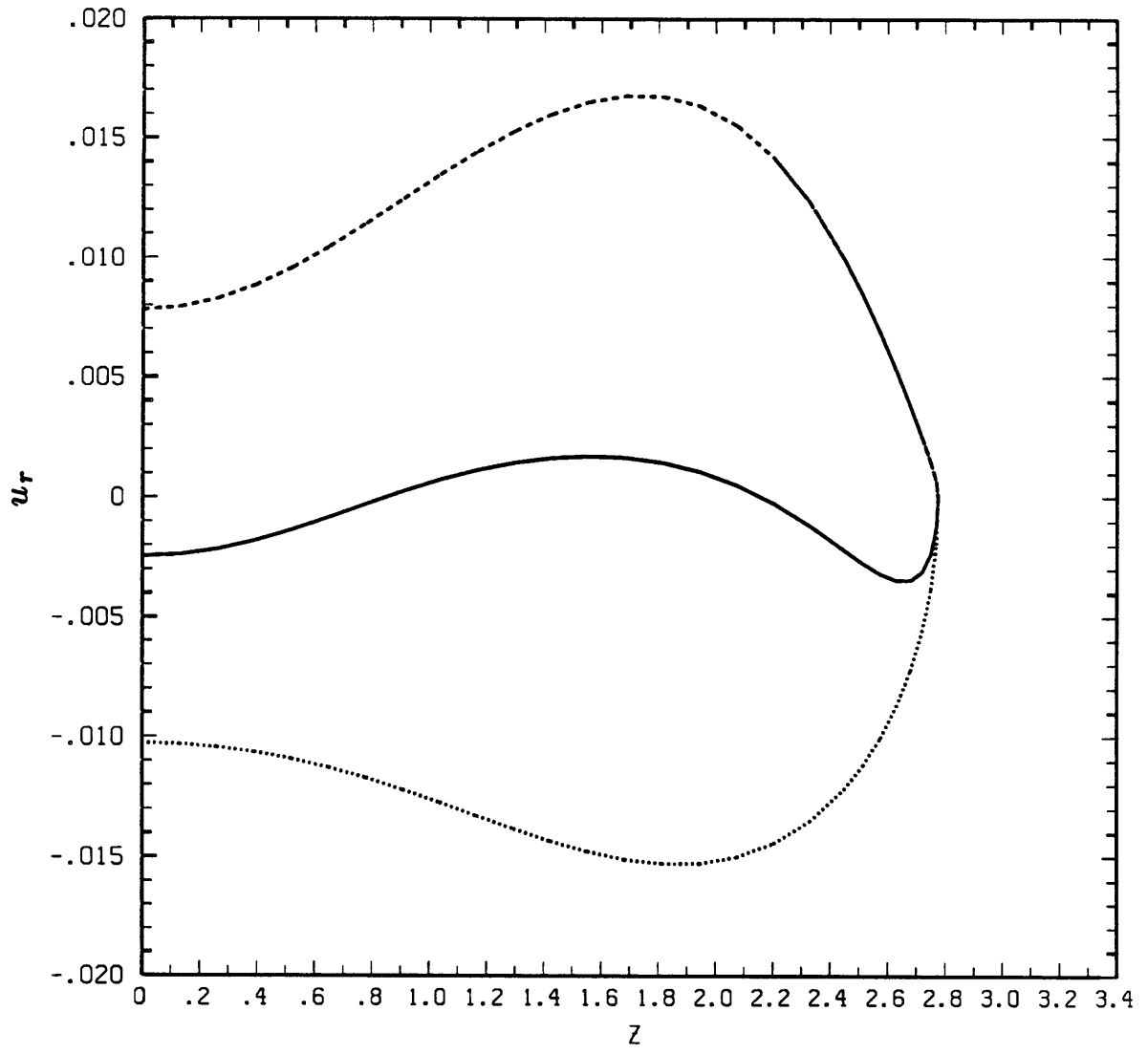


Figure 18b

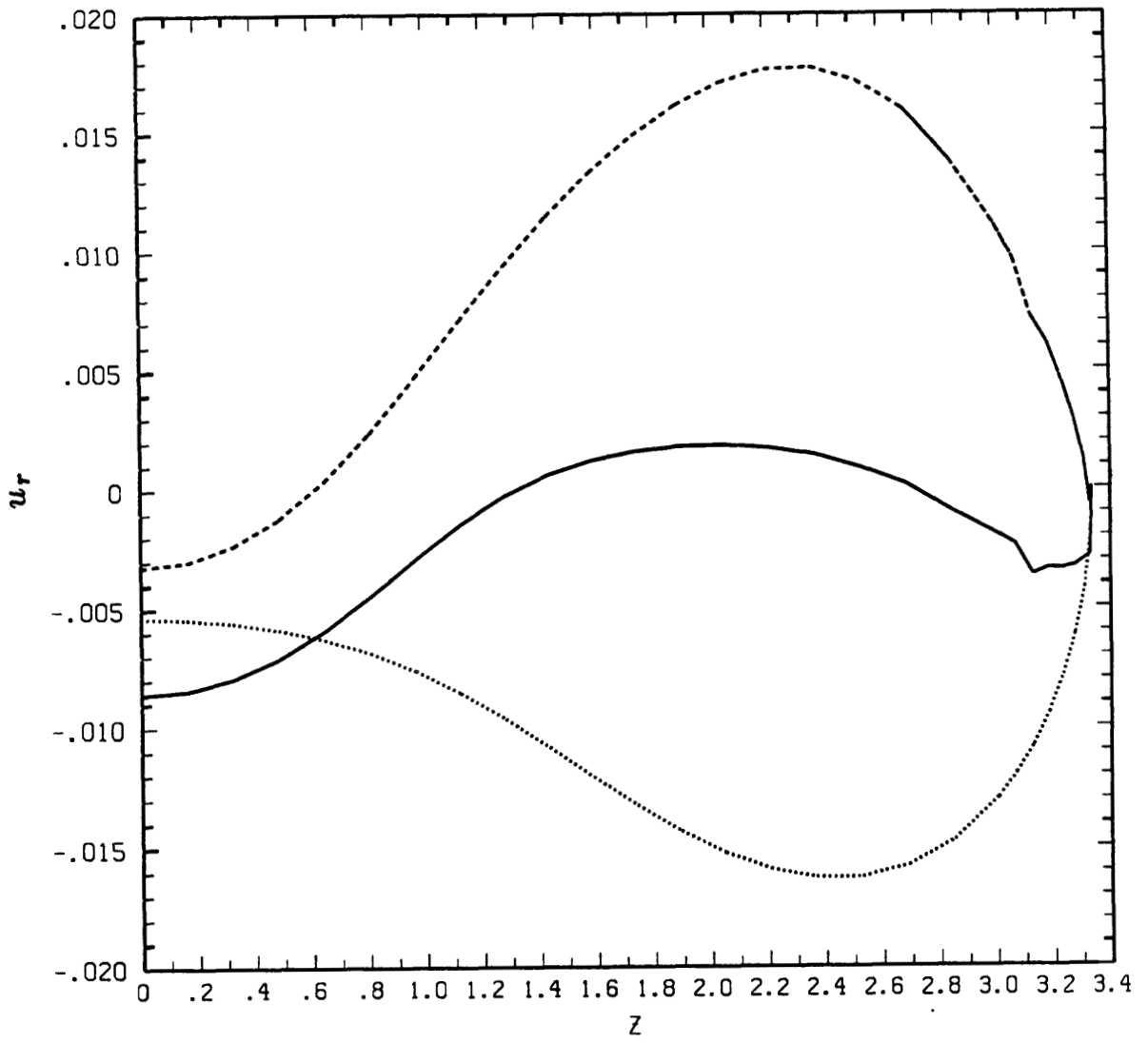


Figure 18c

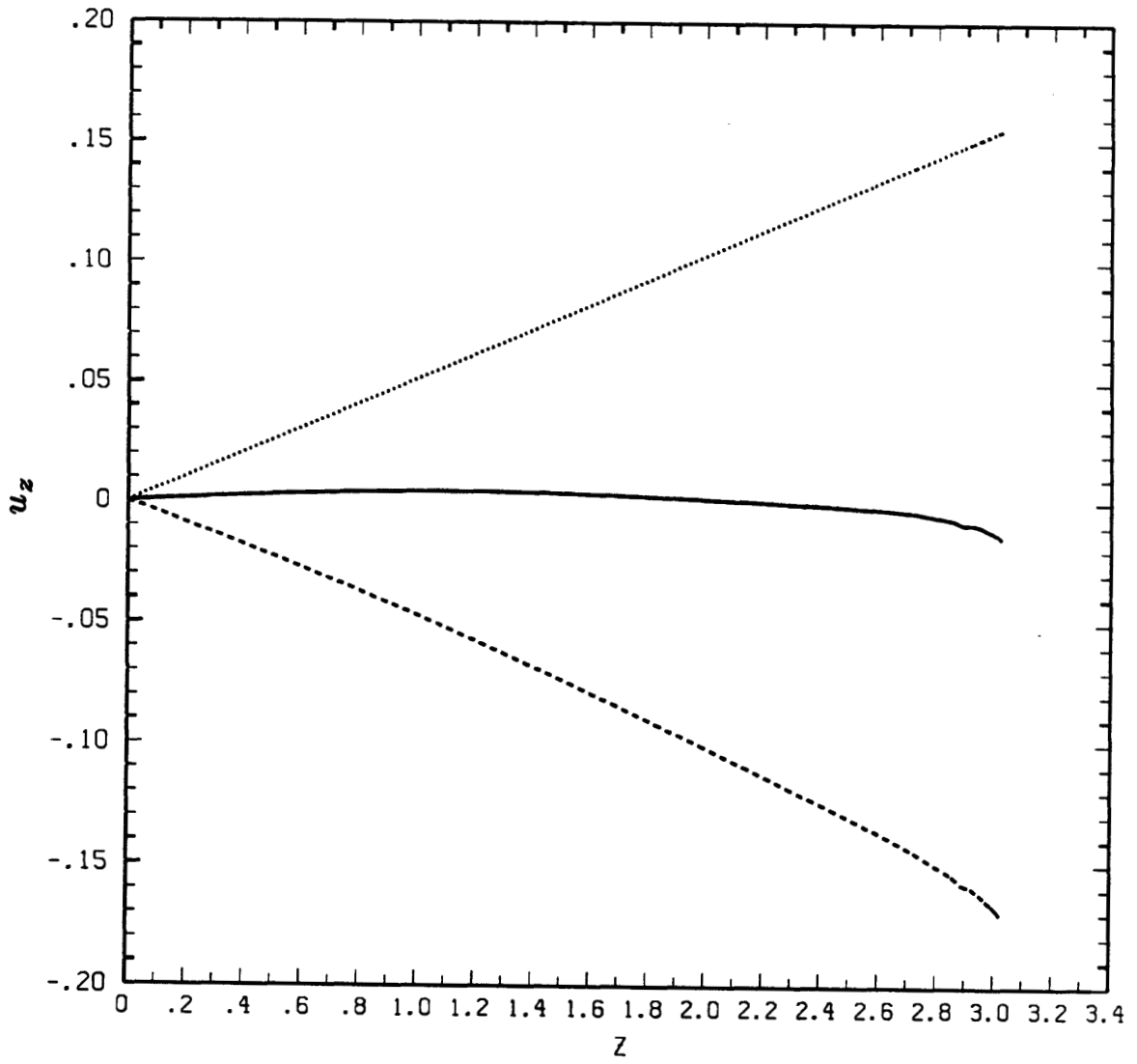


Figure 18d

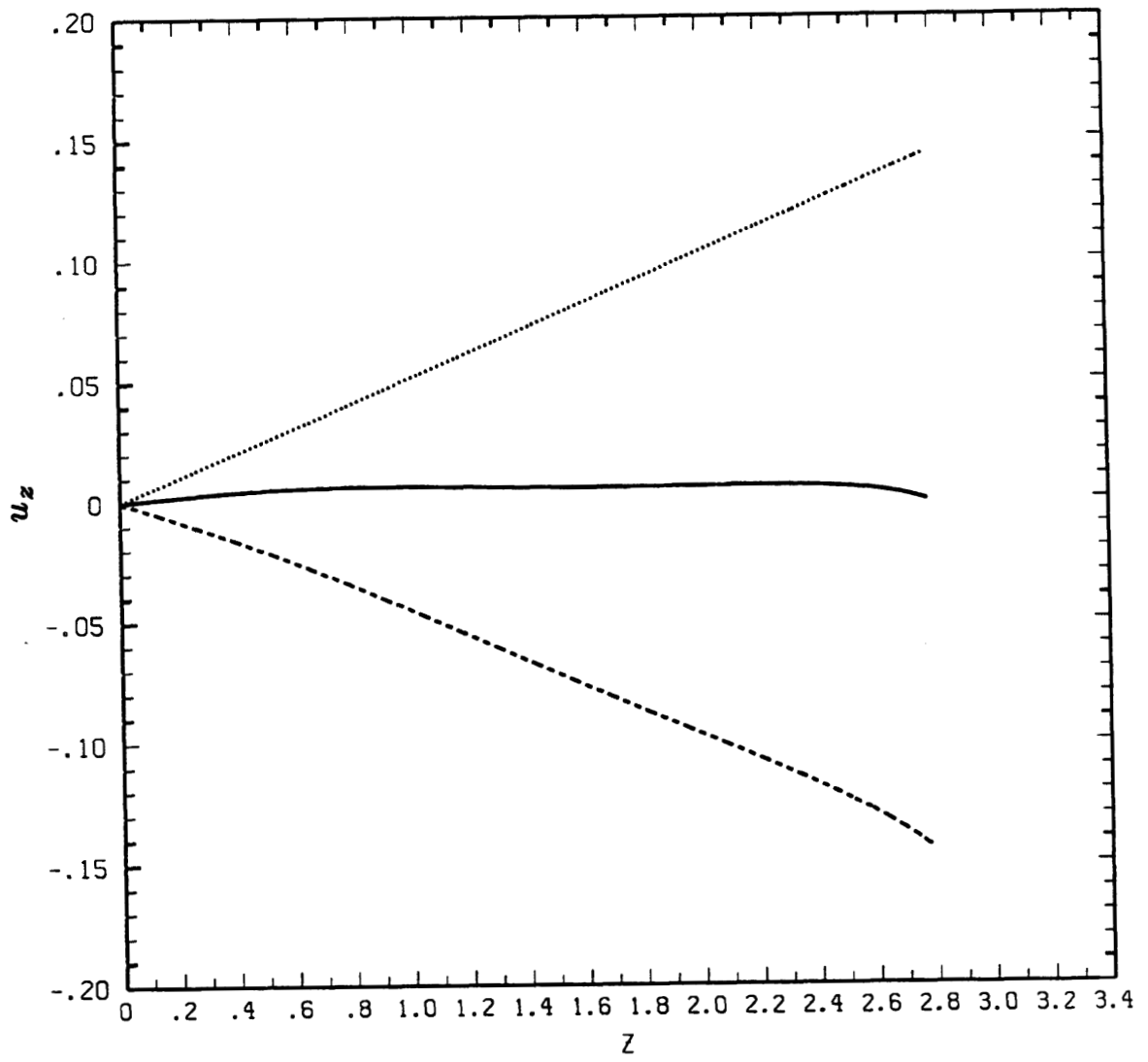


Figure 18e

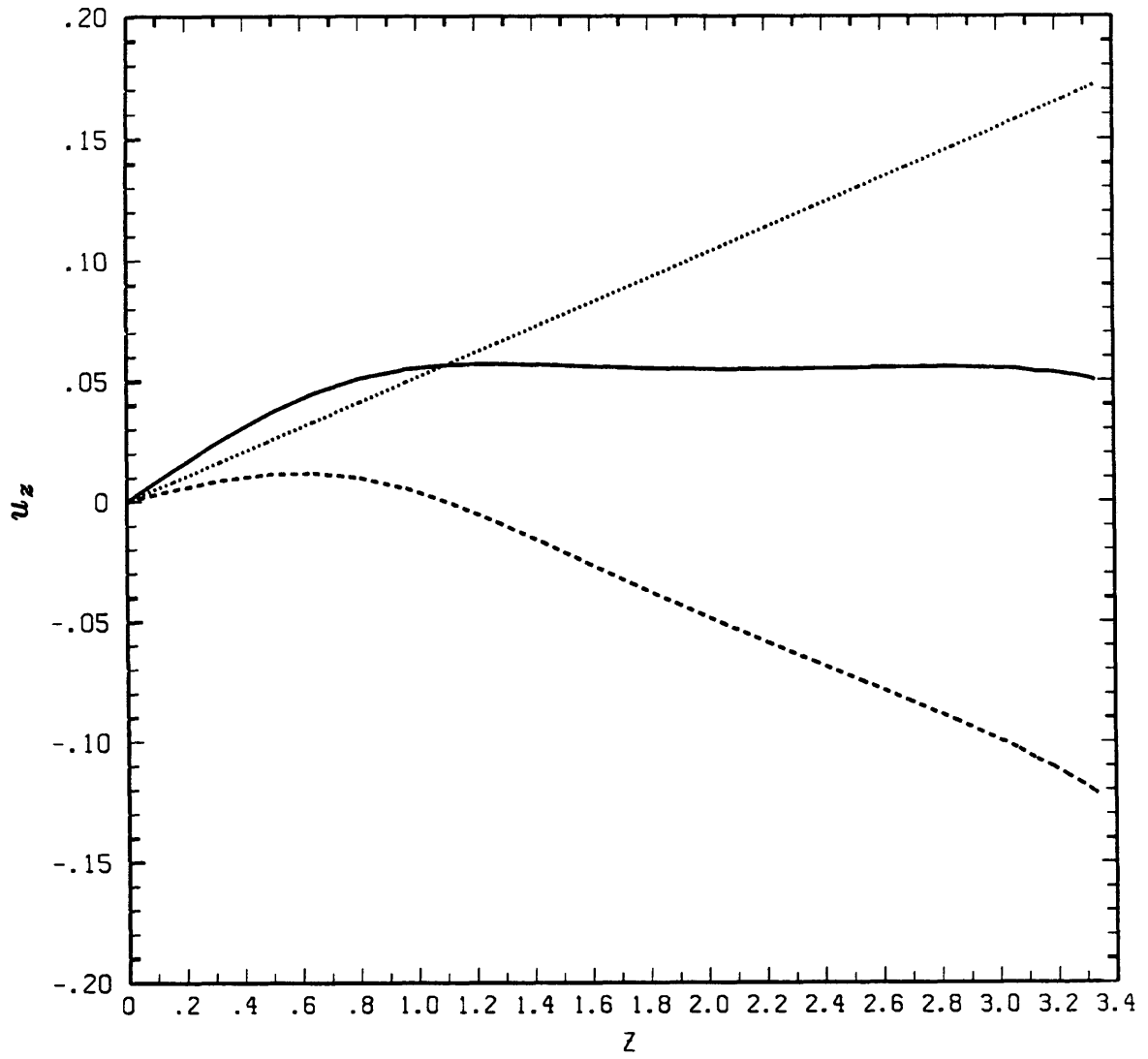


Figure 18f

$\lambda = 1.0$

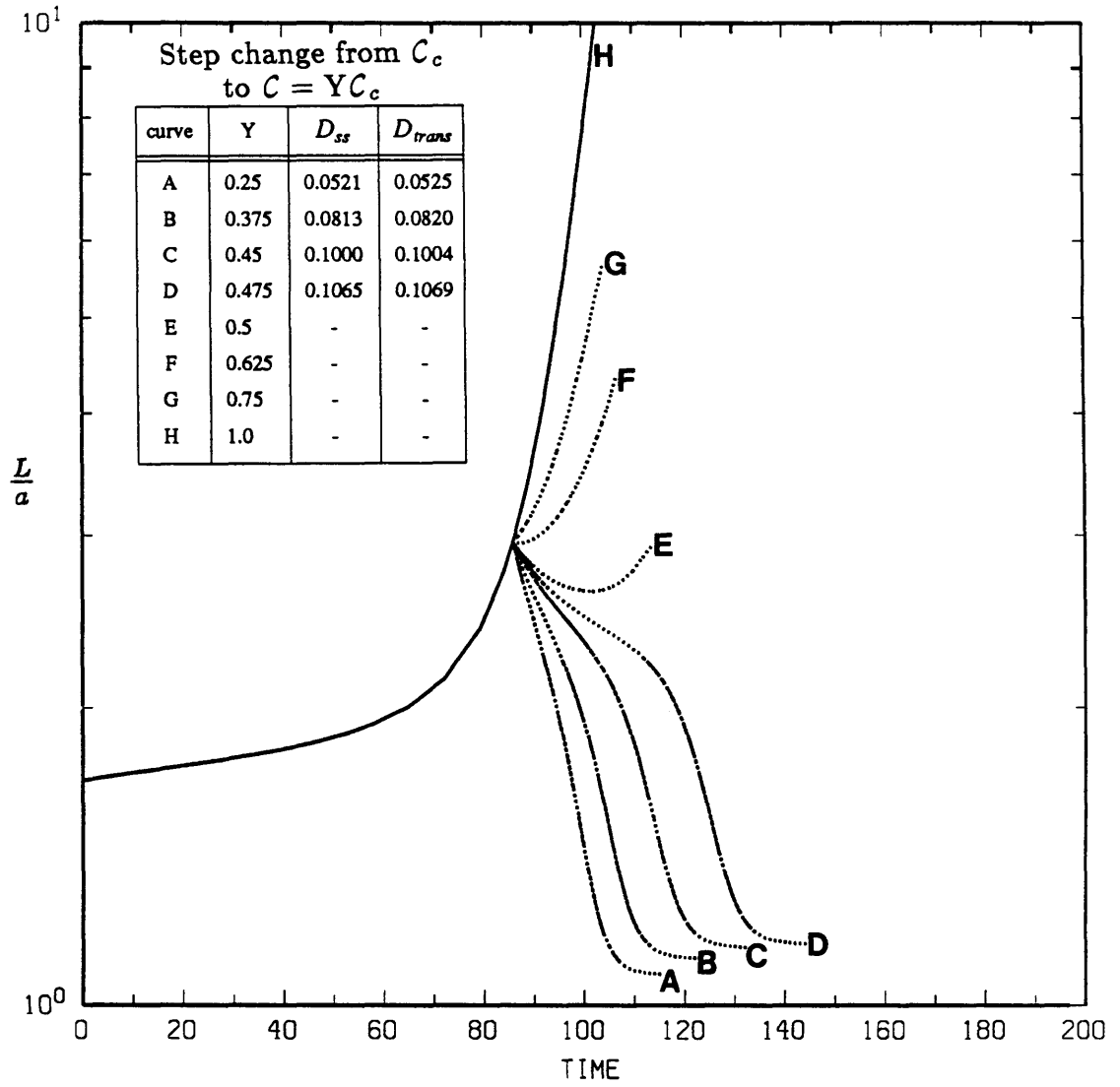


Figure 19

$\lambda = 10.0$

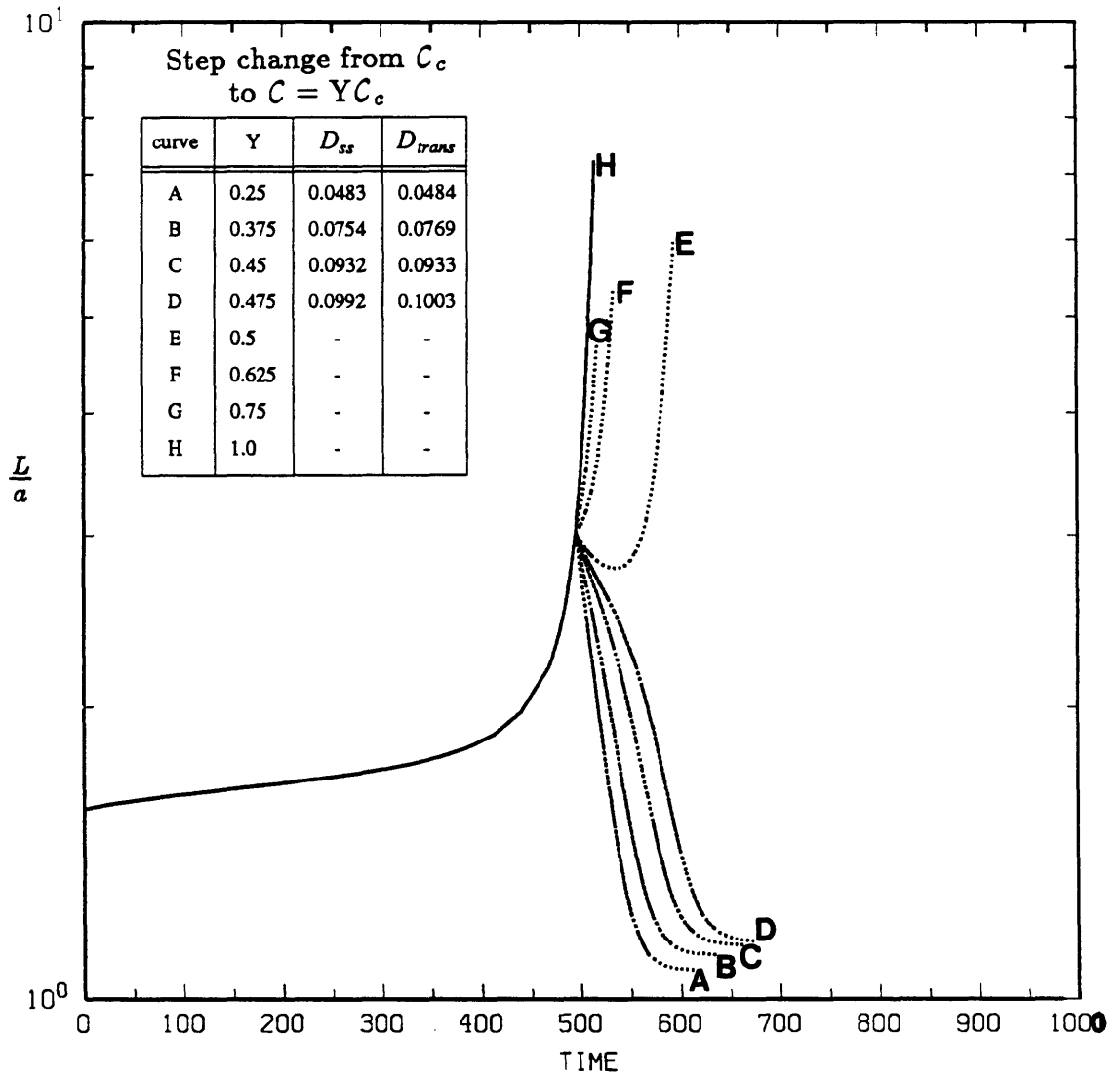


Figure 20

$$\lambda = 19.0$$

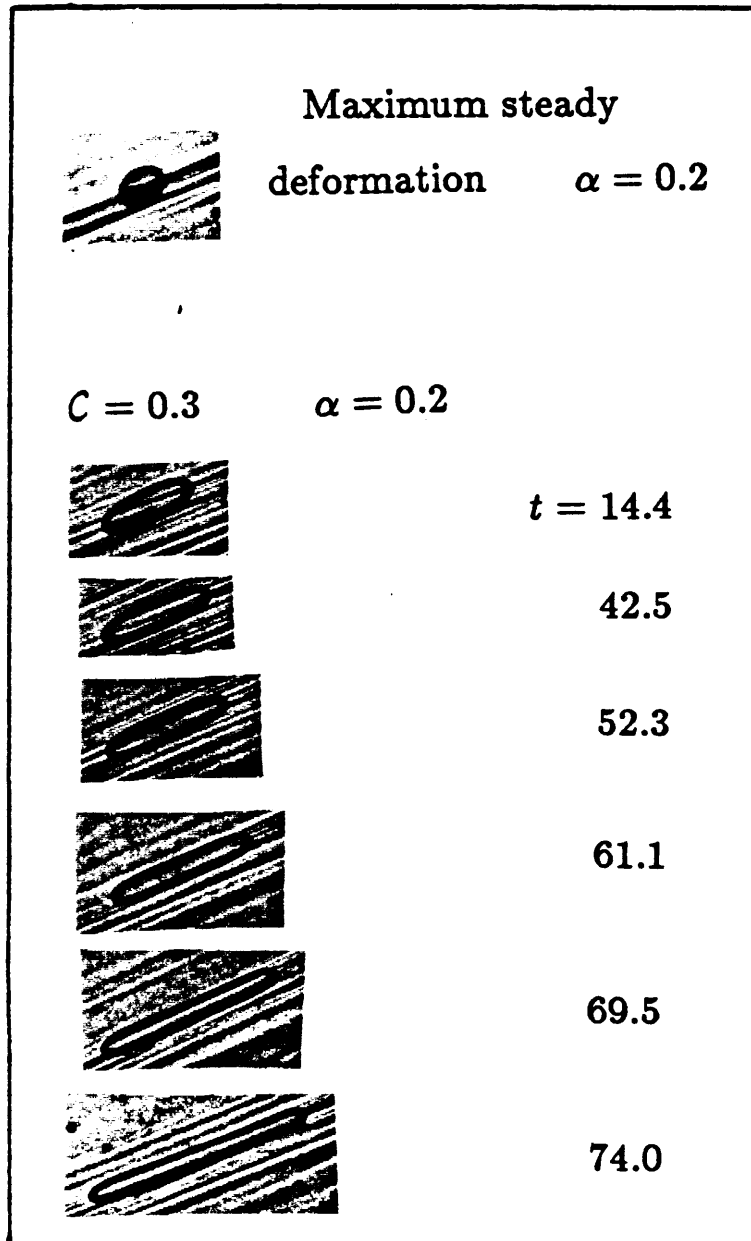


Figure 21

new flow conditions	critical elongation for breakup
$0.0C_c$	$3.4 < \frac{L}{a} < 4.5$
$0.2C_c$	$3.14 < \frac{L}{a} < 3.35$
$0.4C_c$	$2.93 < \frac{L}{a} < 3.2$
$0.65C_c$	$2.44 < \frac{L}{a} < 2.66$
$0.9C_c$	$2.08 < \frac{L}{a} < 2.25$
final steady shape	$\frac{L}{a} \approx 1.6$

Table 1. The critical elongation necessary for breakup as a function of a change from stretching at the critical capillary number to subcritical flow conditions; step reduction in shear rate only. $\lambda = 0.46$.

new flow conditions	critical elongation for breakup
$0.0C_c$	$7.6 < \frac{L}{a} < 8.2$
$0.35C_c$	$3.21 < \frac{L}{a} < 3.38$
$0.5C_c$	$2.57 < \frac{L}{a} < 2.95$
$0.75C_c$	$2. < \frac{L}{a} < 2.41$
final steady shape	$\frac{L}{a} \approx 1.6$

Table 2. The critical elongation necessary for breakup as a function of a change from stretching at the critical capillary number to subcritical flow conditions; step reduction in shear rate only. $\lambda = 5.3$.

CHAPTER 5

**BREAKUP OF CONCENTRIC
DOUBLE EMULSION DROPLETS
IN LINEAR FLOWS**

Breakup of concentric double emulsion droplets in linear flows

H.A. Stone and L.G. Leal

Department of Chemical Engineering

California Institute of Technology

Pasadena, California 91125

January 1988

ABSTRACT

The behaviour of concentric double emulsion droplets in linear flows is examined analytically, for the case when both fluid-fluid interfaces remain nearly spherical, and numerically, for the effect of finite interface deformation. In addition to determining the velocity fields and the first effects of flow-induced deformation, the theoretical analysis is used to calculate the effective viscosity of a dilute emulsion of these compound multiphase droplets. The numerical simulations allows for a complete investigation of the finite deformation of both the outer drop and the encapsulated particle. For example, the critical capillary number for globule breakup depends on the relative size and viscosity of the inner droplet. Also, for these concentric multiphase particles, there appear to be two distinct mechanisms of globule breakup, either continuous extension of the globule or contact of the two interfaces at the globule center even though the globule is only modestly deformed. The breakup behaviour is principally dependent on the radius ratio of the two droplets and the different mechanisms are directly related to the hydrodynamic interaction that occurs due to finite deformation of the fluid-fluid interfaces. The effect of different flow-types, i.e., uniaxial or biaxial extensional flows, is shown, in some instances, to suggest breakup of the inner droplet even though the outer droplet maintains a steady shape.

1. INTRODUCTION

Fundamental studies of encapsulated particles or drops are a relatively recent topic of interest in the fluid mechanics literature. An encapsulated particle is a particle or drop (or, more generally, multiple particles or drops) that is completely engulfed by a second immiscible fluid drop. This larger droplet is itself suspended in an immiscible fluid. In order to distinguish these compound double emulsion droplets from single phase droplets, which have been studied widely for many years, we will follow the precedent set by previous authors and use the term globule for these multiphase drops.

There exist a wide variety of processes where multiphase droplets and similar multiphase particles are found. The most well-known applications of double emulsions occur as liquid membranes for selective mass transport, but multiphase droplets also arise in other heat and mass exchange systems and combustion processes. The use of liquid membranes for the separation of hydrocarbons was proposed originally by Li (1971a,b) and has subsequently been extended to artificial blood oxygenation, water purification, recovery of heavy metals, and even the controlled release of drugs (Maugh 1976). The globules are efficient for mass transfer processes because of the high interfacial area per unit volume that can be generated, coupled with the short diffusion distances associated with transport between phases. The globules typical of these applications are very small (the undeformed radii are generally $10^{-3} - 10^{-1}$ cm) so that inertial effects are small and Stokes equations can be used as a first approximation. Because aspects of several industrial operations involve multiphase droplets rising through an otherwise quiescent fluid, the majority of theoretical analyses of these systems have focussed on the sedimentation problem.

Initial low-Reynolds-number studies of streaming flow past droplets coated with thin fluid films are presented by Johnson (1981) and Johnson & Sadhal (1983). Rushton & Davies (1983) study the translation of concentric spherical droplets in an infinite fluid. This work has been extended recently by Sadhal &

Oguz (1985) who allow for nonconcentric, though spherical, drops and account for the relative motion of the inner and outer droplets. An important feature of this study is the investigation of the stability of eccentric configurations of encapsulated particles. Also, Brunn & Roden (1985) calculate the first effects of inertia for concentric spherical droplets. These analyses have in common the assumption that the shapes and locations of the fluid-fluid interfaces are a priori known.

Chervenivanova & Zapryanov (1987) use the velocity fields computed by Sadhal & Oguz to determine the first corrections to the inner and outer drop shapes due to viscous stresses generated by the fluid motion. An interesting result of the analysis is that, even at small capillary numbers, the effect of the flow may be to cause deformation of both droplets at zero Reynolds number, unlike the classical Hadamard-Rybczynski result whereby a sedimenting single phase droplet remains exactly spherical at zero Reynolds number, independent of the magnitude of the capillary number. Furthermore, Chervenivanova & Zapryanov, accounting for eccentricity of the droplets, and Brunn & Roden, allowing for the first effects of inertia, observe that the flow created by the sedimenting globule causes the outer droplet to deform into a prolate spheroid while the inner droplet deforms into an oblate spheroid. These deformation analyses, though, are limited to cases where only small distortions from a spherical shape are produced. Additional aspects of the behaviour of compound drops are discussed in a recent review article by Johnson & Sadhal (1985).

There is a class of studies at high Reynolds number that has many qualitative features in common with the above mentioned studies. Typically, the high Reynolds number investigations of encapsulated particles are concerned with centering of bubbles in fluid droplets (Tsamopoulos & Brown 1987). These configurations arise, for example, in the formation of spherically symmetric shells of metal and glass that are used as fuel targets in inertial confinement studies and in particles that have been suggested as additives in high strength composite

systems. In addition to the obvious geometric similarity, the interaction between flow-induced prolate and oblate shapes of the inner and outer droplets, observed in the low-Reynolds-number work discussed above, is found in these studies also.†

As pointed out by Ulbrecht, Stroeve & Prabodh (1982), mass transfer operations are hindered by breakup of the globules. The relationship of this breakup to specific transport processes involving liquid membranes is discussed by Stroeve & Varanasi (1982). The process equipment involved in many applications expose the double emulsion particles to a wide range of velocity fields and varying degrees of hydrodynamic forces. As a first step in understanding the breakup problem for multiphase droplets, Ulbrecht, Stroeve & Prabodh and Stroeve & Varanasi (1984) conducted experimental studies of the breakup of double emulsions in simple shear flows. The results are interpreted by drawing direct analogies with the single phase drop breakup studies. In the experiments reported, the globule contained many subdrops. It is very difficult to be very specific about any overall trends since these multiphase systems exhibit shear thinning and normal stress differences. However, the studies suggest that the effect of velocity gradients should be explored and also raises the question of whether and when is it applicable to draw simple analogies with the single phase droplet results.

A related study, though with a different motivation, is presented by Davis & Brenner (1981). These authors are interested in the creation of emulsions consisting of smaller droplet sizes. Davis & Brenner examined the deformation of a fluid drop, with a solid sphere occluded at the center, in a simple shear flow. Under certain conditions (the viscosity ratio of the two fluid phases is order one and the flows are weak), the presence of the solid phase destabilizes the globule in the sense that the globule is more deformed than it would be

† We wish to thank Prof. R. A. Brown for directing our attention to these investigations.

without the solid. With the hypothesis that increased deformation makes the system more susceptible to rupture, this small deformation theory implies that the solid sphere enhances the conditions for breakup. Davis & Brenner also calculated the rheological properties of a dilute emulsion of these particles.

A final related research area involving multiphase particles that has several features in common with the problems discussed above is the behaviour of viscous fluid drops enclosed by an elastic membrane. These particles have been called 'capsules.' The time-dependent and steady deformation properties of these capsules due to a general linear flow have been studied by Barthes-Biesel (1980), Barthes-Biesel & Rallison (1981) and by Brunn (1980,1983) as models for red blood cell behaviour. Constitutive equations for the bulk stress-strain behaviour of dilute emulsions of these capsules are calculated also.

Our concern is the effect of nonuniform flow on the deformation and breakup of compound multiphase droplets. As many of the above studies imply, there is much to be learned by analogy with the behaviour of single phase droplets. The deformation and breakup of single phase droplets due to an imposed velocity gradient has been widely studied and interested readers are referred to review articles by Acrivos (1983) and Rallison (1984). It is well-documented that so-called strong flows, i.e., flows where the magnitude of the rate-of-strain tensor is greater than the magnitude of the vorticity tensor, are more effective in deforming a microstructure than a flow in which fluid elements predominantly rotate (Grace 1971, Olbricht, Rallison & Leal 1982, Bentley & Leal 1986). Hence, it is necessary and very informative to examine the effect of extensional flows on the dynamics of multiphase droplets, in addition to the simple shear flow studies already performed.

The effect of strong flows on concentric double emulsion droplets will be examined in this paper. This investigation represents an initial step towards describing and understanding breakup of double emulsion droplets and indicates situations when useful comparison with results available for single droplets are

applicable. The study of the concentric configuration in extensional flows is simpler than eccentrically configured particles and more straightforward than the case of multiple subdrops, but it is not just a mathematical diversion. Double emulsions consisting of a droplet containing a single internal droplet have been prepared experimentally by Florence & Whitehill (1981). Furthermore, this study will generalize the results of Davis & Brenner (1981) to account for the presence of a droplet of arbitrary viscosity at the center of a larger droplet that is suspended in a general linear flow. A consequence of this approach is to generalize some of the breakup observations of Stroeve & Varanasi (1984), which are confined to a simple shear flow.

The hydrodynamic stability of the concentric drop configuration is not examined here. The thermodynamic stability of similar multiphase drops, which depends on the interfacial tensions of all three fluid-fluid pairs, has been addressed by Torza & Mason (1969, 1970). Also, Torza & Mason (1970) briefly discuss the behaviour of double emulsions in simple shear flows.

The small deformation theory presented in the first part of this paper demonstrates the first effects of flow-induced deformation and examines the effects of the different fluid properties. In addition, the rheological behaviour of a dilute emulsion of these particles can be calculated. Several aspects of the globule deformation are very interesting and suggest that the effect of large deformations be examined in more detail.

The effect of finite deformation and possible breakup is addressed in the second part of this paper using a complete numerical solution to this free-boundary problem. As suggested by Davis & Brenner, the presence of the inner droplet may lead to globule breakup at a smaller capillary number than would have been necessary had the inner phase not been present. The numerics illustrate that breakup may occur due to large scale stretching of the globule into a cylindrical shape, similar in many respects to the breakup of single phase droplets. However, the numerics also indicate systems where globule breakup is more likely

to occur because of the inner droplet causing the rupture of the outer interface without excessive globule deformation. In addition, an example is documented where the inner droplet approaches breakup because of the flow-induced deformation caused by circulation inside the globule even though the globule itself maintains a steady, nearly spherical shape. Although there are clearly several similarities with single drop breakup studies, the results of this paper indicate significant differences due to interface-interface interaction that accompanies finite deformation of double emulsion droplets in extensional flows.

2. PROBLEM STATEMENT

Consider the double emulsion droplet shown in figure 1. We restrict our study to the case where the centers of mass of the two droplets remain coincident. The undeformed radius of the outer droplet is R_1 and the undeformed radius of the inner droplet is R_2 . The ratio $\kappa = \frac{R_2}{R_1}$ characterizes the initial state of the system. The three distinct Newtonian fluid phases are immiscible with viscosities μ_i and densities ρ_i . The interfacial tension (assumed constant) of the ij interface is denoted by σ_{ij} . With respect to a coordinate system fixed to the center of the globule, we consider the case where the imposed flow field varies linearly with position. This assumption is good provided that the bulk flow varies on a length scale that is large compared to R_1 . In these instances, the flow-induced deformation due to a local velocity gradient will be significant. Thus, far from the droplet the velocity is given by

$$\mathbf{u}_\infty = \boldsymbol{\Gamma} \cdot \mathbf{x} \tag{1}$$

where $\boldsymbol{\Gamma}$ is the velocity gradient tensor and is traceless as a consequence of continuity. Alternatively, the undisturbed velocity field may be decomposed into a symmetric and an antisymmetric part, in which case (1) may be written as

$$\mathbf{u}_\infty = \mathbf{E} \cdot \mathbf{x} + \frac{1}{2} \boldsymbol{\omega} \wedge \mathbf{x} \tag{2}$$

where \mathbf{E} , the rate-of-strain tensor, is the symmetric part of Γ and ω is the vorticity of the undisturbed flow.

In this paper we will present an analytic solution for the velocity and pressure fields internal and external to the globule. These calculations, though, are restricted to the case where both the inner and outer droplets remain nearly spherical due, for example, to a large interfacial tension. This solution is used to calculate the first corrections to the shape of the droplets that occur because of viscous forces generated at the two fluid-fluid interfaces. Specific computations are presented for the case of axisymmetric flows where $\omega = 0$ and \mathbf{E} has the diagonal form

$$\mathbf{E} = \pm \frac{G}{2} \begin{pmatrix} -1 & 0 & 0 \\ 0 & -1 & 0 \\ 0 & 0 & 2 \end{pmatrix}. \quad (3)$$

The + sign corresponds to a uniaxial extensional flow and the - sign corresponds to a biaxial extensional flow. G denotes the fluid shear rate.

When significant deformation occurs, as must certainly happen if the globule begins to break, the analytic procedure breaks down and we must resort to a complete numerical solution of the problem. This is described in Section 4. In this case, we also restrict our calculations to the axisymmetric flows described by equation (3). Nevertheless, we will first see that the small deformation procedure described here is quite useful in understanding certain features of the flow-induced deformation and the rheology of these multiphase systems.

For the small droplets typical of many processes involving double emulsions, inertial effects are negligible and the fluid motion in each phase is governed by the quasi-steady Stokes equations. Nondimensionalizing all lengths by $l_c = R_1$, velocities by $u_c = GR_1$, times by $t_c = G^{-1}$ and the pressure in phase i by $p_{c,i} = \frac{\mu_i u_c}{R_1}$, the governing equations for phase i are

$$\nabla^2 \mathbf{u}_i = \nabla p_i \quad (4a)$$

$$\nabla \cdot \mathbf{u}_i = 0 \quad (4b)$$

Here (\mathbf{u}_i, p_i) represent the dimensionless velocity and pressure fields in phase i . The boundary conditions for the three phases are

$$\mathbf{u}_1 = \Gamma \cdot \mathbf{x}, \quad p \rightarrow p_\infty \quad \text{as } |\mathbf{x}| \rightarrow \infty \quad (5a)$$

$$\mathbf{u}_1 = \mathbf{u}_2 \quad \text{for } \mathbf{x}_s \in S_{21} \quad (5b)$$

$$\mathbf{u}_2 = \mathbf{u}_3 \quad \text{for } \mathbf{x}_s \in S_{32} \quad (5c)$$

$$\mathbf{n}_2 \cdot \mathbf{T}_1 - \lambda_{21} \mathbf{n}_2 \cdot \mathbf{T}_2 = \frac{1}{C} \mathbf{n}_2 (\nabla_s \cdot \mathbf{n}_2) \quad \text{for } \mathbf{x}_s \in S_{21} \quad (5d)$$

$$\mathbf{n}_3 \cdot \mathbf{T}_2 - \lambda_{32} \mathbf{n}_3 \cdot \mathbf{T}_3 = \frac{\Omega}{C \lambda_{21}} \mathbf{n}_3 (\nabla_s \cdot \mathbf{n}_3) \quad \text{for } \mathbf{x}_s \in S_{32} \quad (5e)$$

where

$$\lambda_{21} = \frac{\mu_2}{\mu_1}$$

$$\lambda_{32} = \frac{\mu_3}{\mu_2}$$

$$\Omega = \frac{\sigma_{32}}{\sigma_{21}}$$

$$C = \frac{GR_1 \mu_1}{\sigma_{21}} .$$

The stress tensor \mathbf{T} has the usual definition

$$\mathbf{T} = -p\mathbf{I} + \nabla \mathbf{u} + (\nabla \mathbf{u})^T .$$

In these equations S_{ij} denotes the interface separating phases i and j , \mathbf{n}_i is the unit normal directed outward from phase i and $\nabla_s \cdot \mathbf{n}$ is the mean curvature of the interface (see figure 1). The capillary number C is defined using the properties of phase 1 and provides a measure of viscous forces responsible for deformation of the globule relative to interfacial tension forces that resist deformation. The dimensionless parameters λ_{21} , λ_{32} and Ω represent simple ratios of fluid viscosities and interfacial tensions, respectively.

The fluid-fluid interfaces evolve according to the kinematic conditions which may be stated as

$$\frac{d\mathbf{x}_s}{dt} = \mathbf{n}_i (\mathbf{u}_i \cdot \mathbf{n}_i) \quad (6)$$

where \mathbf{x}_s denotes a point on the interface.

We are interested in studying the deformation and breakup characteristics of double emulsion droplets as a function of the five dimensionless parameters: $\lambda_{21}, \lambda_{32}, \Omega, C$ and $\kappa = \frac{R_2}{R_1}$. In addition to direct dependence on C , the type of external flow, for example biaxial or uniaxial extensional flow, will play a significant role in the breakup problem.

The study of time-dependent phenomena using the quasi-steady Stokes equations requires that both local and convective inertial effects be small compared to viscous effects. For steady flow situations this requires that

$$\frac{\rho G R_1^2}{\mu} \ll 1 \quad \text{and} \quad \frac{\rho \sigma R_1}{\mu^2} \ll 1 .$$

As discussed by Davis & Brenner (1981) the assumption of concentric droplets is valid provided that migration because of gravitational settling or flow-induced motion is negligible during the time scale of the experiment. Small droplets, nearly comparable fluid densities or viscous fluids are necessary. Although many systems will differ from these idealized conditions, it is nevertheless hoped that the analysis and numerics presented in this paper will shed light on the complicated dynamics of these free-boundary multiphase problems.

The degree of interface deformation is characterized by the dimensionless deformation parameter $D = \frac{L-B}{L+B}$, where L and B represent the half-length and half-breadth of the interface position, respectively. The half-length L will always be measured in the z -direction and the half-breadth B in the radial (\bar{r}) direction (see figure 1). With this definition, prolate spheroidal shapes are characterized by $D > 0$ and oblate spheroidal shapes by $D < 0$.

3. SMALL DEFORMATION ANALYSIS

We first outline an analytical approach using the established methods of domain perturbation to study the initial effects of flow-induced deformation of double emulsion droplets. Section 3.1 outlines the method of solution and Section 3.2 summarizes the results of this analysis. Typical streamline patterns,

interface deformation, the effect of varying fluid properties, and the rheology of a dilute suspension of these droplets are discussed.

3.1 Analytic solution

Knowledge of the velocity fields is a necessary first step in the analysis of heat and mass transfer problems. The emphasis in this section will be to calculate the velocity and pressure fields internal and external to a compound multiphase droplet that is immersed in a general linear flow field. In general, the free-boundary nature of the droplet complicates the solution procedure since the interface location is not known a priori and must be found as part of the solution to the problem. In order to make progress, the drops comprising the double emulsion globule are treated as concentric and initially spherical. The velocity field is calculated everywhere using the continuity of velocity and continuity of tangential stress boundary conditions. This procedure produces the first term in an asymptotic expansion for the velocity field based upon a small droplet deformation. The resulting flow generates viscous stresses that tend to deform the globule and the normal stress balance is used to determine the approximate, perturbed steady-state shape.

The basic assumption in the analysis reported here is that the inner and outer droplets remain nearly spherical. From analysis of the single phase droplet deformation problem, there are two independent limits where the droplet will remain nearly spherical. In the first instance, low capillary numbers (in other words, weak flows or large interfacial tensions) correspond to small droplet deformation and, in the second instance, large internal droplet viscosity gives rise to small deformations. We will deal principally with the low C case.

The governing equation and boundary conditions are outlined in Section 2. The most general form of the solution to Stokes equation is given by Lamb (1932) in terms of an expansion in spherical harmonics (alternatively, this can be thought of as a multipole expansion; e.g., Brunn 1982). This method of solution is particularly well-suited to problems with spherical symmetry and has been

applied to the related problem of single phase drop deformation and breakup by Taylor (1932, 1934), Cox (1969), Frankel & Acrivos (1970), Barthes-Biesel & Acrivos (1973a) and Rallison (1980) and to the deformation of drops with elastic shells by Barthes-Biesel (1980), Barthes-Biesel & Rallison (1981) and Brunn (1980,1983). We follow a similar procedure here, although we are content with the $O(1)$ result for the general case $\lambda_{21} = O(1)$ and $\lambda_{32} = O(1)$. This approach provides good physical insight and motivates the numerical simulations discussed in Section 4.

As a result of the assumption of small deformation, both the governing equations and the applicable boundary conditions are linear. Since the droplets are assumed concentric and the undisturbed fluid motion is generated by the second order tensor Γ , the velocity and pressure fields in the suspending fluid (phase 1: $r = |\mathbf{x}| \geq 1$) may be written in the following general form, where the only second order tensors retained correspond to spherical harmonics that decay as $|\mathbf{x}| \rightarrow \infty$,

$$\mathbf{u}_1(\mathbf{x}) = \mathbf{E} \cdot \mathbf{x} + \frac{1}{2}\omega \wedge \mathbf{x} + \frac{1}{2}\mathbf{x} \frac{\mathbf{x} \cdot \mathbf{B}_1 \cdot \mathbf{x}}{r^2} + \frac{1}{r^5} \left[2\mathbf{C}_1 \cdot \mathbf{x} - 5\mathbf{x} \frac{\mathbf{x} \cdot \mathbf{C}_1 \cdot \mathbf{x}}{r^2} \right] + \frac{\mathbf{D}_1 \wedge \mathbf{x}}{r^3} \quad (7a)$$

$$p_1(\mathbf{x}) = p_\infty + \frac{\mathbf{x} \cdot \mathbf{B}_1 \cdot \mathbf{x}}{r^5}. \quad (7b)$$

The position vector \mathbf{x} is measured from the center of the globule. We consider the external flow, represented by \mathbf{E} and ω , to be prescribed. The constant second order tensors \mathbf{B}_1 and \mathbf{C}_1 depend linearly on \mathbf{E} and must therefore be symmetric, while the vector \mathbf{D}_1 depends linearly on ω . The last three terms on the right hand side of equation (7a) represent the disturbance motion caused by the globule.

The velocity and pressure fields in the inner droplet (phase 3: $|\mathbf{x}| \leq \kappa$) must remain bounded as $r \rightarrow 0$ and have the general form

$$\mathbf{u}_3(\mathbf{x}) = 2\mathbf{F}_3 \cdot \mathbf{x} + \mathbf{G}_3 \wedge \mathbf{x} + \frac{r^2}{21} \left[5\mathbf{H}_3 \cdot \mathbf{x} - 2\mathbf{x} \frac{\mathbf{x} \cdot \mathbf{H}_3 \cdot \mathbf{x}}{r^2} \right] \quad (8a)$$

$$p_3(\mathbf{x}) = p_3^* + \mathbf{x} \cdot \mathbf{H}_3 \cdot \mathbf{x} . \quad (8b)$$

In the annular region (phase 2: $\kappa \leq |\mathbf{x}| \leq 1$), spherical harmonics of both positive and negative degree are necessary so that

$$\begin{aligned} u_2(\mathbf{x}) = & 2\mathbf{F}_2 \cdot \mathbf{x} + \mathbf{G}_2 \wedge \mathbf{x} + \frac{1}{2}\mathbf{x} \left(\frac{\mathbf{x} \cdot \mathbf{B}_2 \cdot \mathbf{x}}{r^5} \right) + \frac{1}{r^5} \left[2\mathbf{C}_2 \cdot \mathbf{x} - 5\mathbf{x} \frac{\mathbf{x} \cdot \mathbf{C}_2 \cdot \mathbf{x}}{r^5} \right] \\ & + \frac{\mathbf{D}_2 \wedge \mathbf{x}}{r^3} + \frac{r^2}{21} \left[5\mathbf{H}_2 \cdot \mathbf{x} - 2\mathbf{x} \frac{\mathbf{x} \cdot \mathbf{H}_2 \cdot \mathbf{x}}{r^2} \right] \end{aligned} \quad (9a)$$

$$p_2(\mathbf{x}) = p_2^* + \frac{\mathbf{x} \cdot \mathbf{B}_2 \cdot \mathbf{x}}{r^5} + \mathbf{x} \cdot \mathbf{H}_2 \cdot \mathbf{x} . \quad (9b)$$

In these equations, p_2^* and p_3^* are constant pressure terms which are related to p_∞ and the curvature of the undeformed static interfaces. The corresponding stress fields are straightforward to calculate and are listed for completeness in Appendix A.

The description of the actual drop shape can be approximated by an expansion in surface spherical harmonics, where we retain at leading order only the second order term (Rallison 1980) (the zero and first order harmonics correspond to translation and dilatation of the droplet only, Cox 1969). Higher order harmonics would appear if additional terms in an asymptotic expansion for the velocity field are desired. These higher order terms have been calculated for the single phase droplet deformation problem by Barthes-Biesel & Acrivos (1973a), although the algebra is very complicated and requires the use of a computer. We are content here to calculate the leading order term in order to develop physical insight about the velocity field and the small deformation produced by the viscous stresses and then use the numerical analysis to study finite deformations. Hence, the shapes of the fluid-fluid interfaces are assumed to be of the form

$$r = 1 + \frac{\mathbf{x} \cdot \mathbf{A}_{21} \cdot \mathbf{x}}{r^2} \quad \text{for } \mathbf{x}_s \in S_{21} \quad (10a)$$

$$r = \kappa \left[1 + \frac{\mathbf{x} \cdot \mathbf{A}_{32} \cdot \mathbf{x}}{r^2} \right] \quad \text{for } \mathbf{x}_s \in S_{32} \quad (10b)$$

where $\kappa = \frac{R_2}{R_1}$ is the ratio of the radii of the initially undeformed droplets. The second order tensors \mathbf{A}_{21} and \mathbf{A}_{32} , which describe the shape correction, are to

be determined as part of the solution to the problem and must depend linearly on \mathbf{E} . This emphasizes that, at the leading order order for the approximations introduced here, the magnitude of the steady drop deformation depends only on the rate-of-strain tensor \mathbf{E} and is independent of the vorticity. Clearly, for this small deformation analysis to be valid, the magnitudes of both \mathbf{A}_{21} and \mathbf{A}_{32} must be small. We will make this qualitative statement more precise below.

If we define the shape function as

$$f_{21} = r - \left[1 + \frac{\mathbf{x} \cdot \mathbf{A}_{21} \cdot \mathbf{x}}{r^2} \right] = \text{constant} = 0$$

then the unit outward normal to the outer interface can be calculated from

$$\mathbf{n}_2 = \frac{\nabla f_{21}}{|\nabla f_{21}|}$$

It follows that the mean curvature of the deformed outer surface is given by

$$\nabla_s \cdot \mathbf{n}_2 = 2 + 4\mathbf{n}_2^\circ \cdot \mathbf{A}_{21} \cdot \mathbf{n}_2^\circ \quad . \quad (11a)$$

where the superscript $^\circ$ denotes the normal to the spherical surface and the deformation is assumed to be small. Similarly for the inner surface we have

$$\nabla_s \cdot \mathbf{n}_3 = \frac{1}{\kappa} \left[2 + 4\mathbf{n}_3^\circ \cdot \mathbf{A}_{32} \cdot \mathbf{n}_3^\circ \right] \quad . \quad (11b)$$

Following standard procedures of domain perturbation, the $O(1)$ velocity field is calculated by applying continuity of velocity and continuity of tangential stress boundary conditions on the undeformed spherical surfaces ($\mathbf{x}_s = \mathbf{n}_2^\circ, r = 1$ on S_{21} and $\mathbf{x}_s = \kappa \mathbf{n}_3^\circ, r = \kappa$ on S_{32}). The normal stress balance is not satisfied and is used to calculate the first correction to the drop shape. Thus, at steady state the normal component of equation (5b) is $\mathbf{n}_2^\circ \cdot \mathbf{u}_1 = \mathbf{n}_2^\circ \cdot \mathbf{u}_2 = 0$ on $\mathbf{x}_s = \mathbf{n}_2^\circ, r = 1$, which yields

$$\mathbf{E} + \frac{1}{2}\mathbf{B}_1 - 3\mathbf{C}_1 = 2\mathbf{F}_2 + \frac{1}{2}\mathbf{F}_2 - 3\mathbf{C}_2 + \frac{3}{21}\mathbf{H}_2 = 0 \quad (12)$$

and, the tangential component of equation (5b) ($\mathbf{t} \cdot \mathbf{u}_1 = \mathbf{t} \cdot \mathbf{u}_2$; \mathbf{t} represents the unit tangent vector to the interface) requires

$$\mathbf{E} + 2\mathbf{C}_1 = 2\mathbf{F}_2 + 2\mathbf{C}_2 + \frac{5}{21}\mathbf{H}_2 \quad (13)$$

$$\frac{1}{2}\omega + \mathbf{D}_1 = \mathbf{G}_2 + \mathbf{D}_2 \quad (14)$$

The normal and tangential components of (5c) yield the relationships

$$2\kappa\mathbf{F}_2 + \frac{1}{2\kappa^2}\mathbf{B}_2 - \frac{3}{\kappa^4}\mathbf{C}_2 + \frac{3\kappa^3}{21}\mathbf{H}_2 = 2\kappa\mathbf{F}_3 + \frac{3\kappa^3}{21}\mathbf{H}_3 = 0 \quad (15)$$

$$2\kappa\mathbf{F}_2 + \frac{2}{\kappa^4}\mathbf{C}_2 + \frac{5\kappa^3}{21}\mathbf{H}_2 = 2\kappa\mathbf{F}_3 + \frac{5\kappa^3}{21}\mathbf{H}_3 \quad (16)$$

$$\kappa\mathbf{G}_2 + \frac{1}{\kappa^2}\mathbf{D}_2 = \kappa\mathbf{G}_3 \quad (17)$$

Similarly, the tangential stress balance at the two interfaces provides the four equations

$$2\mathbf{E} + \mathbf{B}_1 - 16\mathbf{C}_1 = \lambda_{21}(4\mathbf{F}_2 + \mathbf{B}_2 - 16\mathbf{C}_2 + \frac{16}{21}\mathbf{H}_2) \quad (18)$$

$$\mathbf{D}_1 = \lambda_{21}\mathbf{D}_2 \quad (19)$$

$$4\mathbf{F}_2 + \frac{1}{\kappa^3}\mathbf{B}_2 - \frac{16}{\kappa^5}\mathbf{C}_2 + \frac{16\kappa^3}{21}\mathbf{H}_2 = \lambda_{32}(4\mathbf{F}_3 + \frac{16\kappa^2}{21}\mathbf{H}_3) \quad (20)$$

$$\mathbf{D}_2 = 0 \quad (21a)$$

Hence, we can conclude at this point

$$\mathbf{D}_1 = 0, \quad \mathbf{D}_2 = 0 \quad \text{and} \quad \mathbf{G}_2 = \frac{1}{2}\omega = \mathbf{G}_3 \quad (21b)$$

The complete solution of the remaining 8 equations for the 8 remaining unknowns requires some tedious algebra. Each of the constant second order tensors is linearly related to \mathbf{E} and the explicit dependence on κ, λ_{21} and λ_{32} is given in the Appendix B. The steady-state velocity field thus calculated is a uniformly valid first approximation to the flow field for all values of κ, λ_{21} and λ_{32} , provided the interface deformation is small. However, as is clear from the

related analysis of the single phase droplet deformation problem, this velocity field is *not* sufficient to calculate the first correction to the drop shapes for very viscous droplets, either $\lambda_{21} \gg 1$ or $\lambda_{32} \gg 1$. This is because the next term in an asymptotic expansion for the velocity field makes an order one contribution in the normal stress balance if the viscosity ratio is large (Barthes-Biesel & Acrivos 1973a, Rallison 1980 and Davis & Brenner 1981). We have not calculated this correction and have relegated the effect of large viscosity ratios to numerical investigation.

If we consider the case where $\lambda_{21} = O(1)$ and $\lambda_{32} = O(1)$, then for $C \ll 1$ the velocity field just determined can be used in the normal stress balance to calculate the first correction to the drop shape. Equations (5d,e) and (11a,b) relate the constant pressures by

$$p_2^o = \frac{2}{C} + p_\infty$$

$$p_3^o = \left(2 + \frac{2}{\kappa}\right) \frac{1}{C} + p_\infty$$

and provide the two additional equations from which to determine the shape correction functions \mathbf{A}_{21} and \mathbf{A}_{32} at this leading order of approximation,

$$\mathbf{E} - 3\mathbf{B}_1 + 24\mathbf{C}_1 - \lambda_{21}(\mathbf{F}_2 - 3\mathbf{B}_2 + 24\mathbf{C}_2 - \frac{3}{21}\mathbf{H}_2) = \frac{4}{C}\mathbf{A}_{21} \quad (22)$$

$$4\mathbf{F}_2 - \frac{3}{\kappa^3}\mathbf{B}_2 + \frac{24}{\kappa^5}\mathbf{C}_2 - \frac{3\kappa^2}{21}\mathbf{H}_2 - \lambda_{32}(4\mathbf{F}_3 - \frac{3\kappa^2}{21}\mathbf{H}_3) = \frac{4\Omega}{C\lambda_{21}\kappa}\mathbf{A}_{32} \quad (23)$$

Using these equations the shape correction functions \mathbf{A}_{21} and \mathbf{A}_{32} may be expressed in the form

$$\mathbf{A}_{21} = \frac{C}{4} h_{21}(\kappa, \lambda_{21}, \lambda_{32})\mathbf{E}$$

$$\mathbf{A}_{32} = \frac{C\lambda_{21}\kappa}{4\Omega} h_{32}(\kappa, \lambda_{21}, \lambda_{32})\mathbf{E} \quad (24)$$

The functions h_{21} and h_{32} are listed in Appendix B. The form of the solutions (24) confirms the expected conditions for validity of the steady-state small deformation analysis. Namely, for $\lambda_{21} = O(1)$ and $\lambda_{32} = O(1)$, we require $C \ll 1$ and $\frac{C\lambda_{21}\kappa}{\Omega} \ll 1$.

Alternatively, rather than requiring $\mathbf{n} \cdot \mathbf{u} = 0$, the time evolution of the shape functions A_{21} and A_{32} can be determined by using the complete form of the kinematic conditions (equation 6). This is algebraically tedious and is not attempted here. Instead, we will illustrate the time-dependent evolution for finite deformation of the interfaces using the numerical simulations discussed in Section 4.

The effect that deformation of one interface has on the deformation of the other interface would appear at the next order in the perturbation analysis. This is clearly a very important question, especially for the case $\kappa \rightarrow 1$, where the flow field in the thin gap would be significantly affected by any drop deformation. However, this calculation is very complicated and, since a complete numerical study of finite deformation is included, this question is relegated also to the numerical calculations presented in Section 4.

Finally, the approximate solution from this section can be used to determine the effective viscosity of a dilute suspension of identical double emulsion droplets. The analysis of the bulk stress in a dilute suspension of particles has been discussed by Batchelor (1970). The bulk stress, Σ , is related to the velocity gradient in the absence of the particles \mathbf{E} by

$$\Sigma = -p\mathbf{I} + 2\mathbf{E} + \Sigma^{(p)} \quad (25)$$

where

$$\Sigma^{(p)} = \frac{3\phi}{4\pi} \int_{S_{21}} [(\mathbf{T}_1 \cdot \mathbf{n}_2)\mathbf{x} - (\mathbf{u}_1\mathbf{n}_2 + \mathbf{n}_2\mathbf{u}_1)] dS \quad (26)$$

represents the contribution to the bulk stress due to the presence of the particles. Here, ϕ represents the particle volume fraction and the integration is over the outer surface of the globule. Because the approximate solution presented above treats the globule as spherical, it is straightforward to show that the only contribution to this integral comes from the \mathbf{B}_1 term of the solution. Hence,

$$\Sigma^{(p)} = -\phi\mathbf{B}_1 \quad (27)$$

Since \mathbf{B} is linearly related to \mathbf{E} the dilute emulsion of concentric spherical droplets behaves as a Newtonian fluid with a modified value of the viscosity. If we write $\mathbf{B}_1 = B_1\mathbf{E}$ then the effective viscosity of a dilute emulsion of double emulsion globules, μ^* , has the form

$$\frac{\mu^*}{\mu} = 1 + \phi B_1(\kappa, \lambda_{21}, \lambda_{32}). \quad (28)$$

The magnitude of the capillary number plays no role at this level of approximation. Finite deformation, which depends on both the magnitude of the capillary number and the flow type, leads to more complicated rheological properties (e.g. normal stress differences). This has been discussed for a dilute suspension of single phase droplets by Schowalter, Chaffey & Brenner (1968), Frankel & Acrivos (1970) and Barthes-Biesel & Acrivos (1973b).

3.2 Results

The analytic solution presented in Section 3.1 allows for investigation of the velocity fields external and internal to the globule and examination of flow-induced deformation that is ultimately responsible for breakup. The effective viscosity of dilute suspensions of these multiphase particles can be calculated also.

We begin our discussion by illustrating typical streamlines internal and external to the globule. In figure 2*a-c* we exhibit the streamline patterns for $\kappa = 0.2, 0.5$ and 0.8 . The other parameters are fixed at $\lambda_{21} = 1.0, \lambda_{32} = 1.0$. As Ω and C only appears in the normal stress balance, they will play a role in the deformation of the interfaces, but do not effect the velocity field at this order of approximation. The arrows on the streamlines shown in figure 2 correspond to the case of a uniaxial extensional flow. However, because of the assumptions of spherical and concentric drops, the streamline patterns at this level of approximation are identical for uniaxial or biaxial extensional flows; only the direction of flow is reversed in these two cases. As we will see below, however, the effect of these two distinct flows on the droplet deformation is quite different.

In figure 2, we simply observe two vortical flow patterns interior to the globule. The important point to notice is that the vorticity of the motion in the inner droplet is of opposite sign from the vorticity in the annular region. The external fluid motion creates a recirculating flow in the annular region that drives a flow in the inner droplet with opposite signed vorticity. The effect of changing λ_{21} and λ_{32} was examined and found to have very little qualitative effect on the streamline pattern with the change primarily limited to the magnitude of the velocity.

The streamline patterns shown in figure 2 suggest a very interesting aspect of the flow-induced deformation of the globule. The external *uniaxial* flow tends to deform the overall globule shape into a prolate spheroidal shape. Meanwhile, the steady interior flow generated in the annular region creates a *biaxial* extensional flow in the neighborhood of the inner droplet. This deforms the inner droplet into an oblate spheroidal shape. Exactly the reverse situation would occur if a biaxial extensional flow were imposed at infinity: the globule would deform into an oblate ellipsoid and, consequently, the inner droplet would be exposed to a uniaxial extensional flow and deform into a prolate ellipsoid. A typical series of steady-state shapes is shown as a function of capillary number in figure 3 for a globule immersed in a uniaxial extensional flow. The same case, but for a biaxial extensional flow is shown in figure 4. The final shapes shown in figures 3 and 4 have both developed a pinch at the droplet center. This is not physically correct and simply occurs because the asymptotic solution is being used outside its range of validity. For these small deformations, the magnitude of deformation of both the inner and outer droplet increases linearly with capillary number (equation 24). Furthermore, the deformation of the inner droplet is much smaller than the deformation of the outer droplet. Of course, the basic reason for this is that the smaller radius of curvature of the inner droplet make interfacial tension more important. Finally, this simultaneous existence of prolate shapes containing flow-induced oblate shapes, and vice-versa, is sim-

ilar qualitatively to observations of Brunn & Roden (1985), Chervenivanova & Zapryanov (1987) and Tsamapoulos & Brown (1987).

It is well established that the critical capillary number for drop breakup is dependent on the nature of the flow field. For example, in the single phase case, drops of any viscosity ratio can be burst in a two-dimensional extensional flow. However, for simple shear flow there exists a limiting value of the viscosity ratio above which breakup does not occur. Furthermore, even the nature of an extensional flow (uniaxial versus biaxial) can lead to differences in the breakup of single phase droplets. Small deformation studies of single phase droplets in biaxial and uniaxial extensional flows have been performed by Barthes-Biesel & Acrivos (1973a) and a numerical study of bubble deformation and breakup in these flows at intermediate and large Reynolds number has been examined recently by Kang & Leal (1987, 1988). A numerical study of finite deformation of droplets at zero Reynolds in both biaxial and uniaxial flows is presented by Stone (1988). The most notable feature regarding breakup at low Reynolds numbers is that larger capillary numbers are necessary for drop burst in a biaxial flow. This is of particular interest to this study since in the axisymmetric flows discussed above, one drop experiences a uniaxial straining flow, while simultaneously the other droplet experiences a biaxial straining flow. Clearly, this observation has implications with regard to the breakup of globules since these two extensional flows have a different effectiveness in causing breakup. In addition, not only is it of interest to learn what conditions are necessary for burst of the globule (outer drop), but an interesting question is whether it is possible that the outer drop shape remains stable while viscous stresses cause breakup of the inner droplet. Since all of these questions involve finite deformations, complete consideration must await the numerical investigation presented in Section 4. Nevertheless, the small deformation analysis can provide useful insight.

We now consider the effect that the presence of the inner droplet has on the overall deformation of the globule. In a study of the deformation of a droplet

with a small solid sphere at its center, Davis & Brenner (1981) observed that the effect of increasing the size of the solid phase was to increase the deformation of the droplet at a given value of the capillary number. This suggests that the onset of bursting is enhanced due to the presence of the solid phase and, consequently, that breakup occurs at a smaller value of the capillary number than would be possible without the solid sphere. Here we extend the analysis of Davis & Brenner to account for an inner phase of arbitrary viscosity ratio and strong flows.

In figure 5 we present a plot of the globule deformation, D_{outer} , versus capillary number for four different radius ratios, $\kappa = 0.1, 0.3, 0.5,$ and 0.7 . The curve for $\kappa = 0.7$ stops when the analysis predicts that the two interfaces touch. The other parameters are fixed at the values $\lambda_{21} = 1.0, \lambda_{32} = 1.0$ and $\Omega = 1.0$. Although this plot shows prediction of finite deformation we do not imply that these calculations are valid there (it is to be expected from comparable analyses of single phase droplets that these calculations are indicative of deformation trends but are not quantitatively accurate). Clearly, however, the effect of increasing κ is to significantly increase the deformation at a given value of the capillary number. As in the study of Davis & Brenner this suggests that breakup with the occluded phase present will occur at a reduced value of the capillary number. However, it should be remarked as observed in the initial deformation shown in figures 3 and 4, that the inner droplet deforms toward the narrowing waist of the outer droplet so that significant hydrodynamic interactions between the two interfaces will occur. This interaction between the two fluid-fluid interfaces because of finite deformation is not taken into account in the small deformation theory and, at first inspection, it is not at all obvious how this will effect the breakup process. Therefore, in spite of the fact that deformation is initially increased due to the presence of the interior droplet, it is not clear whether the critical capillary number for breakup will actually be reduced relative to the case when no third phase is present. Again, these questions in-

volving finite deformation must be answered with a numerical investigation (see Section 4).

Next we examine the effect of varying the fluid properties. As is clear from equation (24), within the context of this small deformation theory, varying the ratio of interfacial tension Ω is limited to changing the deformation of the inner droplet and has no effect on deformation of the overall globule. For a given capillary number, more deformation of the inner droplet occurs for smaller Ω and larger κ .

The effect of changing the viscosity of the occluded phase is examined in figure 6 by varying λ_{32} . In figure 6a, $\kappa = 0.5$ and the outer globule deforms more if a solid phase is present at the center than if a less viscous fluid droplet is present. In figure 6b, deformation of the inner droplet, D_{inner} , is shown for the same conditions, and it is evident that the inner drop deforms more at a given capillary number for larger λ_{32} (strictly speaking for sufficiently large λ_{32} the predicted deformation needs modification as discussed in Section 3 but for moderate λ_{32} the trends of flow induced deformation should be correct). In figures 6c,d we show similar plots for $\kappa = 0.1$. Interestingly enough, for $\kappa = 0.1$, the deformation of the globule is effectively independent of the viscosity of the occluded phase as values of D_{outer} differ by less than one percent for $10^{-2} \leq \lambda_{32} \leq 10^2$.

For completeness, the effect of varying λ_{21} for two cases $\kappa = 0.5$ and $\kappa = 0.1$ is examined in figure 7. For fixed values of λ_{32} and C , increasing λ_{21} is equivalent to increasing μ_2 and μ_3 by the same amount. If we assume that increased deformation of the globule leads to breakup at a lower value of the capillary number, then from figures 5,6 and 7 we conclude that globule breakup is enhanced due to larger interior drops and more viscous interior fluids. Of course, as with any theory that is restricted to small deformations, nothing can be inferred about the mechanism of breakup.

Finally, we present a brief discussion of the rheology to be expected of a

dilute emulsions of these multiphase globules. The analysis of the bulk stress of a dilute suspension of particles has been described by Batchelor (1970). The contribution to the bulk stress because of the presence of particles is summarized in Section 3.1. Following the notation of Davis & Brenner (1981), the bulk viscosity, μ^* can be written in the form

$$\frac{\mu^*}{\mu} = 1 + \frac{5}{2}\phi\left(1 - \frac{3}{5}K\right) \quad (29)$$

where

$$K = \frac{\delta_1 + \frac{\kappa^3}{1+\lambda_{32}} \delta_2}{\delta_1 + \lambda_{21}\delta_3 + \frac{\kappa^3}{1+\lambda_{32}}(\delta_2 + \lambda_{21}\delta_4)}. \quad (30)$$

The coefficients δ_i only depend on κ and have the specific forms

$$\delta_1 = 4 - 25\kappa^3 + 42\kappa^5 - 25\kappa^7 + 4\kappa^{10}$$

$$\delta_2 = 15 - 42\kappa^2 + 35\kappa^4 - 8\kappa^7$$

$$\delta_3 = 4 - 10\kappa^3 + 10\kappa^7 - 4\kappa^{10}$$

$$\delta_4 = 6 - 14\kappa^4 + 8\kappa^7.$$

In the limit $\lambda_{32} \rightarrow \infty$ (λ_{21} and κ finite) this expression reduces to the result of Davis & Brenner (1981) for a solid sphere occluded at the globule center. As discussed by Davis & Brenner, two other limits follow naturally. In the limit $\lambda_{21} \rightarrow \infty$, the case of a very viscous shell of fluid, equation (30) yields $K \rightarrow 0$ which is the well-known Einstein viscosity of a suspension of solid spheres. Notice that this is true for any κ and λ_{32} and simply says that the interior fluid plays no part in the rheology if the liquid membrane, however thin, is much more viscous than the suspending fluid. The effect of the viscous membrane is to reduce the velocity in the annular region to $O(\frac{1}{\lambda_{21}})$ so that the effective deformation rate in the neighborhood of the inner drop is very small. The limit $\kappa \rightarrow 0$ reproduces the results of Taylor (1932) for the viscosity of a suspension of single phase liquid droplets

$$\frac{\mu^*}{\mu} = 1 + \phi \frac{1 + \frac{5}{2}\lambda_{21}}{1 + \lambda_{21}}.$$

A very interesting limit is found by considering the case of a very thin liquid membrane, $\kappa \rightarrow 1$. In this case we find

$$K = \frac{175\bar{\kappa}^2 + \frac{\bar{\kappa}}{1+\lambda_{32}}(140 - 665\bar{\kappa})}{175\bar{\kappa}^2 + \bar{\kappa}\lambda_{21}(140 - 490\bar{\kappa}) + \frac{1}{1+\lambda_{32}}[140\bar{\kappa} + \lambda_{21}(84 - 476\bar{\kappa})]} + O[(\bar{\kappa}^3)]$$

where $\bar{\kappa} = 1 - \kappa$. Hence, provided $\lambda_{21} = O(1)$ the limit $\kappa \rightarrow 1$ ($\bar{\kappa} \rightarrow 0$) produces $K \rightarrow 0$, which is the result for a suspension of rigid spheres. This dynamic feature of thin liquid membranes to reproduce solid sphere-like rheological behaviour is best appreciated by viewing the velocity field. In figure 8 we show a magnified view of the fluid streamlines for $\kappa = 0.95$. Because of the recirculation set up internal to the droplet, the fluid velocity is forced to change directions over a very thin distance. In order to satisfy continuity of velocity at both interfaces, the tangential velocity is reduced to zero, as it would be at a solid boundary. Therefore, the rheology is equivalent to a suspension of rigid spheres. This result is independent of the viscosity of the inner phase. This consequence of thin membranes was pointed out by Rushton & Davies (1983) for sedimenting double emulsion droplets.

4. NUMERICAL STUDY OF HIGHLY DEFORMED GLOBULES

4.1 Numerical scheme - application of the boundary integral method

Although the analysis presented above is insightful and straightforward, it is nonetheless restricted to small deformations. The effect of large deformations and the possibility of breakup are clearly interesting and significant problems. However, as is characteristic of most free-boundary problems, the study of large deformations is amenable only to numerical study. A very powerful method for solving Stokes flow problems is the boundary integral method (Youngren & Acrivos 1975). The technique has been applied to several aspects of the single phase drop deformation problem (Rallison & Acrivos 1978, Rallison 1980, Stone & Leal 1987), in addition to a variety of other free-boundary studies (Lee & Leal 1982, Sapir & Nir 1985, Sherwood 1987, Stoos & Leal 1987, Ascoli & Leal 1988).

The governing equations and boundary conditions are outlined in Section 2. The general solution to the quasi-steady Stokes equation in the three phases may be written as

$$\mathbf{u}_i(\mathbf{x}) = \mathbf{u}_\infty(\mathbf{x}) + \int_S \mathbf{J} \cdot \mathbf{T}_i \cdot \mathbf{n}_i \, dS(\mathbf{y}) + \int_S \mathbf{u}_i \cdot \mathbf{K} \cdot \mathbf{n}_i \, dS(\mathbf{y}) \quad (31)$$

where S represents all the bounding surfaces for phase i , \mathbf{n}_i is the unit outward normal from phase i (see figure 1), and we define $\mathbf{u}_\infty = 0$ for phase 2 and phase 3. In this equation the kernels \mathbf{J} and \mathbf{K} represent

$$\mathbf{J}(\mathbf{x} - \mathbf{y}) = \frac{1}{8\pi} \left[\frac{\mathbf{I}}{|\mathbf{x} - \mathbf{y}|} + \frac{(\mathbf{x} - \mathbf{y})(\mathbf{x} - \mathbf{y})}{|\mathbf{x} - \mathbf{y}|^3} \right]$$

$$\mathbf{K}(\mathbf{x} - \mathbf{y}) = -\frac{3}{4\pi} \frac{(\mathbf{x} - \mathbf{y})(\mathbf{x} - \mathbf{y})(\mathbf{x} - \mathbf{y})}{|\mathbf{x} - \mathbf{y}|^5}$$

The integral involving \mathbf{J} is known as the single layer and the integral involving \mathbf{K} is known as the double layer. The single layer is continuous for all \mathbf{x} including $\mathbf{x}_s \in S$, while the double layer is discontinuous in the limit $\mathbf{x} \rightarrow S$ and suffers a jump in value (Ladyzenskaya 1969).

We proceed by taking the limit of equations (31) as $\mathbf{x} \rightarrow \mathbf{x}_s \in S_{21}$ from phase 1 and phase 2, respectively. Making use of the continuity of the single layer and the jump condition for the double layer results in the two equations

$$\frac{1}{2} \mathbf{u}_1(\mathbf{x}_s) = \mathbf{u}_\infty(\mathbf{x}_s) - \int_{S_{21}} \mathbf{J} \cdot \mathbf{T}_1 \cdot \mathbf{n}_2 \, dS - \int_{S_{21}} \mathbf{u}_1 \cdot \mathbf{K} \cdot \mathbf{n}_2 \, dS \quad (32)$$

$$\begin{aligned} \frac{1}{2} \mathbf{u}_2(\mathbf{x}_s) = & \int_{S_{21}} \mathbf{J} \cdot \mathbf{T}_2 \cdot \mathbf{n}_2 \, dS + \int_{S_{32}} \mathbf{J} \cdot \mathbf{T}_2 \cdot \mathbf{n}_2 \, dS \\ & + \int_{S_{21}} \mathbf{u}_2 \cdot \mathbf{K} \cdot \mathbf{n}_2 \, dS + \int_{S_{32}} \mathbf{u}_2 \cdot \mathbf{K} \cdot \mathbf{n}_2 \, dS \quad . \end{aligned} \quad (33)$$

These equations are valid for $\mathbf{x}_s \in S_{21}$. The integrands in the integrals over S_{21} are singular, but the integrals themselves are integrable in the sense of a Cauchy principal value. The integrals over S_{32} are well-behaved and represent interaction terms between the two deformable fluid interfaces.

Multiplying (33) by λ_{21} , adding to (32) and making use of the boundary conditions on the velocity and stress fields gives

$$\begin{aligned} \frac{(1 + \lambda_{21})}{2} \mathbf{u}_1(\mathbf{x}_s) &= \mathbf{u}_\infty(\mathbf{x}_s) - \frac{1}{C} \int_{S_{21}} \mathbf{J} \cdot \mathbf{n}_2 (\nabla_s \cdot \mathbf{n}_2) dS \\ &\quad - (1 - \lambda_{21}) \int_{S_{21}} \mathbf{u}_1 \cdot \mathbf{K} \cdot \mathbf{n}_2 dS + \lambda_{21} \int_{S_{32}} \mathbf{J} \cdot \mathbf{T}_2 \cdot \mathbf{n}_2 dS \\ &\quad + \lambda_{21} \int_{S_{32}} \mathbf{u}_2 \cdot \mathbf{K} \cdot \mathbf{n}_2 dS. \end{aligned} \quad (34)$$

This equation describes the velocity \mathbf{u}_1 at the S_{21} interface in terms of integrals over both interfaces. Unlike the single phase droplet deformation problem where only the surface curvature $\nabla_s \cdot \mathbf{n}$ is necessary to determine the interface evolution (Rallison & Acrivos 1978), in this multiphase droplet problem the velocity and stress on the second interface are needed also. As a consequence, all integrals are written in terms of \mathbf{u}_1 and $\mathbf{T}_2 \cdot \mathbf{n}_2$ for the surface S_{21} and in terms of \mathbf{u}_3 and $\mathbf{T}_2 \cdot \mathbf{n}_2$ for the surface S_{32} .

In a similar manner, taking the limit of equation (31) as $\mathbf{x} \rightarrow \mathbf{x}_s \in S_{32}$ from phase 2 and phase 3 results in the two equations

$$\begin{aligned} \frac{1}{2} \mathbf{u}_2(\mathbf{x}_s) &= \int_{S_{21}} \mathbf{J} \cdot \mathbf{T}_2 \cdot \mathbf{n}_2 dS + \int_{S_{32}} \mathbf{J} \cdot \mathbf{T}_2 \cdot \mathbf{n}_2 dS \\ &\quad + \int_{S_{21}} \mathbf{u}_2 \cdot \mathbf{K} \cdot \mathbf{n}_2 dS + \int_{S_{32}} \mathbf{u}_2 \cdot \mathbf{K} \cdot \mathbf{n}_2 dS \end{aligned} \quad (35)$$

$$\frac{1}{2} \mathbf{u}_3(\mathbf{x}_s) = - \int_{S_{32}} \mathbf{J} \cdot \mathbf{T}_3 \cdot \mathbf{n}_3 dS - \int_{S_{32}} \mathbf{u}_3 \cdot \mathbf{K} \cdot \mathbf{n}_3 dS \quad (36)$$

Multiplying (36) by λ_{32} , adding to (35) and using the boundary conditions yields

$$\begin{aligned} \frac{(1 + \lambda_{32})}{2} \mathbf{u}_3(\mathbf{x}_s) &= - \frac{\Omega}{C \lambda_{21}} \int_{S_{32}} \mathbf{J} \cdot \mathbf{n}_3 (\nabla_s \cdot \mathbf{n}_3) dS - (1 - \lambda_{32}) \int_{S_{32}} \mathbf{u}_3 \cdot \mathbf{K} \cdot \mathbf{n}_3 dS \\ &\quad + \int_{S_{21}} \mathbf{J} \cdot \mathbf{T}_2 \cdot \mathbf{n}_2 dS + \int_{S_{21}} \mathbf{u}_1 \cdot \mathbf{K} \cdot \mathbf{n}_2 dS \end{aligned} \quad (37)$$

Equations (32), (34), (36) and (37) represent four integral equations for the four unknowns, \mathbf{u}_1 and $\mathbf{T}_2 \cdot \mathbf{n}_2$ for $\mathbf{x}_s \in S_{21}$ and \mathbf{u}_3 and $\mathbf{T}_2 \cdot \mathbf{n}_2$ for $\mathbf{x}_s \in$

S_{32} . If \mathbf{u}_∞ , C , the fluid properties (λ_{21} , λ_{32} and Ω) and the shape of the fluid-fluid interfaces are specified, then these equations can be used to solve uniquely for the interfacial velocities. The evolution of the interfaces is followed using the kinematic conditions (equation 6) and, consequently, the globule shape is determined for all times by an initial condition and the time history of the flow (Rallison 1984).

This system of equations is coupled; for example, determination of \mathbf{u}_1 requires knowledge of \mathbf{u}_3 and vice-versa. Nevertheless, these equations illustrate the principal strength of the boundary integral method: namely, only two-dimensional surface integrals need to be calculated instead of having to solve for the velocity field throughout the entire three dimensional domain. The basic numerical procedure for this problem is very similar to the one used in our earlier time-dependent studies of drop relaxation and breakup (Stone & Leal 1987). Rather than repeating the details here, the important aspects are summarized below.

We will consider concentric double emulsion drops and axisymmetric flows, where \mathbf{u}_∞ is given by (3). In such cases, the azimuthal (θ) integration can be performed analytically and the surface integrals are reduced to line integrals. The integral equations are solved by discretizing each of the interfaces into $2N-2$ elements with node points at the end of each element. The unknowns (both velocities and stresses) are assumed to vary linearly over each element. This representation yields smoother and more accurate interfacial velocity and stress distributions than the assumption of a constant value over each element. Typically, for the calculations presented in this paper, we choose $N=15-20$. At each node point there are four unknowns: two components of velocity (u_r, u_z) and two components of stress ($(\mathbf{T} \cdot \mathbf{n})_r, (\mathbf{T} \cdot \mathbf{n})_z$). Due to the fore-aft symmetry of the extensional flow, the net number of unknowns is halved so that the largest linear system generated is 160×160 . This linear system of equations is solved by Gaussian elimination.

The drop shapes are represented accurately by parameterizing each interface using a normalized measure of arclength, s ($0 \leq s \leq 1$), and describing the location of the surface node points using the cylindrical coordinates $r(s)$ and $z(s)$. Cubic splines are used to generate twice-continuously differentiable representations of the drop shape. The unit normals and curvature ($\nabla_s \cdot \mathbf{n}$) are calculated using this cubic spline representation.

After the interfacial velocities are calculated, the kinematic condition is used to update the interface shape. A simple Euler method is used for this purpose. Velocities are typically $O(10^{-3})$ so that the time-step chosen is typically $\Delta t = 0.3 - 0.5$. After each iteration, the collocation points are redistributed evenly, based upon arclength, along the interface. This minimizes convection of points that leads to uneven node point distributions and is a principal cause of numerical difficulties. A typical simulation to determine the deformation parameter D as a function of capillary number requires approximately 5000 iterations to map the entire steady deformation curve. Choosing $N=20$, one iteration takes about one minute of CPU time on a SUN 3/160 workstation with a floating point accelerator. The steady shapes are calculated by requiring the normal velocities on both interfaces to be typically less than $2 \times 10^{-4} - 3 \times 10^{-4}$ at each node point.

The numerical algorithm has been checked against the analytical results of Barthes-Biesel & Acrivos (1973a) for the deformation of single phase droplets in axisymmetric extensional flows (this comparison is reported in Stone & Leal 1987). The agreement is excellent. Comparison with the small deformation analysis presented in Section 3 is shown in the results section that follows. The volume of the both the inner and outer droplets are monitored as time progressed and for $\lambda_{21} = O(1)$ and $\lambda_{32} = O(1)$ are found to change by less than a percent over several thousand iterations. As other researchers have found, larger volume changes occur for smaller λ , say $\lambda \approx 0.1$.

4.2 Results of the numerical investigation

In this section we summarize our numerical observations of the deformation and breakup of double emulsion droplets in axisymmetric extensional flows. Both steady-state and time-dependent effects are discussed.

We begin our discussion with a short comparison of the numerical simulations with the small deformation analysis outlined in Section 3. In figure 9a,b, the differences between the numerically predicted deformation of the inner and outer surfaces and the analytically calculated deformations ($D_{numer} - D_{theory}$) are plotted as a function of capillary number in a uniaxial extensional flow for several different combinations of $\lambda_{21}, \lambda_{32}, \kappa$ and Ω . Beginning with a spherical initial shape, the capillary number is increased in small increments (typically $\Delta C = 0.005$), the steady shape is calculated and then the capillary number is incremented again. As discussed in Section 3, a double emulsion globule placed in a uniaxial extensional flow will deform into a prolate ellipsoidal shape ($D > 0$) and at steady state the inner droplet will deform into an oblate ellipsoidal shape ($D < 0$). In figure 9a,b, the basic trend we observe is good agreement between numerics and theory for sufficiently small capillary, but, as the capillary number is increased, the theory consistently underpredicts the numerical values for the outer shape and overpredicts the deformation of the inner surface. This level of agreement is comparable to the predictive capability of the first order small deformation theory for single phase droplet deformation. Although insightful, the small deformation analysis of Section 3 is quantitatively limited even for relatively small values of C and for the remainder of this paper we will use the numerical simulation to focus on the effects of finite deformation.

The time-dependent response of these multiphase droplets is quite interesting. Before examining the transient behaviour that accompanies breakup we illustrate a typical response to a step change in shear rate for a uniaxial extensional flow. As discussed in Section 3, a globule placed in such a flow, deforms into a prolate spheroid ($D > 0$). At steady-state, the recirculating flow set up

in the annular region creates a biaxial extensional flow so that the inner droplet deforms into an oblate spheroid ($D < 0$). However, the approach to this steady configuration is quite interesting. Figure 10a,b shows plots of the deformation of the inner and outer interfaces as a function of time for the case of a step change in shear rate from $C = 0.04 \rightarrow C = 0.08$ in a uniaxial extensional flow. The other parameters are $\lambda_{21} = \lambda_{32} = 1.0$, $\Omega = 1.0$ and $\kappa = 0.5$.

The initial response of the globule to the step change in shear rate for a uniaxial extensional flow is to lengthen along the z -direction. This stretching process sets up a transient uniaxial stretching flow internal to the globule that results initially in a corresponding stretching of the inner droplet. Because the inner droplet has been deformed into an oblate spheroidal shape due to the biaxial character of the initial steady flow, the effect of this transient stretching process is to *decrease* the degree of deformation of the inner droplet. In other words, the inner droplet begins with a steady oblate shape and responds to the step change by deforming towards a spherical shape. However, as the new steady globule shape is approached, the flow in the annular region becomes a recirculating vortical motion (see figure 3, Section 3) and the inner droplet once again begins to stretch into an oblate spheroidal shape due to the biaxial character of the flow. Overall, the outer interface monotonically approaches the new steady shape, while the inner droplet relaxes initially then rapidly deforms back toward the shape it had prior to the step change. Finally, the inner droplet asymptotically approaches a new steady shape. The horizontal dashed lines in figures 10a and 10b denote the steady shapes observed at $C = 0.08$ by beginning with a spherical initial shape and making small increments in the capillary number ($\Delta C = 0.005$). Clearly, the same steady shape is determined using either large or small increments in the capillary number.

We next address the matter of finite deformation and breakup of compound double emulsion droplets. In figure 11 the solid curve shows a complete numerical simulation of the steady-state deformation as a function of capillary number

for a globule suspended in a uniaxial extensional flow ($\lambda_{21} = \lambda_{32} = 1.0, \Omega = 1.0$ and $\kappa = 0.5$). The dashed curve is the equivalent single phase droplet deformation. The lowest solid line is the absolute value of the deformation of the inner droplet. Numerically generated shapes are also shown. The numerical simulation is stopped when a steady shape is no longer calculated and the globule begins to stretch. The symbols are the theoretical results of Section 3.

This simulation is very informative. As mentioned above, the small deformation theory of Section 3 provides a good approximation to the actual deformation at small capillary numbers. Next, notice how the deformation is affected by the presence of the occluded particle. Initially, the deformation of the globule is significantly larger with the occluded droplet present than without it present. The increased deformation is maintained until the critical capillary number is approached. At $C \approx 0.116$ the globule begins to undergo a continuous stretching process so that breakup is characterized in this case by nonexistence of a steady drop shape. The numerics clearly indicate that the critical capillary number for breakup is lower with the inner droplet present than without it present. This was suggested by the small deformation analysis and stated first by Davis & Brenner (1981). However, it should be clear that the linear analysis presented in Section 3 is no longer valid near the critical capillary number as finite deformation has occurred. Also, the numerics indicate that the globule has a slightly more extended final steady shape with the occluded droplet present. However, the difference relative to the single phase droplet behaviour is small and because the determination of the steady shape is difficult as the critical capillary number is approached, the result mainly indicates that the overall globule shape changes very little due to the presence of the occluded particle. Nevertheless, it is easier to break. In this simulation the critical capillary number necessary for breakup is reduced by approximately five percent.

Finally, it is interesting to examine the deformation of the inner droplet. The inner droplet monotonically deforms until near the critical capillary num-

ber where its deformation levels off and then even decreases slightly. Overall, however, there is very little deformation since the radius of curvature is small and the flow strength internal to the globule is damped due to viscous dissipation. The steady-state velocity field in the annular region will still be biaxial in nature. Nevertheless, the leveling off of the deformation is due to a combination of hydrodynamic interaction between the finitely deformed fluid-fluid interfaces and the effect the deformed interface shapes have on the velocity field internal to the globule.

The time-dependent breakup process for the droplet considered in figure 11 is very interesting. In order to examine the dynamics of breakup, figure 12 presents a plot of the dimensionless globule length, $\frac{L_{outer}}{R_1}$, as a function of time at the critical capillary number (the solid curve). The evolution of the dimensionless inner droplet length, $\frac{L_{inner}}{R_2}$ is also plotted in this figure (the dashed curve). Numerically generated shapes are shown. Similar to the stretching of a single phase droplet, the extension is very slow initially. The extended character of the globule is similar to the breakup of single phase droplets at the critical capillary number. The midsection becomes cylindrical and as the globule becomes more extended it stretches more rapidly. The most important feature to notice is that as the globule begins to stretch, characteristic of nonexistence of a steady shape, the flow field internal to the globule is extensional so that the inner droplet also begins to lengthen and deforms into a prolate spheroidal shape. However, the thinning of the globule occurs more rapidly than the inner droplet can deform and the result is the formation of a very thin film between the two interfaces. Shortly after the final shape illustrated, the numerical scheme begins to introduce unrealistic oscillations on the inner surface. Additional collocation points are necessary to accurately describe the variations in interfacial velocity and stress that occur for these elongated globules with thin films between the surfaces. The formation of a thin film configuration suggests the possibility of breakup of this extended globule due to fracture at the middle

induced by the presence of the inner droplet. It might have been expected if the inner droplet also began to stretch, that at later times, the globule would begin to approach a configuration similar to a concentric multiphase fluid cylinder. However, it appears that breakup due to pinching about the occluded particle occurs instead.

In figure 13 we present another complete simulation of the steady-state deformation curve for a double emulsion drop in the case $\lambda_{21} = 1.0, \lambda_{32} = 10.0, \Omega = 1.0$ and $\kappa = 0.5$. Here we specifically examine the effect of a large viscosity of the occluded particle. The two solid curves represent the deformation of the outer and inner surfaces. The short dashed line is the deformation of a single phase droplet with $\lambda = 1.0$ and the long dashed line is the deformation of a single phase droplet with $\lambda = 10.0$ (for single phase drops λ represents the ratio of drop fluid viscosity to suspending fluid viscosity). Notice that the critical capillary number for breakup of the globule is bounded by the single phase droplet results. Also, the inner droplet is observed to deform monotonically until the critical capillary number is approached at which point the deformation levels off and decreases a little. This is similar to the deformation shown in figure 12. It is also interesting to notice how the single phase drop with $\lambda = 10.0$ is initially less deformed than the double emulsion droplet, but as the capillary number is increased the single phase drop deforms more and breaks at a lower capillary number.

The effect of changing λ_{32} is illustrated clearly in figure 14. Although the magnitude of the final steady-state deformations differ by a small amount, this calculation is very difficult and time-consuming close to the breakup point and presumably the actual differences are small. Nevertheless, at any given capillary number the globule (D_{outer}) is more deformed for larger viscosities of the internal droplet, as suggested by the small deformation analysis. Also, it is evident that as the viscosity of the inner droplet is increased the critical capillary number needed for breakup of the globule *decreases*. The breakup occurs via

the continuous stretching process characteristic of the nonexistence of a steady shape, as shown in figure 12.

In figure 15 we examine the deformation and breakup of a globule containing a large internal droplet. For this simulation we choose $\kappa = 0.8$, $\lambda_{21} = 1.0$, $\lambda_{32} = 1.0$ and $\Omega = 1.0$. In this case, the surfaces are separated initially by a small amount and it might be expected that any finite deformation can have a significant effect. On the plot of deformation versus capillary number, numerically generated globule shapes are included to illustrate the interfacial evolution. As in previous figures the effect of the uniaxial extensional flow is to deform the outer drop into a prolate spheroidal shape while the inner drop becomes oblate spheroidal. However, in this case, the numerics predict that at the globule center, the two interfaces make contact at $C = 0.066$. The calculations are stopped at this point. Physically, the numerical contact of the two interfaces suggests breakup of the globule as a consequence of the inner droplet breaking through the outer surface. The breakup of the globule occurs in this case without any large scale stretching. Although the numerics cannot capture the actual breakup process since intermolecular forces that become very important at small separations are not included, this example demonstrates a second mechanism of globule breakup.

The effect of κ on the globule deformation and the critical capillary number for breakup is illustrated in figure 16. Clearly, the conjecture, based on the small deformation analysis, that the presence of the occluded particle leads to lower capillary numbers for breakup, is indeed true. However, as illustrated in figure 15, the very low capillary number breakup suggested for $\kappa = 0.8$ is *not* a consequence of large deformation of the globule, but rather occurs due to the inner drop making contact with the outer surface.

Finally, we consider the case of a globule suspended in a *biaxial* extensional flow. Figure 17 shows the deformation versus capillary number plot and also presents intermediate steady shapes typical of the deformation process. The

parameters chosen are $\lambda_{21} = \lambda_{32} = 1.0$, $\kappa = 0.5$ and $\Omega = 0.1$. In this case the biaxial flow deforms the globule into an oblate spheroidal shape and the steady *uniaxial* flow established in the annular region deforms the inner drop into a prolate spheroidal shape. Because lower capillary numbers are needed for breakup of a droplet in uniaxial extensional flows we have purposely chosen a low value of Ω . Clearly, the outer droplet deforms very little. However, viscous stresses generated internal to the globule stretch the occluded droplet into a rather extended prolate spheroid. Even though the flow is damped in the annular region, the low value of Ω coupled with the uniaxial nature of the flow field in the annular region produces a large distortion of the inner droplet. The deformation of the inner droplet is approaching the most highly deformed steady shape observed for a single phase drop suspended in an unbounded uniaxial extensional flow. This suggests that the inner drop may undergo breakup even though the outer drop is itself not very deformed. Shortly after the final steady shape shown the numerical scheme begins to break down and additional collocation points and a smaller time step are necessary to continue the calculations further. Nevertheless, this example illustrates that, in some instances, the effect of flow-type coupled with the flow-induced deformation *internal* to the double emulsion droplet can produce large distortions.

5. CONCLUSIONS

The analytic and numerical results presented above are very informative with regard to the deformation and possible breakup mechanisms of double emulsion droplets in extensional flows. In addition, the simulations provide insight as to when analogies with single phase droplet behaviour may be useful. The most important observations are:

- (1) The effective viscosity of a dilute emulsion of these drops behaves like a suspension of solid spheres in the limit of almost equal-sized inner and encapsulating drops, $\kappa \rightarrow 1$.
- (2) A uniaxial extensional flow deforms the globule into a prolate spheroidal

shape while the steady recirculating flow generated in the annular region deforms the occluded drop into an oblate spheroidal shape. The reverse holds for a globule placed in a biaxial extensional flow.

- (3) The presence of the internal droplet produces breakup at a lower value of the capillary number than is necessary if no third phase was present. Also, as the viscosity of the occluded phase is increased, the critical capillary number for breakup decreases.
- (4) For $\kappa < 0.5$ breakup of the globule occurs by a continuous stretching mode. However, for $\kappa \approx 0.8$ the inner and outer interfaces make contact even though the globule is not very deformed. This suggests an alternative mechanism for breakup.
- (5) The application of a biaxial flow produces a uniaxial flow internal to the globule that is capable of producing large distortions of the occluded drop. For a low value of the interfacial tension of the inner drop ($\Omega = 0.1$), a simulation is illustrated suggesting breakup of the inner phase even though the outer drop is not very deformed.

ACKNOWLEDGEMENTS

This work was supported by a grant from the fluid mechanics program of the National Science Foundation. One of the authors (HAS) was partially supported through an IBM Graduate Research Fellowship.

APPENDIX A

In this appendix we report the form of the stress fields corresponding to the velocity and pressure fields reported in section III. They are :

$$\begin{aligned} \mathbf{T}_1(\mathbf{x}) = & 2\mathbf{E} + \frac{(\mathbf{B}_1 \cdot \mathbf{x})\mathbf{x} + \mathbf{x}(\mathbf{B}_1 \cdot \mathbf{x})}{r^5} - 5\frac{\mathbf{xx}(\mathbf{x} \cdot \mathbf{B}_1 \cdot \mathbf{x})}{r^7} - 20\frac{(\mathbf{C}_1 \cdot \mathbf{x})\mathbf{x}}{r^7} \\ & - 20\frac{\mathbf{x}(\mathbf{C}_1 \cdot \mathbf{x})}{r^7} - 10\frac{\mathbf{I}(\mathbf{x} \cdot \mathbf{C}_1 \cdot \mathbf{x})}{r^7} + 70\frac{\mathbf{xx}(\mathbf{x} \cdot \mathbf{C}_1 \cdot \mathbf{x})}{r^9} + 4\frac{\mathbf{C}_1}{r^5} \\ & - 3\left[\frac{\mathbf{x}(\mathbf{D}_1 \wedge \mathbf{x}) + (\mathbf{D}_1 \wedge \mathbf{x})\mathbf{x}}{r^5}\right] \end{aligned}$$

$$\begin{aligned} \mathbf{T}_2(\mathbf{x}) = & 2\mathbf{F}_2 + \frac{(\mathbf{B}_2 \cdot \mathbf{x})\mathbf{x} + \mathbf{x}(\mathbf{B}_2 \cdot \mathbf{x})}{r^5} - 5\frac{\mathbf{xx}(\mathbf{x} \cdot \mathbf{B}_2 \cdot \mathbf{x})}{r^7} - 20\frac{(\mathbf{C}_2 \cdot \mathbf{x})\mathbf{x}}{r^7} \\ & - 20\frac{\mathbf{x}(\mathbf{C}_2 \cdot \mathbf{x})}{r^7} - 10\frac{\mathbf{I}(\mathbf{x} \cdot \mathbf{C}_2 \cdot \mathbf{x})}{r^7} + 70\frac{\mathbf{xx}(\mathbf{x} \cdot \mathbf{C}_2 \cdot \mathbf{x})}{r^9} + 4\frac{\mathbf{C}_2}{r^5} \\ & - 3\left[\frac{\mathbf{x}(\mathbf{D}_2 \wedge \mathbf{x}) + (\mathbf{D}_2 \wedge \mathbf{x})\mathbf{x}}{r^5}\right] + \frac{6}{21}[\mathbf{x}(\mathbf{H}_3 \cdot \mathbf{x}) + (\mathbf{H}_3 \cdot \mathbf{x})\mathbf{x}] \\ & + \frac{10}{21}r^2\mathbf{H}_3 - \frac{25}{21}\mathbf{I}(\mathbf{x} \cdot \mathbf{H}_3 \cdot \mathbf{x}) \end{aligned}$$

$$\mathbf{T}_3(\mathbf{x}) = 4\mathbf{F}_3 + \frac{6}{21}[\mathbf{x}(\mathbf{H}_3 \cdot \mathbf{x}) + (\mathbf{H}_3 \cdot \mathbf{x})\mathbf{x}] + \frac{10}{21}r^2\mathbf{H}_3 - \frac{25}{21}\mathbf{I}(\mathbf{x} \cdot \mathbf{H}_3 \cdot \mathbf{x})$$

APPENDIX B

In this appendix we report the form of the tensor functions \mathbf{B}_1 , \mathbf{C}_1 , etc. Because of the linear nature of the problem each of these functions is proportional to the rate-of-strain tensor \mathbf{E} and we denote these functions as

$$\mathbf{B}_1 = B_1 \mathbf{E}$$

$$\mathbf{C}_1 = C_1 \mathbf{E}$$

etc.

The scalar functions B_1 , C_1 , etc. are listed below:

$$B_1 = \frac{3[(4 - 25\kappa^3 + 42\kappa^5 - 25\kappa^7 + 4\kappa^{10}) + \frac{\kappa^3}{1+\lambda_{32}}(15 - 42\kappa^2 + 35\kappa^4 - 8\kappa^7)]}{\eta_1 + \frac{\kappa^3}{1+\lambda_{32}}\eta_2} - 5$$

$$B_2 = \frac{3[\kappa^3(10 - 14\kappa^2 + 4\kappa^7) + \frac{\kappa^3}{1+\lambda_{32}}2(-3 + 7\kappa^2 - 4\kappa^7)]}{\eta_1 + \frac{\kappa^3}{1+\lambda_{32}}\eta_2}$$

$$C_1 = \frac{\frac{1}{2}[(4 - 25\kappa^3 + 42\kappa^5 - 25\kappa^7 + 4\kappa^{10}) + \frac{\kappa^3}{1+\lambda_{32}}(15 - 42\kappa^2 + 35\kappa^4 - 8\kappa^7)]}{\eta_1 + \frac{\kappa^3}{1+\lambda_{32}}\eta_2} - \frac{1}{2}$$

$$C_2 = \frac{\kappa^5(3 - 5\kappa^2 + 2\kappa^5) + \frac{\kappa^3}{1+\lambda_{32}}\kappa^2(-3 + 7\kappa^2 - 4\kappa^5)}{\eta_1 + \frac{\kappa^3}{1+\lambda_{32}}\eta_2}$$

$$F_2 = -\frac{\frac{3}{2}[(2 - 7\kappa^5 + 5\kappa^7) + \frac{\kappa^3}{1+\lambda_{32}}7\kappa^2(1 - \kappa^2)]}{\eta_1 + \frac{\kappa^3}{1+\lambda_{32}}\eta_2}$$

$$F_3 = -\frac{\frac{3}{2(1+\lambda_{32})}(-3 + 7\kappa^2 - 7\kappa^5 + 3\kappa^7)}{\eta_1 + \frac{\kappa^3}{1+\lambda_{32}}\eta_2}$$

$$H_2 = \frac{21[(2 - 5\kappa^3 + 3\kappa^5) + \frac{\kappa^3}{1+\lambda_{32}}3(1 - \kappa^2)]}{\eta_1 + \frac{\kappa^3}{1+\lambda_{32}}\eta_2}$$

$$H_3 = \frac{\frac{21}{\kappa^2(1+\lambda_{32})}(-3 + 7\kappa^2 - 7\kappa^5 + 3\kappa^7)}{\eta_1 + \frac{\kappa^3}{1+\lambda_{32}}\eta_2}$$

where

$$\eta_1 = (4 - 25\kappa^3 + 42\kappa^5 - 25\kappa^7 + 4\kappa^{10}) + \lambda_{21}(4 - 10\kappa^3 + 10\kappa^7 - 4\kappa^{10})$$

$$\eta_2 = (15 - 42\kappa^2 + 35\kappa^4 - 8\kappa^7) + \lambda_{21}(6 - 14\kappa^4 + 8\kappa^7)$$

Finally, we give the shape functions h_{21} and h_{32} that describe the first flow-induced changes in drop shape (see equation 24):

$$\begin{aligned} h_{21} = & 5 + [-(6 + 4\lambda_{21}) + (30\kappa^3 - 24\kappa^5)(1 - \lambda_{21})]F_2 \\ & + [(-3 + 63\kappa^5 - 60\kappa^7)(1 - \lambda_{21})]H_2 + (-30\kappa^3 + 24\kappa^5)(1 - \lambda_{21})F_3 \\ & + (-63\kappa^5 + 60\kappa^7)(1 - \lambda_{21})H_3 \end{aligned}$$

and

$$h_{32} = 10F_2 - (6 + 4\lambda_{32})F_3 - 3\kappa^2(1 - \lambda_{32})H_3.$$

REFERENCES

- Acrivos, A. 1983 The breakup of small drops and bubbles in shear flows. *4th Int Conf. on Physicochemical Hydrodynamics, Ann. N.Y. Acad. Sci.* **404**, 1-11.
- Ascoli, E.P. & Leal, L.G. 1987 Drop deformation and drag due to motion normal to a planar wall. (in preparation).
- Barthes-Biesel, D. & Acrivos, A. 1973a Deformation and burst of a liquid droplet freely suspended in a linear shear field. *J. Fluid Mech.* **61**, 1-21.
- Barthes-Biesel, D. & Acrivos, A. 1973b The rheology of suspensions and its relation to phenomenological theories for non-Newtonian fluids. *Intl J. Multiphase Flow* **1**, 1-24.
- Barthes-Biesel, D. 1980 Motion of a spherical microcapsule freely suspended in a linear shear flow. *J. Fluid Mech.* **100**, 831-853.
- Barthes-Biesel, D. & Rallison, J.M. 1981 The time-dependent deformation of a capsule freely suspended in a linear shear flow. *J. Fluid Mech.* **113**, 251-267.
- Batchelor, G.K. 1970 The stress system in a suspension of force-free particles. *J. Fluid Mech.* **41**, 545-570.
- Bentley, B.J. & Leal, L.G. 1986 An experimental investigation of drop deformation and breakup in steady two-dimensional linear flows. *J. Fluid Mech.* **167**, 241-283.
- Brunn, P. 1980 On the rheology of viscous drops surrounded by an elastic shell. *Biorheology* **17**, 419-430.
- Brunn, P.O. 1982 The general solution to the equations of creeping motion of a micropolar fluid and its application. *Intl J. Engng. Sci.* **20**, 575-585.
- Brunn, P.O. 1983 The deformation of a viscous particle surrounded by an elastic shell in a general time-dependent linear flow field. *J. Fluid Mech.* **126**, 533-544.

- Brunn, P.O. & Roden, T. 1985 On the deformation and drag of a type-A multiple drop at low Reynolds number. *J. Fluid Mech.* **160**, 211-234.
- Chervenivanova & Zapryanov 1987 On the deformation of compound multiphase drops at low Reynolds number. Submitted to *Int. J. Multiphase Flow*.
- Cox, R.G. 1969 The deformation of a drop in a general time-dependent fluid flow. *J. Fluid Mech.* **37**, 601-623.
- Davis, A.M.J. & Brenner, H. 1981 Emulsions containing a third solid internal phase. *J. Eng. Mech. Div., ASCE* **107**, 609-621.
- Florence, A.T. & Whitehill, D. 1981 Some features of breakdown in water-in-oil-in-water multiple emulsions. *J. Colloid Interface Sci.* **79**, 243-256.
- Frankel, N.A. & Acrivos, A. 1970 The constitutive equation for a dilute emulsion. *J. Fluid Mech.* **44**, 65-78.
- Grace, H.P. 1971 Dispersion phenomena in high viscosity immiscible fluid systems and application of static mixers as dispersion devices in such systems. *Eng. Found. Res. Conf. Mixing, 3rd Andover, N.H.* Republished 1982 in *Chem. Engng Commun.* **14**, 225-277.
- Johnson, R.E. 1981 Stokes flow past a sphere coated with a thin fluid film. *J. Fluid Mech.* **110**, 217-238.
- Johnson, R.E. & Sadhal, S.S. 1983 Stokes flow past bubbles and drops partially coated with thin films. Part 2. Thin films with internal circulation - a perturbation solution. *J. Fluid Mech.*, **132**, 295-318.
- Johnson, R.E. & Sadhal, S.S. 1985 Fluid mechanics of compound multiphase drops and bubbles. *Ann. Rev. Fluid Mech.* **17**, 289-320.
- Kang, I.S. & Leal, L.G. 1987 Numerical solution of axisymmetric, unsteady free-boundary problems at finite Reynolds number I. Finite-difference scheme and its application to the deformation of a bubble in a uniaxial straining flow. *Phys. Fluids* **7**, 1929-1940.

- Kang, I.S. & Leal, L.G. 1988 Numerical solution of axisymmetric, unsteady free-boundary problems at finite Reynolds number II. Deformation of a bubble in a biaxial straining flow (in preparation).
- Ladyzhenskaya, O. 1969 *The Mathematical Theory of Viscous Incompressible Flow*. New York: Gordon & Breach. 2nd ed.
- Lamb, H. 1932 *Hydrodynamics* 6th ed. Dover Publications.
- Lee, S.H. & Leal, L.G. 1982 The motion of a sphere in the presence of a deformable interface. II. A numerical study of the translation of a sphere normal to an interface. *J. Colloid Interface Sci.* **87**, 81-106.
- Li, N.N. 1971a Separation of hydrocarbons by liquid membrane permeation. *Ind. Eng. Chem. Process Des. Dev.* **10**, 215-221.
- Li, N.N. 1971b Permeation through liquid surfactant membranes. *AIChE J.* **17**, 459-463.
- Maugh II., T.H. 1976 Liquid membranes: New techniques for separation, purification. *Science* **193**, 134-137.
- Olbricht, W.L., Rallison, J.M. & Leal, L.G. 1982 Strong flow criteria based on microstructure deformation. *J. Non-Newtonian Fluid Mech.* **10**, 291-318.
- Rallison, J.M. 1980 Note on the time-dependent deformation of a viscous drop which is almost spherical. *J. Fluid Mech.* **98**, 625-633.
- Rallison, J.M. 1981 A numerical study of the deformation and burst of a viscous drop in general shear flows. *J. Fluid Mech.* **109**, 465-482.
- Rallison, J.M. 1984 The deformation of small viscous drops and bubbles in shear flows. *Ann. Rev. Fluid Mech.* **16**, 45-66.
- Rallison, J.M. & Acrivos, A. 1978 A numerical study of the deformation and burst of a viscous drop in an extensional flow. *J. Fluid Mech.* **89**, 191-200.
- Rushton, E. & Davies, G.A. 1983 Settling of encapsulated droplets at low Reynolds numbers. *Intl J. Multiphase Flow* **9**, 337-342.

- Sadhal, S.S. & Oguz, H.N. 1985 Stokes flow past compound multiphase drops: the case of completely engulfed drops/bubbles. *J. Fluid Mech.* **160**, 511-529.
- Sapir, T. & Nir, A. 1985 A hydrodynamic study of the furrowing stage during cleavage. *Physicochemical Hydrodynamics* **6**, 803-814.
- Schowalter, W.R., Chaffey, C.E. & Brenner, H. 1968 Rheological behaviour of a dilute emulsion. *J. Colloid Interface Sci.* **26**, 152-160.
- Sherwood, J.D., 1987 Drop breakup in electric and magnetic fields. (to appear).
- Stone, H.A. & Leal, L.G. 1987 Relaxation and breakup of an initially extended drop in an otherwise quiescent fluid. *J. Fluid Mech.* (submitted).
- Stone, H.A. 1988 Dynamics of drop breakup at low Reynolds number. *Ph.D. Thesis* California Institute of Technology.
- Stoos, J.A. & Leal, L.G. 1987 The creeping motion of a spherical particle in a linear axisymmetric straining flow normal to a deformable interface. *J. Fluid Mech.* (submitted).
- Stroevé, P. & Varanasi, P.P. 1982 Transport processes in liquid membranes: double emulsion separation systems. *Sep. Purif. Methods* **11**, 29-69.
- Stroevé, P. & Varanasi, P.P. 1984 An experimental study on double emulsion drop breakup in uniform shear flow. *J. Colloid Interface Sci.* **99**, 360-373.
- Taylor, G.I. 1932 The viscosity of a fluid containing small drops of another fluid. *Proc. R. Soc. Lond.* **A138**, 41-48.
- Taylor, G.I. 1934 The formation of emulsions in definable fields of flow. *Proc. R. Soc. Lond.* **A146**, 501-523.
- Torza, S. & Mason, S.G. 1969 Coalescence of two immiscible liquid drops. *Science* **163**, 813-814.
- Torza, S. & Mason, S.G. 1970 Three-phase interactions in shear and electrical fields. *J. Colloid Interface Sci.* **33**, 67-83.

Tsamopoulos, J.A. & Brown, R.A. 1987 Dynamic centering of liquid shells.

Phys. Fluids **30**, 27-35.

Ulbrecht, J.J., Stroeve, P. & Prabodh P. 1982 Behaviour of double emulsions in

shear flows. *Rheo. Acta* **21**, 593-597.

Youngren, G.K. & Acrivos, A. 1975 Stokes flow past a particle of arbitrary shape;

a numerical method of solution. *J. Fluid Mech.* **69**, 377-403 (corrigendum

69, 813).

FIGURE CAPTIONS

- Figure 1 Concentric double emulsion droplet. Definition of variables.
- Figure 2 Streamlines in and around the compound droplet as a function of the internal droplet size, $\lambda_{21} = \lambda_{32} = 1.0$. (a) $\kappa = 0.2$; (b) $\kappa = 0.5$; (c) $\kappa = 0.8$.
- Figure 3 Deformation of a double emulsion droplet in a uniaxial extensional flow; $C = 0.0, 0.04, 0.08, 0.12$.
- Figure 4 Deformation of a double emulsion droplet in a biaxial extensional flow; $C = 0.0, 0.04, 0.08, 0.12$.
- Figure 5 Overall globule deformation D_{outer} as a function of capillary number. $\kappa = 0.1, 0.3, 0.5$ and 0.7 . The $\kappa = 0.7$ curve is stopped when the analysis predicts that the interfaces overlap.
- Figure 6 Deformation of the inner and outer droplets due to varying λ_{32} . (a),(b) $\kappa = 0.5$; (c),(d) $\kappa = 0.1$. $\lambda_{21} = 1.0$, $\Omega = 1.0$.
- Figure 7 Deformation of the inner and outer droplets due to varying λ_{21} . (a),(b) $\kappa = 0.5$; (c),(d) $\kappa = 0.1$. $\lambda_{32} = 1.0$, $\Omega = 1.0$.
- Figure 8 The velocity profile in the annular region of the globule in the limit $\kappa \rightarrow 1.0$. $\kappa = 0.95$. The boundary of the globule acts effectively as a noslip surface in this limit so that a dilute emulsion of these droplets behaves as a suspension of rigid spheres.
- Figure 9 A comparison of numerical and theoretical predictions for globule deformation and wide range of parameter values. (a) D_{outer} vs. C (b) D_{inner} vs. C . Typically agreement is good at low capillary numbers, but worsens as the capillary number, and hence the deformation, increases.
- Figure 10 Time-dependent response of the globule deformation to a step change in shear rate, $C = 0.04 \rightarrow C = 0.08$. (a) D_{outer} vs. time (b) D_{inner} vs. time. The dashed horizontal line indicates the steady state established by approaching $C = 0.08$ using small increments in the capillary

number. $\lambda_{21} = 1.0, \lambda_{32} = 1.0, \Omega = 1.0, \kappa = 0.5$.

Figure 11 Complete numerical simulation of deformation as a function of the capillary number in a uniaxial extensional flow. $\lambda_{21} = \lambda_{32} = 1.0, \Omega = 1.0, \kappa = 0.5$. Several numerically generated steady shapes are included. The upper solid line represents D_{outer} vs. C , the lower solid line represents $|D_{inner}|$ vs. C and the symbols are predictions of the small deformation theory. The dashed curve represents the deformation of a single phase droplet of comparable viscosity. The curves are stopped when breakup is indicated by continuous stretching of the droplet.

Figure 12 Globule length versus time for elongation at a slightly supercritical capillary number. The solid curve is the globule length $\frac{L_{outer}}{R_1}$ and the dashed curve is the length of the inner droplet $\frac{L_{inner}}{R_2}$.

Figure 13 Double emulsion deformation as a function of capillary number for a viscous occluded particle. $\lambda_{21} = 1.0, \lambda_{32} = 10.0, \kappa = 0.5$ and $\Omega = 10.0$. The solid curves are the outer and inner droplet deformations respectively. The short dashed line is a single phase droplet with $\lambda = 1.0$ and the long dashed line is a single phase droplet with $\lambda = 10.0$.

Figure 14 The effect of λ_{32} on drop deformation and the critical capillary number for breakup. $\lambda_{21} = 1.0, \Omega = 1.0$ and $\kappa = 0.5$.

Figure 15 Deformation as a function of capillary number for a large internal droplet. $\lambda_{21} = \lambda_{32} = 1.0, \Omega = 1.0$ and $\kappa = 0.8$.

Figure 16 The effect of κ on the deformation as a function of capillary number and effect on the critical capillary number necessary for breakup. The curve for $\kappa = 0.3$ shows the same trends as smaller κ and the calculation is stopped at an intermediate deformation.

Figure 17 Deformation of a double emulsion droplet in a biaxial extensional flow. $\lambda_{21} = \lambda_{32} = 1.0, \kappa = 0.5$ and $\Omega = 0.1$.

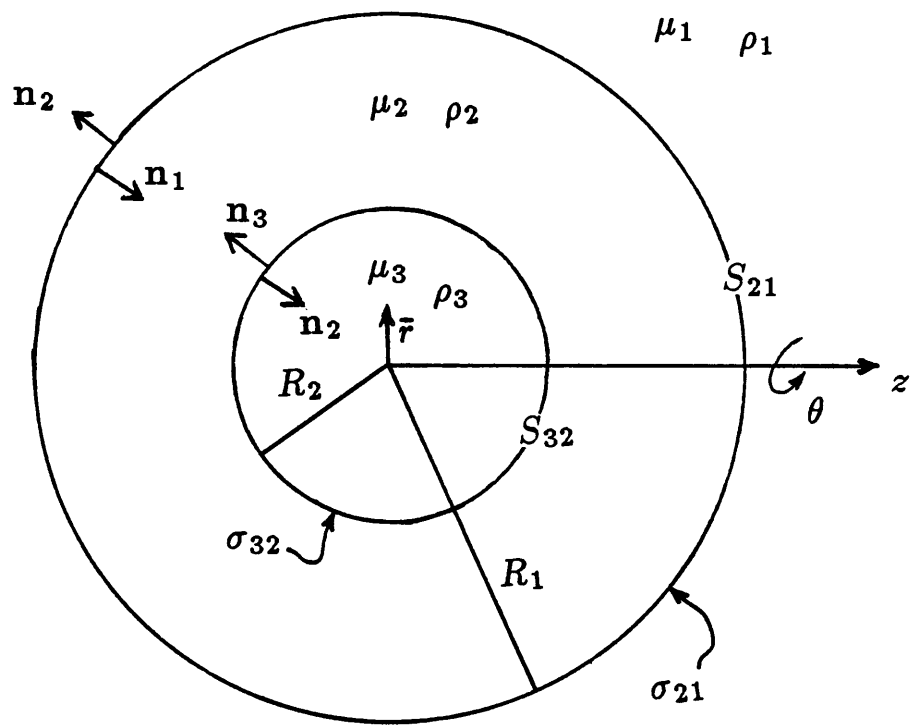


Figure 1

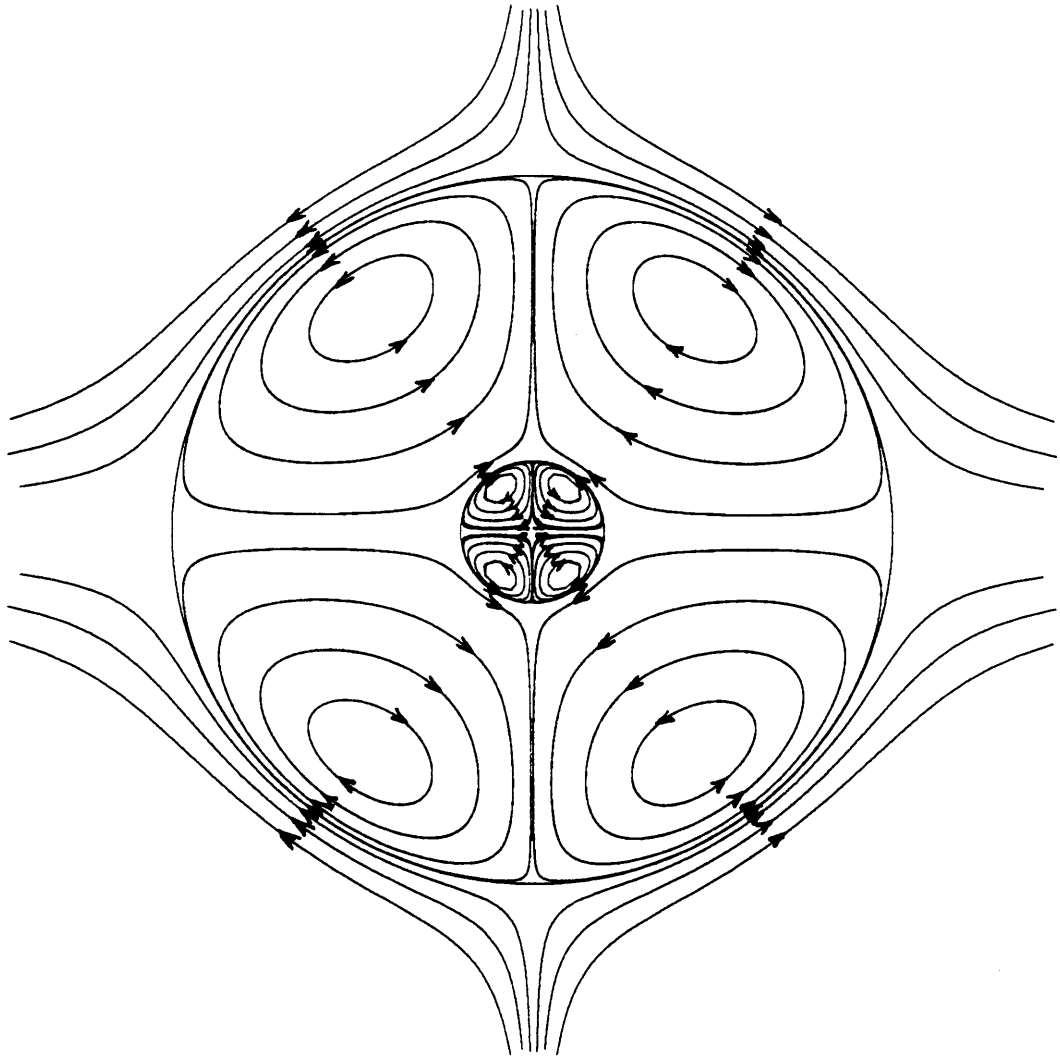


Figure 2a

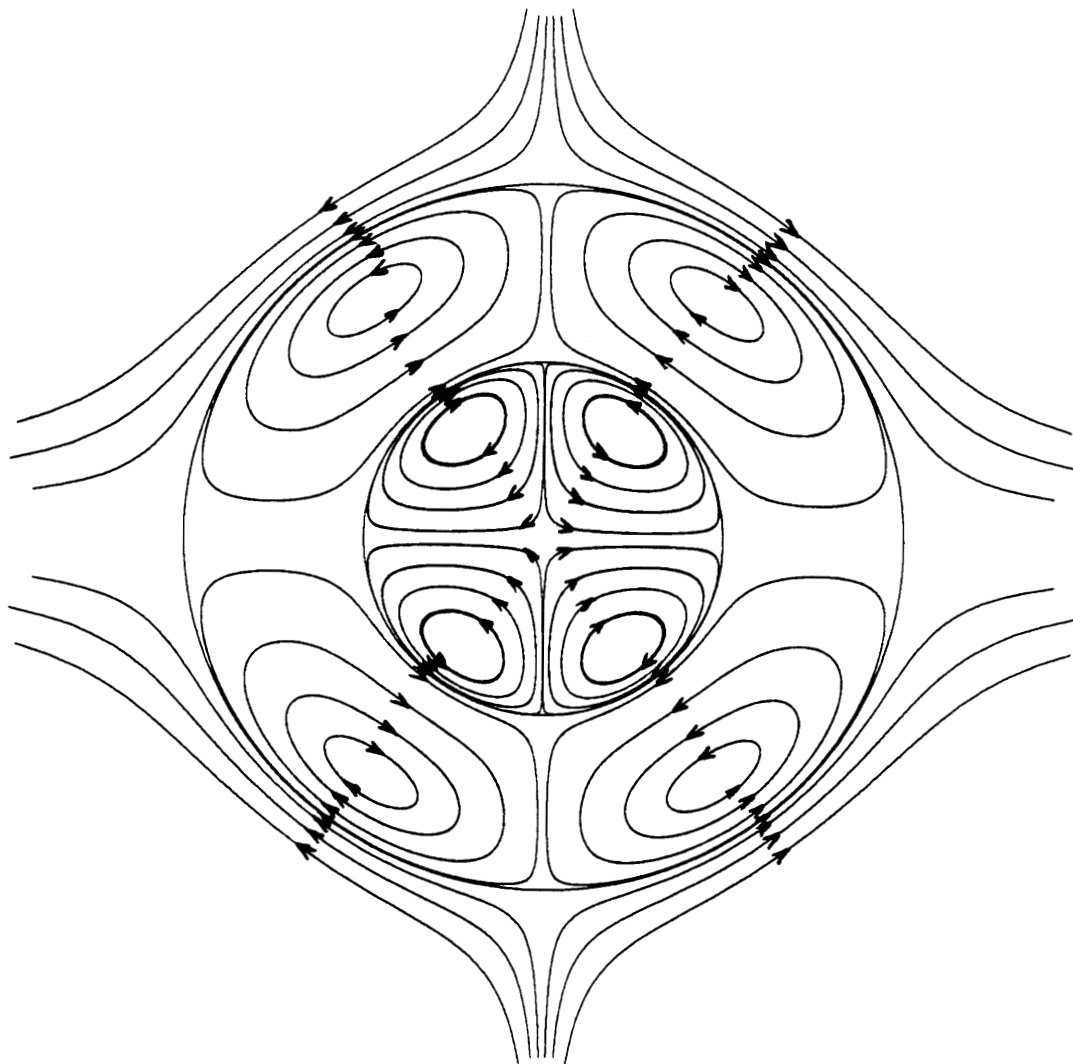


Figure 2b

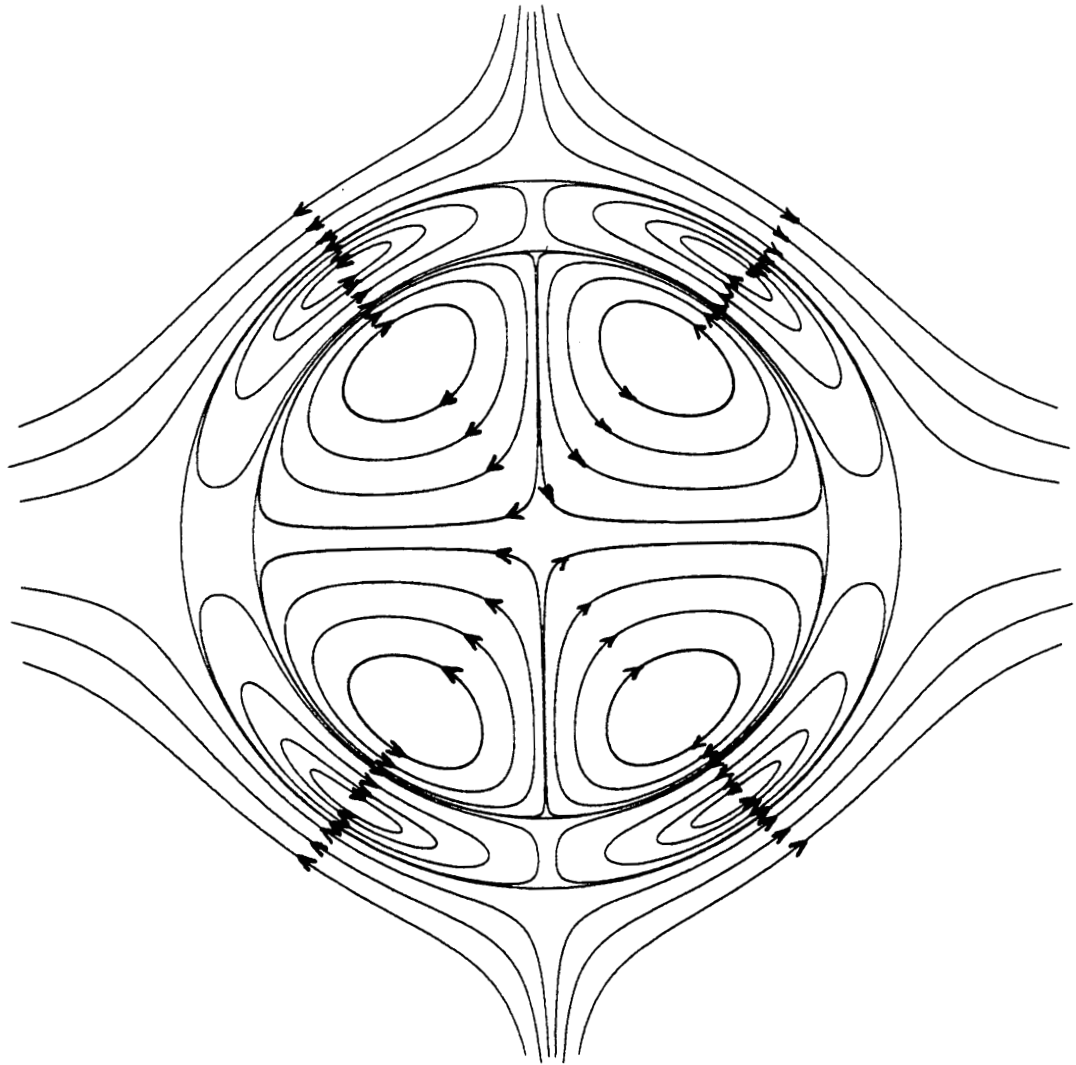


Figure 2c

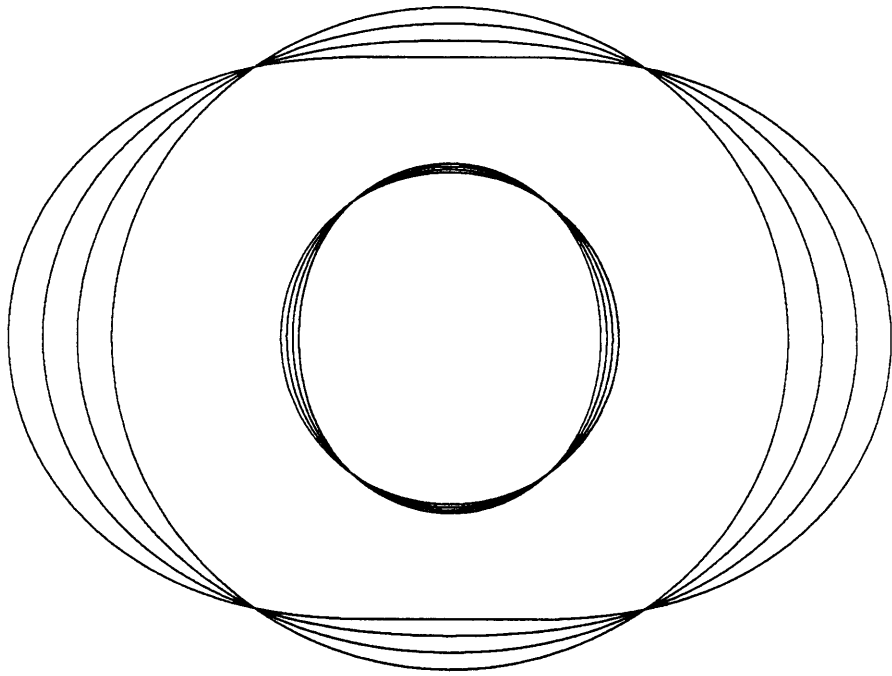


Figure 3

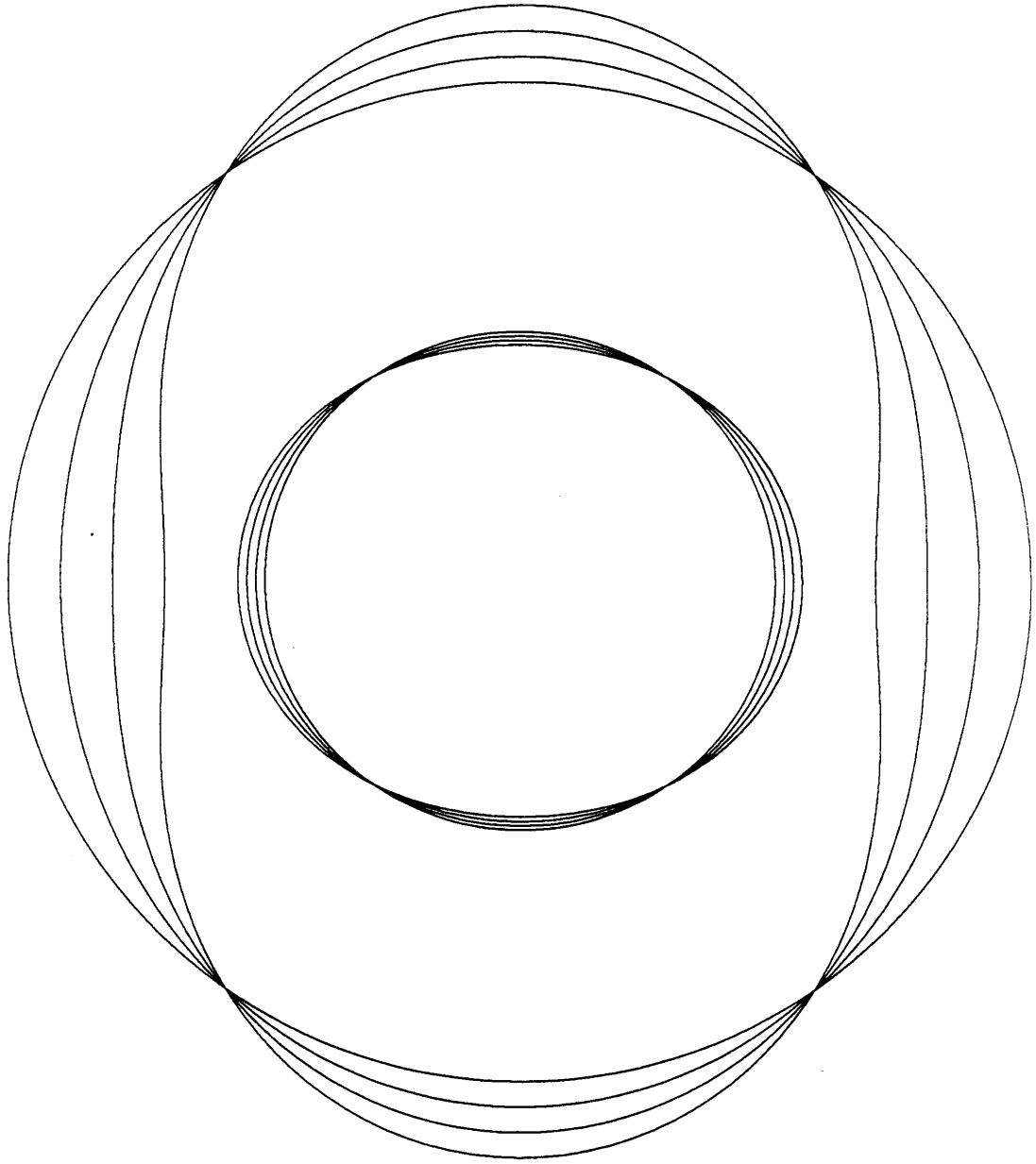


Figure 4

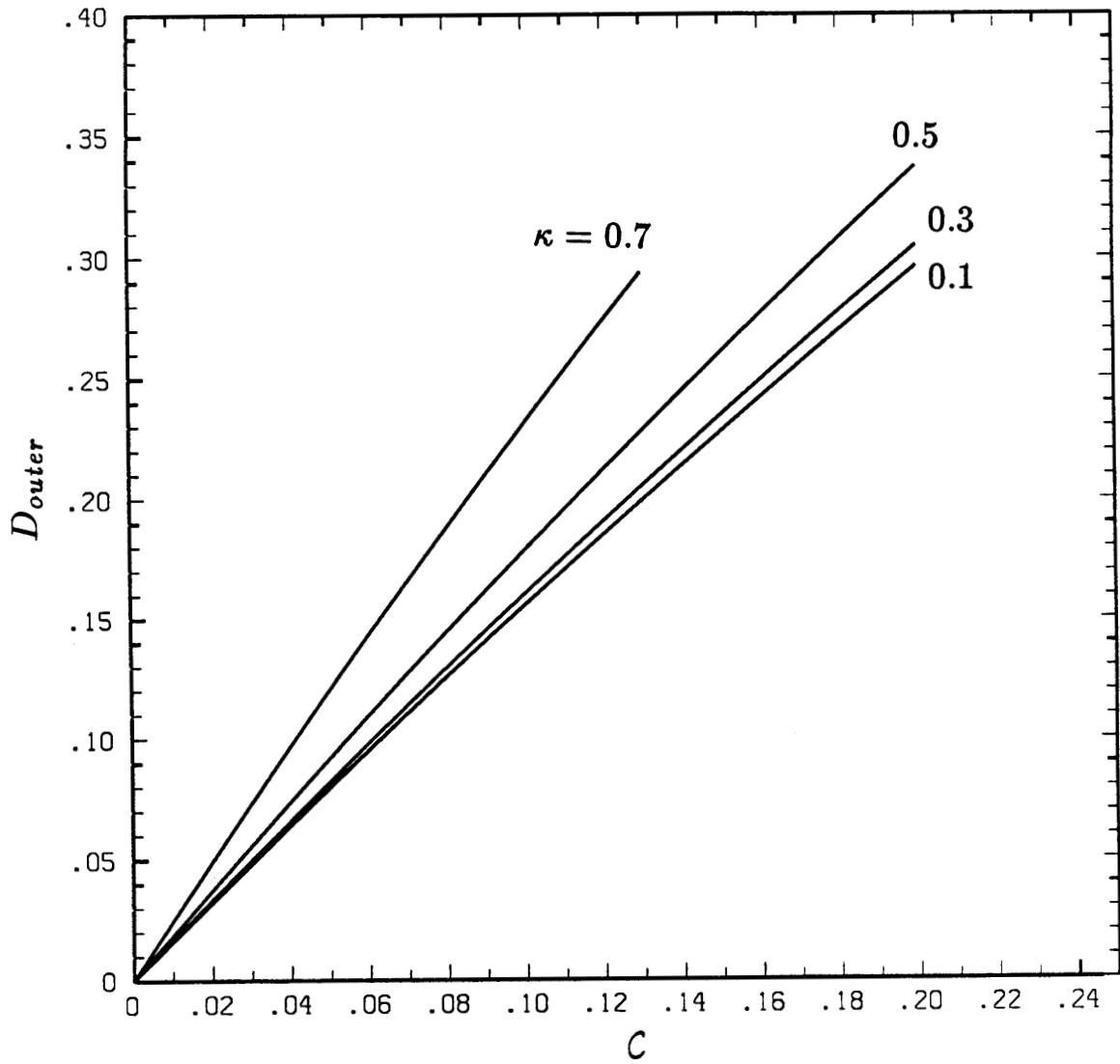


Figure 5

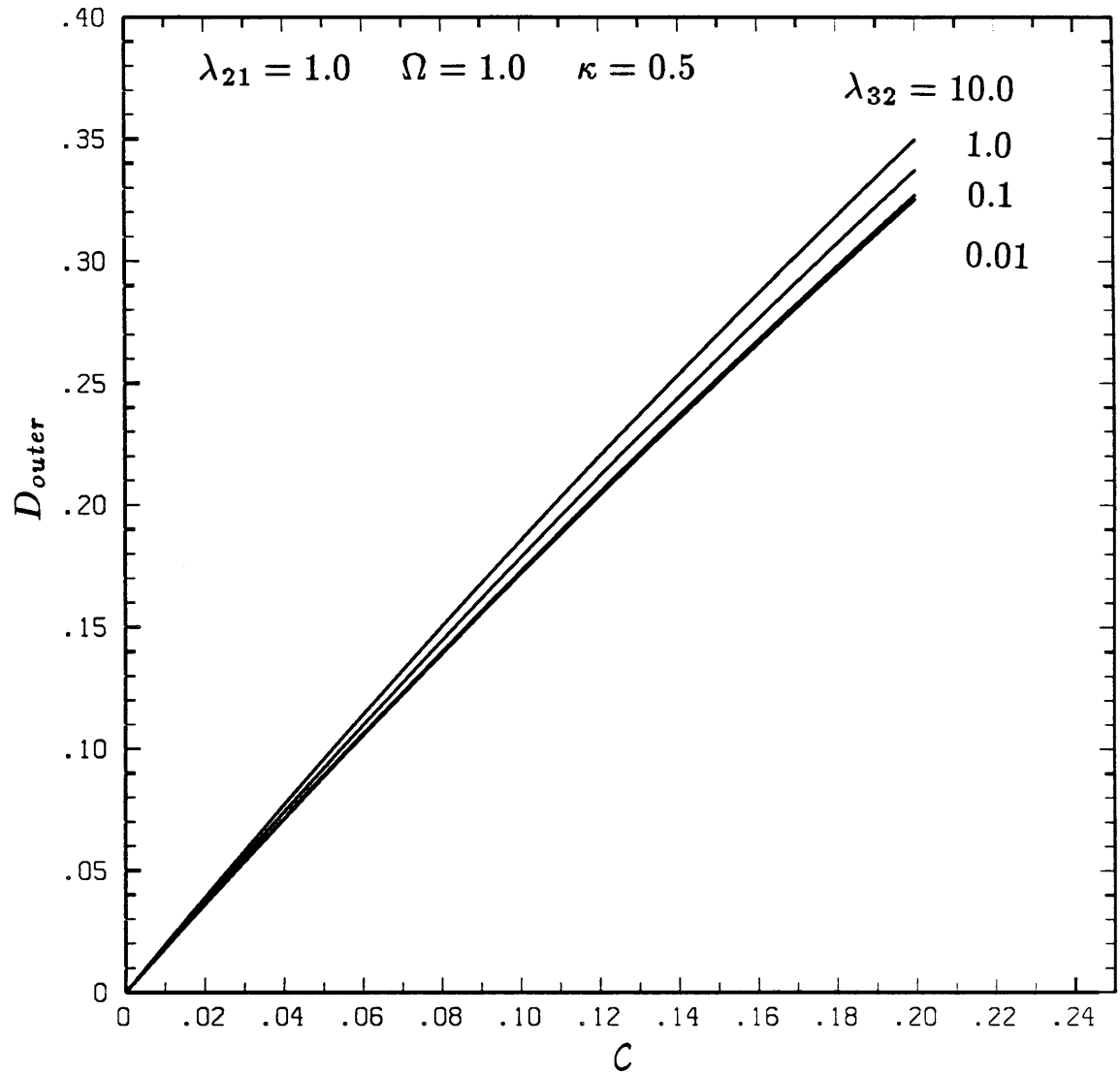


Figure 6a

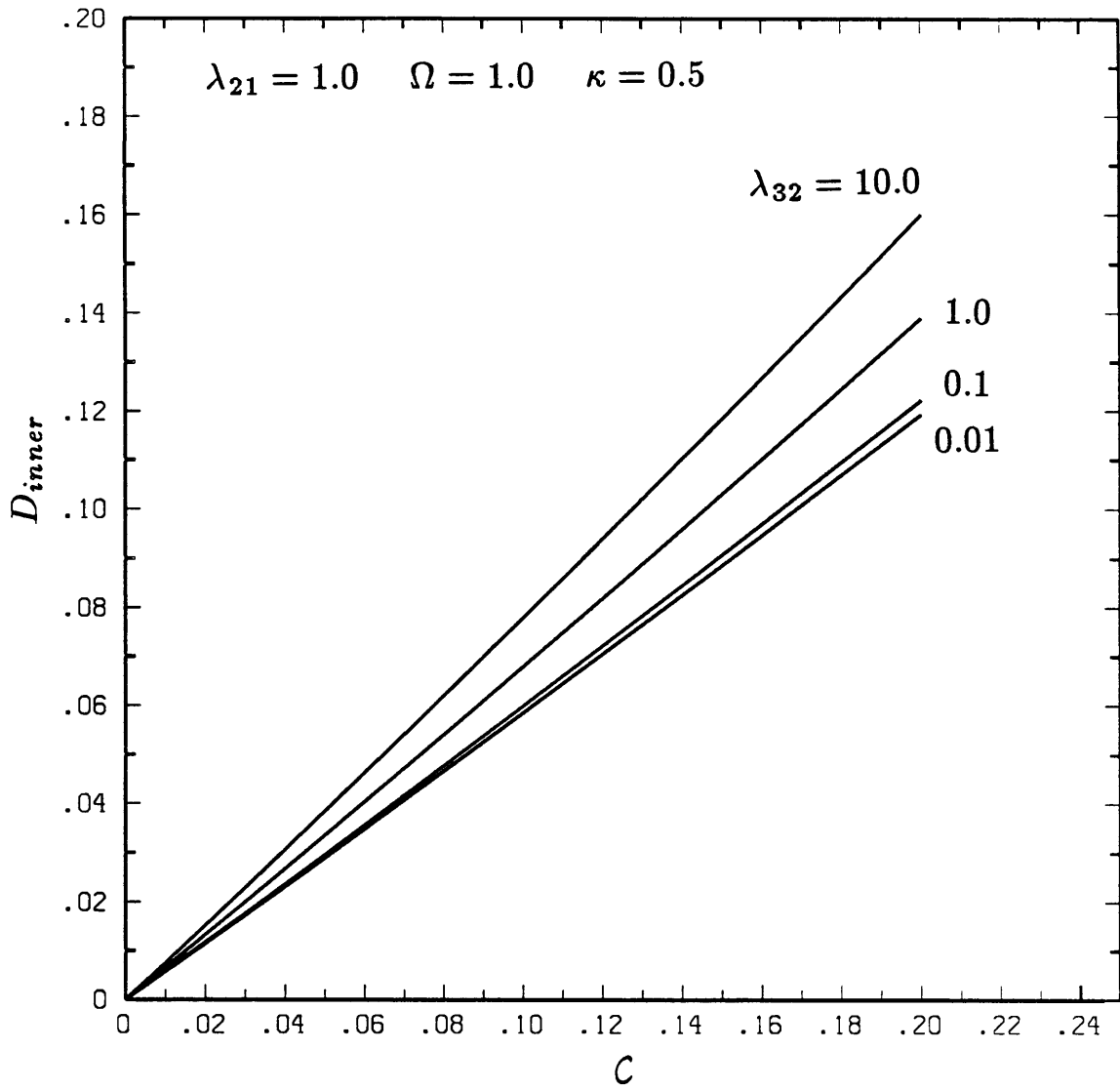


Figure 6b

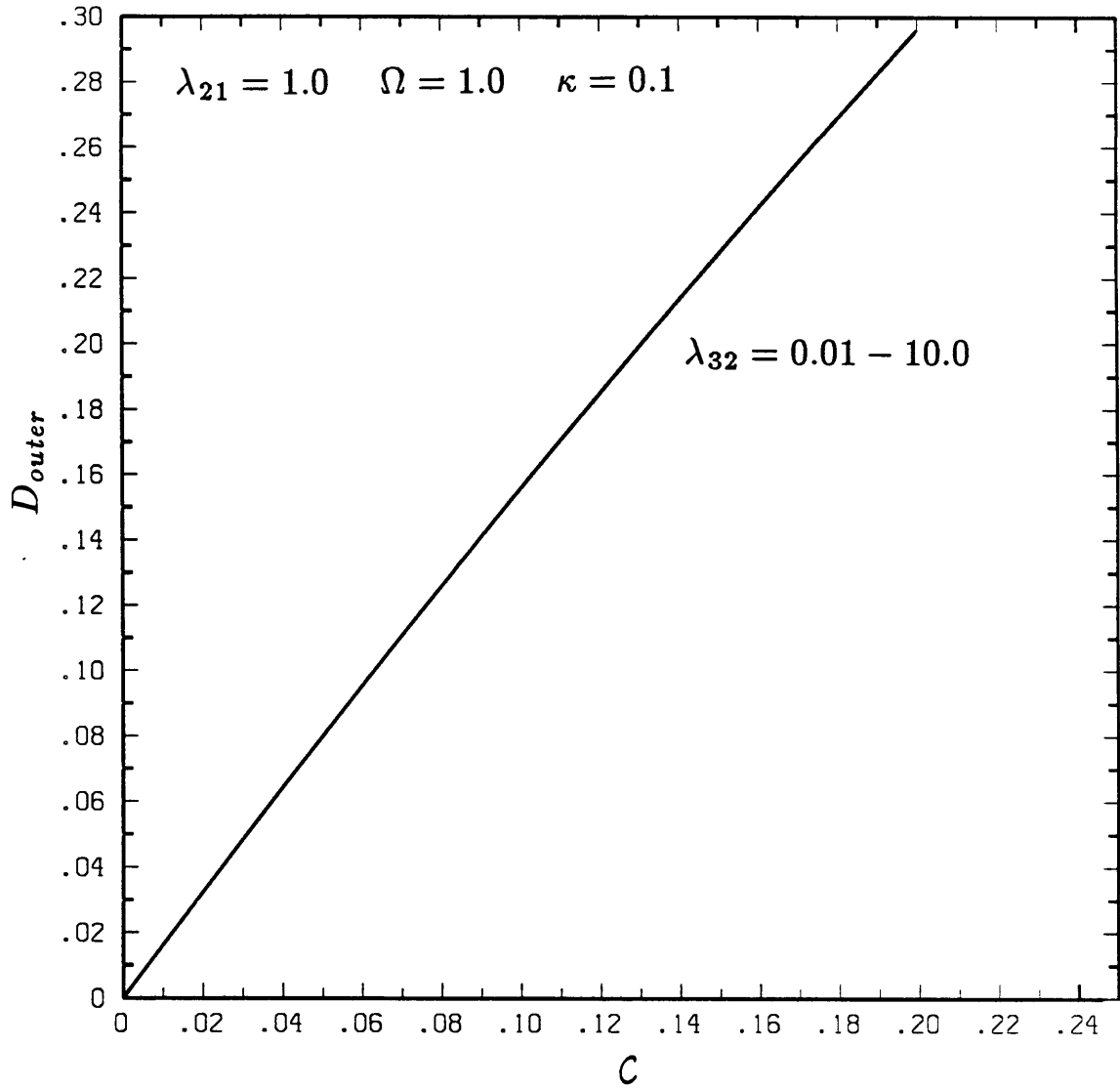


Figure 6c

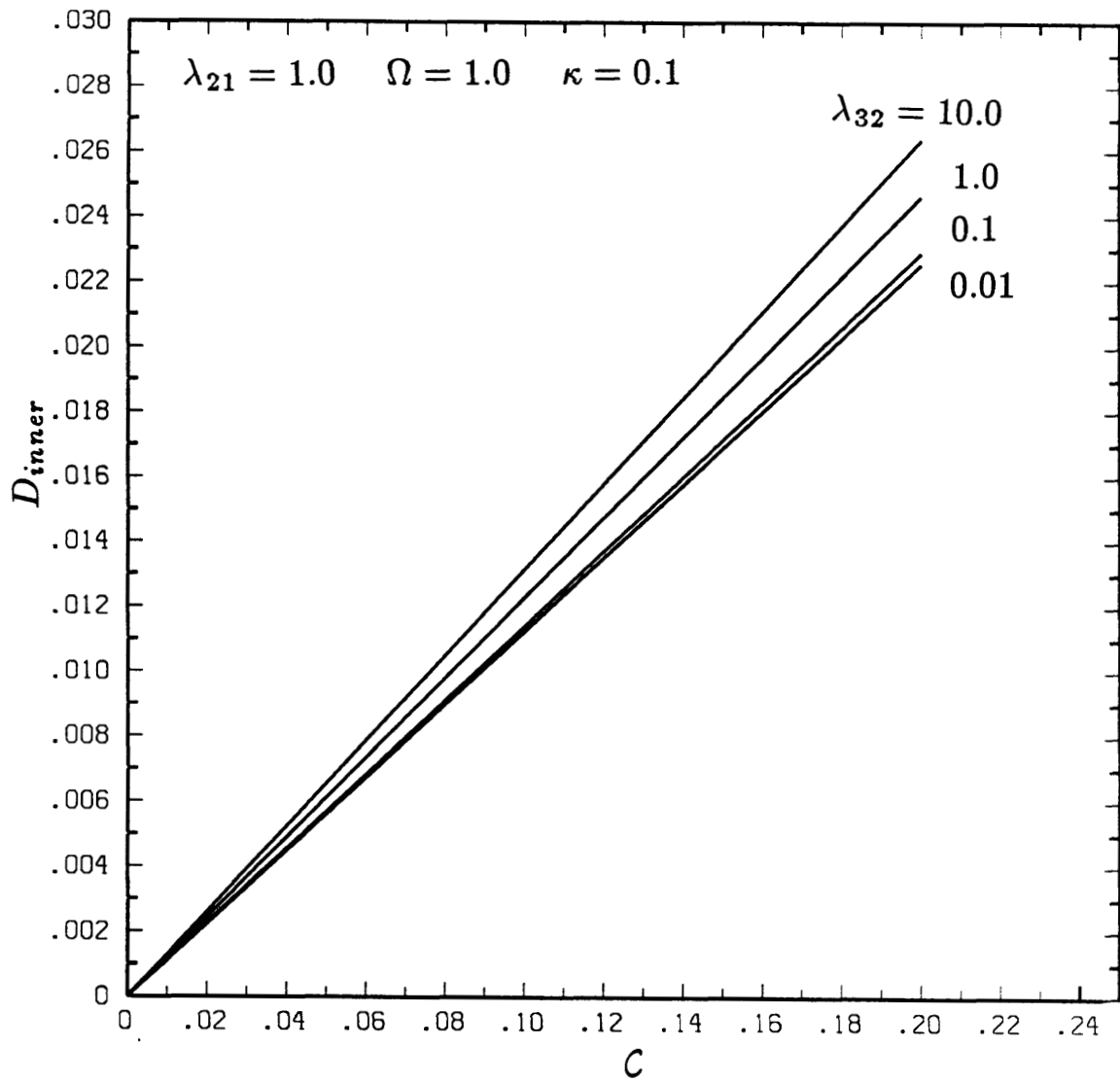


Figure 6d

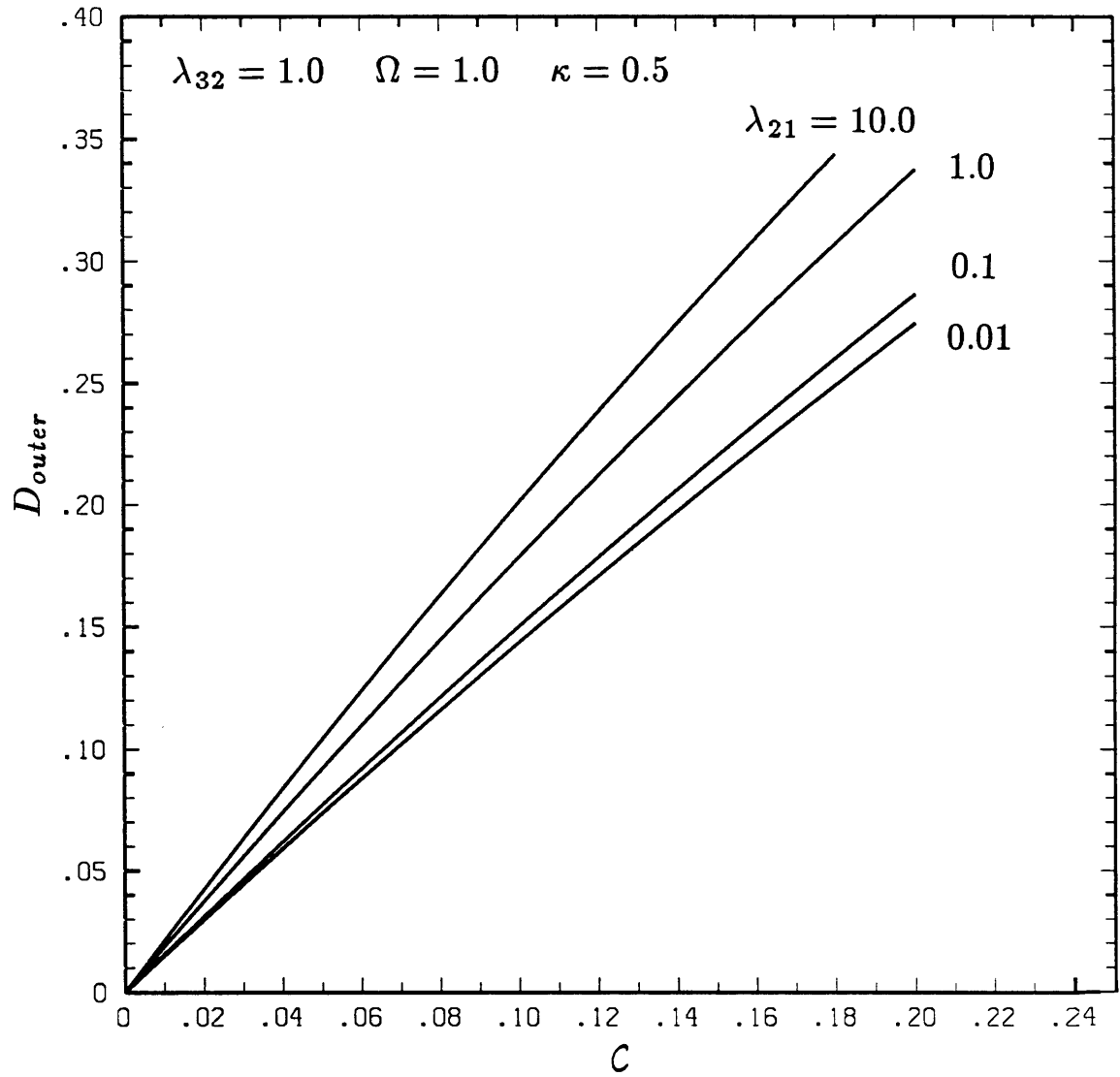


Figure 7a

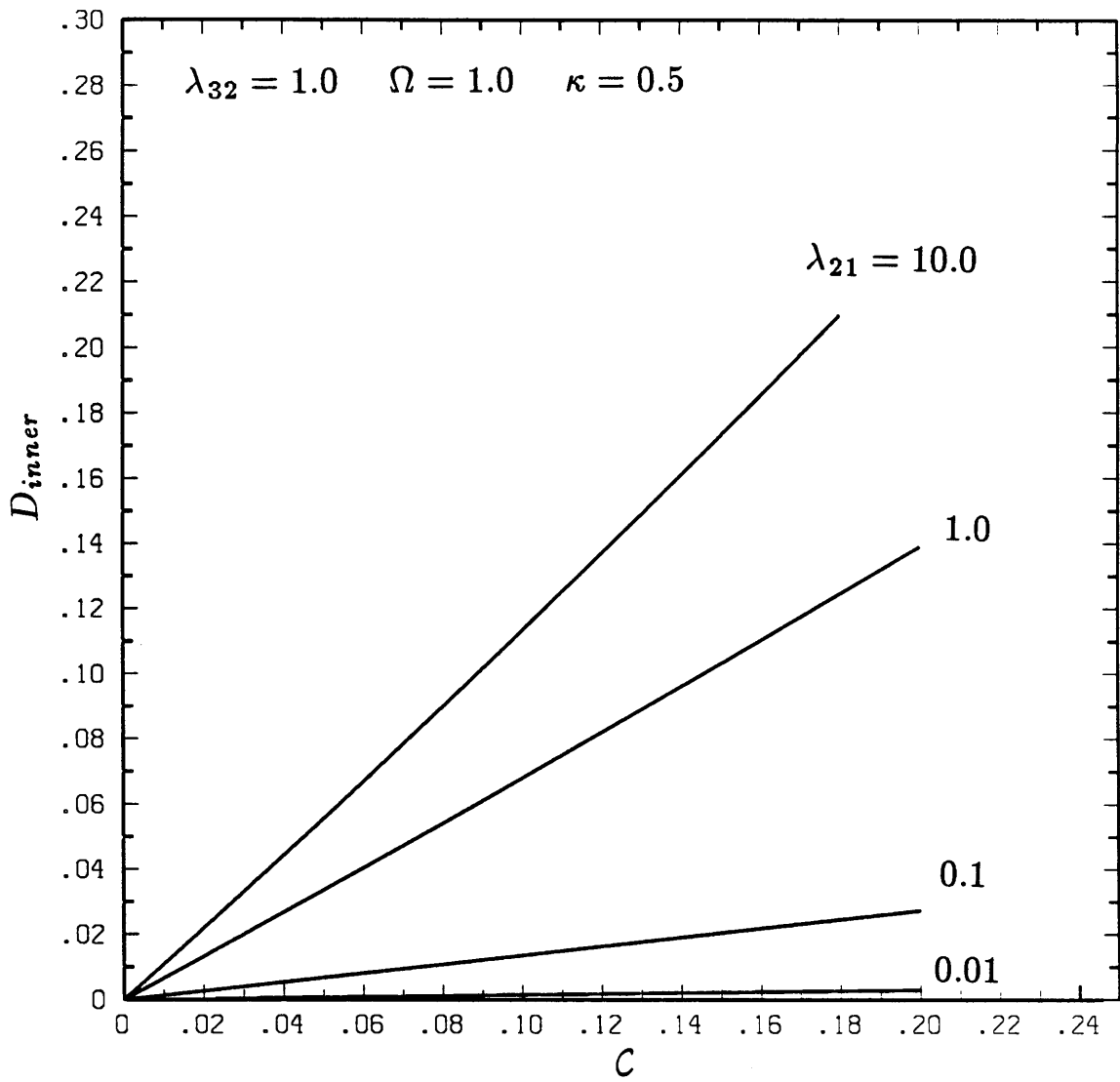


Figure 7b

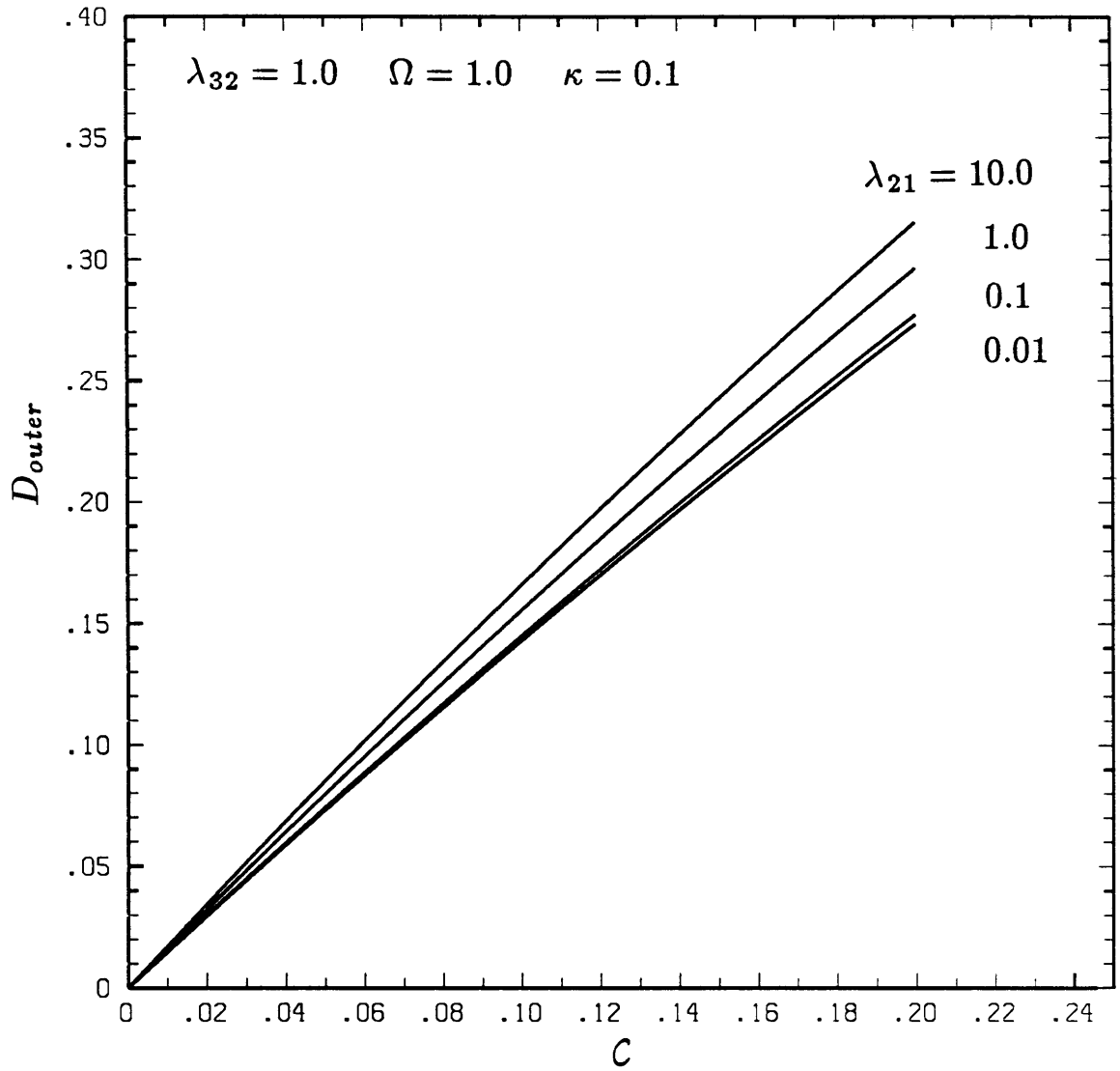


Figure 7c

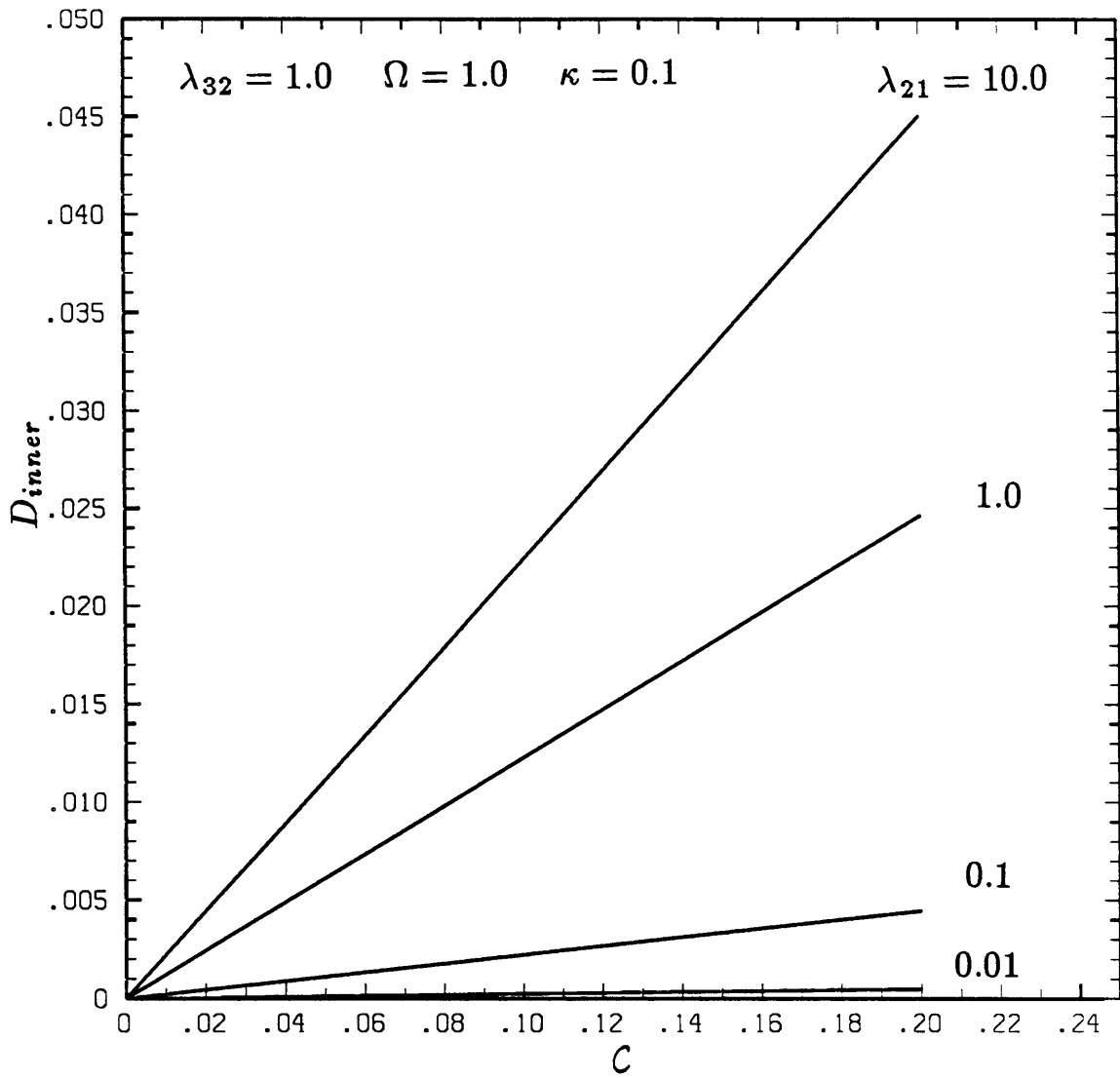


Figure 7d

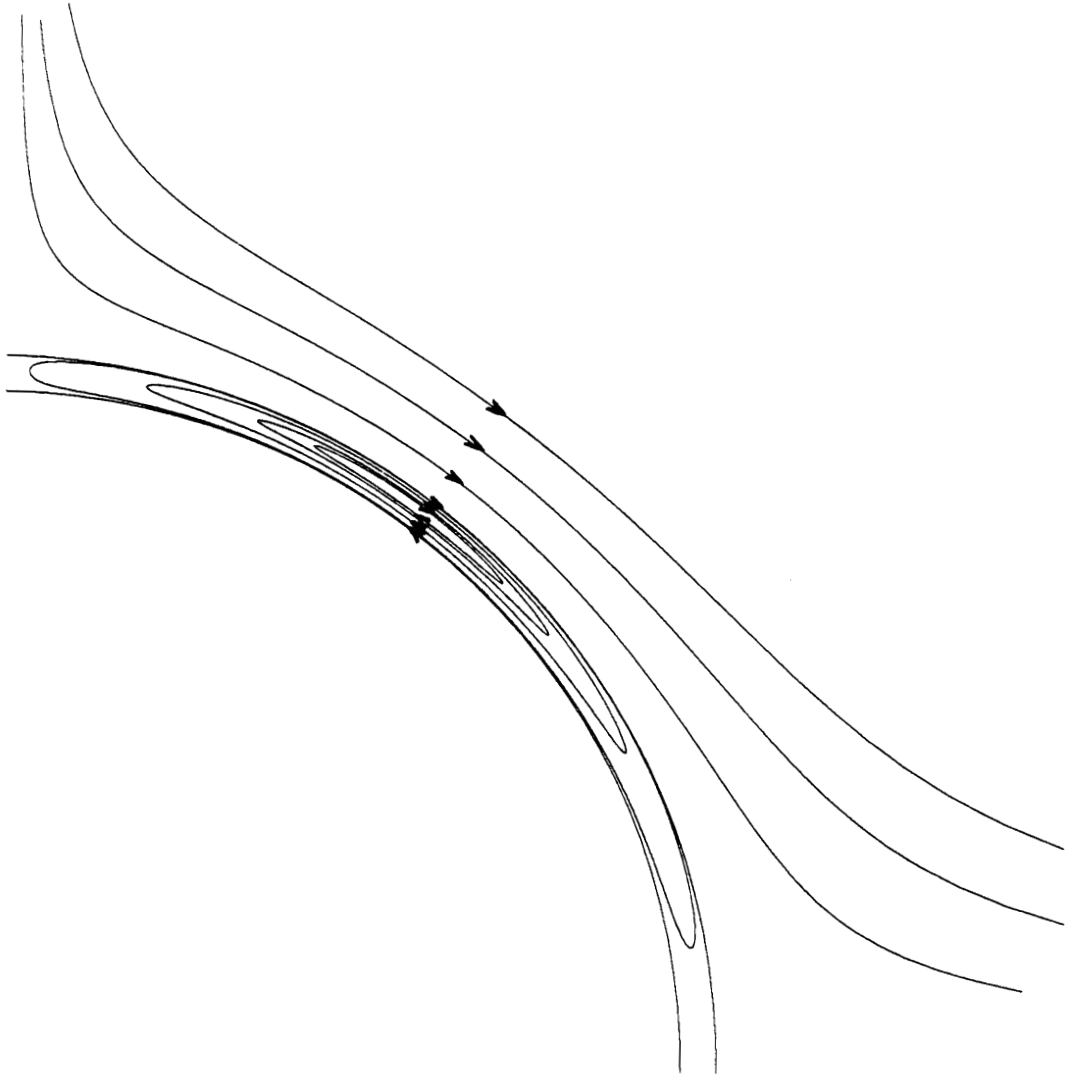


Figure 8

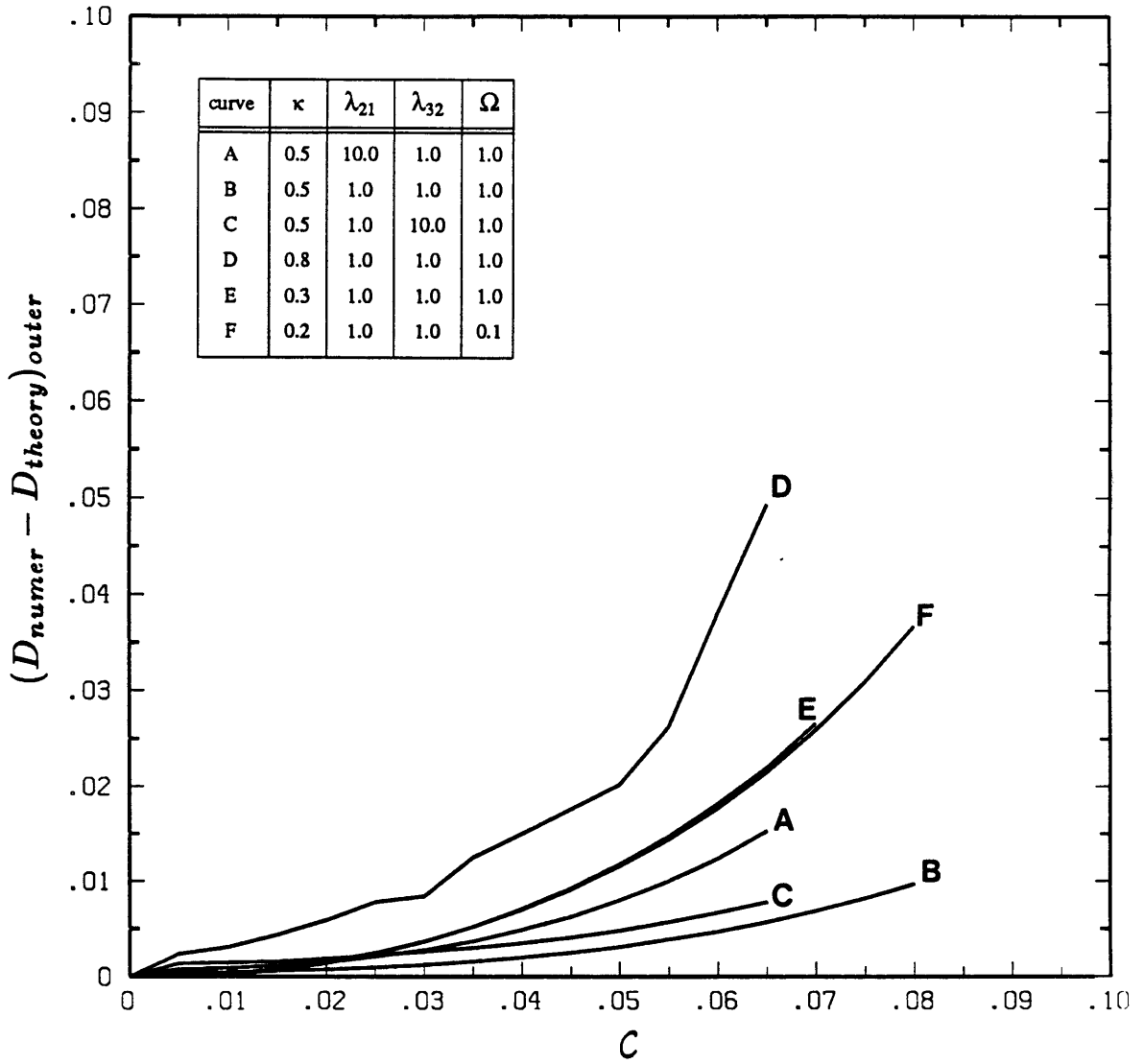


Figure 9a

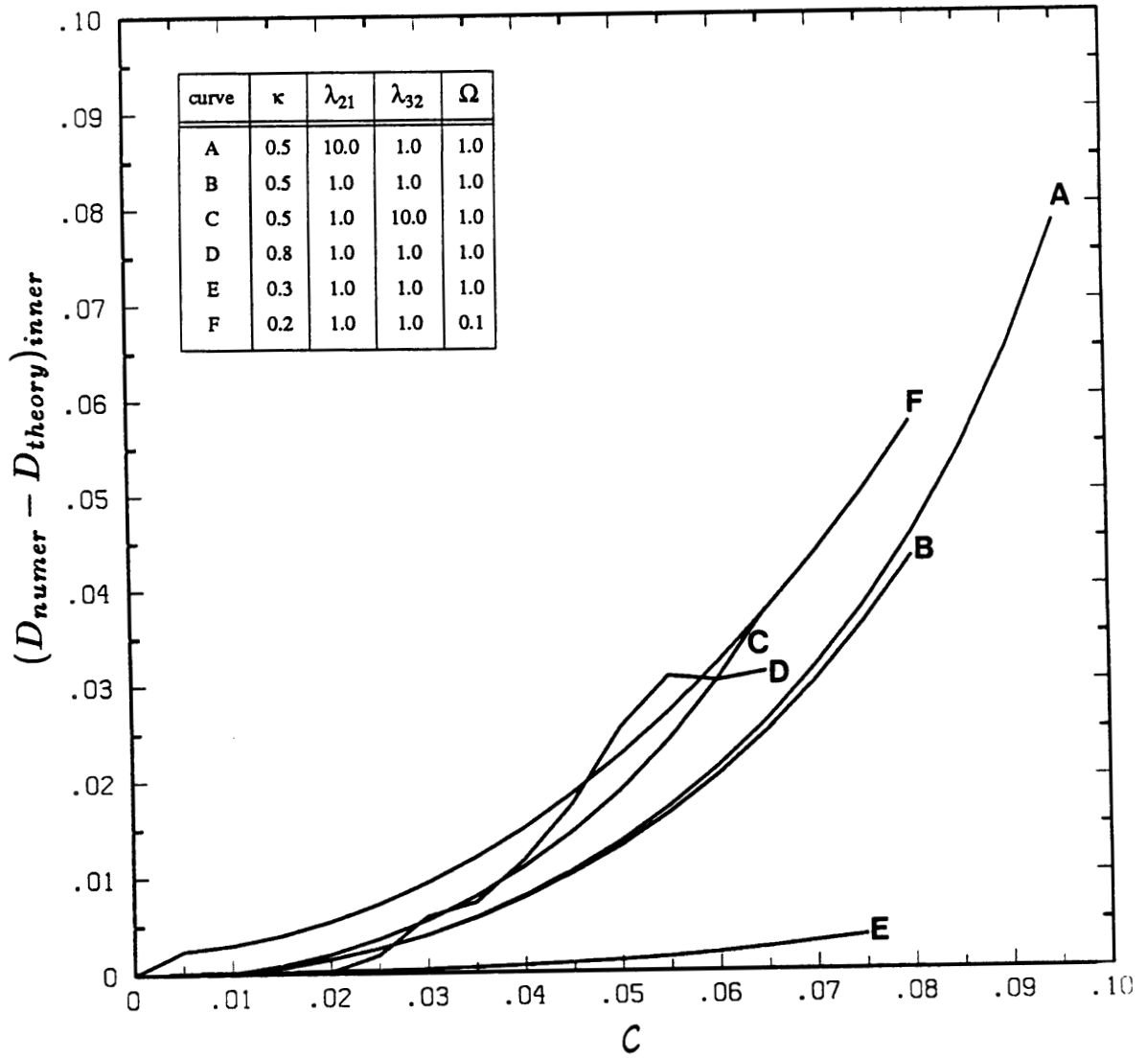


Figure 9b

Step change: $C = 0.04 \rightarrow C = 0.08$

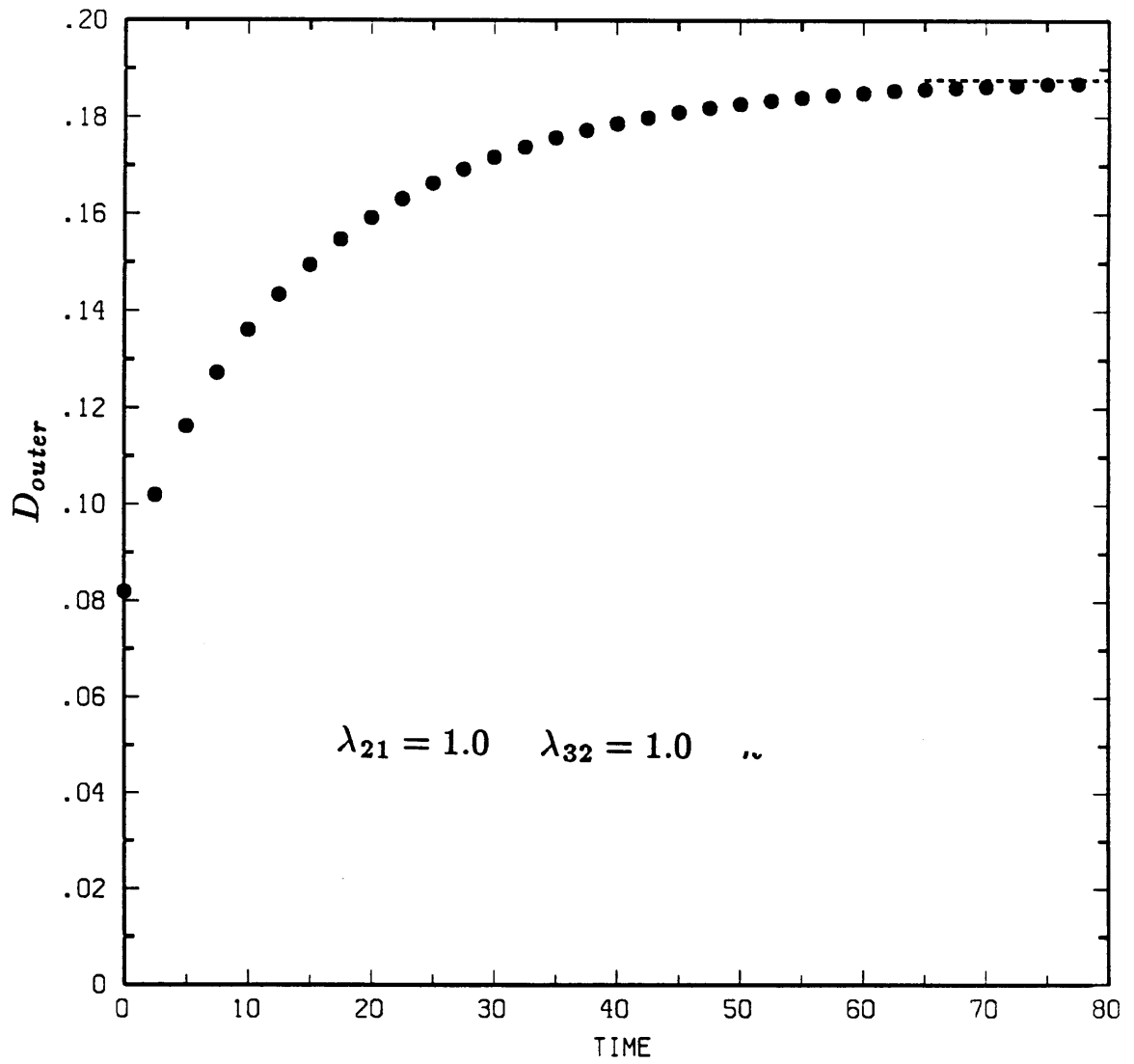


Figure 10a

Step change: $C = 0.04 \rightarrow C = 0.08$

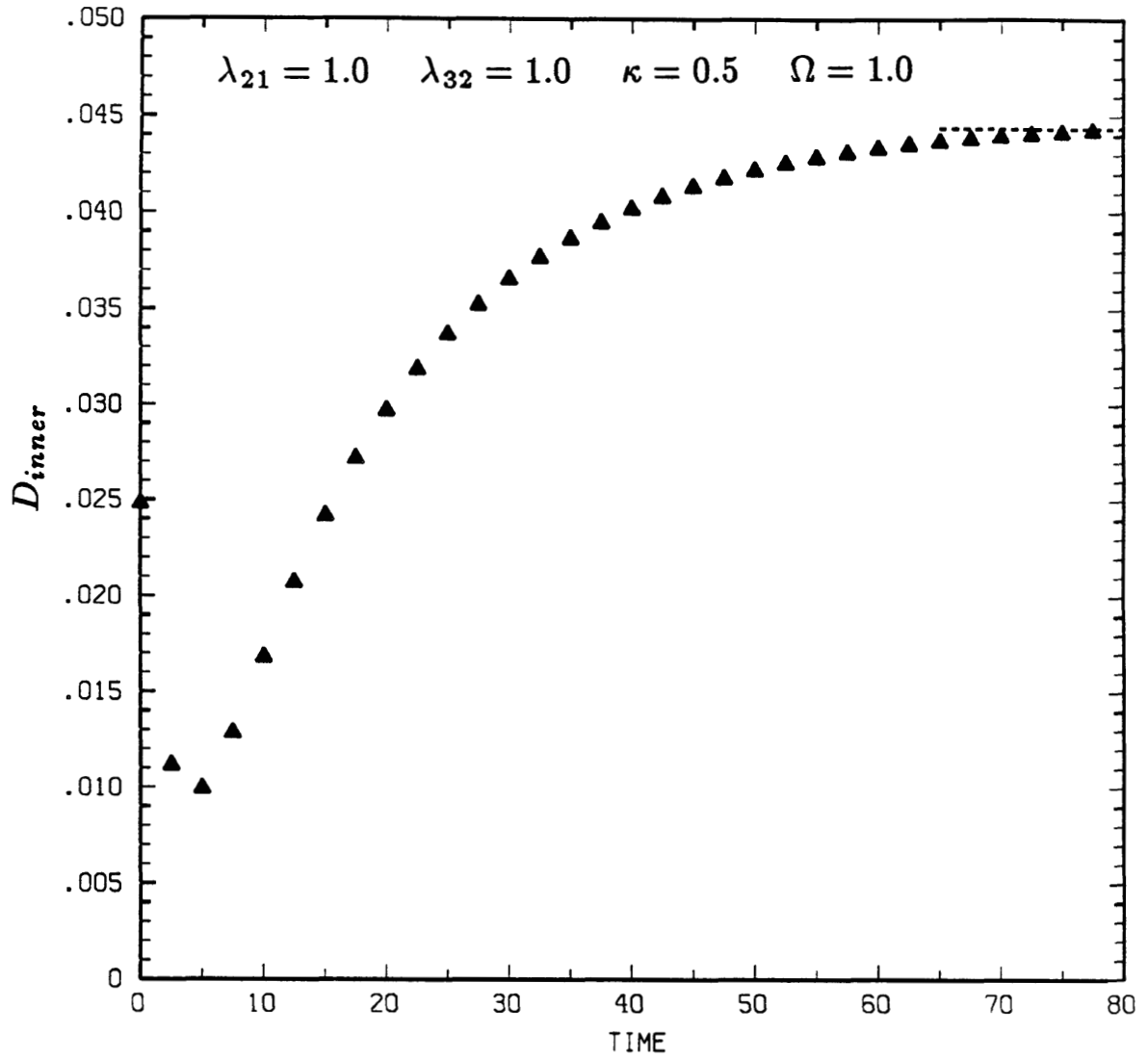


Figure 10b

$$\lambda_{21} = 1.0 \quad \lambda_{32} = 1.0 \quad \kappa = 0.5 \quad \Omega = 1.0$$

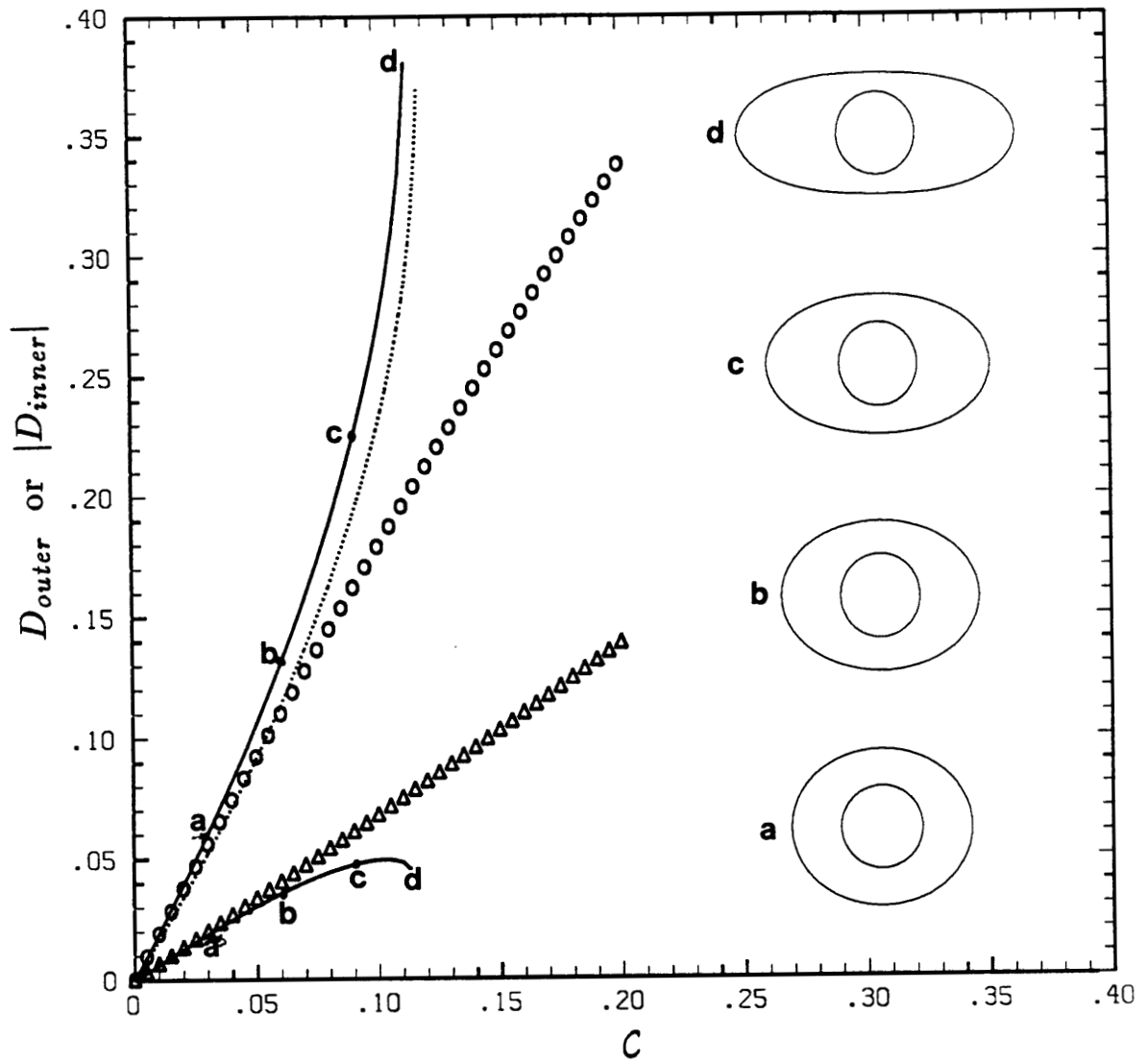


Figure 11

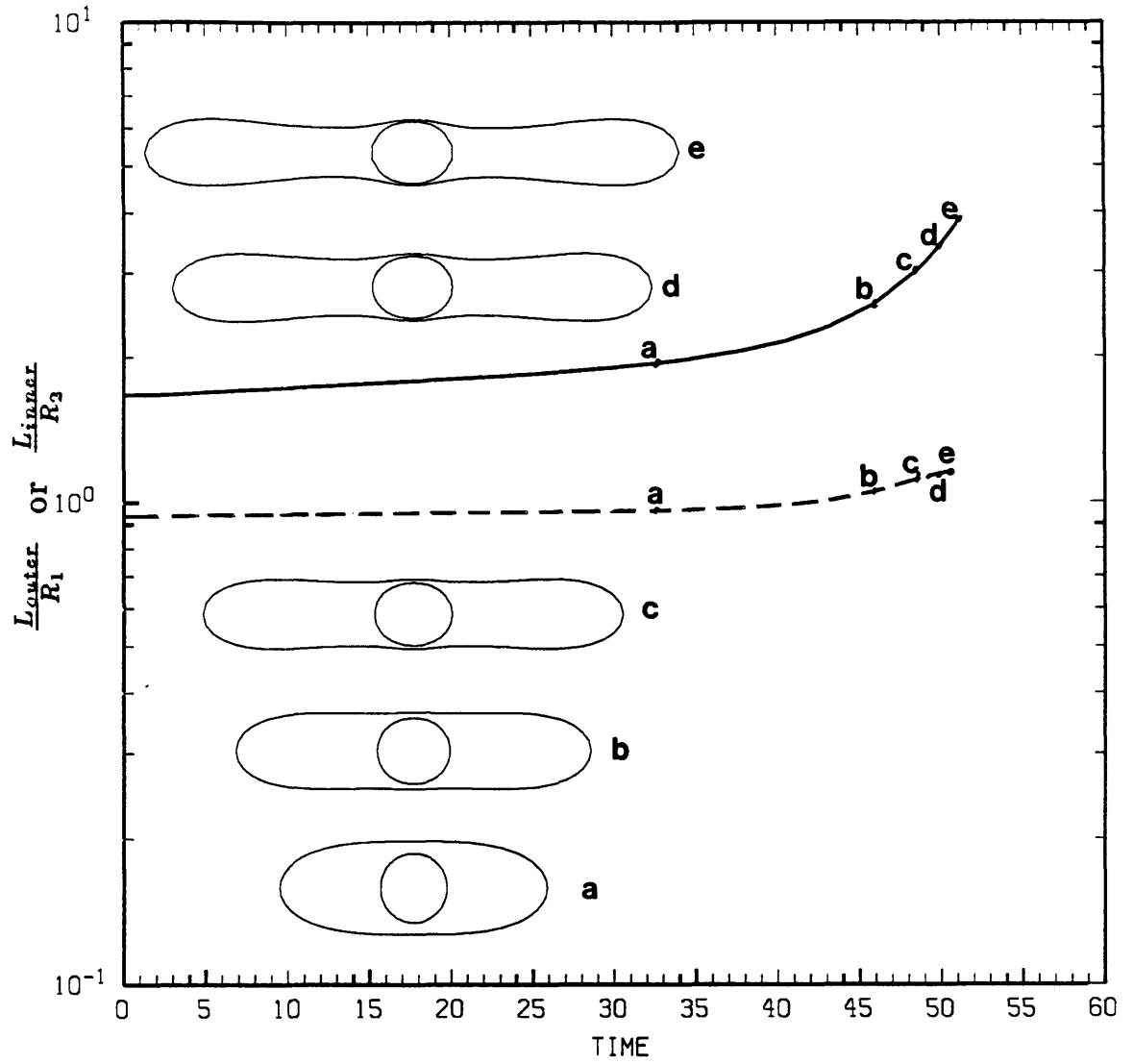


Figure 12

$$\lambda_{21} = 1.0 \quad \lambda_{32} = 10.0 \quad \kappa = 0.5 \quad \Omega = 1.0$$

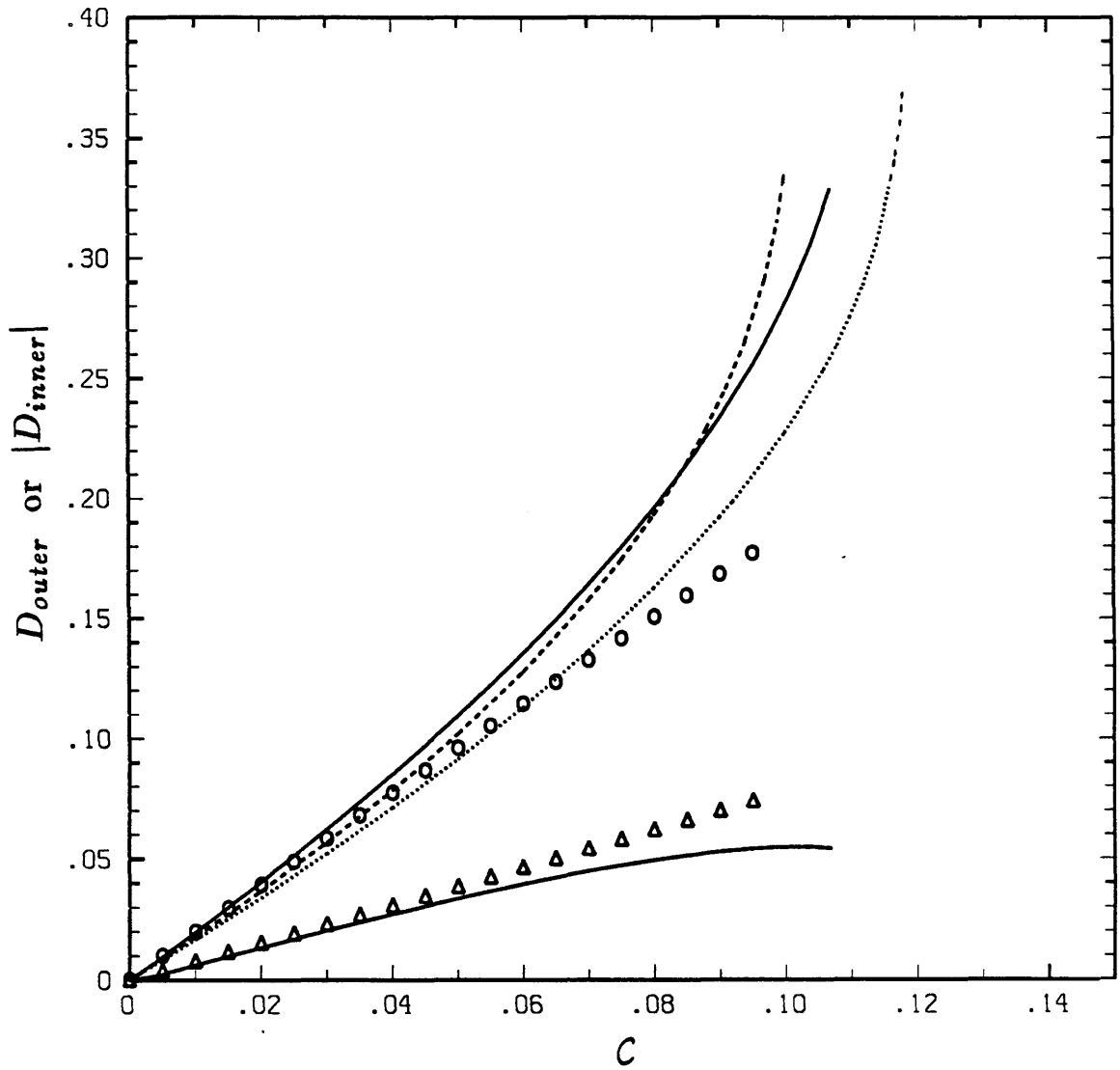


Figure 13

$\lambda_{21} = 1.0$ $\Omega = 1.0$ $\kappa = 0.5$

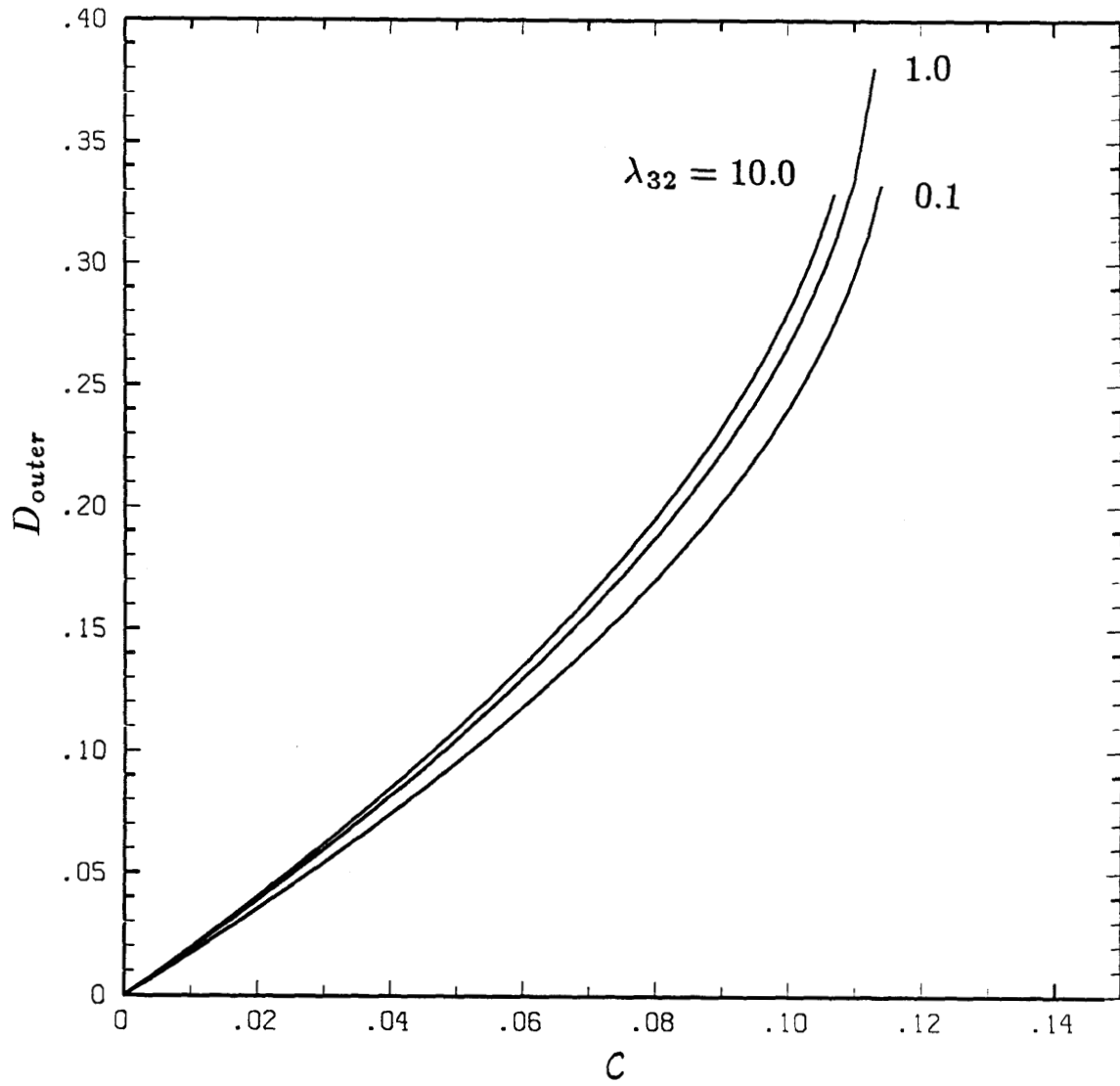


Figure 14

$$\lambda_{21} = 1.0 \quad \lambda_{32} = 1.0 \quad \kappa = 0.8 \quad \Omega = 1.0$$

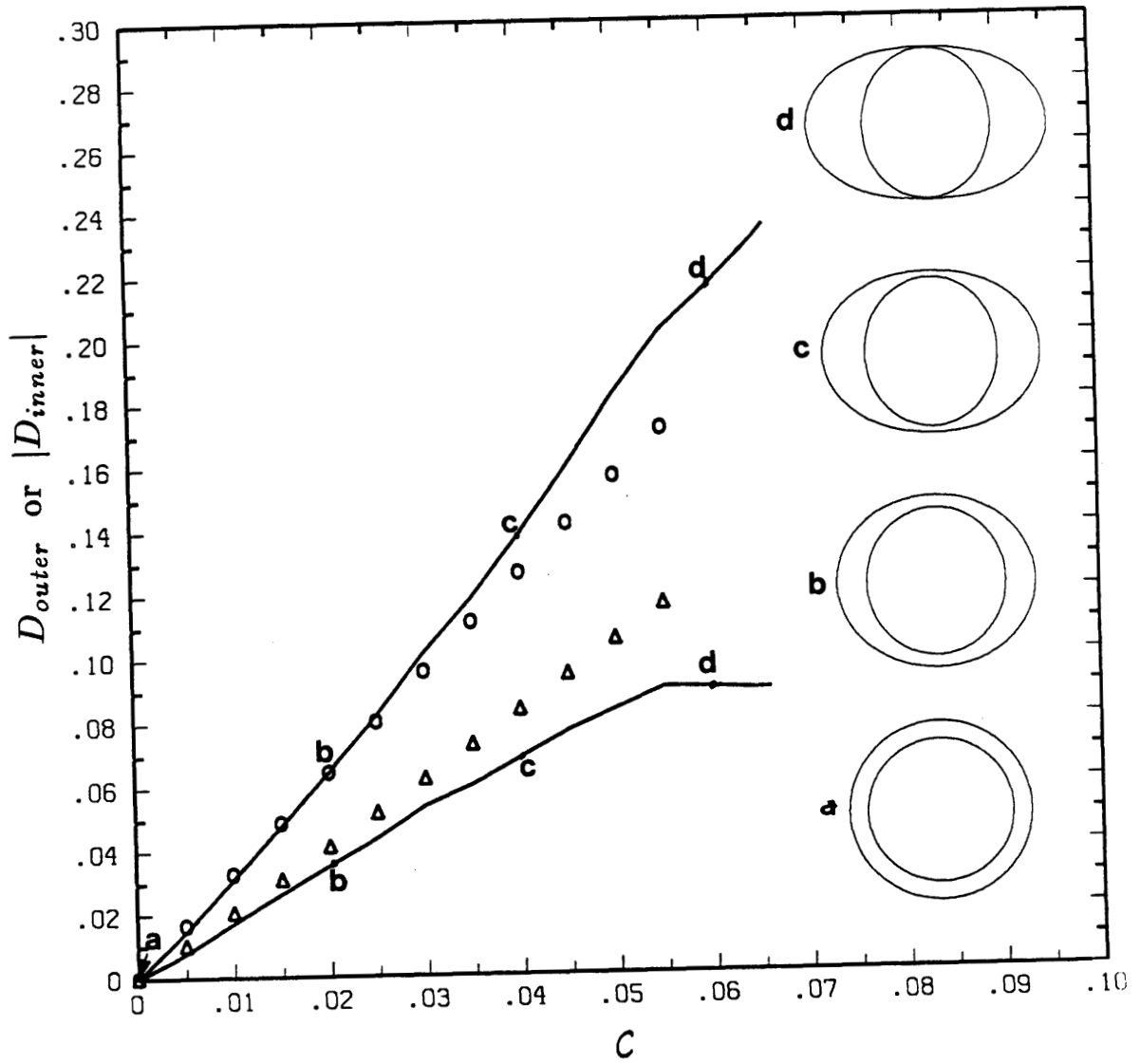


Figure 15

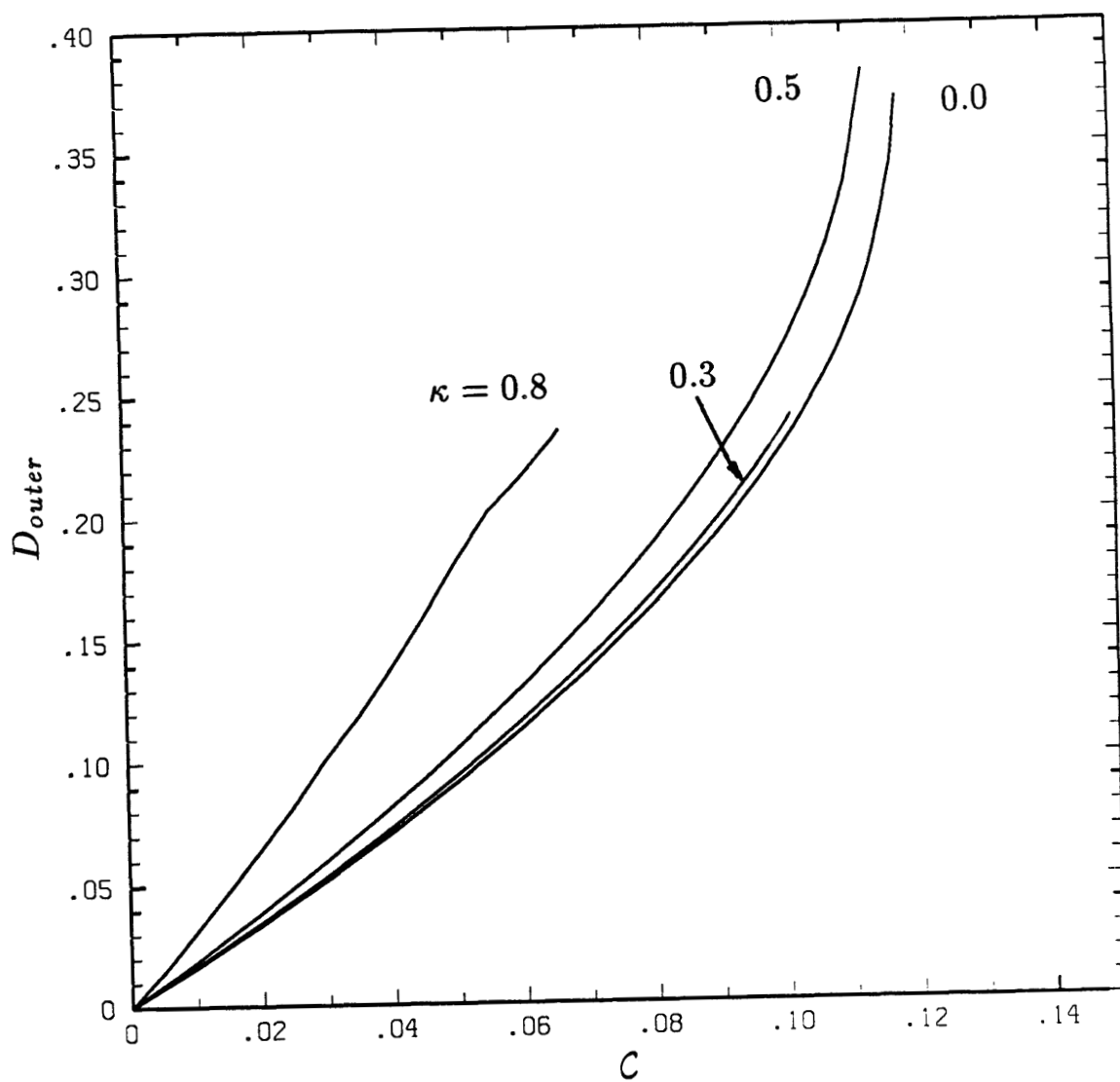


Figure 16

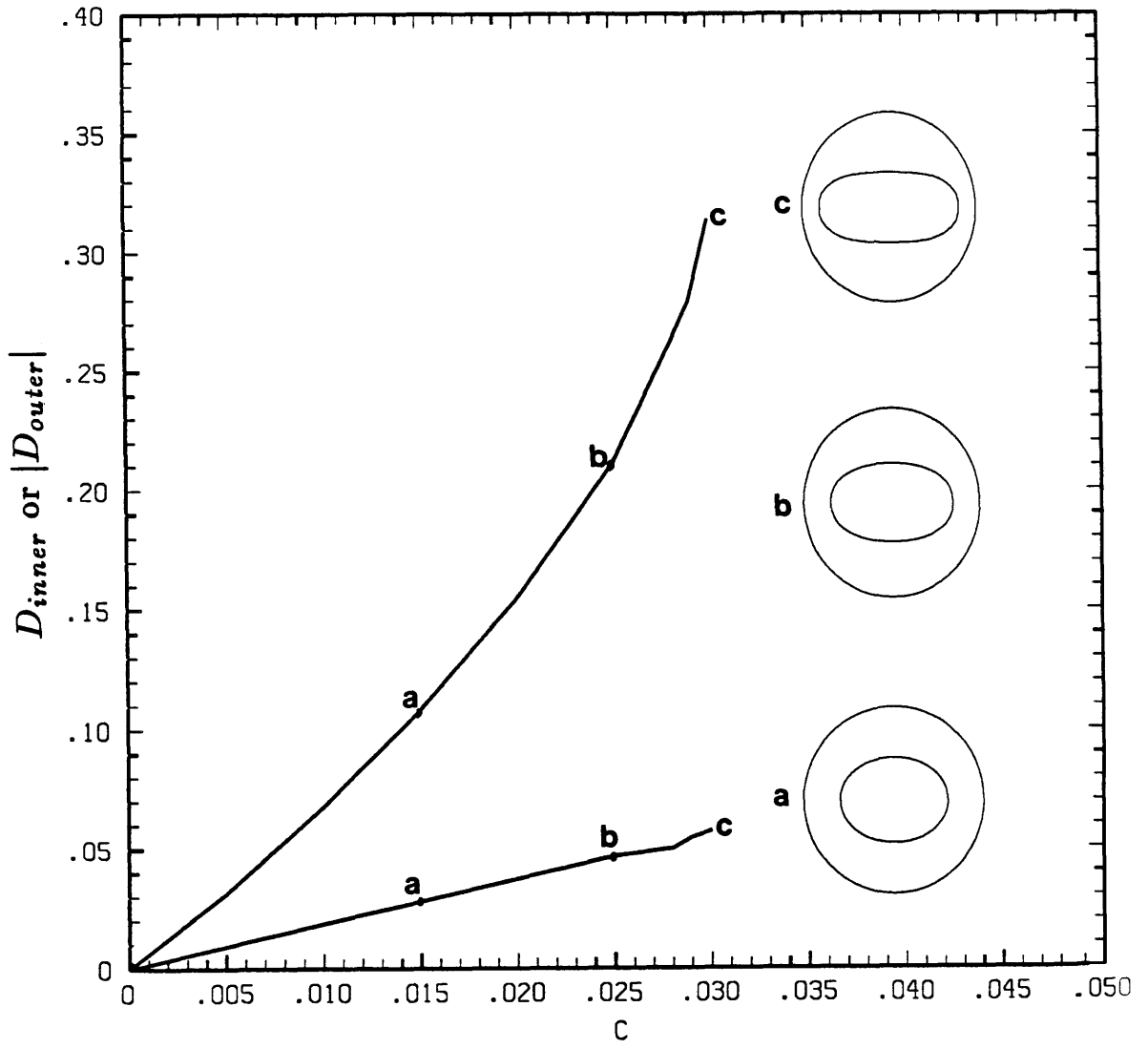


Figure 17

CHAPTER 6

**A NUMERICAL STUDY
OF THE EFFECT OF SURFACTANTS
ON DROP DEFORMATION AND BREAKUP**

ABSTRACT

We discuss the effect surface-active agents have on the deformation and breakup of droplets suspended in extensional flows at low Reynolds numbers. In order to couple the interfacial tension variation produced by a nonuniform surfactant distribution with the transient, finite deformation of the droplet, the boundary integral method is used in conjunction with the convective-diffusion equation for surfactant transport. We only examine the case of an insoluble surfactant. The results, though not extensive, indicate that at low capillary numbers the surfactant causes larger deformations than occur on a clean interface. The increased deformation occurs due to the surfactant being swept to the end of the drop where it acts to locally lower the interfacial tension, which in turn requires increased deformation to satisfy the normal stress balance. At larger capillary numbers the deformation is observed in some cases to be lower than in the surfactant-free case. This appears to be due to the increase in interfacial area accompanying finite deformation, which tends to decrease the local surfactant concentration, thereby increasing the effective interfacial tension. Finally, the formulation allows for an arbitrary equation of state relating the interfacial tension to the local concentration of the surface active agent, although calculations are only presented for the common linear equation of state.

1. INTRODUCTION

It is well-established that interfacial tension variations and/or interfacial viscosity and elasticity can have dramatic qualitative and quantitative effects on free-surface flows. The drag on a fluid sphere obeying Stokes law rather than the ideal Hadamard-Rybczynski result in all but very clean systems, bubble migration in a temperature gradient, and the damping of ocean waves due to the existence of a thin oil film are just a few examples. Furthermore, it is clear that the effects of surfactants must be properly understood if the results of fundamental (model) problems are to be useful in real engineering applications. In this paper, we will study the effect interfacial tension variations, due to the presence of surface-active agents, have on the deformation and breakup of Newtonian liquid droplets.

There have been many previous studies concerned with the effect of surfactants on drop and bubble motion in quiescent fluids. For example, it is observed that even a small amount of surfactant can reduce the terminal and interfacial velocity of drops and significantly reduce the rate of solute transport to or from the drop. A valuable compendium related to this topic is the classic treatise on *Physicochemical Hydrodynamics* by Levich (1962). Additional theoretical analyses of different aspects of this problem have been discussed by Newman (1967), Haber & Hetsroni (1971), Saville (1973), LeVan & Newman (1976), and Holbrook & LeVan (1983a,b). A common assumption made in all of these studies is to treat the droplet shape as spherical and calculate the steady-state velocity and surfactant concentration fields. The small, flow-induced steady deformation of a translating drop has been calculated by Sadhal & Johnson (1986).

A major interest in our laboratory is the deformation and breakup of droplets due to extensional flows. This topic stems from G.I. Taylor's classical experimental and theoretical studies (1932, 1934) that were motivated by an interest in emulsion formation. Although much work has been performed in the interim, it focusses mainly on droplet deformation and neglects any effects

due to such dynamic interfacial properties as surface tension gradients. Theoretical efforts, limited to nearly spherical deformations and a uniform interfacial tension, are reported by Cox (1969) and Barthes-Biesel & Acrivos (1973), experimental studies are discussed by Mason & coworkers (e.g., Rumscheidt & Mason 1961 and Torza, Cox & Mason 1972) and Bentley & Leal (1986), and numerical work is presented by Rallison & Acrivos (1978). Two excellent review articles describing much of this work have been written by Acrivos (1983) and Rallison (1984).

Recently, we reported on several investigations undertaken in our laboratory in order to examine the drop breakup process under well-defined flow conditions (Stone, Bentley & Leal 1986 and Stone & Leal 1987, 1988). An experimental investigation examined the transient stretching process that occurs at the critical capillary number and a combined experimental and numerical study examined the relaxation and breakup of these stretched droplets in subcritical flows or in an otherwise quiescent fluid. In many cases, the relaxation dynamics are sufficient to cause complete fracturing of the droplet and the effect of viscosity ratio, capillary number and drop shape are examined. It is demonstrated that the relaxational motion is a consequence of an interfacial-tension-driven flow due to curvature variations along the surface (the interfacial tension is constant). An obvious question, though, is how these motions are affected by dynamic interfacial properties; e.g., surface tension variations because of an adsorbed surfactant at the fluid-fluid interface.

The related problem of finite drop deformation, incorporating dynamic interfacial properties, has received very little attention in the literature. To our knowledge, the only study which addresses this question is reported by Flumerfelt (1980). Flumerfelt examined the deformation and orientation of nearly spherical drops in simple shear and extensional flows incorporating interfacial tension variations as well as effects due to surface shear and dilational viscosity. Related experiments in simple shear flow are reported by Phillips, Graves

& Flumerfelt (1980). Clearly, because the analysis is restricted to small deformations, it is difficult to extract information about drop breakup, since this necessarily involves finite deformation.

The great difficulty in treating these free-boundary problems stems from the a priori unknown location of the fluid-fluid interface. The presence of surfactants complicates matters further because the distribution of surfactant is intimately coupled to the drop shape and interface mobility, which in turn affect the time-dependent evolution of the drop shape. In order to properly solve such free-boundary problems it is necessary to couple equations describing the fluid motion to the boundary conditions at the fluid-fluid interface. Included in such a formulation must be a prescription of the interface behaviour. A rigorous discussion of the dynamics of a fluid interface is given by Scriven (1960) and Aris (1962). The interface is treated as a two-dimensional surface and the time-dependent effects associated with interface deformation are explicitly included.

Unfortunately, due to the complexity introduced because of the coupling of the partial differential equations describing both the bulk fluid motion and the interface evolution, analytic methods have only been applied to rather well-defined problems where the interface departs very little from its equilibrium shape. In addition to the work of Flumerfelt (1980) on small droplet deformation, Quinn & Saville (1974) and Whitaker (1976) have used linear stability analysis to study the effects of various interfacial properties on the evolution of infinitesimal disturbances on a cylindrical thread of fluid.

In this paper, which is concerned with finite drop deformation and drop breakup, we will neglect any effects of interfacial shear or dilational viscosity and only consider effects that arise because of interfacial tension variations due to presence of adsorbed surfactant on the fluid-fluid interface. We will also restrict our examination to the case of insoluble surfactant. In this case the surfactant has an extremely low solubility in either of the bulk phases so that it may be assumed to reside only at the fluid-fluid interface.

Even with these restrictions, there is a large class of flows related solely to effects due to interfacial tension. A classic, general review of different aspects of interfacial-tension-driven flows is provided by Levich & Krylov (1958). As discussed by these authors there exist two distinct classes of motion associated with interfacial tension. The first, so-called Marangoni flows, are much discussed in the literature and arise due to variations in interfacial tension along the boundary. This produces an unbalanced *tangential* stress that drives the motion. The second class of motions arise due to changes in curvature along the boundary (interfacial tension is constant). These produce unbalanced *normal* stresses that drive motion. In the case of droplet deformation examined here both mechanisms come into play.

In this paper interfacial tension variations are produced by gradients in surfactant concentration. Alternatively, temperature gradients can produce variations in interfacial tension that result in several well-known examples of fluid motion: bubble migration in a temperature gradient (Young, Goldstein & Block 1958) and cellular Marangoni convection (Pearson 1958). The effect of finite deformation due to drop motion normal to a solid planar boundary as a result of a prescribed temperature gradient is examined numerically by Ascoli & Leal (1988).

It is interesting to note that the dynamical effects and fluid motions produced by interfacial tension gradients have proven useful in fluid mechanical modelling of cell division and cell motion (Greenspan 1978 and Sapir & Nir 1985). Greenspan provides a vivid experimental illustration of drop breakup caused by surface tension variations along the surface produced by the deliberate addition of a surfactant. Sapir & Nir have applied the boundary integral method in order to examine aspects of the mechanism of cell cleavage using ideas similar to those discussed by Greenspan.

2. PROBLEM STATEMENT

Consider a Newtonian liquid droplet, undeformed radius a , density $\hat{\rho}$, viscosity $\hat{\mu}$ suspended in a second immiscible Newtonian fluid, density ρ and viscosity μ , undergoing an axisymmetric extensional flow characterized by the shear rate G . The fluids are isothermal. The fluid-fluid interface is assumed to be characterized completely by the interfacial tension σ and all stresses associated with the rate-of-deformation of the interface (surface shear and dilatational viscosity) are neglected. The interfacial tension, though, may vary with position along the interface due to the presence of adsorbed surface-active material. The surfactant is assumed to be insoluble in either the droplet fluid or the suspending fluid so that convection and diffusion of surfactant in the bulk phases may be neglected. Therefore, with the exception of σ , all fluid properties are treated as constants.

We begin by assuming that the Reynolds numbers characterizing motion in both fluids are small so that inertia may be neglected completely and the quasi-steady Stokes equations apply for both fluid phases. The low Reynolds number assumption is valid for the small droplets typical of many industrial applications. In order to be consistent with our prior studies concerning drop breakup, it is convenient to nondimensionalize all velocities by $u_c = \frac{\sigma_o}{\mu}$, lengths by the undeformed drop radius $l_c = a$, pressures by $p_c = \frac{u_c \mu}{a}$, $\hat{p}_c = \frac{u_c \hat{\mu}}{a}$ and times by $t_c = \frac{a \mu}{\sigma_o}$. Here σ_o represents a mean value of the interfacial tension (defined more precisely below). The governing equations for the velocity and pressure fields (\mathbf{u}, p) in the suspending fluid and in the droplet fluid $(\hat{\mathbf{u}}, \hat{p})$ are

$$\nabla^2 \mathbf{u} = \nabla p \quad \nabla^2 \hat{\mathbf{u}} = \nabla \hat{p} \quad (1)$$

$$\nabla \cdot \mathbf{u} = 0 \quad \nabla \cdot \hat{\mathbf{u}} = 0.$$

The velocity far from the droplet is an axisymmetric extensional flow

$$\mathbf{u} \rightarrow \mathbf{u}_\infty = \pm \frac{C}{2} \begin{pmatrix} -1 & 0 & 0 \\ 0 & -1 & 0 \\ 0 & 0 & 2 \end{pmatrix} \quad \text{as } |\mathbf{x}| \rightarrow \infty \quad (2)$$

where the + sign corresponds to a uniaxial extensional flow, the - sign corresponds to a biaxial extensional flow and the capillary number, $C = \frac{Ga\mu}{\sigma_0}$, provides a measure of viscous forces tending to deform the droplet relative to interfacial tension forces tending to maintain the droplet spherical.

At the fluid-fluid interface continuity of velocity and the stress balance may be written as

$$\mathbf{u} = \hat{\mathbf{u}} \quad \text{for } \mathbf{x}_s \in S \quad (3)$$

and

$$\mathbf{n} \cdot \mathbf{T} - \lambda \mathbf{n} \cdot \hat{\mathbf{T}} = \frac{\sigma}{\sigma_0} \mathbf{n} (\nabla_s \cdot \mathbf{n}) - \nabla_s \left(\frac{\sigma}{\sigma_0} \right) \quad \text{for } \mathbf{x}_s \in S. \quad (4)$$

In these equations \mathbf{x}_s represents a point on the fluid-fluid interface S , \mathbf{n} is the unit outward normal directed from the droplet phase to the continuous phase (see figure 1), $\nabla_s \cdot \mathbf{n}$ is the mean curvature of the interface, ∇_s is the surface gradient operator ($\nabla_s = (\mathbf{I} - \mathbf{nn}) \cdot \nabla$) and $\lambda = \frac{\hat{\mu}}{\mu}$ denotes the viscosity ratio of the two fluids.

The interface evolves according to the kinematic condition, which may be written as

$$\frac{d\mathbf{x}_s}{dt} = \mathbf{n}(\mathbf{u} \cdot \mathbf{n}). \quad (5)$$

The interfacial tension σ depends on the local concentration Γ^* of surfactant, which generally acts to lower the interfacial tension and is given by an equation of state

$$\sigma = \sigma(\Gamma^*). \quad (6)$$

Here Γ^* denotes a dimensional surface density, i.e., the mass of surfactant per unit of interfacial area.

The effect of interface mobility and flow-induced drop deformation will change the distribution of surfactant on the interface. The changes in surfactant concentration at a phase interface are governed by a time-dependent convective-diffusion equation that may be written in the dimensionless form (Aris 1962)

$$\frac{\partial \Gamma}{\partial t} + \nabla_s \cdot [\Gamma \mathbf{u}_s - \frac{1}{Pe_s} \nabla_s \Gamma] + \frac{\Gamma}{2\bar{a}} \frac{\partial \bar{a}}{\partial t} = j_n \quad (7)$$

where the surfactant concentration Γ has been made dimensionless with respect to a mean value Γ_o ($\Gamma = \frac{\Gamma^*}{\Gamma_o}$), \mathbf{u}_s represents the velocity tangent to the interface ($\mathbf{u}_s = (\mathbf{I} - \mathbf{nn}) \cdot \mathbf{u}$), \bar{a} is the determinant of the surface metric tensor and \mathbf{j}_n represents the dimensionless net flux of surface-active material to and from the interface from either of the bulk phases. The importance of convection relative to diffusion is measured by a surface Peclet number

$$Pe_s = \frac{u_c \bar{a}}{D_s} = \frac{\sigma_o \bar{a}}{\mu D_s} \quad (8)$$

where D_s is the surface diffusivity. The fourth term in equation (7) is a source-like contribution to the surface-equivalent of the convective-diffusion equation and accounts for changes in the local surface concentration due to stretching and contraction of the interface (i.e., the total interfacial area changes as the drop deforms). For the case of insoluble surfactant to be studied here, $\mathbf{j}_n = 0$.

Equations (1)-(7) clearly indicate the difficulty in solving problems where surface-active agents are important. Determination of the interfacial velocity field requires knowledge of the distribution of surfactant which, in turn, necessitates knowledge of the interfacial velocity. The free-boundary character of this problem is an additional nontrivial complication as the interface location is a priori unknown and must be found as part of the solution to the problem.

The problem is completely formulated by specifying an equation of state (equation 6). Although, in principle, the numerical procedure described in Section 3 could incorporate any functional form of $\sigma = \sigma(\Gamma^*)$, we will focus on well-known (and simple) approximations. If the surfactant is present in dilute concentrations, then a linear relationship exists between σ and Γ^* , which is typically written as (Adamson 1976)

$$\sigma_{solvent} - \sigma = \pi = \Gamma^* RT \quad (9)$$

where π is known as the "spreading pressure", R is the gas constant, T is the absolute temperature and $\sigma_{solvent}$ is the interfacial tension of the clean interface.

This simple equation of state has been used widely by prior researchers who have examined the effects of interfacial tension gradients on the drag and interface mobility of rising drops, etc. Because of the form of this equation it is often called the two-dimensional gas law. Other relations between σ and Γ^* are possible. For example, in order to account for nonideality (e.g. the finite area occupied by the surfactant molecules in addition to intermolecular forces), versions of equation (7) similar to the well-known Van der Waals equation of state are written as

$$\left(\pi + \frac{v}{A^2}\right)(A - A^\circ) = RT \quad (10)$$

where A represents the area per molecule, $A = \frac{1}{\Gamma^*}$, A° is the excluded area per molecule and v accounts for the attraction between surfactant molecules (Adamson 1976). Clearly, the more complicated the equation of state, the more parameters are necessary to specify the problem completely. Therefore, we restrict ourselves to the linear equation (9).

If Γ_o represents a characteristic surfactant concentration then the choice of the characteristic value of the interfacial tension $\sigma_o = \sigma(\Gamma_o)$ is

$$\sigma_o = \sigma_{solvent} - \Gamma_o RT. \quad (11)$$

We choose Γ_o to be the surfactant concentration on the initially uniformly contaminated surface. In dimensionless form the equation of state is

$$\frac{\sigma}{\sigma_o} = \frac{1 - \Gamma\beta}{1 - \beta} \quad (12)$$

and

$$\frac{d\left(\frac{\sigma}{\sigma_o}\right)}{d\Gamma} = \frac{-\beta}{1 - \beta} \quad (13)$$

where $\beta = \frac{\Gamma_o RT}{\sigma_{solvent}}$ is a physicochemical parameter that provides a direct measure of changes in interfacial tension that occur for a given change in surfactant concentration. Given the form of the equation of state we also require $0 \leq \beta \leq 1$. Notice that the capillary number defined here using the interfacial tension of the

contaminated surface is related to the capillary number of the clean interface

$$C_{clean} = \frac{Ga\mu}{\sigma_{solvent}} \text{ by}$$

$$C = \frac{C_{clean}}{1 - \beta}.$$

If we wish to focus attention on effects due to β and Pe_s alone, then C is the proper definition of the capillary number for a droplet initially uniformly covered by surfactant.

We wish to solve this coupled drop deformation and surfactant transport problem. In this paper, we will consider an initially spherical drop with uniformly distributed surfactant, concentration Γ_0 ; i.e., a dimensionless concentration $\Gamma = 1$. We examine the deformation of the droplet in a uniaxial extensional flow with a goal of understanding the coupled effects of C , Pe_s , and β . As discussed by Rallison (1981) the calculations with $\lambda = 1.0$ should provide qualitative insight into the behaviour for all viscosity ratios so here we limit our calculations in this paper to $\lambda = 1.0$. The numerical method for solving this problem is outlined in Section 3.

It is convenient to characterize the degree of drop deformation using a single scalar parameter. In this study we will focus on modest deformation beginning with a spherical initial shape and it is appropriate in such instances to define the deformation parameter $D = \frac{L-B}{L+B}$, where L and B represent the half-length and half-breadth of the drop, respectively.

3. NUMERICAL METHOD/IMPLEMENTATION

In this section we will discuss the numerical procedure used to solve this coupled free-boundary and surface transport problem. It should be emphasized that there have been very few calculations performed to determine the effect of surfactant transport on drop deformation in extensional flows. To our knowledge the only calculation is due to Flumerfelt (1980) who studied the surfactant distribution for a drop that is spherical and then used the imbalance in normal stresses to calculate the first (small) correction to the drop shape. Flumerfelt also allowed for elasticity of the interface and incorporated mass transfer from the bulk fluids.

The numerical procedure described here accounts for finite deformation of the interface and could be used to study the effect of surface-active agents on rising drops and bubbles. In such cases, although the entire effect is due to the existence of surface tension gradients, very little deformation occurs, and the numerical results may not prove very insightful. However, flows that are predominantly extensional are capable of producing large distortions to a deformable microstructure, even in the absence of surface tension gradients, and it is in these situations that the formulation described below is most useful.

In Section 3.1 we describe the calculation of the interfacial velocity and outline the procedure used to discretize and represent the drop surface. The convective-diffusion equation is examined in detail in Section 3.2 and is simplified to a form suitable for this axisymmetric problem. The coupling of the unknown drop shape and the evolving surfactant distribution makes solution of the simultaneous system of equations extremely difficult, so in Section 3.3 we outline an approximate procedure for numerically solving this problem.

3.1 Calculation of the interfacial velocity using the boundary integral method

The boundary integral method is a powerful technique for solving Stokes flow problems. It is particularly well-suited for free-boundary studies since only

the boundary of the domain must be discretized and the interfacial velocity is calculated directly.

The first application of the boundary integral method to Stokes flow problems was presented by Youngren & Acrivos (1975) in a study of streaming flow past arbitrary solid bodies. The technique was generalized to studies of droplet deformation by Rallison & Acrivos (1978) and, since that time, has been used by many investigators for a wide-range of free-boundary studies. For example, the motion of particles normal to a deformable fluid-fluid interface has been discussed by Lee & Leal (1982) and Stoos & Leal (1988), the mechanism of breakup has been investigated by Stone & Leal (1987,1988), drop deformation and breakup in electric and magnetic fields has been discussed by Sherwood (1987), multiple droplet interactions have been described by Higdon & Schnepfer (1987) and the application of the method to peristaltic flows is discussed by Pozrikides (1987). A closely related investigation to the work reported here is the numerical study by Ascoli & Leal (1988) of drop migration normal to a solid planar wall due to a temperature gradient.

Following the procedure of Rallison and Acrivos (1978), the interfacial velocity can be written as

$$\frac{(1+\lambda)}{2}\hat{\mathbf{u}}(\mathbf{x}_s) = \mathbf{u}_\infty(\mathbf{x}_s) - \int_S \mathbf{J} \cdot [\mathbf{n} \cdot \mathbf{T} - \lambda \mathbf{n} \cdot \hat{\mathbf{T}}] dS(\mathbf{y}) - (1-\lambda) \int_S \mathbf{n} \cdot \mathbf{K} \cdot \hat{\mathbf{u}} dS(\mathbf{y}) \quad (14)$$

where

$$\mathbf{J} = \frac{1}{8\pi} \left[\frac{\mathbf{I}}{|\mathbf{x} - \mathbf{y}|} + \frac{(\mathbf{x} - \mathbf{y})(\mathbf{x} - \mathbf{y})}{|\mathbf{x} - \mathbf{y}|^3} \right]$$

$$\mathbf{K} = -\frac{3}{4\pi} \frac{(\mathbf{x} - \mathbf{y})(\mathbf{x} - \mathbf{y})(\mathbf{x} - \mathbf{y})}{|\mathbf{x} - \mathbf{y}|^5}.$$

Here \mathbf{x}_s denotes a point at the fluid-fluid interface, \mathbf{y} is the integration variable and \mathbf{u}_∞ is given by equation (2). Making use of the normal stress boundary

condition we can rewrite (14) as

$$\begin{aligned} \frac{(1 + \lambda)}{2} \hat{\mathbf{u}}(\mathbf{x}_s) = & \mathbf{u}_\infty(\mathbf{x}_s) - \int_S \mathbf{J} \cdot \left[\frac{\sigma}{\sigma_o} \mathbf{n}(\nabla_s \cdot \mathbf{n}) - \frac{d(\frac{\sigma}{\sigma_o})}{d\Gamma} \nabla_s \Gamma \right] dS(\mathbf{y}) \\ & - (1 - \lambda) \int_S \mathbf{n} \cdot \mathbf{K} \cdot \hat{\mathbf{u}} dS(\mathbf{y}) \end{aligned} \quad (15)$$

This integral equation of the second kind highlights the principal advantage of the boundary integral method, namely that it is only necessary to compute two-dimensional surface integrals rather than performing calculations over the entire three dimensional fluid domain. Once the interfacial velocity is determined the drop shape can be updated using the kinematic condition. Clearly, the physicochemical character of the problem enters through $\sigma = \sigma(\Gamma)$ and $\frac{d\sigma}{d\Gamma}$, which is specified once an equation of state is chosen, so that the solution of equation (15) is no more difficult for more complicated equations of state. However, in this study, we will just examine the linear relation discussed in Section 2.

The solution of this integral equation for the interfacial velocity must be accomplished numerically. The approach taken is to first discretize the interface, write the integral equation at each node point and reduce (15) to an equivalent set of linear algebraic equations that is straightforward to solve using Gaussian elimination. Assuming for the moment that the surface concentration Γ is known, there are three important aspects necessary for an accurate numerical solution of this integral equation: (1) the geometry must be accurately represented so that the interface curvature, which involves second derivatives, can be computed; (2) the functional representation of the unknown velocity field $\mathbf{u}(\mathbf{x}_s)$ must be chosen; and (3) accurate evaluation of integrals is required, including careful resolution near the singular points $\mathbf{y} \rightarrow \mathbf{x}_s$, where the kernels \mathbf{J} and \mathbf{K} are singular, although the integrals themselves are integrable in the sense of a Cauchy principal value.

We have dealt with these difficulties in a manner outlined in our previous investigations of the breakup of highly elongated droplets (Stone & Leal 1987,

1988). The results of these studies give us confidence that these aspects of the problem are well-resolved. Here we summarize our approach.

We only consider axisymmetric drop shapes. Referring to the cylindrical coordinate system shown in figure 1, the azimuthal integration in equation (15) can be performed analytically. This reduces the surface integrals to line integrals. Then, the interface is discretized into $2N-2$ boundary elements with node points placed at the end of each element and $\mathbf{u}(\mathbf{x}_s)$ is assumed to vary linearly over each element. At each node point there are two unknown components of the interfacial velocity vector (u_r, u_z) . The interface location is parametrized using a normalized measure of arclength s ($0 \leq s \leq 1$). In this case, the surface collocation points are labeled using cylindrical coordinates (r, z) and cubic splines are used to generate twice continuously differentiable representations for $r = r(s)$ and $z = z(s)$. Finally, because of the fore-aft symmetry of the flow fields, drop shapes and surfactant distributions considered in this paper, the number of unknowns is halved and a $2N-2$ system of equations and unknowns is solved using Gaussian elimination.

3.2 Calculation of the surfactant distribution using the convective-diffusion equation

We first make some general remarks concerning the general form of the convective-diffusion equation appropriate for a two-dimensional surface imbedded in a three-dimensional space. Time-dependent effects are also included. In general, the two-dimensional surface can be represented by $\mathbf{x}_s = \mathbf{x}_s(v^1, v^2)$ where the v^α represent surface coordinates. For a discussion of the differential geometry of surface coordinates the reader is referred to McConnell (1957) and Aris (1962). The convective term can be written using index notation and the summation convention as

$$\nabla_s \cdot (\Gamma \mathbf{u}_s) = \frac{1}{\bar{a}^{\frac{1}{2}}} \frac{\partial}{\partial v^\alpha} (\Gamma \bar{a}^{\frac{1}{2}} u^\alpha) \quad (16)$$

where the surface velocity \mathbf{u}_s is defined with respect to the surface base vectors

\mathbf{a}_α as

$$\mathbf{u}_s = u^\alpha \mathbf{a}_\alpha, \quad \mathbf{a}_\alpha = \frac{\partial \mathbf{x}_s}{\partial v^\alpha} \quad \alpha = 1, 2 \quad (17)$$

and \bar{a} is the determinant of the surface metric tensor. A differential element of surface is related to \bar{a} and differential changes in the surface coordinates by

$$dS = \bar{a}^{\frac{1}{2}} dv^1 dv^2. \quad (18)$$

The surface Laplacian can be written as

$$\nabla_s^2 \Gamma = \frac{1}{\bar{a}^{\frac{1}{2}}} \frac{\partial}{\partial v^\alpha} (\bar{a}^{\frac{1}{2}} a^{\alpha\beta} \frac{\partial \Gamma}{\partial v^\beta}) \quad (19)$$

where $a^{\alpha\beta}$ are the surface covariant components of the surface metric tensor.

The convective-diffusion equation (7) can then be written in the more compact form

$$\frac{\partial(\bar{a}^{\frac{1}{2}} \Gamma)}{\partial t} + \frac{\partial}{\partial v^\alpha} (\Gamma \bar{a}^{\frac{1}{2}} u^\alpha) + \frac{1}{Pe_s} \frac{\partial}{\partial v^\alpha} (\bar{a}^{\frac{1}{2}} a^{\alpha\beta} \frac{\partial \Gamma}{\partial v^\beta}) = 0 \quad (20)$$

where the local time derivative and the source-like term due to changes in interfacial area have been combined into the first term in equation (20).

In general the drop surface can be parametrized using the surface coordinate system (s, θ) where θ is the azimuthal angle ($0 \leq \theta \leq 2\pi$) and s is the normalized measure of arclength introduced in Section 3.1 (see figure 1). In this axisymmetric problem (20) reduces to

$$\frac{\partial(\bar{a}^{\frac{1}{2}} \Gamma)}{\partial t} + \frac{\partial}{\partial s} (\Gamma \bar{a}^{\frac{1}{2}} u^s) + \frac{1}{Pe_s} \frac{\partial}{\partial s} (\bar{a}^{\frac{1}{2}} a^{11} \frac{\partial \Gamma}{\partial s}) = 0. \quad (21)$$

where $\Gamma = \Gamma(s, t)$, the time-dependent metric \bar{a} is given by

$$\bar{a}(s, t) = \det(a_{\alpha\beta}) = r(s)^2 \left[\left(\frac{\partial r}{\partial s} \right)^2 + \left(\frac{\partial z}{\partial s} \right)^2 \right]$$

and

$$a^{11} = \frac{1}{\left(\frac{\partial r}{\partial s} \right)^2 + \left(\frac{\partial z}{\partial s} \right)^2}.$$

Since the surface base vectors \mathbf{a}_α are not unit vectors, the surface velocity u^s in equation (21) is related to the tangential velocity component $\mathbf{u}(\mathbf{x}_s) \cdot \mathbf{t} = \bar{u}^s$ calculated using the boundary integral technique described in Section 3.1 by (\mathbf{t} is the unit tangent vector to the surface)

$$u^s = \sqrt{a^{11}} \bar{u}^s.$$

Therefore, we can write (21) in the relatively simple form

$$\frac{\partial(\bar{a}^{\frac{1}{2}}\Gamma)}{\partial t} + \frac{\partial}{\partial s}(\Gamma r(s)\bar{u}^s) + \frac{1}{Pe_s} \frac{\partial}{\partial s} \left[\frac{r(s)}{\sqrt{(\frac{\partial r}{\partial s})^2 + (\frac{\partial z}{\partial s})^2}} \frac{\partial \Gamma}{\partial s} \right] = 0. \quad (22)$$

This is the proper form of the convective-diffusion equation for transport on the axisymmetric surface, including effects due to the change in shape of the interface with time.

In order to solve equation(22) numerically it is convenient to write it as

$$\frac{\partial(\bar{a}^{\frac{1}{2}}\Gamma)}{\partial t} + \Lambda_1(s,t)\Gamma(s,t) + \Lambda_2(s,t)\frac{\partial \Gamma}{\partial s} + \Lambda_3(s,t)\frac{\partial^2 \Gamma}{\partial s^2} = 0. \quad (23)$$

where the coefficients Λ_i depend on the surface velocity, surface shape and the Peclet number.

We can summarize progress to this point by saying that equation (15) describes the interfacial velocity $\mathbf{u}(\mathbf{x}_s)$ if the surfactant distribution is known. The tangential component of $\mathbf{u}(\mathbf{x}_s)$ is necessary in equation (22) to determine convective transport and the normal component is used in the kinematic condition to adjust the interfacial shape. Furthermore, the local rate of change of the interfacial area appears in the first term in equation (22). An approximate method for solving this coupled set equations is described next.

3.3 Approximate numerical solution of the coupled system of equations

The highly coupled drop deformation / surfactant transport problem is solved in a step-wise manner. Although the method is approximate, we feel that it contains the correct “physics.” Results described in Section 4.1 demonstrate that decreasing the magnitude of the time step does not change the evolution of the shape or concentration field, nor does it affect the steady state calculated for the small time steps used in this study. Consequently, the simulations presented in Section 4 provide the first picture of the evolution of the surfactant concentration field simultaneously with the drop shape evolution on a finitely deformed drop. Such a transient procedure is necessary for an accurate description of drop breakup in the presence of surface-active agents.

The approximate numerical procedure is now described. Given an initial surfactant distribution, equation (15) is solved for the instantaneous interfacial velocity field at time t . The interface shape is then updated by solving the kinematic condition using an explicit Euler method. This shape is assumed to be the correct shape at the new time $t + \Delta t$. To this point the method is the same as the one used in our previous studies of drop deformation.

In order to determine $\Gamma(t + \Delta t)$ on this new shape the convective-diffusion equation (22) is then solved using an implicit Euler method. However, because the velocity field corresponding to this new shape is *not* known, we *assume* that the velocity field at any node point at $t + \Delta t$ is well-approximated by the velocity of this node point at time t . Clearly, this is not exactly correct. However, for the small time steps used in this study the interface evolves very slowly and this method provides a very good approximation to the convective term in equation (22). The basic idea is that the evolution of the shape and concentration field from one steady state to another steady state occurs on a long time scale relative to the time step Δt .

In order to actually calculate the surfactant distribution, $\Gamma(s, t)$ is dis-

cretized using the same grid introduced in Section 3.1 to describe the drop surface, equation (23) is written in finite difference form and $\Gamma(s)$ is assumed to vary quadratically between node points. Therefore, if Γ_i denotes the surfactant concentration at node point i , $\frac{\partial \Gamma}{\partial s}$ and $\frac{\partial^2 \Gamma}{\partial s^2}$ at each collocation point can be written in terms of Γ_{i-1} , Γ_i and Γ_{i+1} . Equation (23) is then written in implicit form at each node point and the linear system of equation that is produced for the surfactant distribution is solved using Gaussian elimination. This procedure produces the approximate shape and surfactant distribution at time $t + \Delta t$ that is then used in equation (15) to calculate a new velocity field, etc. An obvious improvement of this method is to use the new velocity field in an iteration scheme to determine the concentration field for a given shape. However, since the explicit/implicit procedure described above is convergent when the (small) time step is decreased (see Section 4.1) we have not tried to further refine our technique.

We should add that using the same step-wise procedure an attempt was made to solve the convective-diffusion equation (23) using an explicit Euler method. The numerical solution in this case proved to be very unstable. Using the implicit procedure provided a very stable and smooth solution.

Steady states are calculated by marching along until the normal velocity is very small (typically $|\mathbf{u} \cdot \mathbf{n}| < 4 \times 10^{-4}$) at each collocation point and the concentration field at any node point changes by a negligible amount between two time steps. Typically, we choose $N = 15 - 20$ node points and a time step $\Delta t = 0.02 - 0.05$. The numerical procedure can be monitored as time progresses by following the change in volume of the drop and the change in the total amount of surfactant, which must remain constant for the case of an insoluble surfactant. Typically, volume changes and changes in the total amount of surfactant are less than one percent over a thousand iterations.

4. RESULTS

In this section we discuss some of the numerical results we have obtained in our study of the effect of surfactants on drop deformation in extensional flows. The results are not extensive, but they do indicate that the numerical procedure described in Section 3 can resolve both the evolution of the surfactant concentration and the drop shape. Also, several interesting physical observations are described.

4.1 Convergence of the numerical method

To begin with we should test the accuracy of the numerical procedure by comparing with known analytic results. Unfortunately, there exists at this time no straightforward analytic result. Therefore, we tested the numerical scheme by decreasing the magnitude of the time step and comparing the calculated steady-state deformations and surfactant concentration distributions at different capillary numbers. In all cases, for the small time steps used in these simulations, the calculations using a smaller time step were identical with calculations performed with a larger time step. For example, in figure 2 we show the steady-state drop deformation D as a function of the capillary number for the case $\beta = 0.9$ and $Pe_s = 10.0$. The open squares are the numerical results using a time step $\Delta t = 0.05$ and incrementing the capillary number between steady shapes by $\Delta C = 0.01$ and the solid circles are the numerical results with $\Delta t = 0.025$ and $\Delta C = 0.005$. In both cases the numerical scheme smoothly approaches the same steady state. In figure 3, we show a similar comparison for the case $\beta = 0.1$ and $Pe_s = 10.0$. Notice that in figure 2 there is a small difference developing at larger values of C . This is a consequence of the evolutionary nature of the problem and results from the accumulation of numerical errors in the solution using larger values of the time step. With the level of accuracy indicated in figures 2 and 3 we use the numerical method to examine the effects of β , Pe_s , and C on finite drop deformation.

4.2 Initial observations

We first present some typical steady deformation results. In figure 4 the solid curve is the numerically calculated steady drop shape as a function of the capillary number for $\beta = 0.1$ and $Pe_s = 10.0$. Numerically generated shapes are also shown. For reference, the dashed line is the result for a clean surface, $\beta = 0.0$. Recall that the capillary number is defined with respect to the interfacial tension of the initial uniformly contaminated undeformed surface so the difference between the two curves is solely dependent on interfacial tension variations that arise because $\beta \neq 0$. In the case of surfactant, the calculations have not been continued until breakup. For each of the intermediate shapes shown, the surfactant distribution along the drop surface is shown in figure 5. In figures 6 and 7 we show additional simulations for the drop shape and surfactant distribution for $\beta = 0.7$, $Pe = 10.0$ and in figures 8 and 9 we show the case $\beta = 0.8$ and $Pe = 10.0$.

We make a number of observations immediately. First of all, in each of the simulations, at low values of the capillary number the deformation in the presence of surfactants is larger than without the surfactant. This difference initially increases as the capillary number increases. In figure 5 it is also evident that for small values of β the concentration gradient along the surface becomes quite large as the deformation and capillary number increase. In the sense that the drop shape is more deformed with surfactant than without surfactant, the surfactant might be considered, at least qualitatively, to be destabilizing. However, as illustrated in figure 8 (and the trend in figure 7 suggests a similar effect) as the capillary number is increased further the drop deforms to a lesser degree than the clean interface case! As figure 8 shows, at $C \approx 0.107$ the drop with surfactant, hence interfacial tension variations, actually has the same deformation D as a drop with no surfactant at all! This result is quite striking and, in the sense that steady shapes are calculated for capillary numbers greater than the critical value necessary for breakup of a surfactant-free drop, the net

effect of interfacial tension variations appears to be *stabilizing*. The calculations have not been continued until breakup but there is obviously motivation for continuing this type of study.

The striking effect due to interfacial tension variations displayed above deserves comment. The interfacial tension variation along the drop surface is affected by the capillary number in two competing ways. The first, direct effect of the velocity gradient is to convect surfactant toward the end of the droplet. This acts to decrease the interfacial tension near the end and increase the interfacial tension near the center of the drop. At least at small capillary numbers the principal effect of this “convection mode” that lowers the interfacial tension in the neighborhood of the end is to require a larger curvature at the end, hence more deformation.

On the other hand, the capillary number also plays an indirect competing role due to flow-induced deformation of the drop. As the drop deforms, the interfacial area increases. In the case of insoluble surfactant, the qualitative effect of an increase in interfacial area would be to *lower* the local surfactant concentration, hence increase the interfacial tension, thereby making deformation more difficult. At least in a qualitative sense, this is what is observed in the numerical simulations. Due to the limited number of simulations performed at this time, we haven’t been able to test this idea further.

4.3 The effect of Pe_s

In figure 9 we compare steady-state deformation curves for the same value of β but different values of the surface Peclet number. Low values of Pe_s correspond to cases where the surface diffusivity is large. In these cases very small concentration gradients are observed and the surfactant remains uniformly distributed. However, large values of the Peclet number (low surface diffusivity) are accompanied by large concentration gradients. The basic observation is that at a given value of the capillary number the drop is more deformed for larger values of Pe_s . Because larger concentrations of surfactant near the end of the

drop produce a sharp decrease in the interfacial tension, the drop appears to compensate by increasing the curvature near the end via increased deformation.

5. CONCLUSIONS

In this paper we have set out to study drop deformation in extensional flows in the presence of surface-active agents. An approximate numerical scheme based on the boundary integral method has been developed that appears capable of analyzing this time-dependent, coupled free-boundary / surfactant transport problem.

Although the numerical simulation presented are not extensive, the results suggest several interesting physical effects, including an apparent stabilizing influence of surfactant since steady drop shapes are calculated at capillary numbers greater than the critical capillary number for a surfactant-free drop. Clearly these results pose several questions that deserve further attention.

REFERENCES

- Acrivos, A. 1983 The breakup of small drops and bubbles in shear flows. *4th Int Conf. on Physicochemical Hydrodynamics, Ann. N.Y. Acad. Sci.* **404**, 1-11.
- Adamson, A.W. 1976 *Physical Chemistry of Surfaces*. Third edition. John Wiley & Sons. 698 pp.
- Aris, R. 1962 *Vectors, Tensors and the Basic Equations of Fluid Mechanics*. Prentice-Hall, Inc. 286 pp.
- Ascoli, E.P. & Leal, L.G. 1988 Thermocapillary migration of a drop normal to a planar wall (in preparation).
- Barthes-Biesel, D. & Acrivos, A. 1973 Deformation and burst of a liquid droplet freely suspended in a linear shear field. *J. Fluid Mech.* **61**, 1-21.
- Bentley, B.J. & Leal, L.G. 1986 An experimental investigation of drop deformation and breakup in steady two-dimensional linear flows. *J. Fluid Mech.* **167**, 241-283.
- Cox, R.G. 1969 The deformation of a drop in a general time-dependent fluid flow. *J. Fluid Mech.* **37**, 601-623.
- Flumerfelt, R.W. 1980 Effects of dynamic interfacial properties on drop deformation and orientation in shear and extensional flow fields. *J. Colloid Interface Sci.* **76**, 330-349.
- Grace, H.P. 1971 Dispersion phenomena in high viscosity immiscible fluid systems and application of static mixers as dispersion devices in such systems. *Eng. Found. Res. Conf. Mixing, 3rd Andover, N.H.* Republished 1982 in *Chem. Engng Commun.* **14**, 225-277.
- Greenspan, H.P. 1978 On fluid-mechanical simulations of cell division and movement. *J. Theor. Biol.* **70**, 125-134.
- Haber, S. & Hetsroni, G. 1971 Hydrodynamics of a drop submerged in an unbounded arbitrary velocity field in the presence of surfactants. *Appl. Sci.*

Res. **25**, 215-233.

Higdon, J.J.L. & Schnepfer, C.A. 1987 Interaction and deformation of viscous droplets. *Paper presented at the AIChE Annual Meeting.*

Holbrook, J.A. & LeVan, M.D. 1983a Retardation of droplet motion by surfactant. Part 1. Theoretical development and asymptotic solutions. *Chem. Eng. Commun.* **20** 191-207.

Holbrook, J.A. & LeVan, M.D. 1983b Retardation of droplet motion by surfactant. Part 2. Numerical solutions for exterior diffusion, surface diffusion, and adsorption kinetics. *Chem. Eng. Commun.* **20**, 273-290.

Lee, S.H. & Leal, L.G. 1982 The motion of a sphere in the presence of a deformable interface. II. A numerical study of the translation of a sphere normal to an interface. *J. Colloid Interface Sci.* **87**, 81-106.

LeVan, M.D. & Newman, J. 1976 The effect of surfactant on the terminal and interfacial velocities of a bubble or drop. *AIChE J.* **22**, 695-701.

Levich, V.G. 1962 *Physicochemical Hydrodynamics*. Prentice-Hall, Inc. 700 pp.

Levich, V.G. & Krylov, V.S. 1958 Surface-tension-driven phenomena. *Ann. Rev. Fluid Mech.* **1**, 293-316.

McConnell, A.J. 1957 *Applications of Tensor Analysis*. Dover 318 pp.

Newman, J. 1967 Retardation of falling drops. *Chem. Eng. Sci.* **22**, 83-85.

Pearson, J.R.A. 1958 On convection cells induced by surface tension. *J. Fluid Mech.* **4**, 489-500.

Phillips, W.J., Graves, R.W. & Flumerfelt, R.W. 1980 Experimental studies of drop dynamics in shear fields: Role of dynamic interfacial effects. *J. Colloid Interface Sci.* **76**, 350-370.

Pozrikidis, C. 1987 A study of peristaltic flows. *J. Fluid Mech.* **180**, 515-527.

Quinn, G.P. & Saville, D.A. 1974 The effects of surface-active materials on the oscillations of a liquid jet. *Chem. Eng. Sci.* **29**, 247-253.

- Rallison, J.M. 1980 A note on the time-dependent deformation of a viscous drop which is almost spherical. *J. Fluid Mech.* **98**, 625-633.
- Rallison, J.M. 1981 A numerical study of the deformation and burst of a viscous drop in general shear flows. *J. Fluid Mech.* **109**, 465-482.
- Rallison, J.M. 1984 The deformation of small viscous drops and bubbles in shear flows. *Ann. Rev. Fluid Mech.* **16**, 45-66.
- Rallison, J.M. & Acrivos, A. 1978 A numerical study of the deformation and burst of a viscous drop in general shear flows. *J. Fluid Mech.* **89**, 191-200.
- Rumscheidt, F.D. & Mason, S.G. 1961 Particle motions in sheared suspensions 12. Deformation and burst of fluid drops in shear and hyperbolic flow. *J. Colloid Sci.* **16**, 238-261.
- Sadhil, S.S. & Johnson, R.E. 1986 On the deformation of drops and bubbles with varying interfacial tension. *Chem. Eng. Commun.* **46**, 97-109.
- Sapir, T. & Nir, A. 1985 A hydrodynamic study of the furrowing stage during cleavage. *Physicochemical Hydrodynamics* **6**, 803-814.
- Saville, D.A. 1973 The effect of interfacial tension gradients on the motion of drops and bubbles. *Chem. Eng. J.* **5**, 251-259.
- Scriven, L.E. 1960 Dynamics of a fluid interface: Equations of motion for Newtonian surface fluids. *Chem. Eng. Sci.* **12**, 98-108.
- Sherwood, J.D., 1987 Drop breakup in electric and magnetic fields. (to appear).
- Stone, H.A., Bentley, B.J. & Leal, L.G. 1986 An experimental study of transient effects in the breakup of viscous drops. *J. Fluid Mech.* **173**, 131-158.
- Stone, H.A. & Leal, L.G. 1987 Relaxation and breakup of an initially extended drop in an otherwise quiescent fluid. *J. Fluid Mech.* (submitted).
- Stone, H.A. & Leal, L.G. 1988 The influence of initial deformation on drop breakup in time-dependent flows at low Reynolds numbers. *J. Fluid Mech.* (submitted).

- Stoos, J.A. & Leal, L.G. 1987 The creeping motion of a spherical particle in a linear axisymmetric straining flow normal to a deformable interface. *J. Fluid Mech.* (submitted).
- Taylor, G.I. 1932 The viscosity of a fluid containing small drops of another fluid. *Proc. R. Soc. Lond.* **A138**, 41-48.
- Taylor, G.I. 1934 The formation of emulsions in definable fields of flow. *Proc. R. Soc. Lond.* **A146**, 501-523.
- Torza, S., Cox, R.G. & Mason, S.G. 1972 Particle motions in sheared suspensions. 27. Transient and steady deformation and burst of liquid drops. *J. Colloid Interface Sci.* **38**, 395-411.
- Whitaker, S. 1976 Studies of the drop-weight method for surfactant solutions III. Drop stability, the effect of surfactants on the stability of a column of liquid. *J. Colloid Interface Sci.* **54**, 231-248.
- Youngren, G.K & Acrivos, A. 1975 Stokes flow past a particle of arbitrary shape; a numerical method of solution. *J. Fluid Mech.* **69**, 377-403 (corrigendum **69**, 813).
- Young, N.O., Goldstein, J.S. & Block, M.J. 1959 The motion of bubbles in a vertical temperature gradient. *J. Fluid Mech.* **6**, 350-356.

FIGURE CAPTIONS

- Figure 1 Schematic of problem: drop deformation in the presence of surface-active agents.
- Figure 2 Testing of numerical procedure. Effect of decreasing the step size from 0.05 to 0.025. The numerical scheme converges to the same steady shape. $\beta = 0.9$, $Pe_s = 1.0$.
- Figure 3 Testing of numerical procedure. Effect of decreasing the step size from 0.05 to 0.025. The numerical scheme converges to the same steady shape. $\beta = 0.1$, $Pe_s = 10.0$.
- Figure 4 Steady state shape versus capillary number. $\beta = 0.1$, $Pe_s = 10.0$.
- Figure 5 Steady state concentration field for the steady shapes shown in figure 4.
- Figure 6 Steady state shape versus capillary number. $\beta = 0.7$, $Pe_s = 10.0$.
- Figure 7 Steady state concentration field for the steady shapes shown in figure 6.
- Figure 8 Steady state shape versus capillary number. $\beta = 0.8$, $Pe_s = 10.0$.
- Figure 9 Steady state concentration field for the steady shapes shown in figure 8.
- Figure 10 The effect of varying Pe_s . $\beta = 0.1$.

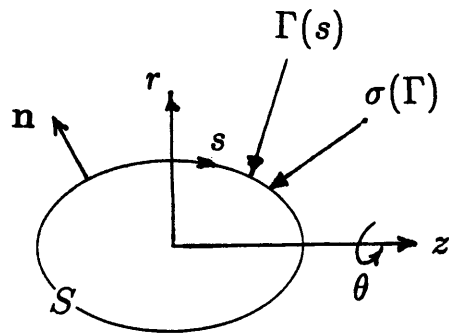


Figure 1

$\beta = 0.9$ $Pe_s = 1.0$

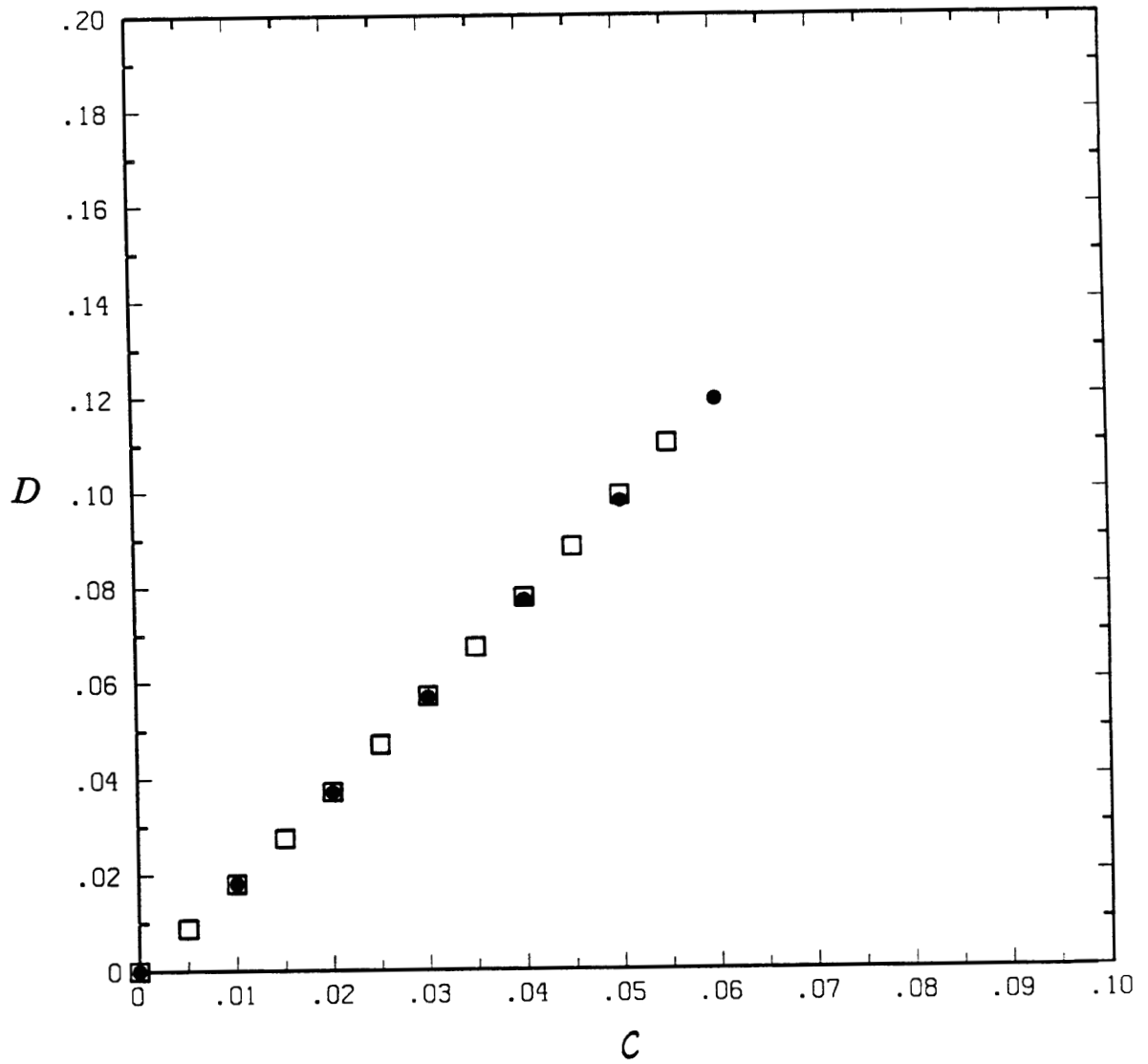


Figure 2

$\beta = 0.1$ $Pe_s = 10.0$

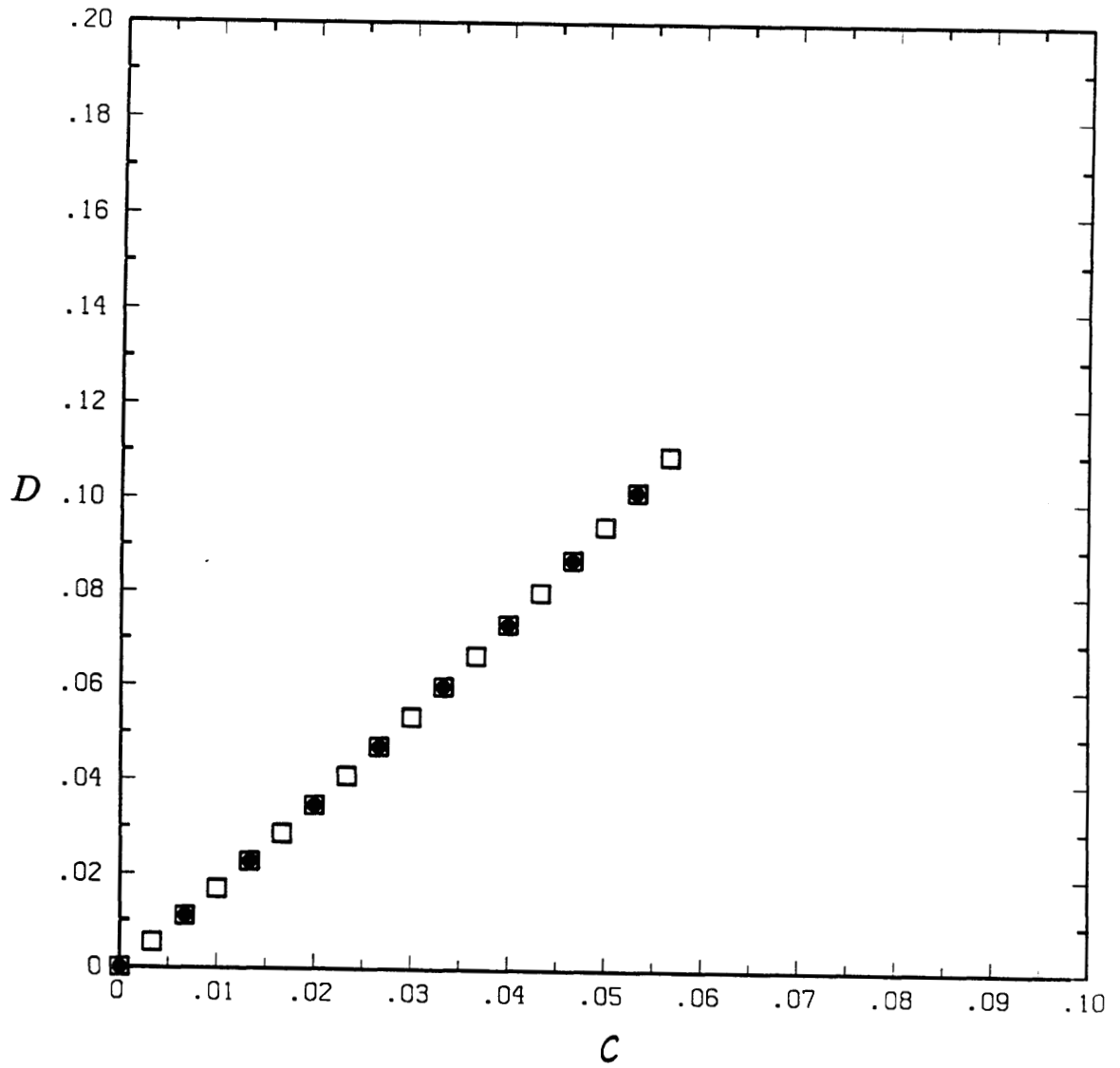


Figure 3

$\beta = 0.1 \quad Pe_s = 10.0$

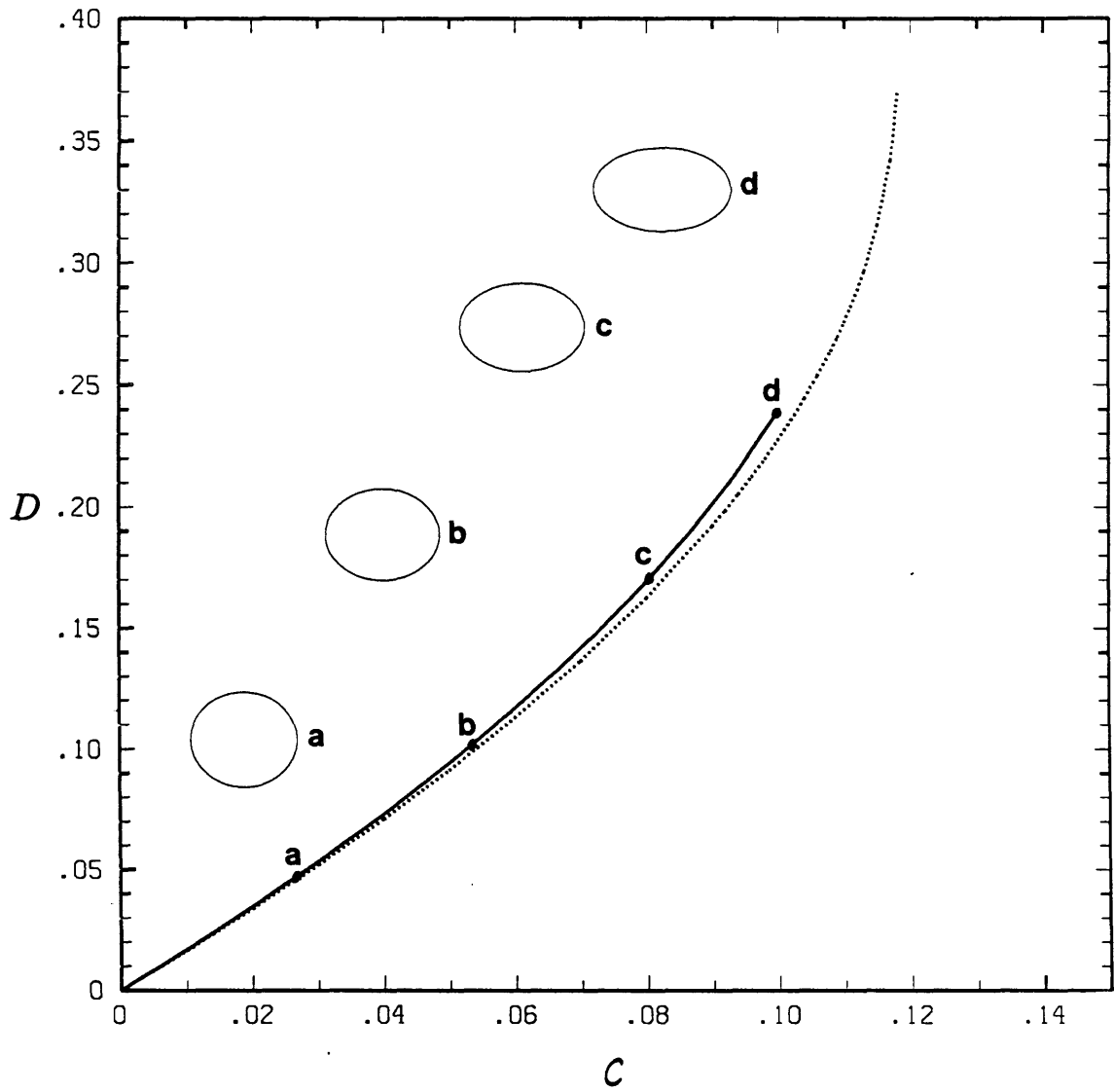


Figure 4

$\beta = 0.1 \quad Pe_s = 10.0$

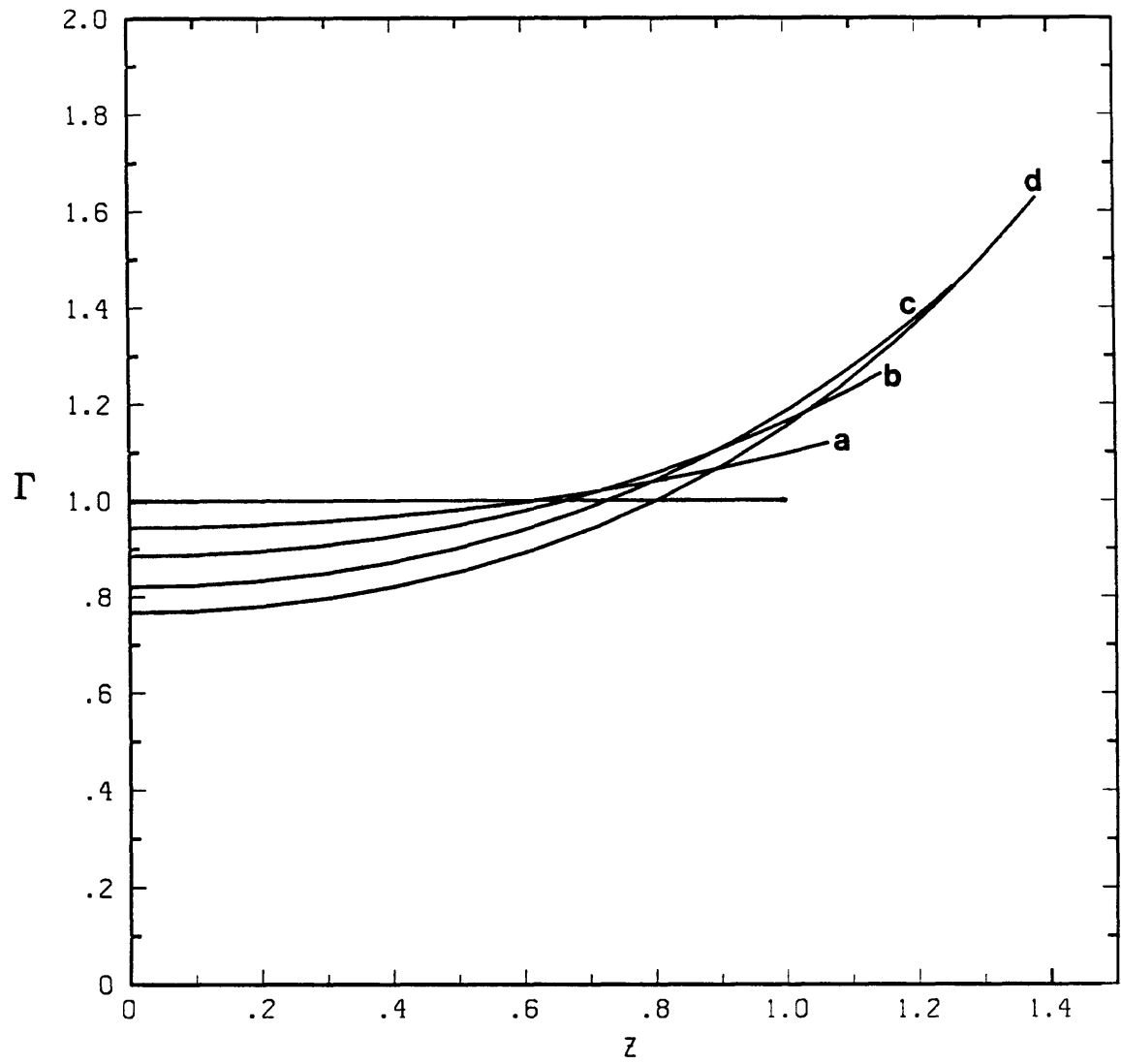


Figure 5

$$\beta = 0.7 \quad Pe_s = 10.0$$

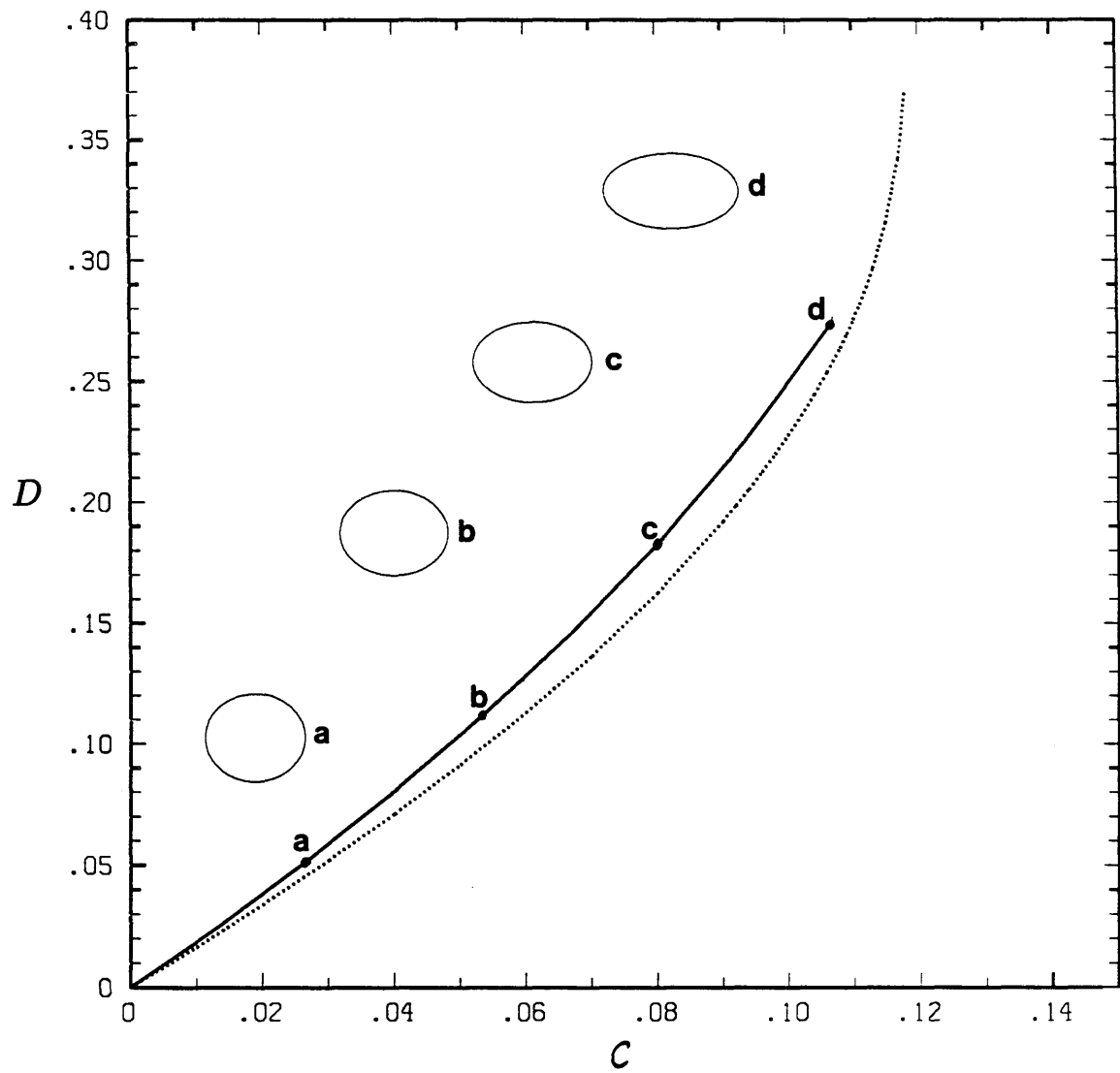


Figure 6

$\beta = 0.7$ $Pe_s = 10.0$

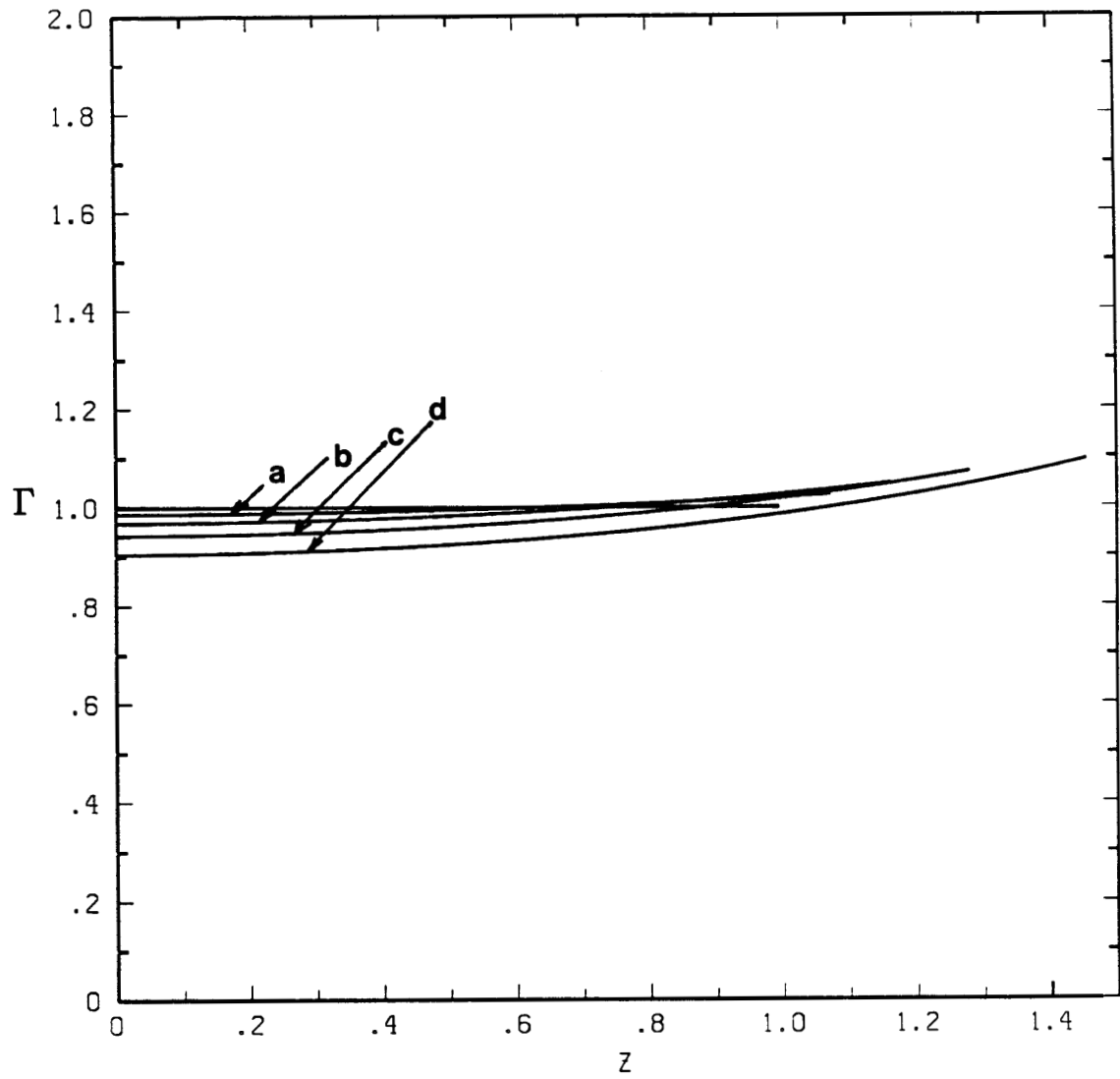


Figure 7

$\beta = 0.8$ $Pe_s = 10.0$

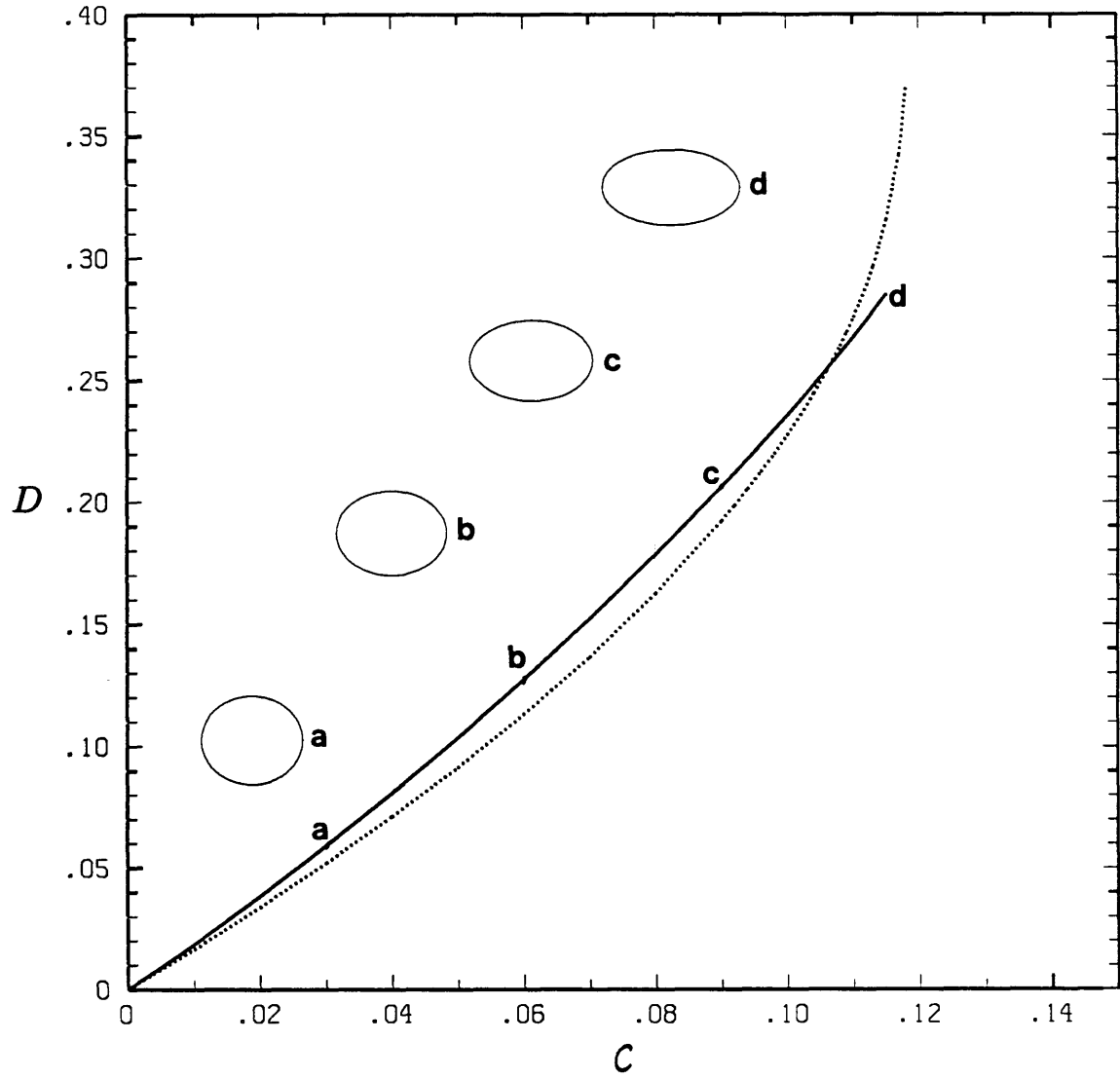


Figure 8

$\beta = 0.8$ $Pe_s = 10.0$

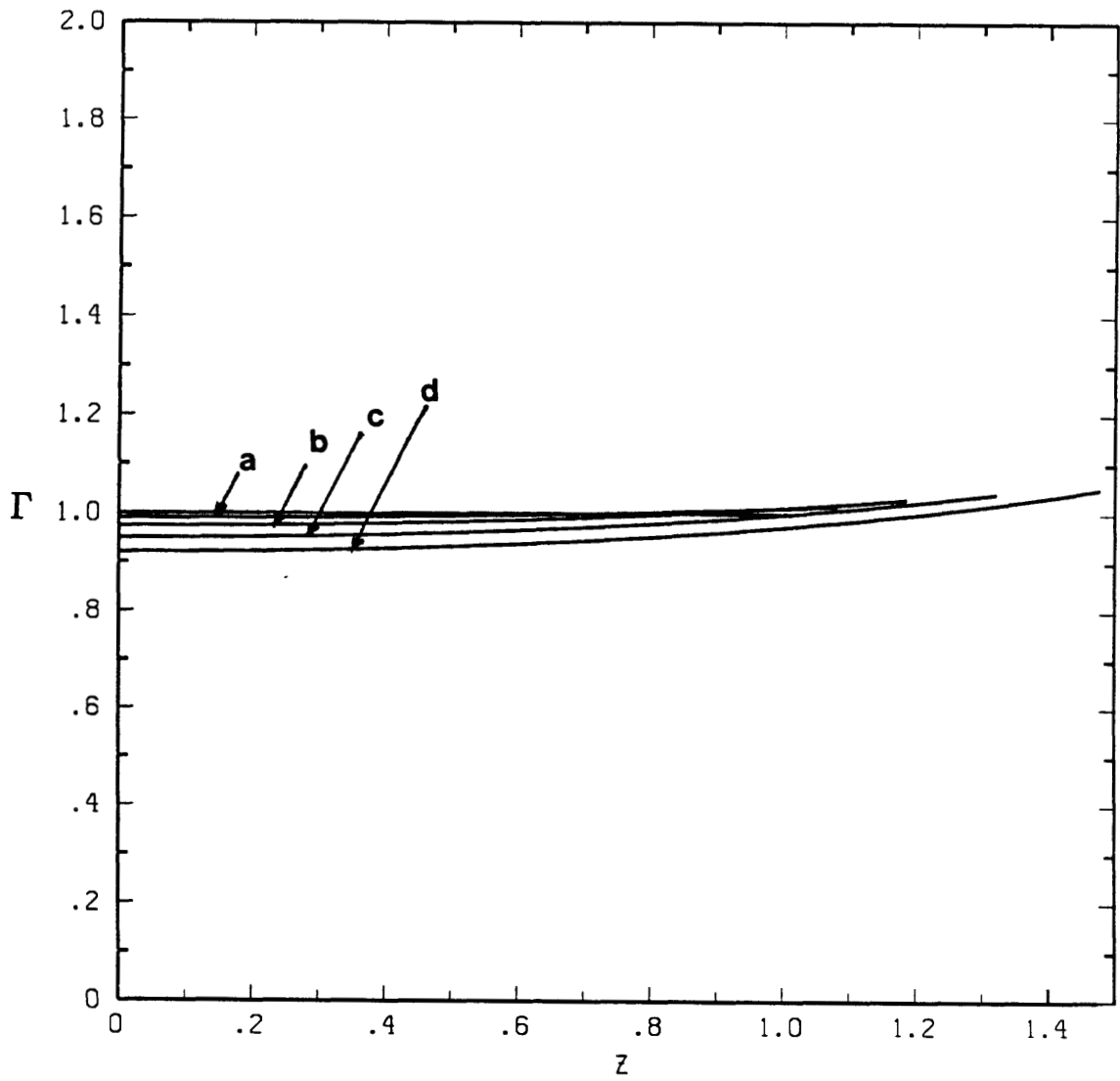


Figure 9

$\beta = 0.1$

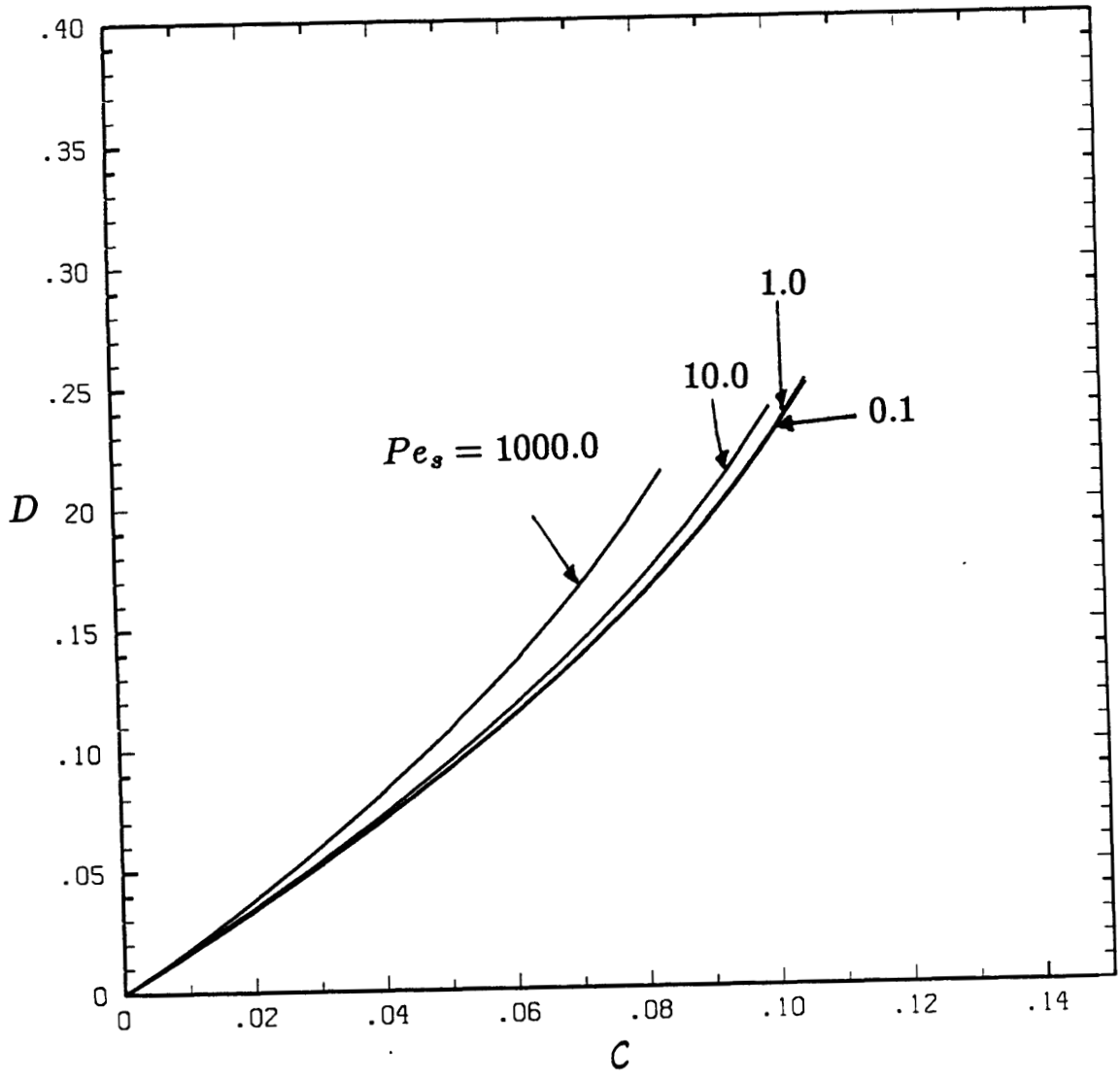


Figure 10

CHAPTER 7

THESIS SUMMARY

In this thesis we have addressed several free-boundary problems associated with drop deformation and breakup at low Reynolds numbers. The major focus of this work concerns the mechanism of drop breakup in simple time-dependent flows. This topic is discussed extensively in Chapters 2-4 and Appendix 1 using both experimental and numerical studies. The ideas and methods developed during the drop breakup investigations are then applied to two related problems: (1) the deformation and breakup of concentric double emulsion drops in linear flows (Chapter 5) and (2) the effect of surfactants on drop deformation (Chapter 6). Below we summarize some of the important conclusions of our work.

DROP BREAKUP

Although the deformation of a liquid droplet has been extensively studied for over 50 years, there have been very few careful and detailed studies of the drop breakup process, the mechanism of breakup and effects due to time-dependent flows. There are basically two reasons for this. First, it has only been in recent years that careful experimental studies of the transient breakup phenomena, characteristic of highly elongated droplets, have become possible. Second, it has also only been in recent years that numerical procedures capable of describing time-dependent free-boundary problems have been developed. We take advantage of both of these developments to study the drop breakup problem with particular emphasis on the interface evolution and the mechanism of breakup. The investigation of simple time-dependent flows presented in this thesis is a necessary first step toward understanding more complicated flow situations.

The experiments are performed in a computer-controlled four-roll mill. As part of these investigations a simple digital image analysis scheme has been developed to monitor the rapid drop shape changes that occur during the many transient experiments performed. The numerical investigation makes use of the boundary integral method. The numerical procedure provides valuable insight into the dynamics of the breakup process and demonstrates application of the

boundary integral method to highly distorted drop shapes.

Included among the experimental studies described in this thesis are the stretching of drops at the critical capillary number, the effect of abruptly halting the flow with the drop in a highly elongated nonequilibrium state and the effect of subcritical flows on drops stretched beyond their maximum steady deformation. The subcritical flow studies examine step reductions in shear rate and/or the abrupt addition of vorticity to the flow.

It is demonstrated experimentally that complete fragmentation of a highly elongated droplet in an otherwise quiescent fluid may occur due to a deterministic interfacial-tension-driven flow established by curvature variations along the fluid-fluid interface. Because it is observed that the ends of the drop rapidly bulb up and then break off from the central portion of the drop, this process is called "end pinching." The experiments are then extended to consider subcritical flows and it is observed that an interfacial-tension-driven flow is responsible for complete drop breakup in a subcritical flow without large scale stretching of the drop. Overall, the relaxation and breakup process depend in a relatively complicated manner on the interaction of the external flow, which attempts to drain fluid from the middle of the drop while simultaneously seeking to continue to stretch the drop, and the interfacial-tension-driven flow, which, at least initially, is responsible for relaxation of the drop. The interesting feature associated with the sudden addition of vorticity to the external flow is the rapid rotation of the drop to a new steady orientation followed by relaxation and/or breakup according to the effective flow conditions at the new orientation. When relaxation back to a steady state occurs, there is a monotonic approach to the steady state and the steady shape established is the same as is observed by starting with a spherical initial shape in the subcritical flow.

A complementary numerical study provides valuable insight into the dynamics of the interface evolution and the flow processes responsible for either relaxation or breakup. It is demonstrated that the numerical simulations capture

both the qualitative and the quantitative features of the breakup phenomena assuming that the interfacial tension is constant along the surface.

A number of other transient aspects of the deformation and breakup phenomenon are discussed also. The role of capillary waves during the breakup process is examined both experimentally and numerically. Capillary waves only appear to play a role in breakup on the midsection of very elongated drops when end effects are negligible. In addition, many photographs and numerical simulations of complete drop fragmentation are shown throughout this thesis. Also, several instances of rather interesting free-surface configurations of the final stages of the breakup are seen to involve a conically tipped thread connected to an almost spherical end.

A comparison of drop deformation and breakup in uniaxial and biaxial flows is provided in Appendix 1. The results are discussed in terms of the strong flow ideas of microstructure deformation presented by Olbricht, Rallison & Leal (1982).

The net result of the experimental and numerical investigations reported in this thesis is a much improved understanding of the drop breakup process. Effects of the capillary number, viscosity ratio, flow-type, subcritical flow and initial conditions are presented and discussed.

CONCENTRIC DOUBLE EMULSION DROPLETS

In Chapter 5, the deformation and breakup of concentric double emulsion droplets in linear flows are described. An analytic investigation of nearly spherical interfaces is complemented by a complete numerical solution, again using the boundary integral method, to study highly deformed globules. Effects of capillary number, flow-type, the ratio of the different fluid viscosities, and the ratio of interfacial tensions are discussed. The main interest is to compare and contrast the multiphase drop behaviour with single phase drop results to understand when single phase studies may be relevant to the compound drop problem.

Several interesting observations are made in this free-boundary problem. In

a uniaxial extensional flow, the outer drop is deformed into a prolate ellipsoidal shape while the inner drop is deformed into an oblate ellipsoidal shape. Two interesting breakup processes are directly related to this flow-induced deformation. It is demonstrated that the finite deformation of the globule may cause the inner interface to come into contact with the outer interface even though the globule is itself not highly deformed. This suggests a mechanism for globule rupture that does not involve highly stretched shapes. Furthermore, because of the increased effectiveness of uniaxial flows at producing finite deformation relative to biaxial flows, a numerical example is shown where the globule deforms very little when placed in a biaxial flow, but the inner drop is exposed to a uniaxial flow and rapidly becomes very deformed. This suggests that the outer shape may be stable, but, nevertheless, the flow-induced deformation internal to the globule may produce breakup of the internal particle.

THE EFFECT OF SURFACTANTS ON DROP BREAKUP

Finally, an introduction to the effect of surfactants on drop deformation is provided in Chapter 6. The deformation and surfactant transport problem is highly coupled and an approximate numerical solution is described. Although the results are not extensive, these calculations are among the first describing Marangoni effects on finitely deformed drops.

APPENDIX 1

DROP DEFORMATION IN BIAXIAL FLOWS

1. INTRODUCTION

In this appendix we present numerical calculations of the finite deformation and breakup of Newtonian liquid droplets in biaxial extensional flows at low Reynolds numbers. The boundary integral method is used to determine steady-state drop shapes as a function of the capillary number. In addition, the ability of the numerical method to investigate time-dependent free-boundary problems and highly distorted drop shapes is used to examine some unsteady aspects of the dynamics of the deformation and breakup process. For completeness, comparison with the small deformation theory of Barthes-Biesel and Acrivos (1973) is included. These results provide a nice extension to the study of a bubble in a biaxial extensional flow at finite Reynolds numbers presented by Kang & Leal (1988) and to the relatively well-studied problem of a drop in a uniaxial extensional flow at low Reynolds numbers (for example, see Rallison & Acrivos 1978).

The study of drop deformation in biaxial extensional flows has received very little attention in the literature. Nevertheless, the problem is meaningful physically as an example of the general class of linear flows where extension occurs predominantly in two orthogonal directions and, as discussed by Hinze (1955) and Lewis & Davidson (1982), this problem should be considered to better understand bubble and drop breakup phenomena. In addition, biaxial flows are approximated in the region where two impinging jets meet.

As far as we are aware, the only calculations for the deformation characteristics of drops in biaxial extensional flows are due to Frankel & Acrivos (1970) and Barthes-Biesel & Acrivos (1973). Frankel & Acrivos performed a perturbation analysis for nearly spherical droplets of arbitrary ratio of dispersed to continuous phase viscosity and predicted the first small deformation effects produced by the flow. Barthes-Biesel & Acrivos extended the analysis to higher order in the small deformation parameter. In addition, Frankel & Acrivos performed a full numerical solution for the arbitrary deformation of a bubble. Clearly, there remain

many questions regarding the finite deformation and actual breakup process for *drops* in biaxial flows at low Reynolds numbers. For example, the mechanism of breakup, the effect of viscosity ratio and time-dependent features of the breakup process are all interesting, though unanswered, questions.

This scarcity of work was one of the primary motivations for the recent study of Kang & Leal (1988). These authors examined time-dependent features of the *bubble* deformation and breakup process for Reynolds number, \mathcal{R} , $0 \leq \mathcal{R} \leq 200$. One of the main conclusions of their study was that no critical shear rate for the nonexistence of steady-state solutions was found, at least for the range of shear rates examined. Indeed, their calculations at zero Reynolds numbers did not locate a critical capillary number for bubble breakup in spite of the fact that the drops were highly deformed.

One obvious extension of this work is to examine the case of liquid droplets. At low Reynolds numbers this task is accomplished in a straightforward manner using the boundary integral method. Additional insight offered by such a study is to compare droplet deformation and breakup behaviour in biaxial flows with analogous behaviour in uniaxial extensional flows. This provides an interesting comparison of effects due to a change of the *flow-type*.

It is well known that at low Reynolds numbers the effect of vorticity in the undisturbed flow acts to inhibit drop breakup. This was first recognized by G.I. Taylor in the 1930s. Taylor demonstrated that droplets of any viscosity ratio could be made to burst in a two-dimensional extensional flow but droplets that were approximately four times as viscous as the suspending fluid could not be burst in a simple shear flow. This *flow-type* effect is easily understood as an interaction between rate-of-strain of fluid elements, which produces stretching, and rotation of fluid elements, which effectively inhibits breakup. Recently, these ideas were extended to the entire spectrum of two-dimensional linear flows by Bentley & Leal (1986). In the study reported here, however, a difference in flow-type does not arise because of vorticity in the undisturbed flow. Rather,

calculations of drop deformation in biaxial extensional flows can be compared with uniaxial extensional flows to study the effect of changing the principal directions of extension. In this case, as we shall see, the effect of the two different flows is only evident after the drop has undergone finite deformation.

A general framework for examining the effect of a given external flow on a deformable microstructure is presented by Olbricht, Rallison & Leal (1982). An extension of some of these ideas to the breakup of slender drops is discussed by Khakhar & Ottino (1986). The formulation of Olbricht *et al.* incorporates *both* the kinematics of the flow field and a description of the deformation and/or orientation of the suspended microelements (in this case drops). The objective of such an analysis is to delineate “strong” flow conditions. These flow conditions are capable of producing large distortions to a suspended microstructure. The theoretical developments are predicated on two models of the microstructure: (1) a vector model that characterizes the rate-of-change of the length and orientation of the suspended particles and (2) a second order tensor model that describes the first flow-induced deviations of the structure from isotropy. In principle, both models are limited to describing small deviations from a rest state configuration. We will compare our numerical results of the *finite* deformation of drops in biaxial and uniaxial flows with the strong flow results of Olbricht, *et al.*

2. NUMERICAL PROCEDURE

The boundary integral method described in previous chapters is used to study this time-dependent free boundary problem. Before discussing the results, a few remarks about the numerical procedure are required.

All variables are nondimensionalized as described in Chapter 3. For example, the characteristic velocity is chosen as $u_c = \frac{\sigma}{\mu}$ and the characteristic time as $t_c = \frac{a\mu}{\sigma}$ where σ, μ and a represent the interfacial tension, suspending fluid viscosity and undeformed drop radius, respectively. The capillary number, $C = \frac{Ga\mu}{\sigma}$, (G is the local shear rate) provides a measure of viscous forces causing deformation of the drop relative to interfacial tension forces that resist deformation and $\lambda = \frac{\hat{\mu}}{\mu}$ where $\hat{\mu}$ is the viscosity of the droplet phase. The external velocity field is described by equation (3) in Chapter 5 where the $-$ sign corresponds to the biaxial flow field studied here.

The drop surface is parametrized using a normalized measure of arclength s , $0 \leq s \leq 1$ (see figure 1). The collocation points along the discretized interface are labeled using the cylindrical coordinates (r, z) and twice continuously differentiable representations for $r(s)$ and $z(s)$ are generated using cubic splines. Every few iterations the collocation points are evenly redistributed based upon arclength along the surface. This minimizes convection of the collocation points that leads to uneven element distribution, which in turn results in poor resolution of the interface shape, and is a principal cause of numerical difficulties. For the steady-state calculations presented here the number of boundary elements N chosen typically is $N = 20$, although for the highly deformed shapes characteristic of the unsteady stretching process that occurs at the critical capillary number, we choose $N = 30$.

The steady-state results for the drop deformation D as a function of capillary number are determined by beginning with a spherical shape and $C = 0.01$. The steady state is established when the normal velocity at each of the collocation points is very small so that minimal changes in drop shape are occurring.

Typically, we require $|\mathbf{u} \cdot \mathbf{n}| < 6 \times 10^{-4}$. After a steady shape is established, the capillary number is incremented ($\Delta C = 0.01$) and the steady shape at the old value of the capillary number is used as the new initial condition.

The accuracy of the method can be checked by comparing with the small deformation theory of Barthes-Biesel & Acrivos (1973) and the drop volume is monitored as a function of time. Typically, the drop volume changes by less than a percent over a thousand iterations, but as the drop becomes highly deformed or the viscosity ratio is made significantly lower than $O(1)$ larger volume changes occur.

A convenient scalar measure of distortion for modestly deformed drops is the deformation parameter $D = \frac{L-B}{L+B}$ where L is the half-length of the drop and B is the half-breadth. Here we measure the length in the r -direction so that $D > 0$ for the oblate spheroidal shapes formed by the biaxial flows. When the drop becomes highly deformed a more convenient scalar measure of distortion is the dimensionless drop length $\frac{L}{a}$.

3. RESULTS / DISCUSSION

In this section we summarize our numerical observations of drop deformation and breakup in axisymmetric biaxial flows. Throughout this discussion we compare the results with the deformation of drops in uniaxial flows and we make reference to the strong flow ideas of microstructure deformation described by Olbricht, Rallison & Leal (1982).

3.1 Steady-state calculations

In figure 2 the steady-state drop deformation D is plotted as a function of the capillary number for $\lambda = 1.0$. The solid line is the result of the numerical simulation, the short dashed line the result of the $O(C)$ theory of Barthes-Biesel & Acrivos (1973) and the long dashed line is the $O(C^2)$ theory. Several numerically calculated drop shapes are shown. The second order theory is continued up to the turning point. Beyond this point Barthes-Biesel & Acrivos report that the solutions are unstable, although it should be noted that the results given in Barthes-Biesel & Acrivos for the critical capillary number do not agree with the analytic calculations presented here. They predict $C = 0.26$, which is much lower than the theoretical result or numerical simulation shown in figure 2. We have no explanation for this discrepancy.

The numerically calculated curve is stopped when a steady shape no longer exists. We find that at $C = 0.41$ the droplet begins to undergo a continuous extension so that breakup occurs because of the nonexistence of a steady drop shape. The time-dependent stretching that occurs will be discussed more below. The theory of Barthes-Biesel & Acrivos predicts that break up occurs as a result of the drop shape becoming unstable to small disturbances. However, this is a prediction of a small deformation theory, so it does not necessarily follow that predictions applicable near the point of breakup, where the drop deformation is large, should be strictly correct. Rather, it may be surprising that the theory works as well as it does. Clearly, agreement between the theory and numerics is very good, especially for low capillary numbers and are still quite good for

$D \approx 0.4$. The critical capillary number for breakup is approximated quite well also.

It is interesting to note that the final steady shape shown in figure 1 has a midsection that is practically flat. Close examination of this shape shows that there is actually a slight indentation in the middle of the drop. It is not clear whether this is a real physical characteristic of the highly deformed steady shapes produced at larger values of the capillary number or whether it is an artifact due to small numerical errors inherent in the numerical technique. Nevertheless, a small increase in capillary number causes the droplet to continuously extend.

In figure 3 the steady-state deformation results for a drop in a uniaxial extensional flow (dashed curve) are compared with the biaxial flow calculations (solid curve). Several remarks regarding these results are in order. First of all, at low values of the capillary number, the distortions produced by the two flows are the same. This is in accord with the predictions of small deformation theory since both flows produce only slightly nonspherical shapes at low C . The second order tensor model of Olbricht *et al.* is closely related to the small deformation analysis of Barthes-Biesel & Acrivos and, consequently, is also not capable of distinguishing distortions produced by uniaxial and biaxial extensional flows. However, the vector model of Olbricht *et al.* predicts that uniaxial flows produce larger microstructural deformations than biaxial flows for the same shear rate. Indeed, in figure 3 the numerical calculations of finite drop deformation show this to be true. Even though the second order tensor model is identical to the rigorous derivation of nearly spherical distortions of a drop in a linear flow, it nonetheless appears that for *finite* drop deformations the vector model provides a better measure of the effective strength of the flow with regard to microstructural deformations. Also, it is clear that a much larger capillary number is necessary to cause drop burst in a biaxial flow than in a uniaxial flow and the numerics indicate that much larger steady shapes are possible in the biaxial flow.

The numerically calculated steady-state deformation curve for $\lambda = 10.0$

is shown in figure 4. Again, numerically generated shapes are included. The interesting feature of these results is that the $O(C)$ prediction provides a better approximation to the numerical curve than the higher order theory does for a large range of capillary numbers. A similar observation was made by Barthes-Biesel & Acrivos for the case $\lambda = 0$. Drop breakup again occurs by the drop continuously elongating when the capillary number is increased a little beyond the value for the final steady shape shown in figure 4. The capillary number necessary for breakup at $\lambda = 10.0$ is smaller than the critical capillary number determined in figure 2 for $\lambda = 1.0$. An identical trend is found for drop breakup in uniaxial extensional flows.

Before proceeding further, a few remarks are necessary concerning the drop shapes produced by biaxial flows at low Reynolds numbers. At low values of the capillary number the flow generates oblate spheroidal shapes. As the capillary number is increased the drop elongates and the midsections flattens, eventually becoming almost planar. The curvature in this case is very small along most of the interface and decreases as the midsection gets thinner. In uniaxial flows, however, the drop midsection is cylindrical and the curvature increases with increasing deformation (the drop radius decreases). In other words, if ϵ represents the slenderness of the drop it is straightforward to show that the curvature ($\nabla_{\mathbf{s}} \cdot \mathbf{n}$) for the biaxial flow-induced shapes is $O(\epsilon)$ while the curvature for the uniaxial flow-induced shapes is $O(\frac{1}{\epsilon})$.

3.2 Transient effects

Next, we examine the continuous stretching process that is associated with drop breakup at the critical capillary number for $\lambda = 1.0$. The dimensionless drop length $\frac{L}{a}$ is plotted versus time in figure 5. After a very slow elongation, the droplet begins to rapidly extend. This is similar qualitatively to the breakup process in uniaxial flows.

Even more informative, though, are the drop shapes produced during the time-dependent elongation. In figure 6 we show the final steady drop shape

and a sequence of shapes during the transient stretching process at the supercritical capillary number. Shortly after the final shape shown the numerical scheme breaks down due to poor curvature resolution near the end of the drop. Although the drop length increases slowly, the interesting aspect of the simulation is the rapid thinning that occurs near the middle of the drop. This is in marked contrast to the burst process in uniaxial extensional flows where the drop rapidly elongates and the midsection slowly thins but remains cylindrical. In an axisymmetric biaxial flow the drop is rapidly *flattened*. The midsection of the drop becomes *planar* and is enclosed by a large bulbous ring. At least during the stretching process examined here, the planar drop thins almost uniformly in the middle and in the final shape shown in figure 6 the two sides of the midsection are only separated by a dimensionless distance 0.01. As the drop continues to stretch and thin, the distance separating opposite sides of the drop interface rapidly become so short that intermolecular forces (e.g., Van der Waals attraction) would have to be considered in order to properly describe the mechanism of breakup. Clearly, the *finite* drop deformation of drops in biaxial flows is much different than the comparable deformation in uniaxial flows.

The final aspect of this numerical study is an investigation of transient effects associated with simple time-dependent flows. In principle, such a study is similar to the time-dependent effects examined in Chapters 2-4.

In figure 7, we show the relaxation of an initially extended drop in an otherwise quiescent fluid for $\lambda = 1.0$. The initial condition chosen is the most deformed shape shown in figure 6, so this study represents effects due to an abrupt halt of the biaxial flow. It is quite remarkable that the highly deformed initial shape with the very thin planar midsection relaxes back to a sphere. No breakup is observed in this case. As with the droplet relaxation studies examined in Chapters 2 and 3, the magnitude of the interfacial tension only sets the time scale characteristic of the relaxation process but plays no role in the qualitative aspects of the dynamics. Fluid motion is produced by a

deterministic interfacial-tension-driven flow that is due to curvature variations along the fluid-fluid interface. In figure 7 the planar middle slowly thickens, although the predominant motion initially is confined to the end of the drop. Finally, the middle “pops” out as the drop returns to a spherical shape.

After examining the effect of abruptly halting the flow, it is appropriate to examine the effects of subcritical capillary numbers on the deformation and breakup properties of initially extended drops. The response of a drop to step changes from the critical capillary number to subcritical values of the capillary number is examined in figure 8, again for $\lambda = 1.0$. The solid curve is the stretching process already discussed in figure 5. The dashed curves represent the response of the drop to different subcritical shear rates applied while the droplet is in a transient, nonequilibrium state. Step changes from $C = C_c$ to $C = 0.5C_c$, $0.65C_c$ and $0.8C_c$ are studied. In the first two cases, the drop recovers a steady shape, which within the accuracy of the numerical method, is the same steady shape calculated by beginning with a spherical initial condition and the subcritical capillary number. In the case of a step change to $0.8C_c$ the drop midsection continues to thin and the drop slowly stretches indicating that breakup is imminent.

The evolution of the interface in response to a step change from $C = C_c$ to the subcritical shear rate $C = 0.5C_c$ is illustrated in figure 9. It is interesting that the midsection remains very thin and planar while the end retracts. Finally, the interfacial-tension-driven flow produced near the end overwhelms the extensional flow that tries to continue to thin the drop and a steady shape is established.

It appears clear that even though biaxial flows produce quite distorted drop shapes with very thin midsections, complete breakup of the drop is not evident in the biaxial flow for the extensions studied here, nor is it necessarily produced by abruptly changing to subcritical flow conditions. In many ways this is in marked contrast to the behaviour observed in uniaxial extensional flows. The basic reason for these observations of the stability of drops in biaxial flows can

be traced to the interfacial-tension-driven flow associated with the shape of the drop.

4. CONCLUSIONS

Although not extensive the numerical calculations discussed above demonstrate a critical capillary number for drop breakup in a biaxial extensional flow. This is in marked contrast to the result obtained by Kang & Leal (1988) where a bubble at low Reynolds number has an increasingly elongated steady shape as the capillary number is increased. Drop breakup in a biaxial extensional flow requires a much larger capillary number and the maximum steady drop deformation in a biaxial flow is significantly larger than in a uniaxial flow. Furthermore, in subcritical flows the drops produced by the biaxial flows appear more stable than the corresponding uniaxial flow cases in the sense that relaxation back to a steady shape occurs in most of the cases examined, even for highly deformed drops with very thin midsections. This is a direct consequence of the interfacial-tension-driven flow associated with the drop shape, which has a planar midsection with a bulbous surrounding ring.

REFERENCES

- Barthes-Biesel, D. & Acrivos, A. 1973 Deformation and burst of a liquid droplet freely suspended in a linear shear field. *J. Fluid Mech.* **61**, 1-21.
- Bentley, B.J. & Leal, L.G. 1986 An experimental investigation of drop deformation and breakup in steady two-dimensional linear flows. *J. Fluid Mech.* **167**, 241-283.
- Frankel, N.A. & Acrivos, A. 1970 The constitutive equation for a dilute emulsion. *J. Fluid Mech.* **44**, 65-78.
- Hinze, J.O. 1955 Fundamentals of the hydrodynamic mechanism of splitting in dispersion processes. *AIChE J.* **1**, 289-295.
- Kang, I.S. & Leal, L.G. 1988 Numerical solution of axisymmetric, unsteady free-boundary problems at finite Reynolds number I. Deformation of a bubble in a biaxial straining flow. *Phys. Fluids* (in preparation).
- Khakhar, D.V. & Ottino, J.M. 1986 A note on the linear vector model of Olbricht, Rallison and Leal as applied to the breakup of slender axisymmetric drops. *J. Non-Newtonian Fluid Mech.* **21**, 127-131.
- Lewis, D.A. & Davidson, J.F. 1982 Bubble splitting in shear flows. *Trans. Inst. Chem. Eng.* **60**, 283-291.
- Olbricht, W.L., Rallison, J.M. & Leal, L.G. 1982 Strong flow criteria based on microstructure deformation. *J. Non-Newtonian Fluid Mech.* **10**, 291-318.
- Rallison, J.M. & Acrivos, A. 1978 A numerical study of the deformation and burst of a viscous drop in general shear flows. *J. Fluid Mech.* **89**, 191-200.
- Taylor, G.I. 1932 The viscosity of a fluid containing small drops of another fluid. *Proc. R. Soc. Lond.* **A138**, 41-48.
- Taylor, G.I. 1934 The formation of emulsions in definable fields of flow. *Proc. R. Soc. Lond.* **A146**, 501-523.

FIGURE CAPTIONS

- Figure 1 Schematic of drop deformation in a biaxial flow and definition of the variables.
- Figure 2 Drop deformation versus capillary number in a biaxial extensional flow. $\lambda = 1.0$. The solid line represents the numerical simulation, the short dashed line represents the $O(C)$ result of Barthes-Biesel & Acrivos and the long dashed line the $O(C^2)$ result. Several numerically generated shapes are included.
- Figure 3 Comparison of drop deformation in a biaxial extensional flow and in a uniaxial extensional flow. The solid curve is the numerical calculation for a biaxial flow and the dashed curve the numerical calculation for a uniaxial flow.
- Figure 4 Drop deformation versus capillary number in a biaxial extensional flow. $\lambda = 10.0$. The solid line represents the numerical simulation, the short dashed line represents the $O(C)$ result of Barthes-Biesel & Acrivos and the long dashed line the $O(C^2)$ result. Several numerically generated shapes are included.
- Figure 5 Time-dependent drop deformation in a biaxial flow at the critical capillary number. Dimensionless drop length $\frac{L}{a}$ as a function of time. $\lambda = 1.0$.
- Figure 6 Transient deformation at the critical capillary number. $\lambda = 1.0, C_c = 0.41$. The shapes shown are at $t = 0.0, 36.0, 60.0, 72.0$ and 80.0 . The initial shape is the most highly deformed shape shown in figure 2. Notice the very thin, almost planar midsection formed during the stretching process.
- Figure 7 Relaxation of an initially extended drop in an otherwise quiescent fluid. The shapes correspond to times (measured from the instant the flow is stopped) $t = 0.0, 2.0, 4.0, 6.0$ and 12.0 . The initial shape is the most highly deformed shape shown in figure 6.

Figure 8 The effect of subcritical flows on deformation and breakup of an initially extended drop. Step change from $C = C_c$ to $0.5C_c, 0.65C_c$ and $0.8C_c$.

Figure 9 Drop shape evolution during the relaxation of an initially extended drop in a subcritical flow. $C = 0.5C_c$. The shapes correspond to times (measured from the instant the flow is changed) $t = 0.0, 4.0, 10.0, 12.0, 26.0$.

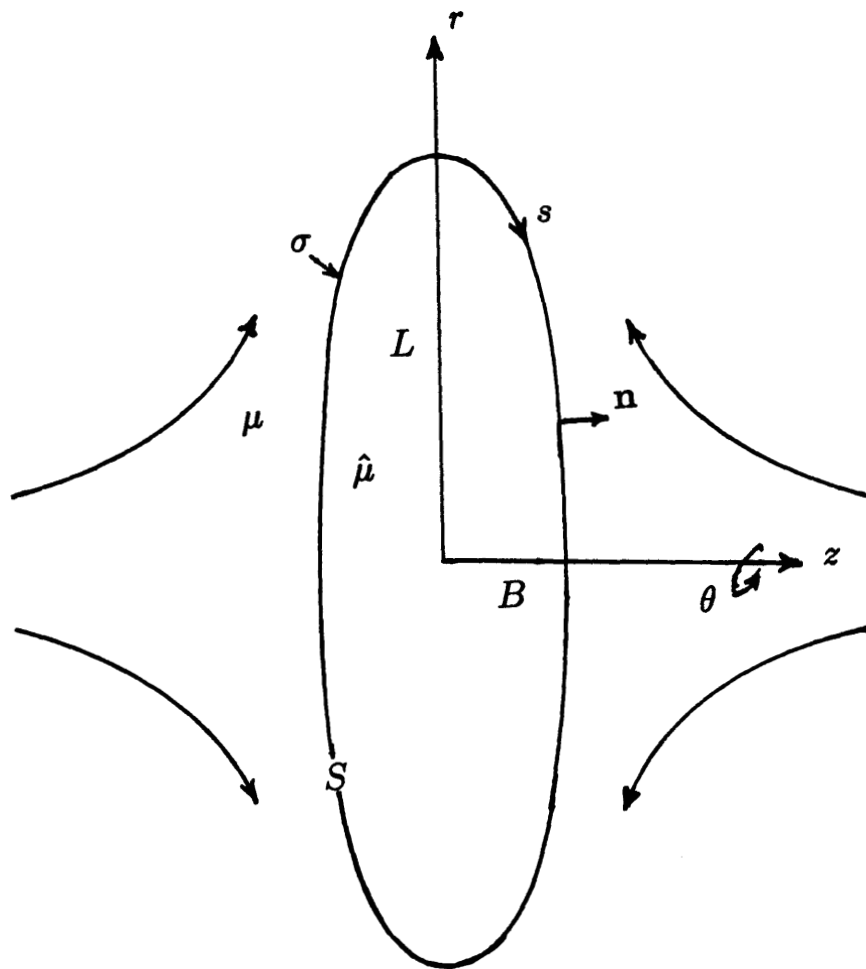


Figure 1

$\lambda = 1.0$

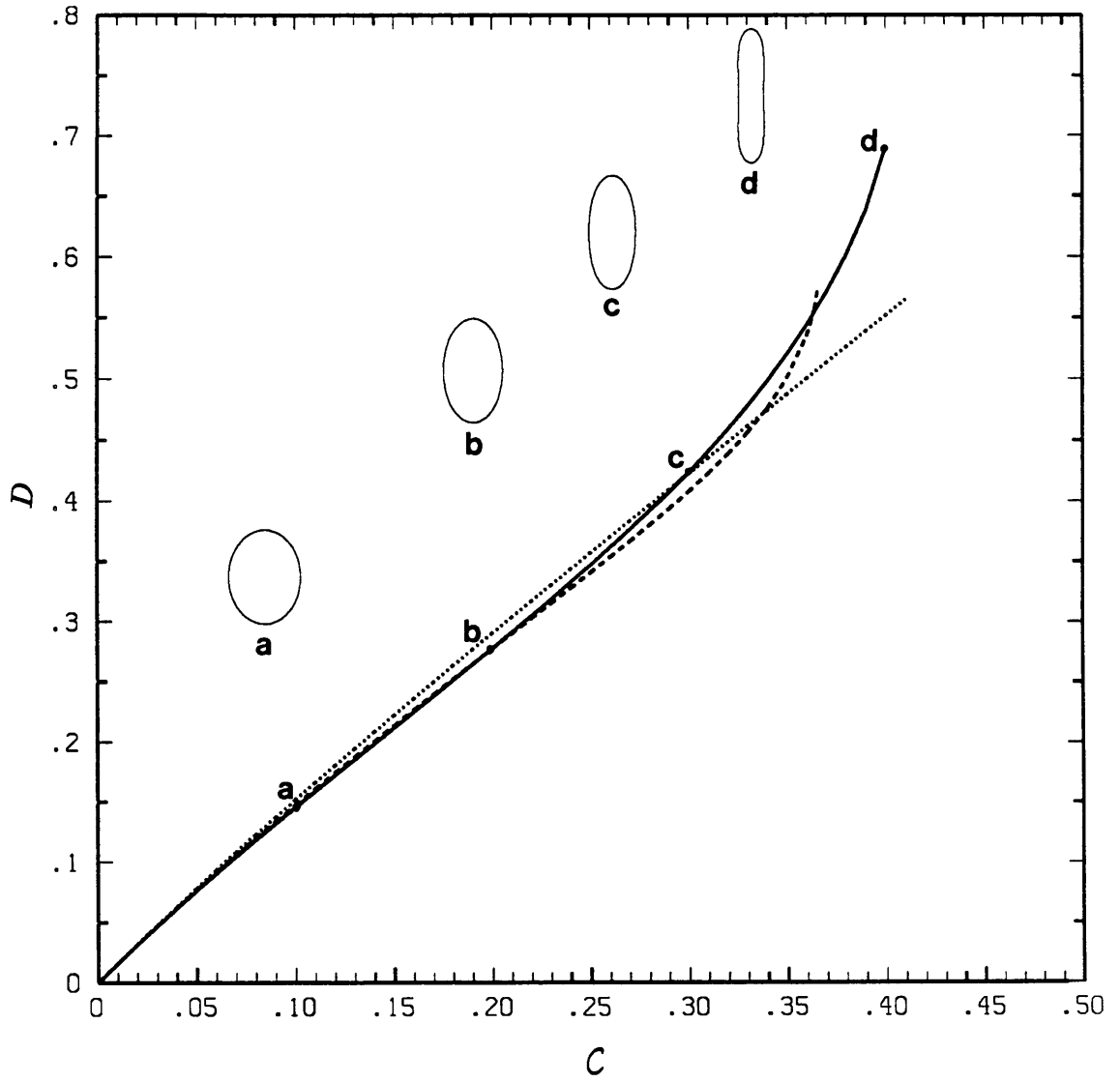


Figure 2

$\lambda = 1.0$

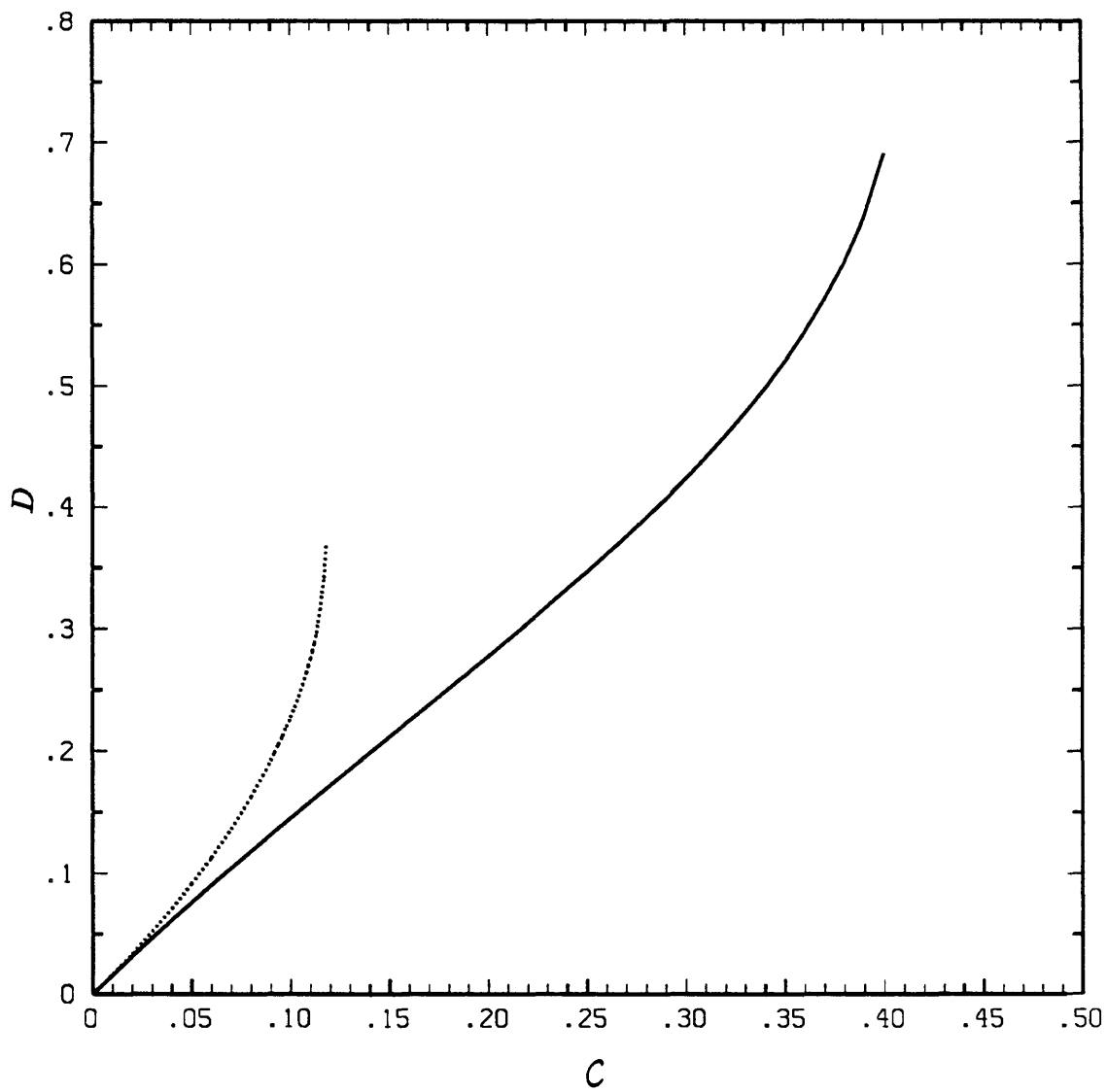


Figure 3

$\lambda = 10.0$

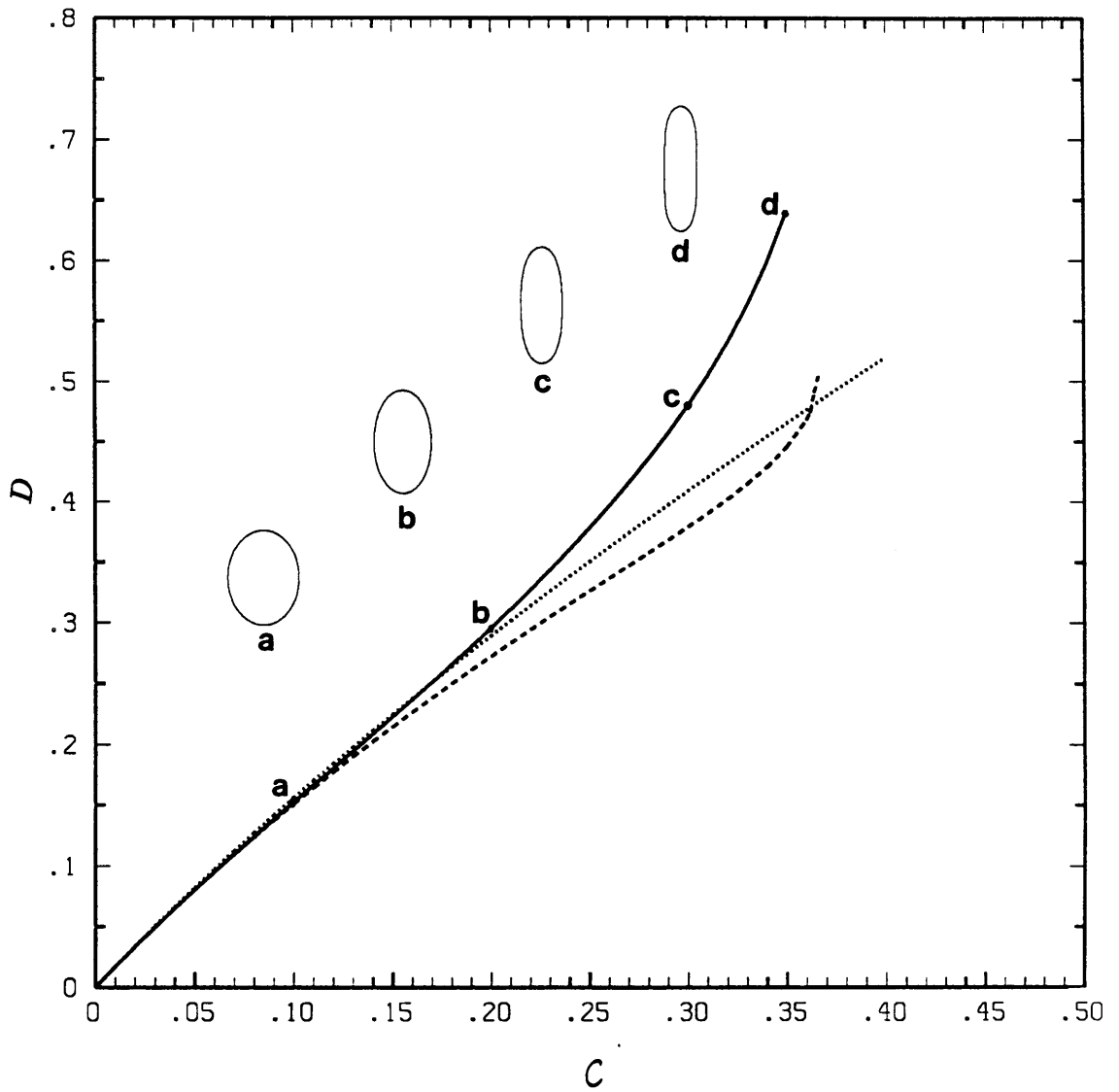


Figure 4

$$\lambda = 1.0$$

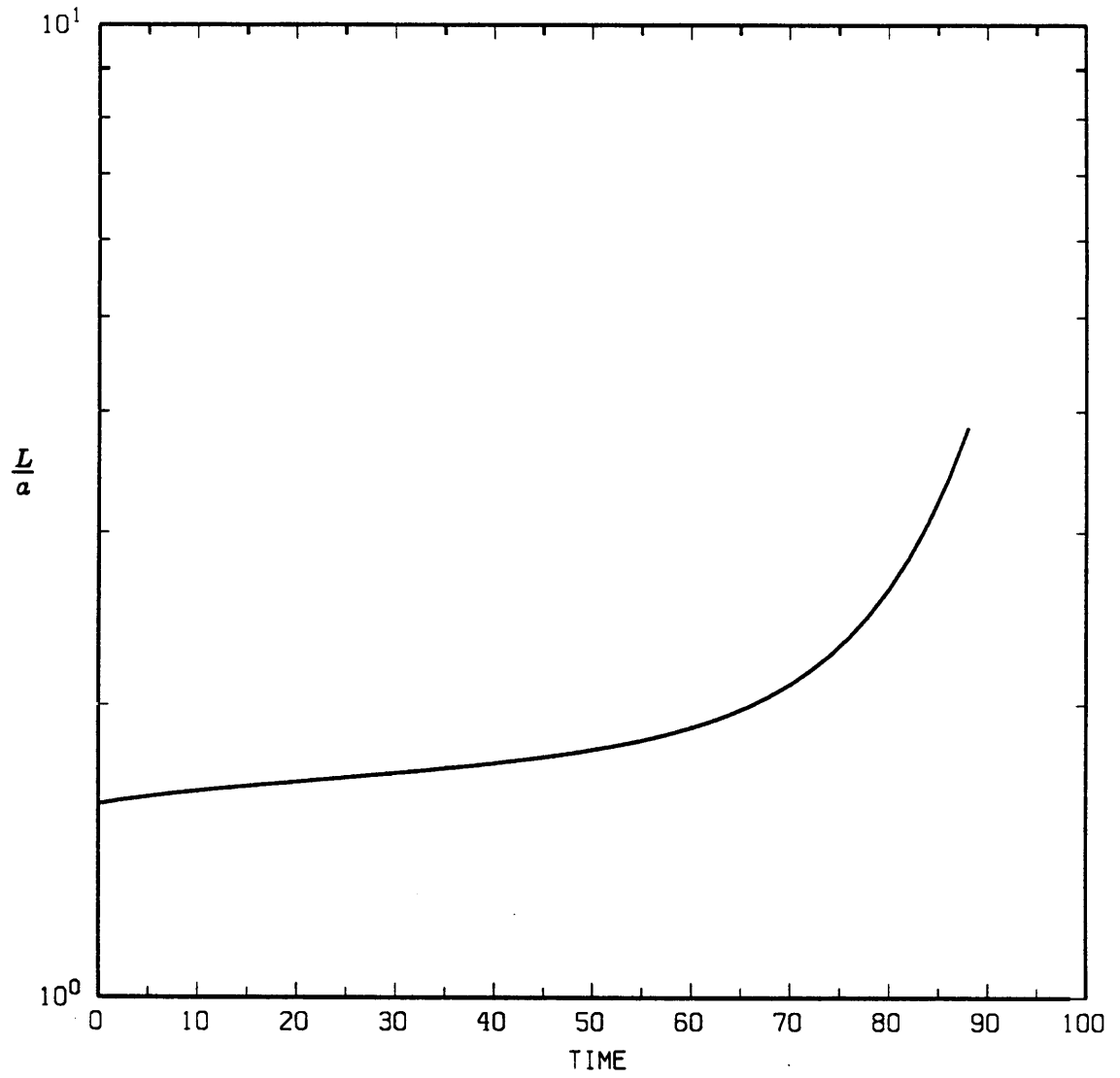


Figure 5

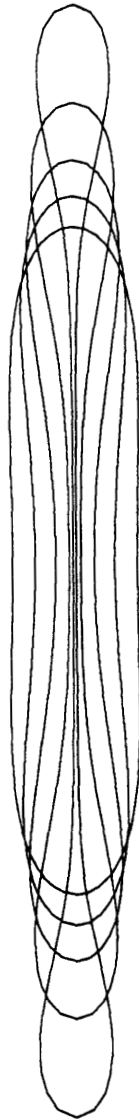


Figure 6

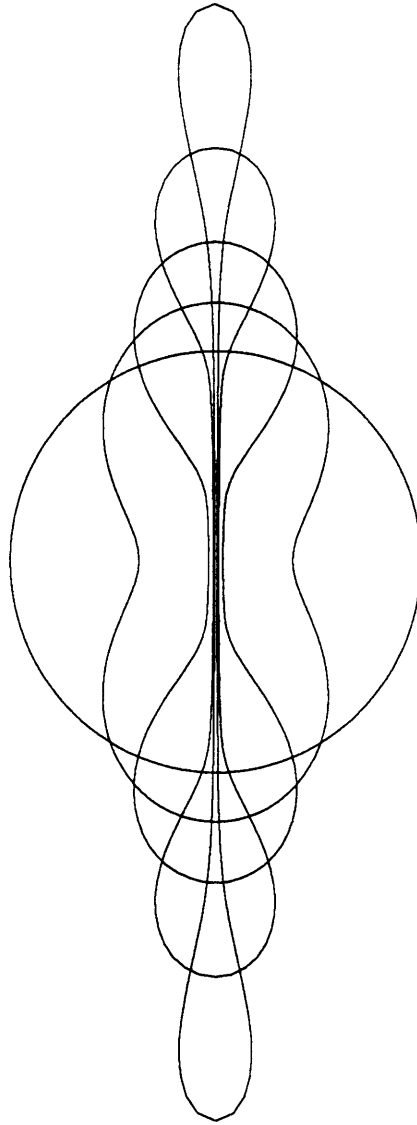


Figure 7

$$\lambda = 1.0$$

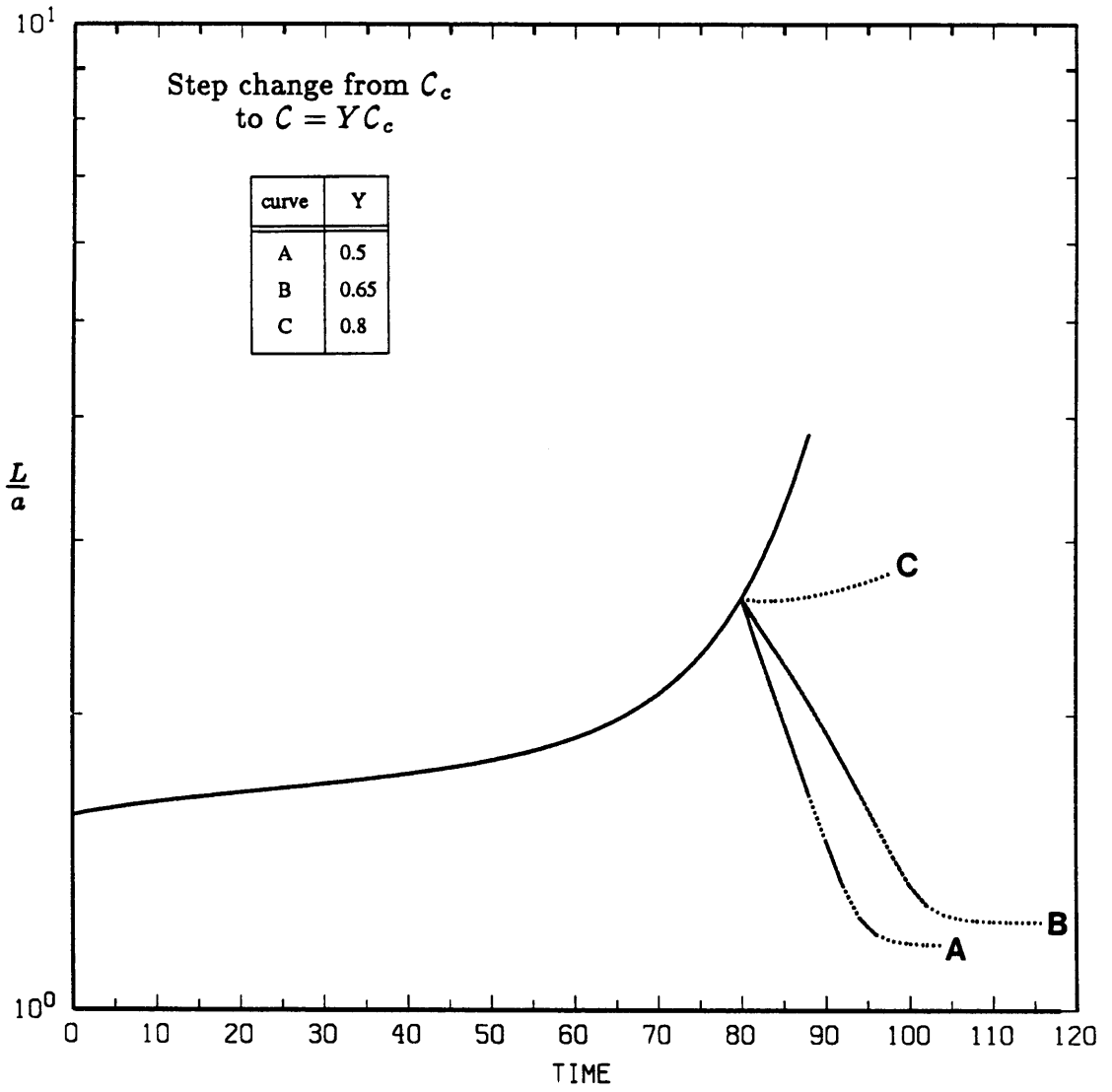


Figure 8

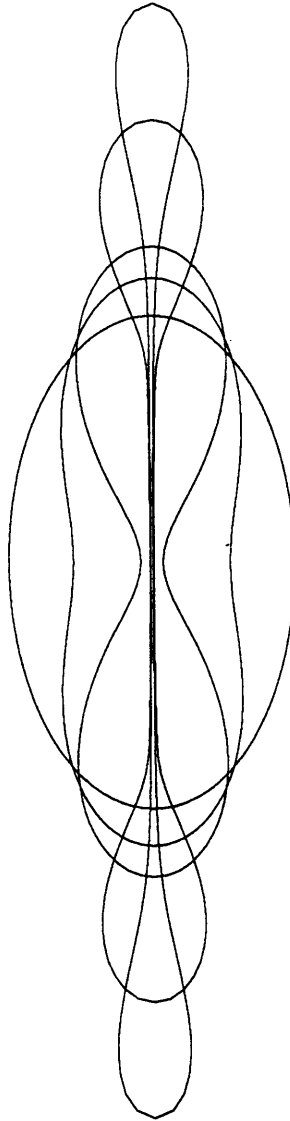


Figure 9

APPENDIX 2

IMPLEMENTING THE BOUNDARY INTEGRAL METHOD

In this appendix we provide additional details concerning the solution of the integral equation that arises in application of the boundary integral method to the drop deformation problem. This is an extended version of the discussion in Chapter 3 and includes most of the results necessary for the actual implementation of the numerical scheme.

1. GOVERNING EQUATIONS

For completeness we summarize the basic equations as they apply to the drop deformation problem. A general discussion is provided by Rallison & Acrivos (1978). The velocity, pressure and stress fields in the continuous phase will be denoted by $(\mathbf{u}, p, \mathbf{T})$ and in the droplet phase by $(\hat{\mathbf{u}}, \hat{p}, \hat{\mathbf{T}})$. Since our initial concern was the relaxation of an extended liquid droplet in an otherwise quiescent fluid, we chose to nondimensionalize velocities by $u_c = \frac{\sigma}{\mu}$, pressures by $p_c = \frac{\mu u_c}{l_c}$, $\hat{p}_c = \frac{\hat{\mu} \hat{u}_c}{\hat{l}_c}$ where l_c is an appropriate length scale, and time by the convective time scale $t_c = \frac{l_c}{u_c}$. The dimensionless form of the governing equations are the quasi-steady Stokes equations and the continuity equation for each phase

$$\nabla^2 \mathbf{u} = \nabla p \quad \nabla^2 \hat{\mathbf{u}} = \nabla \hat{p} \quad (1)$$

$$\nabla \cdot \mathbf{u} = 0 \quad \nabla \cdot \hat{\mathbf{u}} = 0$$

subject to the boundary conditions

$$\mathbf{u} \rightarrow \mathbf{u}_\infty \quad \text{as } |\mathbf{x}| \rightarrow \infty \quad (2a)$$

$$\mathbf{u} = \hat{\mathbf{u}} \quad \text{for } \mathbf{x}_s \in S \quad (2b)$$

$$\mathbf{n} \cdot \mathbf{T} - \lambda \mathbf{n} \cdot \hat{\mathbf{T}} = \mathbf{n} (\nabla_s \cdot \mathbf{n}) \quad \text{for } \mathbf{x}_s \in S \quad (2c)$$

In these equations, the position vector \mathbf{x} locates a point in the fluid domain, \mathbf{x}_s specifically indicates a point on the fluid-fluid interface S , \mathbf{u}_∞ denotes the imposed flow at infinity that is responsible for deforming an otherwise spherical droplet, \mathbf{n} denotes the unit outward normal directed from the droplet phase to

the continuous phase and $\nabla_s \cdot \mathbf{n}$ represents the mean curvature of the fluid-fluid interface. Also, $\lambda = \frac{\hat{\mu}}{\mu}$ denotes the ratio of fluid viscosities and, because of the choice of the characteristic velocity, the capillary number $C = \frac{Ga\mu}{\sigma}$ appears in the dimensionless form of \mathbf{u}_∞ (G denoted the fluid shear rate and a is the undeformed radius of the drop). Finally, the drop shape evolves according to the kinematic condition, which may be stated as

$$\frac{d\mathbf{x}_s}{dt} = \mathbf{n}(\mathbf{u} \cdot \mathbf{n}). \quad (3)$$

In the boundary integral formulation, the velocity and pressure fields in the suspending phase may be written as integrals over the drop surface

$$\mathbf{u}(\mathbf{x}) = \mathbf{u}_\infty - \int_S \mathbf{J}(\mathbf{x} - \mathbf{y}) \cdot (\mathbf{T} \cdot \mathbf{n}) dS(\mathbf{y}) - \int_S \mathbf{n} \cdot \mathbf{K}(\mathbf{x} - \mathbf{y}) \cdot \hat{\mathbf{u}} dS(\mathbf{y}) \quad (4a)$$

$$p(\mathbf{x}) = p_\infty - \int_S \mathbf{L}(\mathbf{x} - \mathbf{y}) \cdot (\mathbf{T} \cdot \mathbf{n}) dS(\mathbf{y}) - \int_S \mathbf{n} \cdot \mathbf{M}(\mathbf{x} - \mathbf{y}) \cdot \hat{\mathbf{u}} dS(\mathbf{y}) \quad (4b)$$

and in the droplet phase as

$$\hat{\mathbf{u}}(\mathbf{x}) = \int_S \mathbf{J}(\mathbf{x} - \mathbf{y}) \cdot (\hat{\mathbf{T}} \cdot \mathbf{n}) dS(\mathbf{y}) + \int_S \mathbf{n} \cdot \mathbf{K}(\mathbf{x} - \mathbf{y}) \cdot \hat{\mathbf{u}} dS(\mathbf{y}) \quad (5a)$$

$$\hat{p}(\mathbf{x}) = p_o + \int_S \mathbf{L}(\mathbf{x} - \mathbf{y}) \cdot (\hat{\mathbf{T}} \cdot \mathbf{n}) dS(\mathbf{y}) + \int_S \mathbf{n} \cdot \mathbf{M}(\mathbf{x} - \mathbf{y}) \cdot \hat{\mathbf{u}} dS(\mathbf{y}) \quad (5b)$$

where \mathbf{y} denotes the variable of integration. The kernels $\mathbf{J}, \mathbf{K}, \mathbf{L}, \mathbf{M}$ are known functions of position:

$$\mathbf{J} = \frac{1}{8\pi} \left[\frac{\mathbf{I}}{|\mathbf{x} - \mathbf{y}|} + \frac{(\mathbf{x} - \mathbf{y})(\mathbf{x} - \mathbf{y})}{|\mathbf{x} - \mathbf{y}|^3} \right] \quad (6a)$$

$$\mathbf{K} = -\frac{3}{4\pi} \frac{(\mathbf{x} - \mathbf{y})(\mathbf{x} - \mathbf{y})(\mathbf{x} - \mathbf{y})}{|\mathbf{x} - \mathbf{y}|^3} \quad (6b)$$

$$\mathbf{L} = \frac{1}{4\pi} \frac{(\mathbf{x} - \mathbf{y})}{|\mathbf{x} - \mathbf{y}|^3} \quad (6c)$$

$$\mathbf{M} = \frac{1}{2\pi} \left[\frac{\mathbf{I}}{|\mathbf{x} - \mathbf{y}|^3} - \frac{3(\mathbf{x} - \mathbf{y})(\mathbf{x} - \mathbf{y})}{|\mathbf{x} - \mathbf{y}|^5} \right] \quad (6d)$$

Here, p_∞ and p_o denote constant reference pressures. Only one of these two values is independent. Specification of one, say p_∞ allows the other, in principle, to be determined using the calculated velocity fields in conjunction with the normal stress balance. The integral involving \mathbf{J} is known as the single-layer and the integral involving \mathbf{K} is known as the double-layer. The single-layer is a continuous function of \mathbf{x} including $\mathbf{x} \rightarrow \mathbf{x}_s \in S$ while the double-layer suffers a discontinuity as $\mathbf{x} \rightarrow \mathbf{x}_s \in S$. Also, both integrands are singular in the limit $\mathbf{y} \rightarrow \mathbf{x}_s$, but in each instance, the integral is integrable in the sense of a Cauchy principal value.

Since we are interested in the evolution of the interface, these equations are written so that the interfacial velocity is calculated directly. Equations valid for points on the interface can be derived by taking the limit of equations (4a) and (5a) as $\mathbf{x} \rightarrow \mathbf{x}_s \in S$ and making use of the well-known jump conditions on the double-layer:

$$\begin{aligned} \frac{1}{2}\mathbf{u}(\mathbf{x}_s) = & \mathbf{u}_\infty(\mathbf{x}_s) - \int_S \mathbf{J}(\mathbf{x}_s - \mathbf{y}) \cdot (\mathbf{T} \cdot \mathbf{n}) dS(\mathbf{y}) \\ & - \int_S \mathbf{n} \cdot \mathbf{K}(\mathbf{x}_s - \mathbf{y}) \cdot \hat{\mathbf{u}} dS(\mathbf{y}) \end{aligned} \quad (7)$$

$$\begin{aligned} \frac{1}{2}\hat{\mathbf{u}}(\mathbf{x}_s) = & \int_S \mathbf{J}(\mathbf{x}_s - \mathbf{y}) \cdot (\hat{\mathbf{T}} \cdot \mathbf{n}) dS(\mathbf{y}) \\ & + \int_S \mathbf{n} \cdot \mathbf{K}(\mathbf{x}_s - \mathbf{y}) \cdot \hat{\mathbf{u}} dS(\mathbf{y}) \end{aligned} \quad (8)$$

Then, multiplying equation (8) by λ , adding to equation (7) and using the boundary conditions yields the following equation for the interfacial velocity:

$$\begin{aligned} (1 + \lambda)\hat{\mathbf{u}}(\mathbf{x}_s) = & 2\mathbf{u}_\infty(\mathbf{x}_s) - 2 \int_S \mathbf{J}(\mathbf{x}_s - \mathbf{y}) \cdot \mathbf{n}(\mathbf{y})(\nabla_s \cdot \mathbf{n}) dS(\mathbf{y}) \\ & - 2(1 - \lambda) \int_S \mathbf{n} \cdot \mathbf{K}(\mathbf{x}_s - \mathbf{y}) \cdot \hat{\mathbf{u}} dS(\mathbf{y}) \end{aligned} \quad (9)$$

Hence, if the drop shape is known at some instant, then the determination of the interfacial velocities that correspond to this drop shape and given values

of C and λ requires the solution of this integral equation of the second kind. Once the interfacial velocities are determined, the kinematic condition (3) can be used to update the drop shape. In principle, with the interfacial velocities established, equations (7) and (8) can be similarly solved to yield the stresses exerted by the interior and exterior fluids on the interface. With the interfacial velocities and stresses thus determined, equations (4) and (5) can be used to compute the velocity and pressure anywhere in the flow domain.

The case $\lambda = 1$ is especially straightforward as the above equations simplify to

$$\mathbf{u}(\mathbf{x}) = \mathbf{u}_\infty(\mathbf{x}) - \int_S \mathbf{J}(\mathbf{x} - \mathbf{y}) \cdot \mathbf{n}(\mathbf{y}) (\nabla_s \cdot \mathbf{n}) dS(\mathbf{y}) \quad (10a)$$

$$p(\mathbf{x}) = p_\infty - \int_S \mathbf{L}(\mathbf{x} - \mathbf{y}) \cdot \mathbf{n}(\mathbf{y}) (\nabla_s \cdot \mathbf{n}) dS(\mathbf{y}) \quad (10b)$$

As discussed by Rallison & Acrivos (1978), these equations are actually valid for all $\mathbf{x} \in V$ and \hat{V} .

2. SIMPLIFICATION FOR AXISYMMETRIC PROBLEMS

In general, there is no known analytic solution to these equations so that we must resort to numerical methods. We restrict our discussion to the case of axisymmetric drop shapes. The fully three-dimensional case has been considered by Rallison (1981) and Higdon & Schnepper (1987) and is numerically more difficult and CPU intensive. In the axisymmetric case the two-dimensional surface integral can be reduced to a one-dimensional line integral by performing the azimuthal integration analytically. In terms of a cylindrical coordinate system (r, z, θ) and the cartesian system (x, y, z) (see figure 1) we write

$$\mathbf{x}_s = r_s \mathbf{e}_x + z_s \mathbf{e}_z \quad (11a)$$

$$\mathbf{y} = r \cos\theta \mathbf{e}_x + r \sin\theta \mathbf{e}_y + z \mathbf{e}_z \quad (11b)$$

$$\mathbf{n} = n_r \cos\theta \mathbf{e}_x + n_r \sin\theta \mathbf{e}_y + n_z \mathbf{e}_z \quad (11c)$$

$$\mathbf{u} = u_r \cos\theta \mathbf{e}_x + u_r \sin\theta \mathbf{e}_y + u_z \mathbf{e}_z \quad (11d)$$

and the differential surface element is given by

$$dS = r \sqrt{1 + \left(\frac{dr}{dz}\right)^2} dz d\theta \quad (11e)$$

where

$$0 \leq z \leq L \quad \text{and} \quad 0 \leq \theta \leq 2\pi.$$

The integration involving θ can be performed analytically in terms of elliptic functions. The result of the integration is

$$\begin{aligned} (1 + \lambda)\mathbf{u}(\mathbf{x}_s) = & 2\mathbf{u}_\infty - \frac{1}{4\pi} \int_s \begin{bmatrix} J_{rr}^* & J_{rz}^* \\ J_{zr}^* & J_{zz}^* \end{bmatrix} \begin{bmatrix} n_r \\ n_z \end{bmatrix} (\nabla_s \cdot \mathbf{n}) d\bar{s} \\ & - \frac{3}{4\pi} \int_s \begin{bmatrix} K_{rr}^* & K_{rz}^* \\ K_{zr}^* & K_{zz}^* \end{bmatrix} \begin{bmatrix} \hat{u}_r \\ \hat{u}_z \end{bmatrix} d\bar{s} \end{aligned} \quad (12)$$

where

$$d\bar{s} = r \sqrt{1 + \left(\frac{dr}{dz}\right)^2} dz.$$

The elements J_{ij}^* and K_{ij}^* are given by

$$J_{rr}^* = E(1, 1, A, B) - r_s r [E(0, 3, A, B) + E(2, 3, A, B)] + (r_s^2 + r^2) E(1, 3, A, B)$$

$$J_{rz}^* = (z_s - z) [r_s E(0, 3, A, B) - r E(1, 3, A, B)]$$

$$J_{zr}^* = (z_s - z) [r_s E(1, 3, A, B) - r E(0, 3, A, B)]$$

$$J_{zz}^* = E(0, 1, A, B) + (z_s - z)^2 E(0, 3, A, B)$$

and

$$K_{rr}^* = -r_s r [n_z(z_s - z) - r n_r] E(0, 5, A, B) + [(n_z(z_s - z) - r n_r)(r_s^2 + r^2) - n_s r_s^2 r] E(1, 5, A, B) + r_s [n_r(r_s^2 + 2r^2) - r(z_s - z)n_z] E(2, 5, A, B) - r r_s^2 n_r E(3, 5, A, B)$$

$$K_{rz}^* = (z_s - z) [r_s (n_z(z_s - z) - r n_r) E(0, 5, A, B) + [n_r(r_s^2 + r^2) - r(z_s - z)n_z] E(1, 5, A, B) - r r_s n_r E(2, 5, A, B)]$$

$$K_{zr}^* = (z_s - z) [-r (n_z(z_s - z) - r n_r) E(0, 5, A, B) + r_s (n_z(z_s - z) - 2r n_r) E(1, 5, A, B) + r_s^2 n_r E(2, 5, A, B)]$$

$$K_{zz}^* = (z_s - z)^2 [(n_z(z_s - z) - r n_r) E(0, 5, A, B) + r_s n_r E(1, 5, A, B)]$$

with

$$A^2 = r_s^2 + r^2 + (z_s - z)^2$$

$$B^2 = 2r_s r .$$

In these equations the integration variables are (r, z) . The point of interest on the drop surface is (r_s, z_s) and the $E(n, m, A, B)$ involve elliptic integrals of the first and second kind and are given by Lee & Leal (1982) (an alternative form is given by Youngren & Acrivos 1975). The fluid-fluid interface is now represented simply as an arc, s .

A similar integration can be performed on the equations for the pressure field. The result is

$$\hat{p}(\mathbf{x}) = p_o + \int_s \begin{bmatrix} L_r^* \\ L_z^* \end{bmatrix} \begin{bmatrix} \hat{t}_r \\ \hat{t}_z \end{bmatrix} d\bar{s} + \int_s \begin{bmatrix} M_r^* \\ M_z^* \end{bmatrix} \begin{bmatrix} \hat{u}_r \\ \hat{u}_z \end{bmatrix} d\bar{s} \quad (13)$$

where (\hat{t}_r, \hat{t}_z) are the two components of the stress vector $\hat{\mathbf{T}} \cdot \mathbf{n}$ and

$$L_r^* = r_s E(1, 3, A, B) - r E(0, 3, A, B)$$

$$L_z^* = (z_s - z) E(0, 3, A, B)$$

$$M_r^* = n_r E(0, 3, A, B) + 3r[(z_s - z)n_z - n_r r] E(0, 5, A, B) \\ + 3[2n_r r_s r - (z_s - z)n_z r_s] E(1, 5, A, B) - 3n_r r_s^2 E(2, 5, A, B)$$

$$M_z^* = n_z E(0, 3, A, B) - 3(z_s - z)[(z_s - z)n_z - n_r r] E(0, 5, A, B) \\ - 3n_r r_s (z_s - z) E(1, 5, A, B)$$

3. DISCRETIZATION OF THE INTEGRAL EQUATION

These integrals equations are solved numerically by discretizing the interface (now simply an arc) and recasting (12) as a system of linear equations, which can be solved using standard Gaussian elimination methods to yield the velocity distribution on the interface. There are three important aspects to the discretization : (1) accurate representation of the drop shape and curvature, (2) approximation of the variation of velocity along the interface (and if the interior and exterior velocity and pressure fields are desired the interfacial stress distribution must similarly be approximated) and (3) accurate evaluation of the integrals. We discuss each of these topics below.

To begin with, because many of the motions we intend to study are driven by the nonequilibrium shape of the drop it is necessary to represent the interface shape of highly elongated drop shapes as accurately as possible. For this reason two alternative methods were developed to approximately represent the interface. In both methods the interface is discretized into $2N-2$ boundary elements with node points at the end of each element (therefore there are $2N-1$ node points). The first scheme makes use of cylindrical coordinates near the middle of the drop, spherical coordinates near the end of the drop (in other words the surface is locally described by $r = r(z)$ and $\rho = \rho(\phi)$, respectively), cubic splines are used to generate twice-continuously differentiable representations of the interface, and the two representations are patched together by requiring the first

and second derivatives to be continuous within some tolerance (typically 10^{-6}) at the point of overlap. In this manner, the drop shape is described by a smooth function that is essentially twice-continuously differentiable everywhere. The second scheme used an arclength parametrization method. Letting s represent a normalized measure of arclength ($0 \leq s \leq 1$), the collocation points on the interface are parametrized so that $z = z(s), r = r(s)$ describes the fluid-fluid interface and a twice-continuously differentiable representation is generated using cubic splines. Both methods work very well, although for similar numbers of points, the former scheme is more successful for very elongated shapes with nearly spherical ends while the latter scheme performs better for very slender shapes with nearly pointed ends. Also, the arclength parametrization scheme is much easier to code and much more flexible for a variety of problems. Consequently, it is the preferred scheme for drop deformation in biaxial flows discussed in Appendix 1 and, as discussed in Chapter 6, the arclength parametrization scheme is the natural approach for drop deformation in the presence of surface-active agents when transport along the interface must be described.

Next it is necessary to approximate the variation of the unknown velocity (and, if desired, the stress) along the interface. In all of our work, the unknown velocity and stress components on the interface are assumed to vary *linearly* over each element. Compared to the more common approximation of treating the unknowns as constant over each element, this approximation yields smoother and more accurate velocity variations, especially for the highly elongated drop shapes, where, in the interest of computation speed, as few collocation points as possible are used. For example, the velocity is expressed as

$$\mathbf{u} = \mathbf{u}^j \left(\frac{z_{j+1} - z}{z_{j+1} - z_j} \right) + \mathbf{u}^{j+1} \left(\frac{z - z_j}{z_{j+1} - z_j} \right) \quad (14)$$

for $0 \leq z_j \leq z \leq z_{j+1}$ where \mathbf{u}^j represents the velocity at the j^{th} node point.

It is then straightforward to discretize the integral equation, although care must be taken to keep track of all the elements. The integral equation is written

at each node point \mathbf{x}_i . For example, the double-layer is discretized as

$$\int_s \mathbf{K}^i \cdot \mathbf{u} \, d\bar{s} = \sum_{j=-(n-1)}^{-1} \int_{s_j} \mathbf{K}^{ij} \cdot \mathbf{u} \, d\bar{s} + \sum_{j=1}^{n-1} \int_{s_j} \mathbf{K}^{ij} \cdot \mathbf{u} \, d\bar{s} \quad (15)$$

where the superscript i on \mathbf{K} denotes evaluation at collocation point \mathbf{x}_i and the superscript j on \mathbf{K} denotes integration over element j . The surface element $j < 0$ corresponds to $z < 0$. We have dropped the star notation introduced in equation (12) to distinguish the general three dimensional case from the axisymmetric situation and now $\mathbf{u} = (u_r, u_z)$.

Substituting the approximation for the velocity field into (15) gives

$$\begin{aligned} \int_s \mathbf{K}^i \cdot \mathbf{u} \, d\bar{s} = & \sum_{j=-(N-1)}^{-1} \int_{s_j} \mathbf{K}^{ij-} \cdot \left[-\mathbf{u}^j \left(\frac{|z| - z_{j+1}}{z_{j+1} - z_j} \right) + \mathbf{u}^{j+1} \left(\frac{|z| - z_j}{z_{j+1} - z_j} \right) \right] d\bar{s} \\ & + \sum_{j=1}^{N-1} \int_{s_j} \mathbf{K}^{ij} \cdot \left[\mathbf{u}^j \left(\frac{z_{j+1} - z}{z_{j+1} - z_j} \right) + \mathbf{u}^{j+1} \left(\frac{z - z_j}{z_{j+1} - z_j} \right) \right] d\bar{s} \end{aligned} \quad (16)$$

where the superscript $-$ on \mathbf{K}^{ij-} reminds us that this kernel is evaluated for $z < 0$. Furthermore the fore-aft symmetry requires

$$u_r(z) = u_r(-z) \quad \text{and} \quad u_z(z) = -u_z(-z) \quad (17)$$

so that

$$\begin{aligned} \int_s \mathbf{K}^i \cdot \mathbf{u} \, d\bar{s} = & \sum_{j=1}^{N-1} \begin{aligned} & u_r^j (\bar{K}_{rr}^{ij-} + \bar{K}_{rr}^{ij}) + u_r^{j+1} (\hat{K}_{rr}^{ij-} + \hat{K}_{rr}^{ij}) \\ & u_z^j (\bar{K}_{zr}^{ij-} + \bar{K}_{zr}^{ij}) + u_z^{j+1} (\hat{K}_{zr}^{ij-} + \hat{K}_{zr}^{ij}) \end{aligned} \\ & + \sum_{j=1}^{N-1} \begin{aligned} & + u_z^j (\bar{K}_{rz}^{ij-} - \bar{K}_{rz}^{ij}) + u_z^{j+1} (-\hat{K}_{rz}^{ij-} + \hat{K}_{rz}^{ij}) \\ & + u_z^j (\bar{K}_{zz}^{ij-} - \bar{K}_{zz}^{ij}) + u_z^{j+1} (-\hat{K}_{zz}^{ij-} + \hat{K}_{zz}^{ij}) \end{aligned} \end{aligned} \quad (18)$$

where

$$\bar{\mathbf{K}}^{ij} = \int_{s_j} \mathbf{K}^{ij} \left(\frac{|z| - z_{j+1}}{z_{j+1} - z_j} \right) d\bar{s} \quad (19a)$$

and

$$\hat{\mathbf{K}}^{ij} = \int_{s_j} \mathbf{K}^{ij} \left(\frac{|z| - z_j}{z_{j+1} - z_j} \right) d\bar{s}. \quad (19b)$$

The absolute value $|z|$ is introduced so that the equations hold for all values of z , including $z < 0$.

The final form of the linear set of equations is

$$\mathbf{H}\mathbf{v} = \mathbf{b} \quad (20)$$

where \mathbf{H} is a $2N \times 2N$ matrix and

$$\mathbf{v} = (u_r^1, u_r^2, \dots, u_r^N, u_z^1, u_z^2, \dots, u_z^N).$$

The elements of the matrix \mathbf{H} are given by

$$\begin{aligned} H_{ij} &= \delta_{ij} - [K_{rr}^{ij} + K_{rr}^{ij-} + \hat{K}_{rr}^{i(j-1)-} + \hat{K}_{rr}^{i(j-1)}] \quad 1 \leq i, j \leq N \\ H_{ij} &= -[K_{rz}^{ij} + K_{rz}^{ij-} + \hat{K}_{rz}^{i(j-1)-} + \hat{K}_{rz}^{i(j-1)}] \quad 1 \leq i \leq N, N+1 \leq j \leq 2N \\ H_{ij} &= -[K_{zr}^{ij} + K_{zr}^{ij-} + \hat{K}_{zr}^{i(j-1)-} + \hat{K}_{zr}^{i(j-1)}] \quad N+1 \leq i \leq 2N, 1 \leq j \leq N \\ H_{ij} &= \delta_{ij} - [K_{zz}^{ij} + K_{zz}^{ij-} + \hat{K}_{zz}^{i(j-1)-} + \hat{K}_{zz}^{i(j-1)}] \quad N+1 \leq i, j \leq 2N. \end{aligned}$$

Also, it is clear from this simplified expression that $\mathbf{K}^{i0} = 0$.

The vector \mathbf{b} represents

$$\mathbf{b} = (b_r^1, b_r^2, \dots, b_r^N, b_z^1, b_z^2, \dots, b_z^N)$$

and, again using the superscript notation to represent evaluation at collocation point \mathbf{x}_i and dropping the $*$ notation

$$\mathbf{b}^i = \int_s \mathbf{J}^i \cdot \mathbf{n} (\nabla_s \cdot \mathbf{n}) d\bar{s}.$$

From the symmetry of the problem

$$u_z^1 = 0 \quad \text{and} \quad u_r^N = 0$$

so that \mathbf{H} is reduced to a nonsingular $2(N-1) \times 2(N-1)$ system before inverting.

All the integrals are performed using a five point Gauss quadrature scheme. In the vicinity of the singularity the integrand varies rapidly and extra care is taken by subdividing the interval of interest into three smaller intervals prior to integrating. A very small region, typically 10^{-3} or 10^{-4} the size of an interval, is cut out around the singularity and the integration over this small region is performed analytically.

REFERENCES

- Higdon, J.J.L. & Schnepfer, C.A. 1987 Interaction and deformation of viscous drops. *Presented at the AIChE National Meeting.*
- Lee, S. H. & Leal, L. G. 1982 The motion of a sphere in the presence of a deformable interface. II. A numerical study of the translation of a sphere normal to an interface. *J. Colloid Int. Sci.* **87**, 81-106.
- Rallison, J.M. & Acrivos, A. 1978 A numerical study of the deformation and burst of a viscous drop in an extensional flow. *J. Fluid Mech.* **89**, 191-200.
- Rallison, J.M. 1981 A numerical study of the deformation and burst of a viscous drop in general shear flows. *J. Fluid Mech.* **109**, 465-482.
- Youngren, G.K. & Acrivos, A. 1975 Stokes flow past a particle of arbitrary shape; a numerical method of solution. *J. Fluid Mech.* **69**, 377-403 (corrigendum **69**, 813).